5-2014

Engineering Bacterial Cellulose Scaffold and its Biomimetic Composites for Bone and Cartilage Tissue Regeneration

Pelagie Marlene Favi
University of Tennessee - Knoxville, pfavi@utk.edu

To the Graduate Council:

I am submitting herewith a dissertation written by Pelagie Marlene Favi entitled "Engineering Bacterial Cellulose Scaffold and its Biomimetic Composites for Bone and Cartilage Tissue Regeneration." I have examined the final electronic copy of this dissertation for form and content and recommend that it be accepted in partial fulfillment of the requirements for the degree of Doctor of Philosophy, with a major in Polymer Engineering.

Roberto Benson, Major Professor

We have read this dissertation and recommend its acceptance:

Madhu Dhar, Kevin Kit, Wei He, Deidra Mountain

Accepted for the Council:

Carolyn R. Hodges

Vice Provost and Dean of the Graduate School

(Original signatures are on file with official student records.)

Engineering Bacterial Cellulose Scaffold and its Biomimetic Composites for Bone and Cartilage Tissue Regeneration

A Dissertation Presented for the
Doctor of Philosophy
Degree
The University of Tennessee, Knoxville

Pelagie Marlene Favi
May 2014

DEDICATION

This dissertation is dedicated to my parents, my sister, my brother, my niece and son. They have supported my every endeavor without reservation and their encouragement enabled this wonderful achievement. Thank you very much for your enduring support.

ACKNOWLEDGEMENTS

I am extremely grateful to the generous grants and fellowships which have supported my education: The National Institute of Health Training Grant – Program for Excellence & Equity in Research (PEER) Graduate Fellowship*, The National GEM Consortium Fellowship sponsored by Oak Ridge National Laboratories, The National Institute for Mathematical and Biological Synthesis (NIMBioS) Graduate Fellowship**, and The Helen Jubin Fellowship. Research support for this work was provided by the Center of Excellence in Livestock Diseases and Human Health Grant, the Physicians Medical and Education Research Foundation Grant, and the Cardiothoracic Surgery Gift Fund.

This thesis would not have been possible without the help and support of many people. It is a pleasure to acknowledge the valuable help of Dr. Roberto Benson who has been an exceptional graduate advisor. Dr. Benson provided me with immense guidance, support and encouragement. I am very grateful for his time and commitment towards my education, and for always having my best interests at heart. Dr. Madhu Dhar and Nancy Neilsen have been invaluable as teachers and friends. They have opened their laboratory to me as my home away from home, taught me a great amount regarding cell biology, and took care of all the details that makes a biological experiment flawless. I am indebted to Dr. Deidra Mountain who allowed me to use her laboratory for the bacterial cultures, for her emotional support and encouragement, and for her guidance and suggestions on my dissertation research. I would like to thank Dr. Kevin Kit and Dr. Wei He for their guidance throughout my dissertation, never accepting less than my best efforts.

Special thanks to Cassandra Bates and Corey Ehinger, who have both made contributions to the work presented in this dissertation. Thanks also to Dr. Cynthia Peterson and Dr. Sekeenia Haynes for awarding me the PEER Fellowship which contributed significantly to my decision to attend the University of Tennessee. I would also like to extend my gratitude to Dr. Souleymane Diallo

for selecting me for the GEM Fellowship, for instructing me on the high resolution Backscattering Silicon Spectrometer at the Spallation Neutron Source, and for his outstanding mentorship during my summer internship at the Quantum Condensed Matter Division at Oak Ridge National Laboratories.

* The National Institute of Health Training Grant (NIH/NIGMS-IMSD: R25 GM086761).

** Sponsored by the National Science Foundation, the U.S. Department of Homeland Security, and the U.S. Department of Agriculture through NSF Awards #EF-0832858 and #DBI-1300426, with additional support from the University of Tennessee, Knoxville.

ABSTRACT

A very promising approach to quickly and safely restore normal function to extensively damages and diseases bone and cartilage tissues is the regeneration of these injured tissues using an engineered support scaffold. This dissertation research focuses on the development and evaluation of native bacterial cellulose (BC) and chemically modified BCs as potential biomaterials for bone and cartilage regeneration using equine-derived bone marrow mesenchymal stem cells (EqMSCs).

The ability of native BC scaffold to maintain cell proliferation, viability, and *in vitro* differentiation of the seeded EqMSCs for application in bone and cartilage tissue engineering was studied. BC morphology was characterized using Scanning Electron Microscopy (SEM). Fluorescence microscopy and MTS assay were used to evaluate cell viability and expansion on the BC scaffolds. EqMSCs differentiation into osteocytes and chondrocytes were assessed using alizarin red and alcian blue differentiation assays, respectively.

Biodegradable, microporous and surface modified BC scaffolds were developed to mimic native bone and cartilage tissues. Microporous BC scaffolds were synthesized using natural wax microspheres. BC scaffolds were chemically modified with periodate oxidation to generate biodegradable BCs. To mimic bone tissue, BCs were mineralized with calcium-deficient hydroxyapatite (CdHAP). Surface amination and carboxylation of BCs were performed to simulate the glycosaminoglycans present in the native cartilage tissue. Native and modified BC scaffolds were characterized using Fourier Transform Infrared Spectroscopy (FTIR), SEM, and mechanical testing. Resulting scaffolds were also characterized for their ability to support and maintain the proliferation, osteogenic and chondrogenic differentiation of EqMSCs using fluorescence microscopy, confocal microscopy, MTS assay, and cell differentiation assays.

Biodegradable, CdHAP tubular-shaped BC composites with oriented nanofibers were developed and evaluated to mimic the hydroxyapatite minerals and inherent oriented collagen fibers in native bone. Tubular-shaped BCs were synthesized under static culture in oxygen-permeable silicone tubes. The scaffolds were characterized using SEM and mechanical testing. The ability of the tubular-shaped BC scaffolds to support and maintain EqMSCs proliferation and osteogenic differentiation were also assessed.

In summary, the material properties and *in vitro* results acquired from the research demonstrate that native and specifically biodegradable microporous BC scaffolds have the ideal properties for bone and cartilage tissue regeneration therapies.

TABLE OF CONTENTS

LIST OF TABLES

LIST OF FIGURES

LIST OF ACRONYMS

Acronym	Full Word
2D	Two-dimensional
3D	Three-dimensional
AE-BC	Aminoethyl Bacterial Cellulose
AE-OBC	Aminoethyl Oxidized Bacterial Cellulose
AE Porous BC	Aminoethyl Microporous Bacterial Cellulose
AE Porous OBC	Aminoethyl Microporous Oxidized Bacterial Cellulose
ALP	Alkaline Phosphatase
ATCC	American Type Culture Collection
ATR	Attenuated Total Reflectance
BC	Bacterial Cellulose
BC-CdHAP	Bacterial Cellulose-Calcium Deficient Hydroxyapatite
BCP	Biphasic Calcium Phosphate
BC-TS	Tubular-shaped Bacterial Cellulose
BC-TS-CdHAP	Tubular-shaped Bacterial Cellulose- Calcium Deficient Hydroxyapatite
BCP	Biphasic Calcium Phosphate
BSA	Bovine Serum Albumin
$CaCl_2$	Calcium Chloride
CD	Cluster of Differentiation
CdHAP	Calcium-deficient Hydroxyapatite
CDMEA	2-Chloro-*N,N*-dimethylethylamine hydrochloride
CEA	2-Chloroethylamine Hydrochloride
CM-BC	Carboxymethyl Bacterial Cellulose
CM-OBC	Oxidized Carboxymethyl Bacterial Cellulose
CM Porous BC	Carboxymethyl Microporous Bacterial Cellulose
CM Porous OBC	Carboxymethyl Microporous Oxidized Bacterial Cellulose
CO_2	Carbon Dioxide
CPD	Critical Point Dried
DAC	Dialdehyde Cellulose
DAPI	4′,6-diamidino-2-phenylindole
DI	Deionized Water
DMAE-BC	Dimethyl Aminoethyl Bacterial Cellulose
DMAE-OBC	Dimethyl Aminoethyl Oxidized Bacterial Cellulose
DMAE Porous BC	Dimethyl Aminoethyl Microporous Bacterial Cellulose
DMAE Porous OBC	Dimethyl Aminoethyl Microporous Oxidized Bacterial Cellulose
DMEM	Dulbecco's Modified Eagle Medium
DMSO	Dimethylsulfoxide
DSC	Differential Scanning Calorimetry

EqMSC	Equine-derived Bone Marrow Mesenchymal Stem Cell
EqMSCs-BC	Equine-derived Bone Marrow Mesenchymal Stem Cell-Bacterial Cellulose
EqMSCs-TCP	Equine-derived Bone Marrow Mesenchymal Stem Cell- Tissue Culture Treated Plates
FACS	Fluorescence Activated Cell Sorter
FBS	Fetal Bovine Serum
FDA	Food and Drug Administration
FITC	Fluorescein Isothiocyanate
FTIR	Fourier Transform Infrared Spectroscopy
GAG	Glycosaminoglycan
GTMEA	Glycidyl Trimethyl Ammonium Chloride
HAP	Hydroxyapatite
HCl	Hydrogen Chloride
HEPES	4-(2-Hydroxyethyl)-1-Piperazineethanesulfonic Acid
IBB	Immunofluorescent Blocking Buffer
ID	Inner Diameter
IR	Infrared
KBr	Potassium Bromide
KCl	Potassium Chloride
MSC	Mesenchymal Stem Cell
MTS	CellTiter 96® Aqueous Non-Radioactive Assay
N_2	Nitrogen
NaCl	Sodium Chloride
Na_2HPO_4	Sodium Phosphate Dibasic
$NaIO_4$	Sodium Metaperiodate
Na-MCA	Monochloro Acetic Acid Sodium Salt
NaOH	Sodium Hydroxide
OBC	Oxidized Bacterial Cellulose
OBC-CdHAP	Oxidized Bacterial Cellulose-Calcium-deficient Hydroxyapatite
OBC-TS	Oxidized Tubular-shaped Bacterial Cellulose
OBC-TS-CdHAP	Oxidized Tubular-shaped Bacterial Cellulose-Calcium Deficient Hydroxyapatite
OD	Optical Density
PAS	Photoacoustic Spectroscopy
PBS	Phosphate-buffered Saline
PE	Polyethylene
PFA	Paraformaldehyde
PI	Propidium Iodide
Porous BC	Microporous Bacterial Cellulose
Porous BC-CdHAP	Microporous Bacterial Cellulose-Calcium Deficient Hydroxyapatite
Porous OBC	Microporous Oxidized Bacterial Cellulose

P/S	Penicillin/Streptomycin Solution
PTFE	Polytetrafluoroethylene
PVA	Polyvinyl Alcohol
SEM	Scanning Electron Microscopy
TCD	Tissue Culture Treated Dishes
TCP	Tissue Culture Treated Plates
TGA	Thermogravimetric Analysis
TGFβ1	Transforming Growth Factor Beta 1
TMAHP-BC	Trimethyl Ammonium Betahydroxy Propyl Bacterial Cellulose
TMAHP-OBC	Trimethyl Ammonium Betahydroxy Propyl Oxidized Bacterial Cellulose
TMAHP Porous BC	Trimethyl Ammonium Betahydroxy Propyl Microporous Bacterial Cellulose
TMAHP Porous OBC	Trimethyl Ammonium Betahydroxy Propyl Microporous Oxidized Bacterial Cellulose
UV	Ultraviolet
UV-Vis	Ultraviolet-Visible
WGA	Wheat Germ Agglutinin

CHAPTER I
Introduction

1.1. Background

Traumatic injury, aggressive tumor ablation, and bone and cartilage diseases, including osteoarthritis and osteoporosis, are common medical conditions that are associated with a high health cost to the patient [1-3]. These conditions often result in wounds with limited regenerative capacity [4]. Current treatment options require medications and reconstructive surgeries; the most frequently performed procedures involving tissues transplanted from healthy sections of the same patient, termed autologous grafts, to repair the wound [5, 6]. Autologous grafts, however, are often unavailable for use [5, 6]. Alternative clinical options have included the use of allogenic grafts, or tissues harvested from another individual. These grafts, however, are often diseased or lack immune compatibility [5, 6]. The current clinical treatment for these wounds stresses the need for bone and cartilage replacement therapies. Thus, developing biological materials that mimic the chemical and structural nature of native bone and cartilage tissue, and can lead to the regeneration of the lost tissue function will be paramount in improving the quality of life for these patients.

A promising alternative approach to treat these disorders is to use tissue engineering methods [4, 5]. In this technique, appropriate cells are seeded on a biomaterial scaffold and delivered to the injury site to facilitate regeneration of the damaged native tissues due to effects of the micro-environment in which it is placed and/or substances that are part of the scaffold [7-11].

1.1.1. Mesenchymal Stem Cells

Mesenchymal stem cells (MSCs) isolated from adult bone marrow stroma are multipotent cells that have the capacity to differentiation into a variety of other cells including bone, cartilage, muscle, ligament, and adipose tissue cells (Figure

1.1) [12-14]. In addition, they are strongly adherent to tissue culture treated polystyrene, possess high self-renewal activity in culture with an attached fibroblastic morphology, have an accessible origin and high *ex-vivo* expansive ability making them an ideal choice for tissue engineering therapies [15-17].

The primary roles of stem cells in mammalian tissues are to replenish the population of stem cells through self-renewal and asymmetric cell division, and to maintain and repair the tissue in which they reside [18]. Stem cells self-renew and divide asymmetrically to form two distinct daughter stem cells [18]. One daughter stem cell is an undifferentiated cell that is genetically and physically identical to the mother stem cell. The developmental potentials of this daughter cell therefore, are identical to those of the mother stem cell. The second daughter stem cell generated from the asymmetric cell division is dissimilar from the mother cell. This daughter stem cell is a mature and differentiated cell with limited developmental potentials and specialized functions such as a bone, muscle or cartilage cells. During proliferation or regeneration, stem cells can symmetrically divide into two daughter cells that are both identical to the mother cell [19].

Self-renewal and differentiation of stem cells are regulated by genes and proteins [18]. During self-renewal or differentiation, specific genes are turned on while others are turned off to allow the cell to proliferate and produce more undifferentiated cells, or differentiate into specialized cells. To proliferate, stem cells isolated from adult tissues undergo a specific self-renewal mechanism that differ at the early and late stages of cell life to meet changing tissue demands or cell regeneration capability (Figure 1.2) [20]. These stem cell self-renewal mechanisms are regulated by a series of signaling factors including the retinoblastoma (Rb) family proteins (pRb, p107 and p130) [20]. Rb family proteins are cell growth signaling factors that inhibit cell cycle progression to prevent excessive cell growth until cell division is needed by the tissue [20, 21].

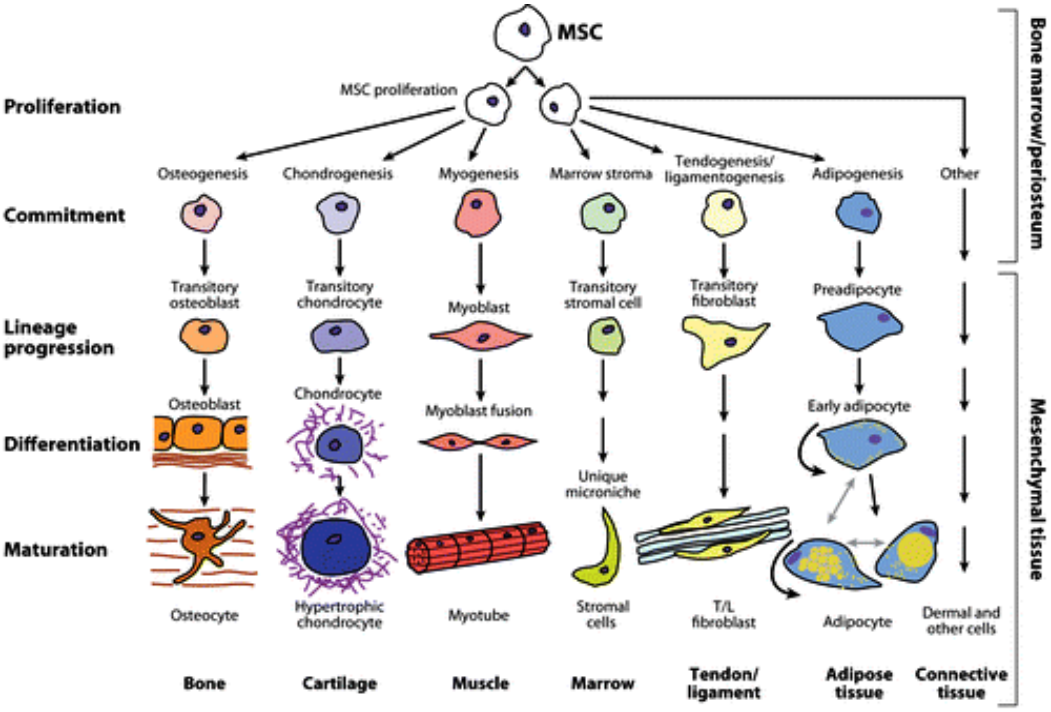

Figure 1.1: Mesenchymal stem cell lineages and resulting tissue cells [22].

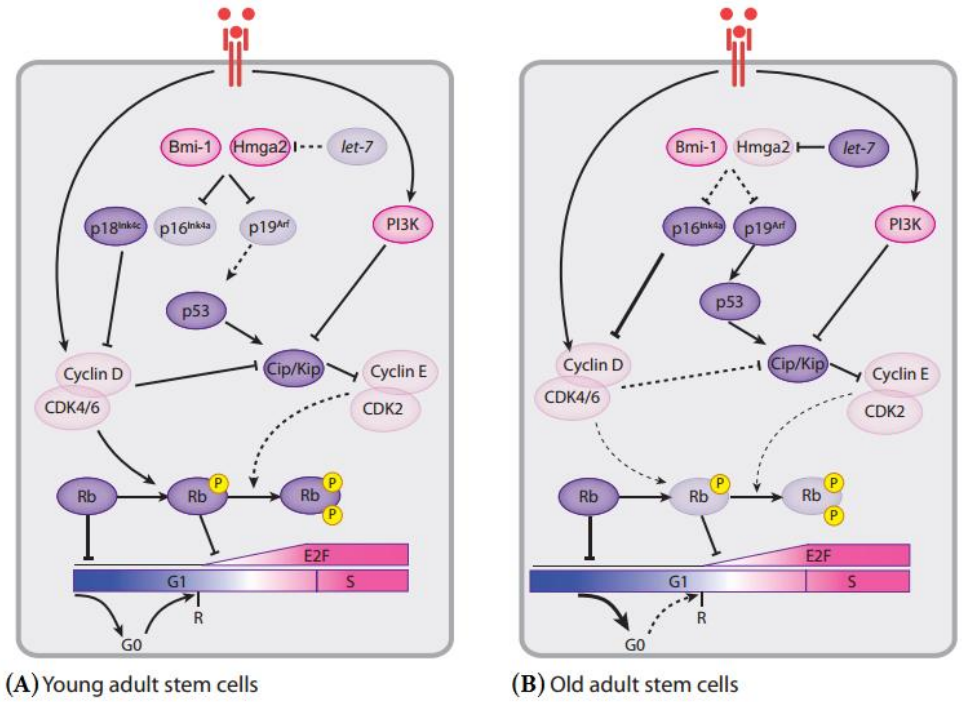

Figure 1.2: Schematic of signaling factor network that controls the proliferation potential of young (A) and old (B) adult stem cell [20].

Differentiation of MSCs into osteoblasts and chondrocytes are regulated by a series of signaling factors following the mechanism illustrated in Figure 1.3. The bone signaling factor bone morphogenetic protein-2 (BMP-2) is involved in the regulation of osteobast formation (Figure 1.3), and has been extensively studied for bone tissue engineering and regenerative medicine applications [23-25]. The growth factor BMP-2 can induce osteoblast differentiation from undifferentiated MSCs and the formation of new bone tissue [26, 27]. Other protein growth factors that can induce undifferentiated MSCs to differentiate into osteoblasts include transforming growth factor β (TGF-β), platelet derived growth factor (PDGF), and insulin-like growth factor (IGF) [27]. Vitamin D_3, ascorbic acid, β-glycerophosphate, and dexamethasone can also promote the differentiation of MSC into osteoblasts [26].

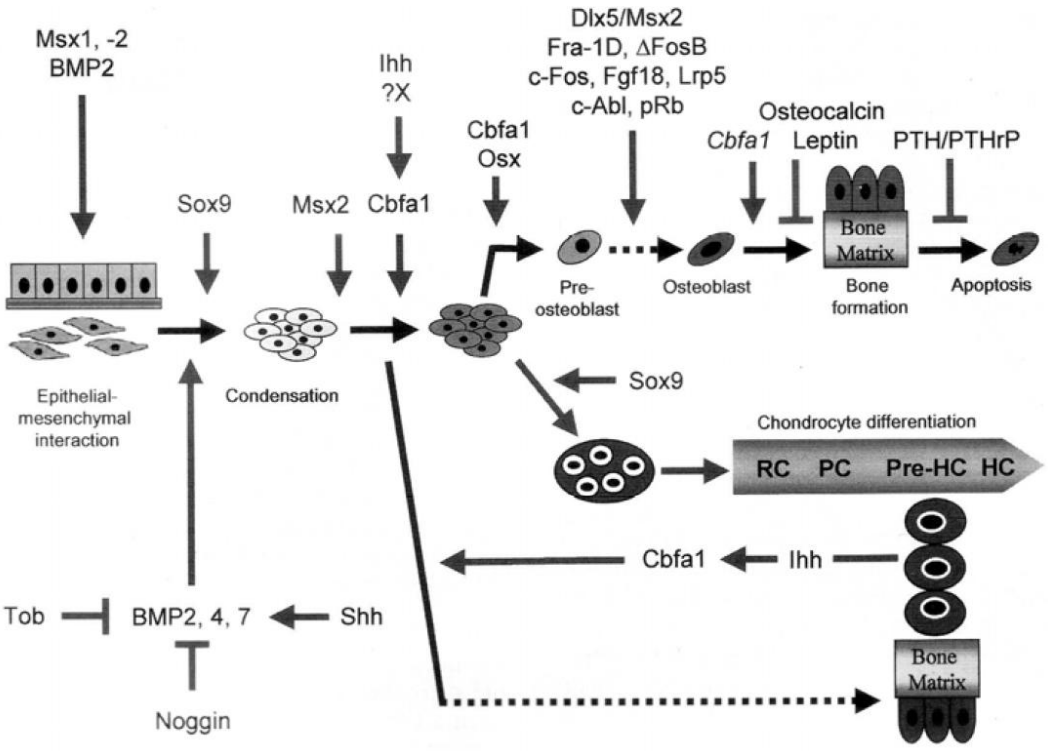

Figure 1.3: Transcription factors involved in osteoblast and chondrocyte differentiation from mesenchymal stem cells [27].

The transcription factor Sox9 is a well studied positive regulator of chondrocyte differentiation from undifferentiated MSCs (Figure 1.3) [27, 28]. Other transcription factors including LSox5, Sox6, and RunX2 have also proven successful in promoting the differentiation of MSCs into chondrocytes [28].

Bone marrow MSCs from various species including chicken, bovine, rabbit, human, goat, canine and porcine have been investigated in combination with scaffolds to assess these constructs' *in vitro* lineage specific differentiation potentials for tissue repair [16, 29-35]. The use of stem cell in therapy and tissue engineering in equine medicine is relatively new, but it is an exciting research field that is rapidly expanding [36]. Due to similarities in size, load and types of joint injuries suffered by horses and humans, a U.S. Food and Drug Administration (FDA) report concluded that the horse was the most appropriate model animal for testing the clinical effects of mesenchymal stem cell-based therapies for joint injuries in humans [37]. Additionally, the economic and welfare costs of performance-related injuries in horses have stimulated interest in stem cell-based therapies in horses [38]. Therefore, the horse can be considered as an animal model for human injuries and osteoarthritis [39]. Currently, bone marrow and adipose tissue are the main sources of MSCs for the treatment of equine musculoskeletal diseases [40, 41], and there are no studies reporting the use of a suitable biomaterial for these injuries.

1.1.2. Tissue Engineering using Equine-derived Bone Marrow Mesenchymal Stem Cells

Besides the cell source, approaches to connective tissue engineering to produce a construct that structurally and functionally mimic the target tissue involve several other design considerations. These involve biocompatible scaffold chemistry and morphology, bioactive signaling factors that promote cellular proliferation, differentiation, and extracellular matrix synthesis, mechanical stimulation and microenvironmental factors [2].

Three-dimensional (3D) biomaterials seeded with MSCs that originate from equine animal model have been used as scaffolds for the treatment of osteochondral defects in horses [42], osteochondritis dissecans in a thoroughbred horse [43], and equine bone fracture [44]. MSCs from equine animal model, seeded on biomaterials, have also been assessed *in vitro* for their abilities to differentiate into osteocytes [45], chondrocytes [46, 47], and tenogenic cells [48, 49]. While MSCs and 3D biomaterial scaffolds have been used to create cell-type specific constructs, there is no report on the successful application of a single three-dimensional natural biopolymer to support equine-derived bone marrow mesenchymal stem cell (EqMSCs) differentiation along the chondrocyte and osteocyte lineages.

Scaffolds designed for use in bone and cartilage tissue engineering must be biocompatible and biodegradable [4]. Biodegradable and biocompatible materials are necessary for tissue engineering applications because they can be designed to erode and be absorbed by the body without adverse effects upon completion of the tissue regeneration. The scaffolds should also mimic the structural and functional properties of the native tissue. For bone and cartilage tissue, replacement scaffold should imitate the native tissue chemistry and morphology, 3D structure and biomechanical properties to properly replicate their function [2, 4]. The scaffold surface and porosity should also enable cell infiltration, adhesion, proliferation and differentiation into the appropriate cellular phenotype [2, 4].

1.2. Anatomy of Bone and Cartilage Tissues

1.2.1. Anatomy of Bone Tissue

Bone is a special type of connective tissue that offers multiple functions [50]. It provides the structural frameworks for the body, helps provide movement, stores minerals, contains blood vessels and provides sites of attachment of tendons and muscles [50, 51]. Bone is composed of approximately 25% water,

15% organic matrix, and 60% inorganic matrix in the form of calcified minerals, by weight [50]. The organic (noncalcified) matrix is 95% collagen type I and 5% nonmineralized base substance such as chondroitin sulfate and keratin sulfate [50, 52]. The primary inorganic (calcified) matrix in bone is calcium-deficient hydroxyapatite (calcium phosphate and calcium carbonate), with small amounts of magnesium hydroxide, fluoride, and sulfate [52].

Bone tissue is formed in layers of lamellae fiber bundles which contain near parallel arrays of collagen type I (1 nm diameter nanofibril structure), which forms 100-200 nm triple helical collagen molecules in the tissue matrix [50, 53]. It has been observed that hydroxyapatite minerals tend to form along the oriented collagen fibers of the bone tissue [50]. The hardness of bone depends on these inorganic mineral salts present in the tissue, and the flexibility of bone tissue depends on its collagen fibers [52]. The elastic modulus of pre-calcified bone has been estimated to be 11.5-13.5 kPa [54], and the elastic modulus for parietal bones of the adult human skull has been reported to be 6-18 GPa [55].

The main types of cells in bone are osteoprogenitor cells (or osteogenic cells), osteoblasts, osteocytes and osteoclasts (Figure 1.4) [50]. Osteoprogenitor cells (Figure 1.4) are unspecialized cells located on the surface of growing bones, in the periosteum, in the endosteum and in the canals of blood vessels [52]. They can differentiate into osteoblasts following the mechanism previously discussed (Section 1.1) and illustrated in Figure 1.3 [50, 52]. Osteoblasts (Figure 1.4) are bone-matrix producing cells [50]. Osteoblasts initiate the process of calcification by synthesizing and secreting collagen fibers and other organic components needed to build the bone matrix [52]. Osteocytes (Figure 1.4) are mature bone cells that do not undergo cell division [50]. They originate from osteoblasts and they maintain the metabolism of bone, including the exchange of nutrients and waste with the blood [52]. Osteoclasts (Figure 1.4) are large, multinucleated cells which are derived from monocytes, a type of white blood cells [50, 52]. The role of osteoclasts is to breakdown bone matrix during the

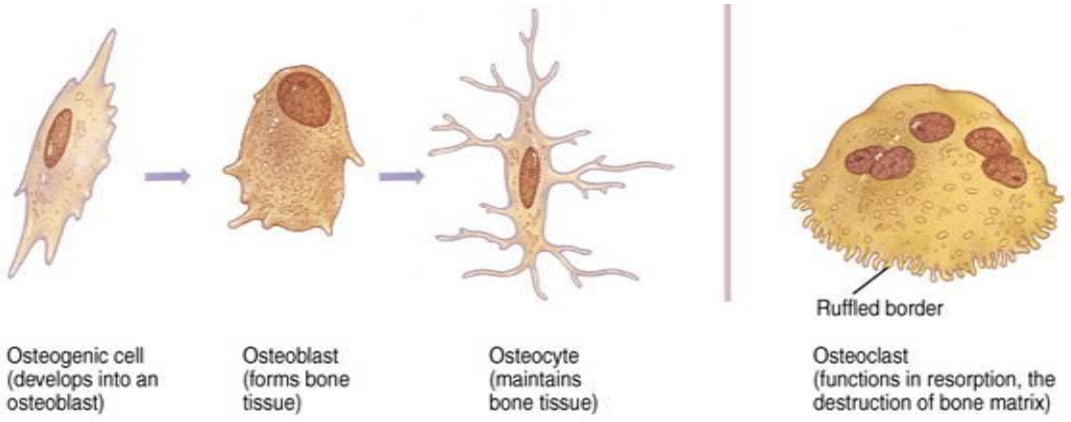

Figure 1.4: Schematic of the different types of cells in bone tissue [52].

normal development and growth of bone [50, 52]. During bone remodeling, they are absorbed by the bone matrix through their pleated cell membranes, termed ruffled border [52]. After absorption by the bone matrix, they release lysosomal enzymes and acids that digest the protein and mineral components of the bone matrix which are restored by the new extracellular bone matrix formed by the osteoblasts [50, 52].

Bone is classified as compact or spongy [52]. Compact (or cortical) bone is a dense tissue that forms on the external surface layer of all bones and on the diaphysis of long bones. Approximately 80% of the skeleton is compact bone [52]. Compact bone is composed of 3D hierarchical tubular structures called osteon or Haversian Systems. In the osteon structures, blood vessels, lymphatic vessels, and nerves from the periosteum infiltrate the compact bone through perforating (Volkmann's) Canals (Figure 1.5). The Volkmann's Canals are perpendicularly arranged channels that link the nerves and blood vessels in the osteon structures. Surrounding the Volkmann's Cannals are concentric rings of lamellae. Lamellae are calcified bone matrixes. Centered in the lamellae are small cavities called lacunae which contain osteocytes. Miniature-sized channels called canaliculi branch out from the lacunae in all directions, and connects the

lacumae with one another. Osteocytes depend on the lacunae spaces and canaliculi channels to access nutrients and oxygen, as well as for the diffusion of waste [52].

Spongy bone tissue is less dense compared to compact bone and it does not contain osteons [52]. It is located at the ends of epiphysis bones and in the narrow rim surrounding the medullary cavities in long bones. Approximately 20% of the skeleton is spongy bone tissue [52]. Spongy bone tissue is composed of trabeculae, a network of connective tissue, which is surrounded by vascularized red bone marrow. In the spongy bone tissue, osteocytes use the lacunae spaces and canaliculi channels to access nutrients and oxygen in the red bone marrow instead of the osteons.

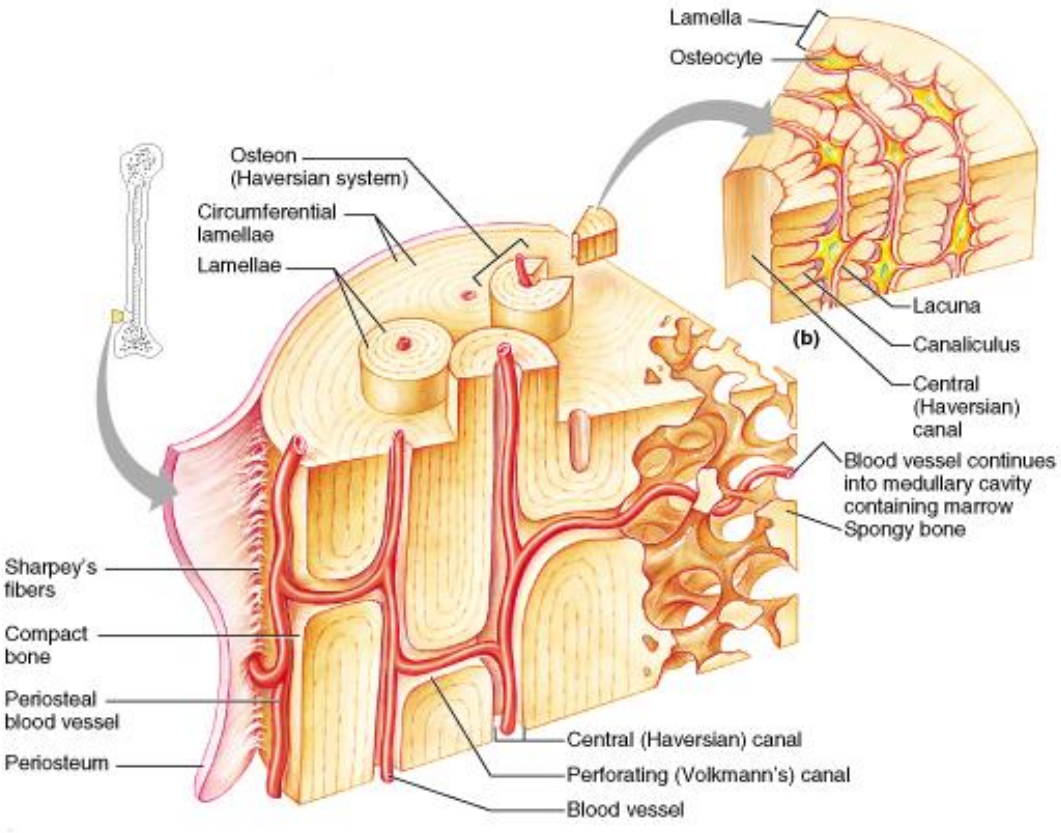

Figure 1.5: Structure of compact and spongy bone [56].

1.2.1. Anatomy of Cartilage Tissue

Cartilage is an avascular specialized form of connective tissue that is found at the ends of bones in joints [50, 52]. It allows frictionless movement of bones at joints, distribution of body loads and provides structural support of soft tissues. Cartilage is composed of approximately 75% water and 5% nonmineralized matrix in the form of fibers and ground substance [50]. The fiber present in cartilage is mainly collagen type II, with small amounts of collagen type I [50]. The ground substances in cartilage include glycoaminoglycans (GAGs), proteoglycans and glycoproteins [50, 52]. Collagen fibers in cartilage are set in chondroitin sulfate, a gel-like component of the ground substance [57]. Under normal circumstances, cartilage is able to withstand mechanical stress without permanent deformation. The strength of cartilage is due to the collagen fibers present in the tissue, and its ability to assume its original shape after deformation is due to the chondroitin sulfate in the tissue [52]. The Young's modulus of cartilage has been estimated to be 11.0-11.2 kPa [54].

The cells present in cartilage include chondrogenic cells, chondroblasts and chondrocytes [50]. Chondrogenic cells are located in the perichondrium, or the dense irregular connective tissue in cartilage, and they can differentiate into chondroblasts to enable cartilage growth [50, 52]. Chondroblasts, derived from chondrogenic cells, can synthesize and deposit cartilage matrix during cartilage growth [50, 52]. Chondrocytes are mature chondroblasts. They align in small columns or rows in the cartilage to contribute to interstitial cartilage growth [50, 52]. The differentiation mechanism of MSCs into chondrocytes follows the mechanism previously discussed (Section 1.1) and illustrated in Figure 1.3.

Cartilage is classified as hyaline cartilage, fibrocartilage, or elastic cartilage (Figure 1.6) [52]. They differ in their concentration of the primary cartilage components (cells, collagen fibers and ground substance) and in their location in the body. Hyaline cartilage (Figure 1.6.A) is the most abundant of the

cartilages. It is also the most flexible. Hyaline cartilage is present in embryonic and fetal skeleton, at the ends of long bones, in the nose, larynx, trachea, and bronchi [52]. With the exception of the articular cartilage in joints and epiphyseal plates, most hyaline cartilages are elastic gel-like materials composed primarily of the fibrous connective tissue called perichondrium. Chondrogenic cells are located in the ground substance of the cartilage, surrounded by a cavity called lacuna.

Fibrocartilage (Figure 1.6.B) is composed of networks of collagen fibers within which chondrocytes are randomly distributed [52]. Unlike hyaline cartilage, fibrocartilage does not have a perichondrium. However, the abundance of collagen fibers present in the matrix contributes to its rigidity and strength. Fibrocartilage is the strongest of the three form s of cartilage. Fibrocartilage is located in tendon of quadriceps, in the femoris and pubic symphysis. They are also present in the discs of intervertebral, in the menisci, and in tendons.

Elastic cartilage (Figure 1.6.C) is consists of finely arranged groups of elastic fibers in the ground substance of the matrix [52]. Similar to hyaline cartilage, elastic cartilage has a perichondrium. Elastic cartilage is located in the epiglottis, auricle and Eustachian tubes.

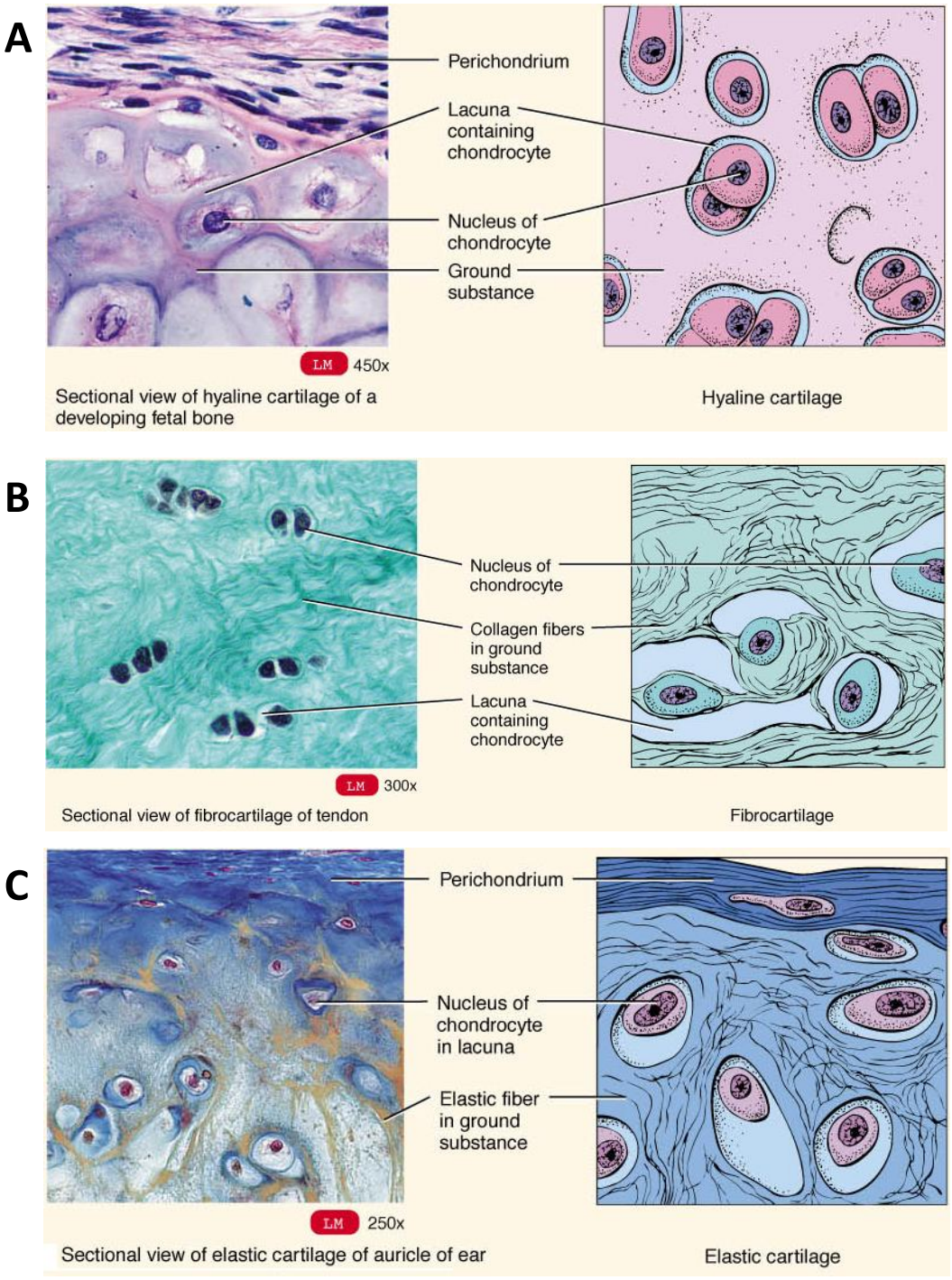

Figure 1.6: Histological images of hyaline cartilage (A), fibrocartilage (B), and elastic cartilage (C) [52].

1.3. Bone Tissue Engineering Using Hydroxyapatite

Calcium-deficient hydroxylapatite, CdHAP or $Ca_9HPO_4(PO_4)_5OH$, is the primary mineral in native bone tissue and it plays a critical role in providing hardness to the matrix [58]. Hydroxyapatite, a chemically similar mineral to CdHAP, has been well investigated as a biomimetic bone replacement material and as a biomaterial for bone tissue engineering [59-66]. Hydroxyapatite, $Ca_{10}(PO_4)_6(OH)_2$, is a calcium phosphate composite produced from precipitates of $Ca(NO_3)_2$ and NaH_2PO_4 solutions [67].

Various methods have been developed to produce hydroxyapatite from calcium and phosphate solutions. Surface mineralization of biomaterials with hydroxyapatite have been achieved by sequential incubation of the biomaterial in the component solutions [68, 69], and by electrospraying dry hydroxyapatite precipitates onto the biomaterial [61]. Three-dimensional solid or porous hydroxyapatite biomaterials have been synthesized by sintering dry hydroxyapatite precipitates at high temperatures (900 – 1300 °C) [66, 67], by combining sintering and freeze-drying techniques [64], and by combining various combinations of compression, sintering, and hydrogen peroxide [70]. Sintering performed by compaction under high pressure have been shown to produce densely packed non-porous hydroxyapatite biomaterials [66, 70]. Porous hydroxyapatite biomaterials have also been generated by adding naphthalene particles to the mineral mixture prior to sintering, followed by removal of the naphthalene particles via sublimation in a freeze-dryer [66].

Hydroxyapatite is composed of calcium and phosphorous, compounds common to mammalian tissues, therefore, concerns regarding non-biocompatibility are minimal. It is a biocompatible material that is non-inflammatory, non-toxic, non-carcinogenic and non-thrombogenic *in vitro* [71-73], and *in vivo* [70, 74-77]. It is also a bioactive material that supports bone ingrowth and osseointegration [67, 70, 74]. Hydroxyapatite prostheses have been shown to favorably influence biointegration between the mineralized material and bone [74, 78], form a direct and firm chemical bond with surrounding bone tissue [67,

74], and permit tissue and cell ingrowth [74]. The biodegradation of non-sintered hydroxyapatite has been proposed to occur readily by the intracellular digestion of fine particles which separate from the sintered biomaterial by physicochemical processes [79-82]. Degradation rate of non-sintered hydroxyapative can be controlled by various factors including hydroxyapative density and porosity. It has been proposed that densely sintered hydroxyapatites have limited biodegradability [70]. Sintered hydroxyapatites have been shown to lack resorption after 9 months *in vivo* which have been attributed to the limited porosity of the densely sintered material [70].

Hydroxyapatite has been synthesized and used for developing various forms of bone implants including auditory canal-wall prostheses [74], incus prostheses [74], osteochondral scaffolds [60, 64], and scaffolds for infrabony [76] and tibiae [70] defects. In addition to its use in bone repairs, hydroxyapatite has also been used to mineralize solid and porous implant surfaces to promote bone ingrowth and osseointegration [60, 61, 68-70].

1.4. Bacterial Cellulose Scaffolds

Bacterial cellulose (BC) is a natural polysaccharide consisting of β-D-glucopyranose units linked together by (1→4)-glycosidic bonds (Figure 1.7) [83]. It is synthesized extracellularly by non-pathogenic bacterium such as *Gluconacetobacter spp* in the form of a hydrogel [69]. The bacteria naturally extrude the cellulose into a highly crystalline (approximately 60% crystallinity index [83]) 3D hydrogel complex. *Gluconacetobacter spp.* generates ultrafine cellulose fibers approximately 1.5 nm in width. These ultrafine fibers crystallize into bundles of nanofibers that sequentially aggregate to form ribbons approximately 1-9 μm L x 70-80 nm W x 3-4 nm H [83]. The ribbons then bend and combine to form a stable gel-like membrane structure with extensive intramolecular and intermolecular hydrogen bonds (Figure 1.8) [83]. The cellulose molecules of BC are aggregated through van der Waals forces and

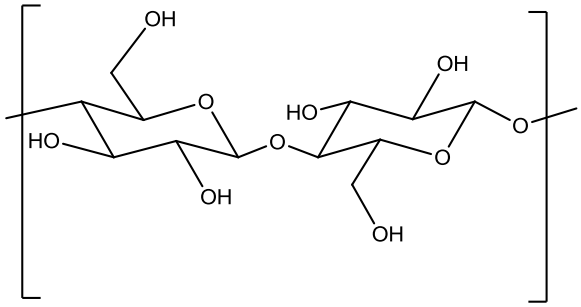

Figure 1.7: Chemical structure of cellulose chain.

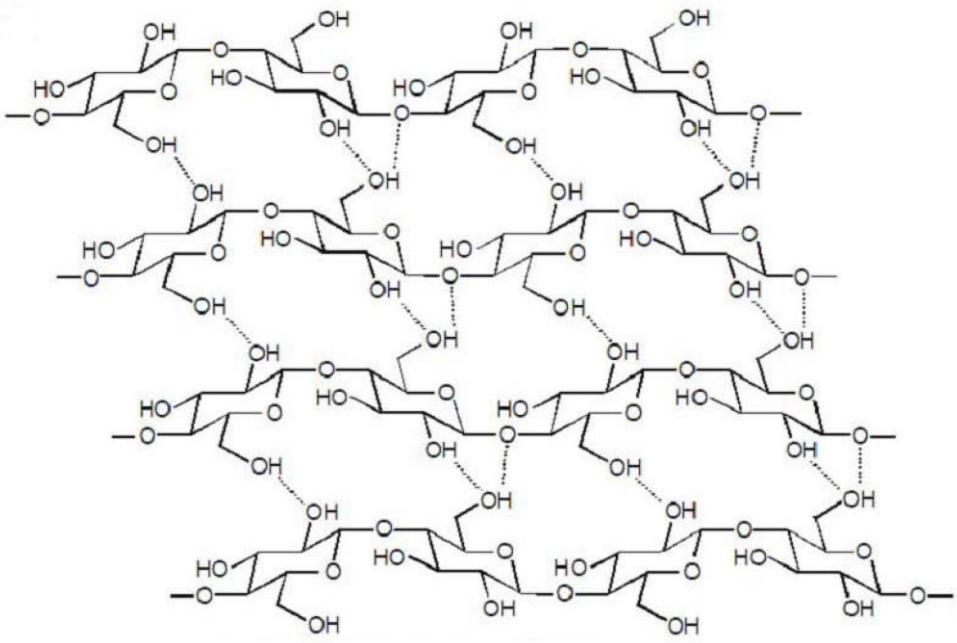

Figure 1.8: Intermolecular (dotted bonds) and intramolecular hydrogen bonding in cellulose chain [84].

both intra- and intermolecular hydrogen bonds. These hydrogen bonds allow BC to retain water in its interstitial spaces. Approximately 99.8% of the volume of the BC matrix is water with approximately 0.2% pure cellulose [85].

The nanofibrous BC material has shown promise as a scaffold for tissue engineering [86]. It can be synthesized cost-effectively by the bacterium and can be purified into a chemically pure 3D hydrogel that is biocompatible, moldable, hydrophilic and highly crystalline scaffold with high-mechanical properties [83, 87-89]. BC has been implanted into rats without eliciting any foreign body or inflammatory response [87], and has been used as a scaffold for treatment of second- or third-degree burn ulcers [57], for chronic venous leg ulcers [90] and for artificial blood vessel [91]. This research group previously studied the conditions necessary to maximize cellulose production and found that the bacteria produced the most cellulose when cultured on mannitol [92].

Native BC is synthesized from the bacterium into a non-biodegradable and nanoporous scaffold that does not degrade *in vivo* [83], and allows limited cell penetration into the scaffold [93]. However, for bone and cartilage tissue engineering applications, a biodegradable and microporous scaffold is desired. Previously, non-degradable BC was made biodegradable through a periodate ring-opening oxidation (Figure 1.9) [68, 83, 94]. Periodic acid (HIO_4) was shown to exclusively cleave the C2-C3 bond in the cellulose chain, convert the adjacent hydroxyl groups into aldehydes, and produce dialdehyde cellulose (or oxidized cellulose) which degrades by simple hydrolysis mechanism *in vivo* (Figure 1.9) [94]. Microporous BC have also been developed by using leachable paraffin wax microspheres [95, 96]. Chemical sulfation [93], phosphorylation [93] and amination [97] of BC have also been performed to mimic the surface charges of GAGs in native cartilage via chemical reactions with sulfamic acid, phosphoric acid and amines, respectively.

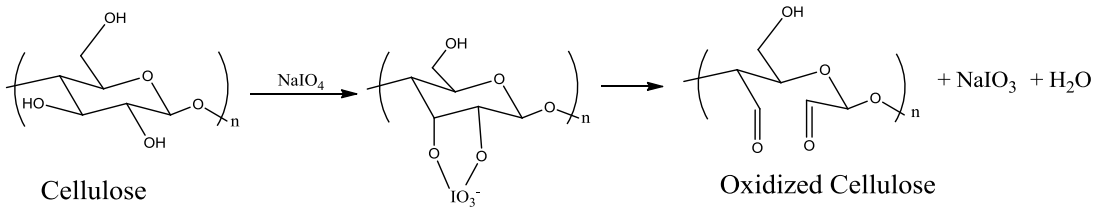

Figure 1.9: Oxidation reaction of cellulose by periodate oxidation (adapted from reference [94, 98]).

As previously discussed, native bone tissue is a 3D hierarchical tubular structure consisting of extracellular matrix, cells, collagen fibers and inorganic salts in the form of hydroxyapatite crystals [50]. Hence, an accurate scaffold designed to replace bone tissue must mimic the mineralized 3D structural composite to properly replicate its function. Several biocompatible materials have been developed to imitate the tubular 3D structure of bone including a biodegradable polymer fiber in a polymer matrix (polylactid acid fibers in a poly 1-caprolactone matrix) [99], hydroxyapatite ceramics [100] and polymer fibers filled with growth factors such as bone morphogenetic protein 7 [101]. Hydroxyapatite ceramics have been shown to permit osteoblast cell adhesion and proliferation [59], however, the use of pure ceramics as scaffold materials for tissue engineering is undesirable because of its brittleness and low strength [102]. The approach of creating polymer-ceramic composites can minimize the brittleness associated with pure ceramic. Thus the approach of creating such composites is optimum for creating biomimetic bone tissue. Our research group have developed and characterized the *in vitro* properties of a polymer-ceramic composite, using BC and physiological calcium-deficient hydroxyapatite (CdHAP), an osteoconductive and bioresorbable mineral, for bone tissue regeneration [68, 69].

Native bone tissue is formed in layers of lamellae fiber bundles which contain near parallel arrays of collagen type I, a 1 nm diameter nanofibril

structure, which forms 100-200 nm triple helical collagen molecules in the tissue matrix [50, 53]. The nanofibril BC hydrogel is a readily moldable scaffold and takes the shape of the vessel in which it is synthesized. Recently, researchers have generated tubular BC (BC-TS) scaffolds with oriented fibers using oxygen permeable silicone tubes that are supplied with oxygen [103, 104]. BC-TS is beneficial for bone tissue engineering because the oriented fibers may be used to imitate the inherent oriented collagen fibers in native bone. Furthermore, in bone, CdHAP minerals form along the oriented collagen fibers of the tissue [50]. As demonstrated in the previously studies, CdHAP can be deposited in BC scaffolds to form BC-CdHAP composites [68, 69]. Here, the structure and function of native bone tissue is mimicked, more specifically the collagen-CdHAP composite in bone, by depositing osteoconductive and bioresorbable CdHAP minerals in BC-TS with oriented fibers. Combined with osteocyte-forming mesenchymal stem cells, this biomimetic fibrous composite could be used for bone defect repair and reconstruction. We hypothesized that aligned mesenchymal stem cell morphology can be induced on the scaffolds due to the orientation of the fibers and as previously reported [105].

An ideal functional tissue engineered substitute would be a single 3D biocompatible scaffold capable of adapting to various connective tissue microenvironments, while supporting selective lineage-specific differentiation of MSCs for multiple connective tissue applications. This dissertation study explores the modification and characterization of 3D, non-biodegradable and nanoporous BC hydrogel scaffolds into degradable and microporous BCs, modified to mimic native bone and cartilage tissues, for potential tissue engineering use. This dissertation describes results that study the use of a microporous scaffold fabrication technique not previously reported (use of beeswax microspheres to create scaffolds with microporous network), a scaffold mineralization technique, a scaffold surface functionalization method, a periodate oxidation method for rendering the bacterial cellulose scaffold degradable under physiological conditions, and a tubular scaffold preparation technique. The

mechanical, morphological, chemical, degradation and cellular response properties of the native BC scaffold and its composites are presented.

CHAPTER II
Materials and Methods

The instruments and procedures used to produce and characterize the BC scaffolds are described in this chapter. Selected methods in this chapter have been published in *Material Science and Engineering C* [106] and *Materials Research Society Symposium Proceedings* [107].

2.1. Materials

All chemicals, cell culture supplements and disposable tissue culture supplies were purchased from Sigma-Aldrich (Saint Louis, MO) unless otherwise noted. During the bone marrow extraction to obtain equine-derived bone marrow mesenchymal stem cell, animal procedures were carried out according to Institutional Animal Care and Use Committee protocol no. 1953.

2.2. Bacterial Cellulose Scaffold Preparation

The procedures used to produce the various forms of BC scaffolds are described in the following section. Scaffold synthesis involves the culturing of native bacterial cellulose, microporous bacterial cellulose or tubular bacterial cellulose. Chemical modifications of the scaffolds were performed using periodate oxidation, amination or carboxylation. Mineralization was completed to produce calcium-deficient hydroxyapatite scaffolds.

2.2.1. Preparation of Native Bacterial Cellulose Scaffold

BC was prepared as previously described [68, 69]. Briefly, cellulose producing bacterial strain *Gluconacetobacter sucrofermentans* was commercially obtained from the American Type Culture Collection (Manassas, VA) (ATCC

700178). The bacteria were grown in a modified Schramm and Hestrin liquid medium composed of mannitol (2.0 % w/v) (Fisher Scientific, Pittsburgh, PA), Difco Bacto™ peptone (0.5 % w/v) (BD, Franklin Lakes, NJ), Difco yeast extract (0.5 % w/v) (BD), sodium phosphate dibasic anhydrous (0.27 % w/v) (Fisher Scientific) and citric acid monohydrate (0.115 % w/v) (Fisher Scientific) [108]. For BC production, pre-cultures of the bacteria were diluted 1:10 in fresh media and incubated in 96- and 24-well tissue culture treated plates (TCPs) for 14 days at room temperature under static conditions [109]. A volume of 200 µl/well of bacterial medium was added to 96-well TCPs and 2.5 ml/well was added to 24-well TCPs. The BC pellicles produced at the surface of the medium were harvested, heated at 90 °C for 2 h in deionized (DI) water to kill the bacteria, treated with 1% NaOH (w/v) washes for 6 days at room temperature, purified in distilled/deionized water to pH = 7, and stored in DI water at room temperature prior to use [109]. The diameter of the produced BC pellicle was dependent on the type of TCP used for cell culture which controlled the TCP well size. The 96-well TCP produced BC discs of ~6.0 mm diameter, ~2.0 mm thickness and ~0.05 g wet weight. The 24-well TCP produced BC discs of ~15.5 mm diameter, ~3.0 mm thickness and ~0.5 g wet weight.

2.2.2. Preparation of Microporous Bacterial Cellulose Scaffold

Beeswax microspheres were produced following a modified method described by Ma and Choi [110]. Briefly, a 0.5% (g/mL) polyvinyl alcohol (PVA, average molecular weight 20,000-30,000) (Fisher Scientific) solution was heated to 70 °C and stirred using a magnetic stirring bar at a setting of 3-5 on a hot plate (Fisher Thermix® Stirring Hot Plate Model 210T, Fisher Scientific). Beeswax (Sunbeam Candles, Ithaca, NY) was heated to melt in a water bath at 90 °C and was then poured slowly into the PVA solution, under stirring, to form beeswax microspheres. The beeswax microspheres were solidified and the solution cooled by the addition of ice-cold water. The microspheres were collected, extensively washed with DI water and sieved (500 µm U.S. standard sieve,

Advantech Manufacturing, New Berlin, WI) to obtain microspheres with diameters of 500 µm or less. The microspheres were sterilized by submersion in 70% ethanol for 1 h under gentle stirring, frozen to -80 °C for 48h, lyophilized (Labconco FreeZone® 4.5 Freeze Dry System, Kansas City, MO) for a minimum of 24 h at -50 °C and 1.0 x 10^{-3} Pa, and stored in a desiccator at 23 °C until use, as previously described [96].

The beeswax microspheres were added to TCPs and tissue culture treated dishes (TCDs) prior to cellulose synthesis. Sterile DI water was first added to 96-well TCPs, 24-well TCPs, and 6-well TCPs, to cover the bottom surfaces of the wells, followed by the addition of the beeswax microspheres. Sterile DI water was added to the TCPs and TCDs to prevent the wax from attaching to their bottom surfaces during sintering. The TCDs and TCPs were packed with beeswax microspheres to 20-30% of their volumes and sintered at 40 °C for 30 min (modified from Zaborowska et al. [96]). The TCPs and TCDs were then cooled to room temperature and the DI water removed under sterile conditions.

Bacterial strain *Gluconacetobacter sucrofermentans* (ATCC 700178) was used to synthesize the cellulose. Pre-cultures of the bacteria were made in a modified Schramm and Hestrin medium [108] and the constituents have been previously described (Section 2.2.1). For microporous BC (porous BC) production, pre-cultures were diluted 1:10 in fresh media. Microporous BC scaffolds with pore sizes of 500 µm or less were prepared by adding the bacterial culture to the sintered beeswax microspheres in the TCPs and TCDs. Approximately 100 µl/well, 1.5 ml/well, 8 ml/well and 15 ml/dish of bacteria in culture media were added to 96-well TCPs, 24-well TCPs, 6-well TCPs and 100-mm TCDs, respectively, and incubated for 14 days at 23 °C under static conditions. During cellulose synthesis, the bacteria extruded cellulose fibers into a web encapsulating the beeswax microspheres (density 0.96 g/cm^3 [111]). An illustration of the microporous BC set-up is shown in Figure 2.1.

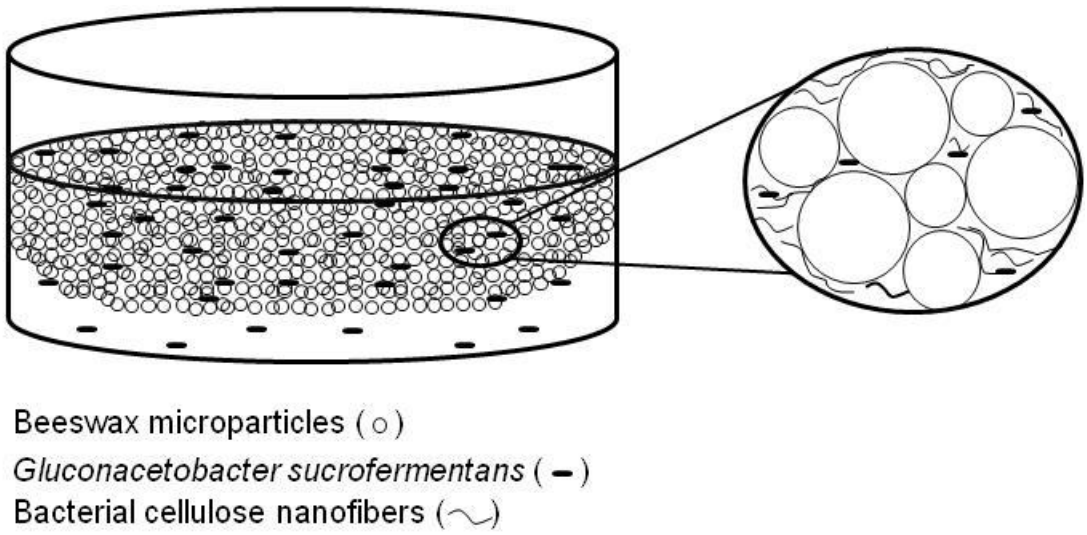

Figure 2.1: Schematic illustration of microporous bacterial cellulose synthesis composed of sintered beeswax microspheres floating in bacterial medium under static conditions.

After synthesis, cellulose pellicles produced at the surface of the medium were harvested. Bacteria were removed from the cellulose pellicles by heating the materials at 90 °C in 1% NaOH (w/v) for 2 h, followed by additional heating at 60 °C in 1% NaOH for 4 h, and then several rinses with DI water to remove bacterial residues.

The beeswax microspheres were leached from the BC by cyclic washing in the surfactant Tween 80 (Fisher Scientific) to create porous and interconnected pores in the bacterial cellulose. A modified method described by Backdahl et al. [95] was used to leach out the beeswax microspheres. The scaffolds were soaked in 1% (v/v) of Tween 80 overnight in a 70 °C shaker, rinsed with DI water and soaked in 99% ethanol for 8 h in a 70 °C shaker. This procedure was repeated at least 15 times to ensure the complete removal of the beeswax from the microporous BC. The beeswax remaining in the microporous BC after leaching from the cellulose is visible under phase contrast microscope. A phase contrast microscope (Zeiss Axiovert 40C microscope, Carl Zeiss

MicroImaging, Inc., Thornwood, NY) equipped with a Nikon Digital Sight DS-Qi1Mc camera (Nikon Instruments Inc., Melville, NY) was used to confirm the diameter of produced beeswax microspheres. Fourier transform infrared spectroscopy was used to confirm the complete removal of the beeswax from the microporous BC scaffolds (see Section 2.3.2 below).

After beeswax leaching, the microporous BCs were soaked in several changes of distilled/deionized water to remove the Tween 80 and ethanol. The cellulose were washed to pH = 7 and the microporous BCs were stored in DI water at room temperature prior to use.

2.2.3. Preparation of Tubular-shaped Bacterial Cellulose Scaffold

Silicone tubes (Fisher Scientific), with inner diameters (ID) of 6.35 mm and 9.525 mm, wall thicknesses of 6.35 mm, and length of 100 mm, were used in the preparation of tubular-shaped bacterial cellulose (BC-TS) samples. The silicone tubes were washed, dried and sterilized in an autoclave (1 bar, 120 °C) for 30 min prior to use. Bacterial strain *Gluconacetobacter sucrofermentans* (ATCC 700178) was used to synthesize the cellulose. Pre-cultures of the bacteria were made in a modified Schramm and Hestrin medium [108] and the constituents have been previously described (Section 2.2.1). For BC-TS production, the sterile silicone tubes were placed in a glass cylinder, pre-culture of bacterial medium was diluted 1:10 in fresh media, and the diluted bacterial medium was poured on the outside surface of the sterile silicone tubes (Figure 2.2.A). In a second preparation method, the diluted bacterial medium was poured inside the sterile silicone tubes (Figure 2.2.B). This method of synthesizing BC-TS is a modification of a method previously described by Putra et al. [104]. The BC-TS were cultured for 14 days and purified in 1% NaOH and distilled/DI water, as previously described (Section 2.2.1).

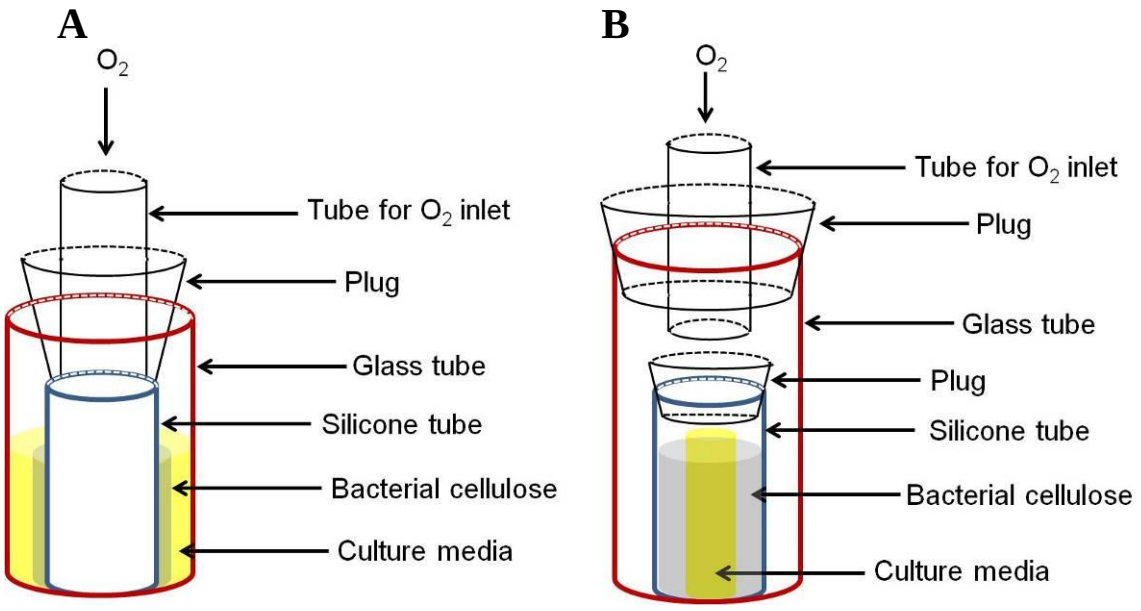

Figure 2.2: Schematic representation of BC-TS produced in silicone tubes. Illustration of BC-TS produced on the outside surface of the silicone tube (A) or on the inside surface of the silicone tube (B).

2.2.4. Surface Amination and Carboxylation of Bacterial Cellulose Scaffolds

Surface amination and carboxylation were completed on native and microporous BCs. Three amination (primary, tertiary, and quaternary amine) and a carboxylation reactions were performed as previously described [97, 112].

Briefly, 100 g of wet native BC pellicles were treated in 0.5 N NaOH at 70 °C for 2 h. A concentration of 39.6 mM of 2-chloroethylamine hydrochloride (CEA) was then added to the mixture and incubate at 70 °C for 5 h to obtain an aminoethyl BC (AE-BC). The scaffolds were neutralized with 6 N HCl after incubation and washed with DI water. The reactants 2-chloro-*N,N*-dimethylethylamine hydrochloride (CDMEA), glycidyl trimethyl ammonium chloride (GTMEA), and monochloro acetic acid sodium salt (Na-MCA) were also reacted with native BC pellicles under the conditions described above to obtain

dimethyl aminoethyl BC (DMAE-BC), trimethyl ammonium betahydroxy propyl BC (TMAHP-BC), and carboxymethyl BC (CM-BC) scaffolds, respectively. Microporous BCs were chemically modified under the same conditions to obtain aminoethyl microporous BC (AE Porous BC), dimethyl aminoethyl microporous BC (DMAE Porous BC), trimethyl ammonium betahydroxy propyl microporous BC (TMAHP Porous BC), and carboxymethyl microporous BC (CM Porous BC). Chemically modified cellulose scaffolds were also prepared using a lower (19.8 mM) and a higher (59.4 mM) concentration of the reactants compared to the initial reactant concentration of 39.6 mM, to access their effects on cell behavior. Table 2.1 illustrates the reactants and reactant concentrations used to produce these chemical functionalities on native and microporous BCs. All samples were stored in DI water prior to use.

2.2.5. Oxidation of Bacterial Cellulose Scaffolds

Periodate oxidation of native BC (OBC), microporous BC (Porous OBC), BC-TS (OBC-TS), and cellulose that have undergone surface amination and carboxylation, was completed to chemically modify these scaffolds into degradable scaffolds. Periodate oxidation was performed as previously described [68]. Briefly, cellulose pellicles were added to a solution of 50 mM $NaIO_4$ in 5% n-propanol. The container of the mixer was caped, covered with aluminum foil and placed on an orbital shaker for 24 h at room temperature. The oxidation reaction was stopped and excess periodate consumed by placing the vessel in an ice bath and adding 0.5 mL of glycerol. The cellulose pellicles were then purified with numerous changes of distilled/deionized water to remove residual oxidation reagents. The cellulose pellicles were stored in DI water at room temperature prior to use.

Table 2.1: Reactants and reactant concentrations used to produce the listed chemical functionalities on native and microporous bacterial cellulose pellicles.

Surface Functionality	Reactant	Concentration (mM)	Non-modified Cellulose
Primary Amine	2-Chloroethylamine hydrochloride (CEA)	19.8	Native BC
		39.6	Microporous BC
		59.4	
Tertiary Amine	2-Chloro-*N,N*-dimethylethylamine hydrochloride (CDMEA)	19.8	Native BC
		39.6	Microporous BC
		59.4	
Quaternary Amine	Glycidyl trimethyl ammonium chloride (GTMEA)	19.8	Native BC
		39.6	Microporous BC
		59.4	
Carboxylation	Monochloro acetic acid sodium salt (Na-MCA)	19.8	Native BC
		39.6	Microporous BC
		59.4	

2.2.6. Mineralization of Bacterial Cellulose Scaffolds

Calcium-deficient hydroxyapatite (CdHAP) was formed within native and modified BC samples by performing an alternating incubation cycle with calcium and phosphate solutions (modified from Hutchens et al. [69]). Briefly, cellulose pellicles were suspended in 1.0 mM $CaCl_2$ under agitation in an ortibal shaker for 24 h (23 °C), rinsed briefly in DI water, and then transferred to 0.6mM Na_2HPO_4 under agitation for another 24 h (23 °C) to obtain CdHAP. Two additional groups of CdHAP synthesis were performed on the BCs using the combination of 2.5 mM $CaCl_2$/1.5 mM Na_2HPO_4 and/or 5 mM $CaCl_2$/3.0 mM Na_2HPO_4 under the same conditions. The cellulose pellicles were stored in DI water at room temperature prior to use. The nomenclature of the mineralized samples is BC-CdHAP, OBC-CdHAP, porous BC-CdHAP, porous OBC-CdHAP, BC-TS-CdHAP, and OBC-TS-CdHAP.

2.3. Bacterial Cellulose Scaffold Characterization

2.3.1. Scanning Electron Microscopy

Scanning Electron Microscopy (SEM) provides topological images of the surface of a sample by scanning a focused beam of electrons over the target area [113]. The signals which results from the refraction of the electron beam with the atoms on the surface of the sample include backscattered and secondary electrons. These signals, emitted from the sample, are detected electronically by a detector and used to form the images of the sample. Conventional SEMs are capable of achieving excellent resolutions (up to approximately 5 nm), a wide range of magnification (approximately 15 – 100,000 X), and producing images with excellent depth of field [113].

The morphology of native and modified BC samples, and beeswax microspheres were analyzed using an SEM. In preparation for SEM analysis, samples were lyophilized or critical point dried (CPD) to remove any water present in the materials. For lyophilization, hydrated samples were placed in a

−80 °C freezer for 24 h and lyophilized in a FreeZone® 4.5 Freeze Dry System for at least 24 h at −50 °C and 1.0×10^{-3} Pa. The CPD samples were prepared by submerging the samples in 3% glutaraldehyde (Electron Microscopy Sciences, Hatfield, PA) for at least 24 h, rinsed with 1X phosphate-buffered saline (PBS) (137 mM NaCl, 10 mM Phosphate, 2.7 mM KCl, and pH 7.4) [114] and dehydrated by incubating consecutively in 30%, 50%, 70%, 90% acetone and then three times in 100% acetone for 10 min. The samples were then dried in liquid CO_2. Lyophilized or CPD samples were mounted on carbon tape and sputtered with gold on a Spi Module Sputter Coater (Spi Supplies, Westchester, PA) at 20 mA for 20 s. The morphology of the samples was examined on a LEO 1525 FE-SEM (Zeiss, Oberkochen, Germany) equipped with a Zeiss SmartSEM Software at various accelerating voltages.

The average fiber diameter of the lyophilized and CPD native BCs were obtained by analyzing SEM images using NIH ImageJ 1.45 software (Shareware provided by National Institutes of Health, http://rsbweb.nih.gov/ij/) following protocols previously described [115, 116]. Images were opened in ImageJ, measurements were calibrated using the micron scale bar on the SEM images and the measure tool in Image J was used to find the average fiber diameter of at least sixty randomly selected fibers per sample, with at least four samples per lyophilized and CPD BCs.

The average pore size of the lyophilized BC was assessed by measuring the cross sections of the SEM images using NIH ImageJ 1.45 software following protocols previously described [117]. Originally, an automated capillary flow porometer (CFP-1100-AI; Porous Materials, Inc: Ithaca, NY) was used to measure the average pore size of lyophilized native BCs. However, it was determined that the pore size of the native BC was smaller than the minimum detectable instrumental pore size of 0.5 μm at the operating pressure of 16 psi using Galwick wetting fluid (surface tension 15.9 dynes/cm). Using the NIH ImageJ 1.45 software, at least thirty randomly selected top-view measurements

from at least four samples were averaged to obtain the mean value and standard deviation of the pore size.

2.3.2. Fourier Transform Infrared Spectroscopy

Fourier Transform Infrared (FTIR) Spectroscopy is a chemical analytical technique that characterizes the molecular level interactions of materials by examining the vibrations between a material's bonded atoms [118]. In FTIR, infrared radiation is passed through a sample, and the sample absorbs radiations whose frequencies are identical to the frequencies of the bond vibration and frequencies that cause a change of dipole in the molecule [119]. Vibrational frequencies are a result of the nature of the inter-atomic bond in a sample such as the functional groups of the bonded atoms and electronic nature of the bond, i.e., ionic, covalent, double and triple bonds. The infrared radiation frequencies from the analysis are passed through an interferometer, where the signal is mathematically processed using Fourier transform, to obtain the spectrum. The resulting FTIR spectrum represents the frequencies at which the functional groups present in the sample absorbs the infrared radiation and the intensities of the molecular absorption. FTIR can be used to identify the chemical structure and molecular orientation of materials. Conventional FTIR is used to characterize bulk specimens. Other techniques derived from FTIR include attenuated total reflectance-FTIR (ATR-FTIR) and photoacoustic spectroscopy-FTIR (PAS-FTIR). ATR-FTIR spectroscopy can be employed to analyze sample surfaces up to 2 microns in depth, and the PAC-FTIR can used to study the structure of materials at different thicknesses within the sample [119].

The chemical structures for native BC, modified BC, and beeswax were analyzed using an FTIR. FTIR was also used to confirm removal of the beeswax. The native and modified BC samples were lyophilized and then further dried for 24 h in a vacuum oven (100 °C at 230 kPa) to remove any water present in the samples prior to performing FTIR analysis. Lyophilization of the cellulose pellicles was performed as previously described (Section 2.3.1). The

lyophilized samples were granulated using a mortar and pestle prior to FTIR analysis. Approximately 1 mg of a granulated sample was mixed with 45 mg of KBr powder and compressed into a disk using a screw-type press. FTIR analysis was performed using a BioRad FTS6000 Spectrometer (Perkin Elmer, Waltham, MA) equipment with Resolutions Pro FTIR Software® (Agilent Technologies, Santa Clara, California). The reported spectra are the result of 256 scans collected with a resolution of 4 cm^{-1}.

Disposable Infrared Cards of and polytetrafluoroethylene (PTFE) was used to obtain the spectra of beeswax, following a previously described method [120]. Briefly, melted beeswax were placed on the Disposable Infrared Card and allowed to dry at room temperature. A Blank card of PTFE was used as backgrounds for the sample. The FTIR analysis of the beeswax sample was performed on the BioRad FTS6000 Spectrometer and the reported spectrum is the result of 256 scans collected with a resolution of 4 cm^{-1}.

The FTIR absorption spectrum for Tween 80 was collected using the BioRad FTS6000 Spectrometer coupled to a BioRad UMA 500 infrared microscope. The sample was analyzed in the ATR mode using a germanium crystal. The first mirror prior to the FTIR laser was set at 50° during sample analysis. The spectrum for Tween 80 was also the result of 256 scans collected with a resolution of 4 cm^{-1}. Because the spectral profile obtained from ATR and transmission method can be different for the same sample due to the physics of these experiments [121, 122], native BC and microporous BC were also analyzed using the ATR method and the results were compared to that of Tween 80.

2.3.3. Thermal Gravimetric Analysis of Beeswax

Thermal gravimetric analysis (TGA) is a thermal analysis technique that determines changes in weight of a sample as a function of temperature in a controlled atmosphere [123]. This technique allows studies of material loss, degradation, and sorption and desorption. In this work, a Mettler Toledo Star

System TGA (Columbus, OH) was used. Beeswax samples were analyzed under the flow of N_2 gas to determine the temperature at which thermal oxidation degradation (degradation temperature) occurs from the weight loss. A sample size of ~10 mg (n = 3) was loaded into an aluminum sample pan. Beeswax sample was analyzed by heating at a rate of 10 °C/min from 25 °C to 500 °C. The analysis was performed under a flow of 20 cc/min of N_2 gas.

2.3.4. Differential Scanning Calorimetry of Beeswax

Differential Scanning Calorimetry (DSC) is a thermal analysis technique in which the exact quantity of heat applied to increase the temperature of a sample is measured as a function of temperature, and compared to an inert reference sample heated using the same heating profiles [123]. Analysis is performed in a controlled atmosphere using a reference material such as alumina or an empty aluminum pan. The resulting thermogram from the analysis provides information on changes of thermal properties of the sample with temperature. More specifically, DSC technique can be used to determine the thermal properties of materials, such as the glass-transition temperatures, fusion enthalpies, crystallization temperatures, crystallinity and melting temperatures [123].

In this work, DSC analysis was performed using a Mettler Toledo Star System DSC and following ASTM D3418-08 [124]. Beeswax samples were analyzed under the flow of N_2 gas to determine the melting temperature of the sample. A sample size of ~7-10 mg (n = 3) was loaded into an aluminum sample pan and an empty pan (aluminum crucible standard pan, Mettler Toledo) was used as reference. Beeswax sample (n = 3) was held at 5 °C for 2 min and then heating at a rate of 5 °C/min from 5 °C to 85 °C. The analysis was performed under a flow of 80 cc/min of N_2 gas. The approximate melting temperature of the beeswax was determined as the maximum in the endothermal melting peak of the obtained thermogram.

2.3.5. Mechanical Testing of Bacterial Cellulose Scaffolds

Biomaterials are used as structural materials, where they are subjected to loading forces during *in vivo* applications. Therefore, it is crucial to determine the mechanical behavior of the biomaterial in order to predetermine their performance following implantation. To increase the chances of a biomaterial's success, it is generally engineered to mimic the *in vivo* tissue or matrix microenvironment it is intended to replace. An instrument that has been widely used to measure the mechanical properties of materials easily and quickly is a tensile tester. During tensile testing, a specimen is subjected to an applied stress which causes a change in the initial length of the sample. The change associated with specimen length is used to determine the strain related to the deformation of the sample. The results from the test can be used to calculate the elastic modulus, ultimate tensile strength, and elongation of the material. The elastic modulus or Young's Modulus characterizes stiffness or brittleness, ultimate tensile strength depicts the absolute breaking force, and elongation represents the stretchability or ductile behavior in a given direction of a material.

In a tensile test, a dog bone (dumbbell) shaped specimen is commonly used and incrementally elongated until it breaks. A dog bone-shaped specimen with offset ends is used to reduce grip effect during materials testing. A stress-strain curve is created from the results of the tensile test. The engineering stress (σ_e) is calculated by dividing the applied load (F) by the initial cross-sectional area of the specimen that will undergo deformation (A_o):

$$\sigma_e = F / A_o. \qquad (2.1)$$

The initial cross-sectional area of the specimen is determined by multiplying the thickness of the initial gage area (T_o) by the width of the initial gage area (W_o):

$$A_o = (T_o)\,(W_o). \qquad (2.2)$$

The engineering strain (ε_e) is obtained by dividing the elongation of the sample ($L - L_o$) by the initial gage length of the specimen (L_o), where L is the gage length after sample deformation:

$$\varepsilon_e = (L - L_o) / (L_o)\,. \qquad (2.3)$$

The Young's elastic modulus (E) is the slope of the stress-strain curve in the elastic region of the curve, and is determined by dividing engineering stress by engineering strain [125]:

$$E = \sigma_e / \varepsilon_e. \qquad (2.4)$$

The ultimate tensile strength is the maximum stress experienced by the specimen on the stress-strain curve.

For mechanical testing, BC hydrogels were synthesized in glassware (360 mm L x 200 mm W x 5 mm H) to enable the production of cellulose pellicles with adequate area for testing. Cellulose synthesis and sample preparations were performed following methods previously described (Sections 2.2.1 - 2.2.2 and 2.2.4 - 2.2.6). The mechanical properties of native and modified BC samples were analyzed according to ASTM D882-09 [126]. A minimum of five hydrated, never dried specimens were analyzed for each type of BC sample. Uniaxial material tests were performed using the Instron ElectroPuls™ E1000 mechanical testing unit (Instron, Norwood, MA) or the Instron 5943 mechanical testing unit (Instron), both equipped with Instron® Bluehill® Software (Instron). A 1.0 kN or 100 N load cell incorporated in the testing unit was used to extend the samples at a rate of 0.5 mm/min until failure. Dog bone templates were used to make samples of the native and modified BC samples. By using the dog bone

template, specimens had a gauge length of 31 mm, an overall width of 6.5 mm, and a total length of 77 mm. The thickness for each specimen was measured using a digital caliper (Mitutoyo Absolute 500-196-20 Digital Caliper, Aurora, IL) before testing. These specimens were anticipated to exhibit random fiber orientation; therefore the mechanical properties of each type of specimen were expected to be similar in all directions. The mechanical properties evaluated include elastic modulus, percent strain at break, and ultimate tensile strength of the cellulose scaffolds.

Mechanical properties including engineering elastic modulus, percent strain at break and ultimate tensile strength of the BC-TS and its composites were examined using the Instron ElectroPuls™ E1000 mechanical testing unit or the Instron 5943 mechanical testing unit, both equipped with Instron® Bluehill® Software. The mechanical integrity of the materials were determined following a previously describe method [104]. Briefly, specimens were analyzed by lengthwise and breathwise elongation. A minimum of three specimens were analyzed for each type of BC-TS sample. Specimen (~25 mm gage length with ~5 mm long gripping tabs) for lengthwise elongation was performed at a rate of 0.5 mm/min until failure using a 1.0 kN or 100 N load cell. Specimen (~6 mm in length) for breathwise elongation was elongated using 2 U-shaped wires inserted through the hollow opening of the sample. The thickness for each specimen for lengthwise and breathwise elongation was measured before testing. All measurements were performed using a digital caliper (Mitutoyo Absolute 500-196-20 Digital Caliper). Analyses were performed at a rate of 0.5 mm/min until failure, using a 1.0 kN or 100 N load cell.

Lengthwise and breathwise sectioned specimens of the BC-TS hydrogels represent the longitudinal and transverse fiber direction of the samples, respectively, in accordance to the potential use. The BC hydrogel samples with aligned fibers should exhibit anisotropic mechanical properties, i.e. different in transverse and longitudinal directions.

The data for the native and modified BCs were analyzed using Microsoft Excel®.

2.4. *In Vitro* Degradation Study of Oxidized Bacterial Cellulose Scaffolds

A degradation study was performed for the native and modified BC samples using a method previously described by Hutchens et al. [68]. The degradation method by Hutchens et al. [68] measures cellulose degradation products using a UV-Vis spectrophotometer. In preparation for degradation analysis HEPES buffer consisting of 25 mM HEPES and 75 mM NH_4Cl was prepared, neutralized using HCl or NaOH, and autoclaved (1 bar, 250 °C) for 30 min prior to use.

The samples were autoclaved in HEPES buffer (1 bar, 250 °C, 30 min) and each sample was placed in a 50 ml conical bottom tube. A volume of 5 ml HEPES solution was added to each sample. Each set of sample was placed in an incubator, and analysis was performed under static and dynamic conditions at 37 °C to simulate physiological temperature. Static incubation was performed using a VWR 1217 Oscillating Heating Water Bath (Sheldon Manufacturing, Inc., Cornelius, OR). Dynamic incubation was conducted using a G24 Environmental Incubator Shaker (New Brunswick Scientific Co. Inc., Edison, NJ). Every 48 h during the incubation period of 14 days, samples were centrifuged at 3,500 rpm for 15 min, and the absorbance of the supernatants was analyzed using a Thermo Scientific™ Evolution™ 600 UV-Vis Spectrophotometer (Thermo Scientific, Pittsburgh, PA) from 220 to 350 nm. A volume of 5 ml of fresh sterile HEPES buffer was added to each sample and the samples were returned to the incubators. After 14 days of incubation, the samples were removed from the HEPES buffer, rinsed with DI water, lyophilized (see Section 2.2.2), and weighed. Corresponding samples that have not undergone degradation were lyophilized and weighed for mass loss comparison with the lyophilized samples remaining after the degradation study. The data for the native and modified BCs were analyzed using Microsoft Excel®.

The samples analyzed for the degradation study were native BC, OBC, BC-CdHAP, OBC-CdHAP, porous BC, porous OBC, porous BC-CdHAP, porous OBC-CdHAP, TMAHP-BC, oxidized TMAHP-BC (TMAHP-OBC), porous TMAHP-BC, and porous oxidized TMAHP-BC (porous TMAHP-OBC). A minimum of three specimens were analyzed for each type of BC sample.

2.5. Cell Isolation, Expansion and Characterization

Equine-derived bone marrow mesenchymal stem cell (EqMSCs) were obtained by centrifugation of bone marrow aspirates from the sternum of a healthy 11-years-old mare according to methods described earlier [127]. The mare was sedated and the sternum was aseptically prepared. Bone marrow aspirates were collected with 300 U/ml of heparin, diluted 1:1 with PBS, layered over 15 ml of ficoll and centrifuged for 20 min at 400 g. The cells at the interface of the PBS and ficoll containing the mononuclear fraction were aspirated and washed in PBS by centrifuging for 10 min at 200 g. The supernatant was aspirated and the cell pellet was resuspended and plated on tissue culture dishes in Dulbecco's Modified Eagle Medium F-12 (DMEM) containing 10% fetal bovine serum (FBS) (Hyclone, Logan, Utah) and 1% penicillin/streptomycin solution (P/S) (Invitrogen, Carlsbad, CA) in a 37 °C, 5% CO_2 incubator (Passage 0). This is the complete growth media. Adherent cells were allowed to reach 80% confluence before harvesting by treatment with trypsin and re-plated for further expansion (Passage 1). At the end of the second passage, EqMSCs were banked in liquid nitrogen in cryopreservation medium (50% FBS, 5% dimethylsulfoxide (DMSO), 45% DMEM). For all cell culture experiments described in this study, cells of passage 2–6 were grown in phenol red-free DMEM complete growth media.

Cellular morphology of EqMSCs and its ability to adhere to TCP was assessed by imaging 5.0 x 10^4 cells/cm^2 seeded in a 24-well TCP after 48 h using a Zeiss Axiovert 40C microscope equipped with a Canon Powershot A620

camera (Cannon USA Inc., Lake Success, NY) and analyzed using ZoomBrowser EX software (Cannon USA Inc., Lake Success, NY).

Immunophenotyping using flow cytometry is an analytical technique used to examine the protein expressed by cells. In this study, the immunophenotype of EqMSCs was characterized by flow cytometric analysis as previously described [128]. For each staining, $7.90 \times 10^5 – 1.58 \times 10^6$ cells/cm^2 seeded in a 96-well plate were used. Cells were prepared in FACS buffer and incubated (37 °C/5% CO_2) with 0.5 mg/ml Mouse BD Fc Block (BD Biosciences, San Jose, CA) for 20 min at 4 °C. The cells were then incubated with 1–10 µg/ml of preconjugated primary antibodies for 60 min in the dark on ice. FITC-conjugated, anti-human CD44 and anti-rat CD90 (Invitrogen, Carlsbad, CA) were used. FITC- conjugated IgG1 (Invitrogen) was the isotype control. Cells were washed by adding 200 µl/well of FACS buffer, and centrifuged at 200 g and 4 °C for 5 min. Cell washing using FACS buffer was repeated. Cell staining was evaluated on a flow cytometer (FACS Vantage SE, Becton Dickinson, Franklin Lakes, NJ) by electronic gating on a dual parameter dot plot of forward and side scatter. For each sample, 10,000 events were measured. Raw data of fluorescence representing the number of positive cells was measured and analyzed by Cell Quest™ software (BD Biosciences).

Osteogenesis and chondrogenesis are the process of forming new bone and cartilage materials, respectively, by cells. In this study, osteogenesis and chondrogenesis were performed using assays, as previously described [128]. Roughly 1.0×10^5 cells/cm^2 were seeded in media on 24-well TCP. Approximately 70–80% confluent cells were induced to differentiate into each of the 2 lineages.

Osteogenic differentiation was induced in growth media supplemented with 100 nM dexamethasone, 10 mM β-glycerophosphate, and 0.25 mM ascorbic acid. Differentiation cell groups (induced cells with osteogenic media) were monitored with control cell groups (non-induced cells without osteogenic media). Media was changed every 3 days, and differentiation was assessed using

alizarin red (Fisher Scientific) staining after 14 days. Cells were fixed in 4% Paraformaldehyde (PFA) for 10 min at room temperature and stained with alizarin red for 30 min for the detection of calcium in differentiated cells. Images were taken with a Zeiss Axiovert 40C microscope equiped with a Canon Powershot A620 camera and analyzed using ZoomBrowser EX software.

Chondrogenic differentiation was induced in a monolayer of cells in growth media supplemented with 100 nM dexamethasone, 0.25 mM ascorbic acid, and 5 ng/ml TGFβ1 (R&D Systems, Minneapolis, MN). Differentiation cell groups (induced cells with chondrogenic media) were monitored with control cell groups (non-induced cells and without chondrogenic media). Media was changed every 3 days, and differentiation was assessed using alcian blue staining after 14 days. Cells were fixed in 4% PFA for 10 min at room temperature and stained with alcian blue 8GX (Fisher Scientific) for 30 min for the detection of glycosaminoglycans. Images were taken with a Zeiss Axiovert 40C microscope equiped with a Canon Powershot A620 camera and analyzed using ZoomBrowser EX software.

2.6. *In Vitro* Study of Cell and Bacterial Cellulose Scaffolds

For cell culture studies, the hydrated, never-dried native and modified BC scaffolds in hydrogel form were used. BC-TS and its composites were prepared as circular discs for the cell study using 6 mm Miltex Inc. disposable biopsy punches (Fisher Scientific) and a 17.46 mm round hole arch punch (McMaster Carr, Atlanta, GA). For cell culture studies, the BC scaffolds, chemically modified BC scaffolds and their composites were sterilized by autoclave (1 bar, 120 °C) for 30 min, and were pre-soaked in phenol red-free growth media for at least 24 h prior to cell seeding.

2.6.1. Cellular Adhesion, Viability and Proliferation Assays

Cell viability and proliferation were assessed at various time points, using the CellTiter 96® Aqueous Non-Radioactive (MTS) assay (Promega, Madison, WI) according to the manufacturer's instructions. All experiments were conducted in triplicate on 96-well TCP, native and modified BC scaffolds. Various cell densities were seeded on the TCP, native and modified BC scaffolds. Cells were incubated in the growth media at 37 °C/5% CO_2. At the end of each specified incubation time, EqMSCs seeded on TCP, and on the native and modified BCs were rinsed three times in PBS, immersed in a mixture containing serum-free cell culture medium and MTS reagent in a 5:1 ratio, and incubated for 3 h at 37 °C/5% CO_2. Then, 100 µL (n=2) was transferred to 96-well plates and the optical density (O.D.) was measured on a microplate fluorescence reader (BioTek, Winooski, VT) using an absorbance of 490 nm. Microporous BC scaffolds and its modified composites seeded with cells were transferred to a new TCP prior to the addition of the serum-free cell culture medium and MTS reagent. Non-seeded TCP and equivalent BC scaffolds in the same media were used as blanks. The recorded absorbance values at 490 nm were subtracted from their respective blank readings to yield the corrected absorbance. Each experiment was conducted in 3 independent biological and 3 technical replicates.

Cell adhesion and viability was assessed at different time periods in culture using calcein-AM (Invitrogen, Eugene, OR) and propidium iodide (PI) (Invitrogen, Carlsbad, CA). EqMSCs were seeded on 96-well TCP, native and modified BC scaffolds using various cell densities. Cells were stained with a solution of 10 µM calcein-AM/500 nM PI for 5 min and subsequently visualized using a Zeiss Axiovert 40C microscope equipped with a Nikon Digital Sight DS-Qi1Mc camera.

Cell adhesion and morphology on TCP, native BC, BC-TS and its composites seeded using different cell densities were assessed at various time points in culture using wheat germ agglutinin (WGA) (Invitrogen, Carlsbad, CA)

for the sialic acid and N-acetylglucosaminyl sugar residues in the plasma membrane, and 4′,6-diamidino-2-phenylindole (DAPI) stain for the nucleus. Samples were stained with WGA (10 µl/ml) for 10 min, washed three times with PBS, and stained with DAPI (0.5 µg/ml) for 5 min. Different cell densities were seeded on the TCP and cellulose scaffolds. Fluorescent images were captured using a Zeiss Axiovert 40C microscope equipped with a Nikon Digital Sight DS-Qi1Mc camera.

2.6.2. Alkaline Phosphatase Staining of Cells

Alkaline phosphatase (ALP) stain is a cell-permeable dye that is used to positively identify pluripotent stem cells. The pluripotent potential of the EqMSCs was evaluated using ALP stain. ALP staining of EqMSCs was assessed by the specific conversion of Naphthol AS-MX phosphate and Fast Red TR into an insoluble Azo Red End Product. EqMSCs were seeded in a 24-well TCP and native BC scaffolds at 5.0 x 10^4 cells/cm^2. Cells were cultured for 12–14 days at 37 °C/5% CO_2 with media changes every 2–3 days until the end of the experiment. The ALP enzymatic reaction was set up by mixing Fast Red TR, Naphthol AS-MX phosphate and PBS (2:1:1). For staining, cells were rinsed with PBS, fixed in 4% PFA for 2 min at room temperature, and stained with the ALP solution for 15 min at room temperature. Images were taken with a Zeiss Axiovert 40C microscope equipped with a Canon Powershot A620 camera and analyzed using ZoomBrowser EX software.

2.6.3. Cell Adhesion and Morphology by Scanning Electron Microscopy

Cell adhesion and morphology on native BC were examined by SEM. EqMSCs were seeded at 5.0 x 10^4 cells/cm^2 on 24-well native BC scaffolds for 10–14 days at 37 °C/5% CO_2 with media changes every 2–3 days, were washed with PBS, and dried using the CPD method described above (Section 2.3.1).

The samples were then sputter-coated with a gold layer as previously described and imaged using a SEM (LEO 1525 FE-SEM and Zeiss SmartSEM Software).

2.6.4. Differentiation Assays

Osteogenesis and chondrogenesis, assays were performed as described above (Section 2.5). Cells were differentiated on TCP, and on native and modified BC scaffolds using different cell seeding densities. Differentiations were monitored by staining at various days in culture. Images of the differentiated cells on the cellulose scaffolds were captured using a Zeiss Axiovert 40C microscope equipped with a Canon Powershot A620 camera or with with a Nikon Digital Sight DS-Fi2 camera.

2.6.5. Confocal Microscopy

Confocal microscopy was used to examine the distance of cellular penetration into the bulk of the modified BC scaffolds. The extent of cell adhesion and viability across the surface of the scaffolds were also assessed using confocal microscopy. The samples examined were OBC and porous OBC. EqMSCs were seeded at 6.3 X 10^4 cell/cm^2 on 96-well sized native and modified BC scaffolds for 9–10 days at 37 °C/5% CO_2 with media changes every 2–3 days. After the incubation periods, cell-scaffold constructs were stained with 200 µl of 10 µM calcein-AM for 5 min, transferred to optical microscope slides and imaged using a Leica TCS SP2 laser scanning confocal microscope (Leica Microsystems, Buffalo Grove, IL) equipped with Leica Confocal Software. The Leica Confocal Software was used to perform a Z-series image mapping of the cells on the seeded scaffolds, by scanning from the top surface of the scaffolds into the bulk of the material until fluorescence could not be visually detected. The Leica Confocal Software was also used to perform an image mapping of the cells on the scaffolds by scanning across the surface of the material. Confocal

images were processed using the Leica Confocal Software and the Nikon NIS-Elements Software (Nikon Instruments Inc.).

CHAPTER III
Analysis of Native Bacterial Cellulose Scaffolds

An ideal functional tissue engineered substitute would be a single three-dimensional (3D) biocompatible scaffold capable of adapting to various connective tissue microenvironments, while supporting selective lineage-specific differentiation of MSCs for multiple connective tissue applications. In this study, 3D nanofibrous BC hydrogel scaffolds were prepared and characterized for their ability to support and maintain differentiation of EqMSCs *in vitro* for potential tissue engineering use. Proliferation, viability and potential to differentiate into osteocytes and chondrocytes of EqMSCs on BC were compared to those grown on TCP. In this chapter, the results and discussions from the study are presented concurrently in Sections 3.1-3.3, and the conclusion is presented in Section 3.4. The results of this study were published in the journal *Material Science and Engineering C* [106].

3.1. Characterization of Native Bacterial Cellulose Scaffold

To examine the nanofibers structure of native BC, SEM was used. Because the SEM required a completely dry sample during analysis to maintain the high vacuum chamber environment, then randomly selected BC hydrogels were dried exclusively for SEM examination. Commonly, either freeze-drying or CPD are recommended for drying hydrogels and biological materials because these methods more effectively preserve the three-dimensional sponge-like matrix during the dehydration process [65, 129]. The morphological characteristics of the BC were assessed to determine the effects of these different drying procedures on the resulting physical properties of the BC network. SEM images of lyophilized and CPD BC scaffolds are illustrated in Figure 3.1.A and 3.1.B. The lyophilized BC (Figure 3.1.A) showed distinct pores, inherent pore interconnectivity, and random distribution of the fiber orientation.

The CPD BC (Figure 3.1.B) demonstrated reduction in pore size and bundled fiber arrangements.

The dehydration method influenced the morphology of the BC networks to different extent. According to the SEM images (Figure 3.1.A, 3.1.B), CPD BC showed a bundled fiber network in contrast to the lyophilized BC. This implies that the changed morphology was a result of the temperature or solvent treatments in the drying process. In lyophilization, samples were frozen to -80 °C and the ice crystals were then transformed to water vapor at a specific temperature and pressure by sublimation [65]. In CPD however, the water in the BC hydrogel was ultimately replaced with liquid CO_2 and the sample was processed above its critical temperature (31.1 °C) and pressure (7.3 MPa) where the liquid CO_2 changes to vapor without change of density [65]. It has been reported that the ice crystal freezing rate in lyophilization and CPD procedures determines the final pore sizes of dehydrated hydrogels [65]. Therefore, the morphology differences reported here as a result of the dehydration methods could be attributed to the formation of ice crystal in the lyophilized BC and its absence in the CPD BC. Even though there are some artifacts due to the ice crystals, the morphology of lyophilized BC (Figure 3.1.A) is more representative of the hydrated native BC morphology compared to the CPD BC morphology

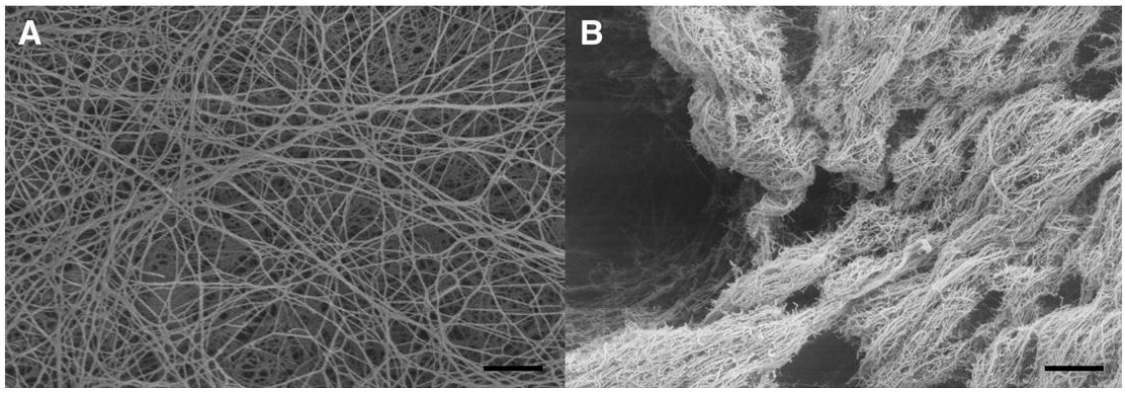

Figure 3.1: Characterization of BC scaffold. SEM of lyophilized BC scaffold (A) and CPD BC scaffold (B). Morphology of the cellulose network varied depending on the drying treatment. Scale bar = 1 μm [106].

(Figure 3.1.2). The SEM image of lyophilized native BC illustrates distinct pores, agreeing with previously reported data [93]. In addition, these authors observed similar non-compacted surface morphologies between lyophilized native BC imaged using SEM and wet BC imaged using confocal microscopy [93].

Intramolecular and intermolecular hydrogen bonding facilitates the retention of water in the interstitial spaces of hydrated BC scaffolds, allowing for extensive water retention [88]. The total volume of the BC matrix is composed of 99.8% water and 0.2% pure cellulose [85]. Hydrogen bonding also allows the BC high strength. This research group previously determined the ultimate tensile strength and Young's modulus (or elastic modulus) of hydrated native BCs to be 25-30 KPa and 3.0-4.5 KPa, respectively [68]. Young's Modulus of dried BCs has been reported to be 15-30 GPa [88].

The average fiber diameter (Table 3.1) of the lyophilized and CPD BCs were 32.08 nm (±10.85 nm) and 29.93 nm (±8.28 nm), respectively. When compared using a Student's t-test ($p \leq 0.05$), these differences were statistically insignificant. Given that either lyophilization or CPD method is required to maintain the sponge-like porous matrix of BC in the dry state, differences in the resulting morphological characteristics (Figure 3.1.A, 3.1.B) were observed but similarities in the fiber diameter of BCs (Table 3.1) prepared following these methods of dehydration. The temperature or solvent treatments in the drying process did not appreciably alter the diameter of the BC fiber (Table 3.1). Therefore, we can conclude that by using either drying methods, fiber diameters of the resulting BCs are statistically indifferent.

Pore size is important in scaffolds because they support cell ingrowth, determine cell adhesion and migration, establish the mechanical properties of the scaffold, maintain the diffusion of nutrients to accommodate cells and guide their growth, and subsequently the success of new tissue regeneration [130]. The average pore size (Table 3.1) of the lyophilized BCs was 254.16 nm (±76.65 nm). Scaffolds with pores of 5-15 μm was proposed to provide a suitable environment for fibroblast ingrowth [131]. Other investigators have proven that human

Table 3.1: Measurement of average fiber diameters of lyophilized and CPD BC. Table illustrates the measured pore size of lyophilized BC from SEM images using ImageJ [106].

	Lyophilized BC	Critical-point-dried BC
Fiber diameter (nm)	32.1	29.9
Standard deviation	10.9	8.3
Pore size (nm)	254.2	-
Standard deviation	76.7	-

chondrocytes and human smooth muscle cells could evade the fibers and penetrate into the scaffold *in vitro* which allows BC to support ingrowth of the cells into the scaffold [93, 132]. An ingrowth of up to 40 μm was observed with human smooth muscle cells cultured on native BC [132]. These features make BC an attractive material for tissue engineering using fibroblast cells.

3.2. Characterization of Equine Adult Mesenchymal Stem Cells

The isolated EqMSCs were characterized to ensure they possessed the criteria used to identify MSCs which are their ability to adhere to TCP, express specific surface antigens and have the potential to differentiate to lineages of mesenchymal tissues, including bone and cartilage [13, 133]. MSCs are identified by the expression of surface markers which allows for rapid identification of the cell population. Surface markers are unique proteins called antigens that protrude from the cell's surface and perform various functions, including cell-cell attachment, serving as receptors for incoming protein signals, and transporting amino acids across the cell membrane [18]. Each cell type has a specific antigen profile. Known surface markers, as analyzed by flow cytometry, have been assigned a cluster of differentiation (CD) identification

number once two specific monoclonal antibodies are shown to bind to the signature cell proteins [18, 134]. CD90 and CD44 have been commonly used as positive MSC surface markers [133, 135].

Isolated EqMSCs adherence to TCP was observed (Figure 3.2.A). Contrast micrograph (Figure 3.2.A) revealed the fibroblast like morphology of the EqMSC with long and thin cell body attached to the surface of the TCP. Flow cytometry expression showed that EqMSCs are positive for stromal cell markers CD90 and CD44 (>90%) (Figure 3.2.B, 3.2.C). IgG1 was the isotype control (Figure 3.2.B, 3.2.C). Osteogenic differentiation of EqMSCs was observed with positive alizarin red staining of calcium deposits in the differentiated cells (Figure 3.2.D) [133]. Undifferentiated (i.e. equal number of cells without any differentiation cocktail) served as negative controls for osteocytes and did not stain positive for alizarin red (Figure 3.2.D). Chondrogenic differentiation of EqMSCs was observed with positive alcian blue staining of glycosaminoglycans in the differentiated cells (Figure 3.2.D) [133]. The undifferentiated cells served as negative controls and did not stain positive for glycosaminoglycans (Figure 3.2.D).

Characterization of isolated EqMSCs revealed that the cells exhibit the morphology (Figure 3.2.A) and cell surface maker expression (Figure 3.2.B, 3.2.C) indicative of mesenchymal phenotype [133, 135]. Alizarin red stains for calcium matrix formations which are characteristic of functional osteocytes in MSCs [133]. The osteocyte induced EqMSCs successfully formed alizarin red positive nodules after 14 days in culture compared to the non-induced control group (Figure 3.2.D). Alcian Blue stains for glycosaminoglycans deposits, which are sulfated proteoglycans associated with collagen-rich extracellular matrix, that are designative of functional chondrocytes [133, 136]. The chondrocyte induced EqMSCs aggregated into nodules and positively stained alcian blue after 14 days in culture (Figure 3.2.D).

Using the three criteria defining stem cells; adherence to TCP (Figure 3.2.A), expression of cluster of differentiation protein markers, CD44 and CD90

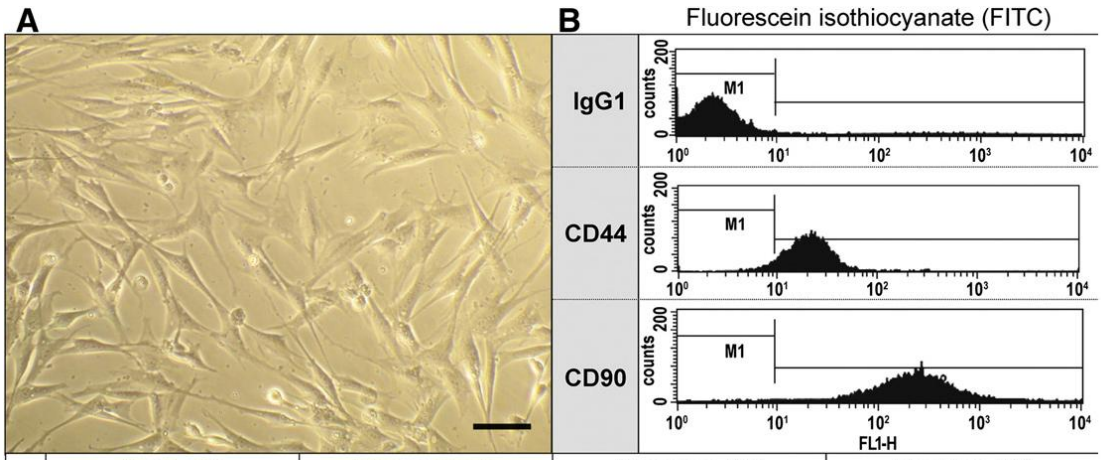

C

Antibody	Flourophore	Negative (%)	Positive (%)
IgG1	FITC	99.30	0.73
CD44	FITC	7.85	92.32
CD90	FITC	0.36	99.65

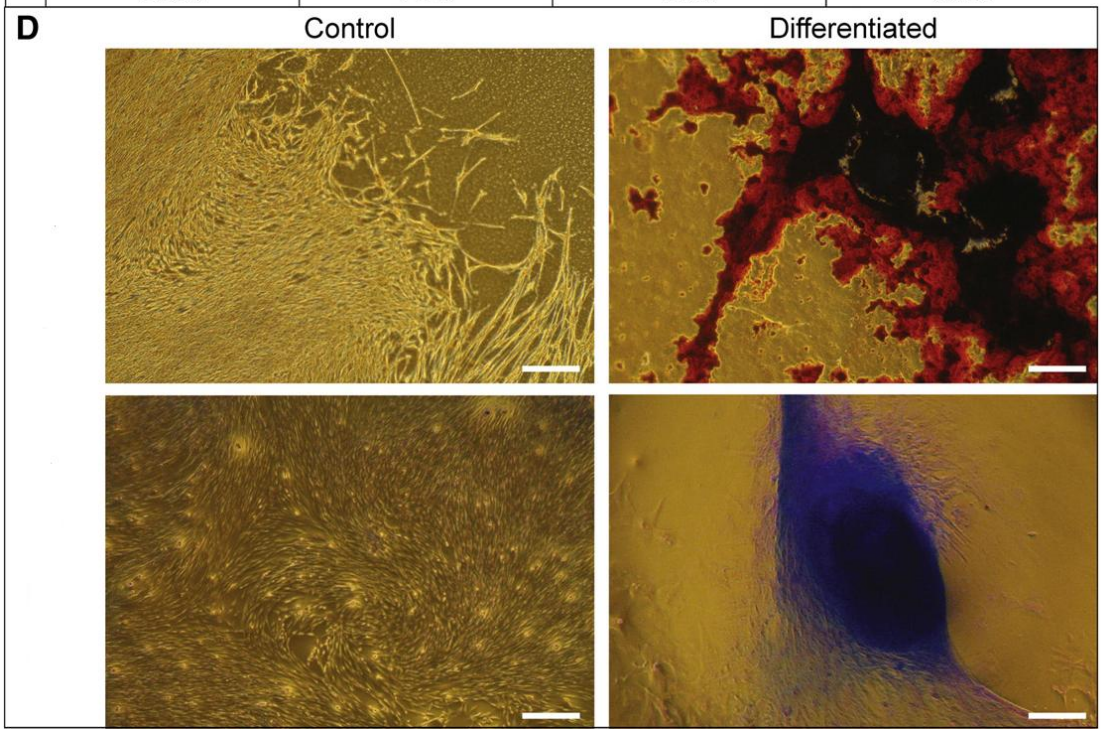

Figure 3.2: Characterization of EqMSCs. (A) Cellular morphology of EqMSCs using phase contrast microscope confirmed fibroblastoid adherent cells (Scale bar = 200 µm). (B) EqMSCs express markers associated with mesenchymal phenotype (positive expression of CD90 and CD44; negative for the isotypic control IgG1). (C) Surface antigen expression on EqMSCs by flow cytometric analysis. Table shows the %-positive cells to the total number of cells analyzed by flow cytometric analysis. (D) Differentiation of EqMSCs into osteocytes (alizarin red staining) and chondrocytes (alcian bl ue staining) at 14 days of differentiation. Scale bar = 200 µm [106].

(Figure 3.2.B, 3.2.C), and finally the potential to differentiate into osteocytes and chondrocytes (Figure 3.2.D), mononuclear cells isolated from bone marrow and expanded in culture were assessed to be the adult MSCs [133]. These isolated adult MSCs are therefore undifferentiated cells with the potential to differentiate into connective tissue cells for musculoskeletal tissue engineering applications.

3.3. Characterization of Cell and Bacterial Cellulose Scaffolds

3.3.1. Cellular Adhesion, Viability and Proliferation Assays

MTS assay analysis was performed to determine the viability of EqMSCs seeded on TCP (EqMSCs-TCP) and on BC (EqMSCs-BC). The MTS assay results of EqMSCs seeded on TCP and BC are shown in Figure 3.3. EqMSCs seeded on TCP (Figure 3.3.A) and on BC (Figure. 3.3.B-3.3.E) demonstrated high growth rates as a function time and represent a high viability and proliferation composition.

MTS assay (3-(4,5-dimethylthiazol-2-yl)-5-(3-carboxymethoxyphenyl)-2-(4-sulfophenyl)-2H-tetrazolium and phenazine methosulfate) is a tetrazolium-based compound that is bioreduced by cells into a brown formazan product that is soluble in tissue culture medium [137]. The quantity of formazan product measured at the absorbance of 490 nm is directly proportional to the number of living cells in culture [137]. The results of MTS assay as shown in Figure 3.3 demonstrate that similar to EqMSCs cultured on TCP (Figure 3.3.A), EqMSCs seeded on BC were able to metabolize MTS into brown formazon product and have a high proliferation rate as a function of time (Figure 3.3.B-3.3.E). Furthermore, the squared correlation coefficient of the MTS Assay results were calculated from these curves. The squared correlation coefficient of approximately 3.16×10^4, 6.32×10^4, 9.48×10^4 and 1.26×10^5 cells/cm^2 seeded on BC were 0.998, 0.991, 0.966 and 0.950, respectively, indicating a linear response between cell number and absorbance at 490nm, further confirming the proliferation of EqMSCs under these conditions (Figure 3.3.B-3.3.E).

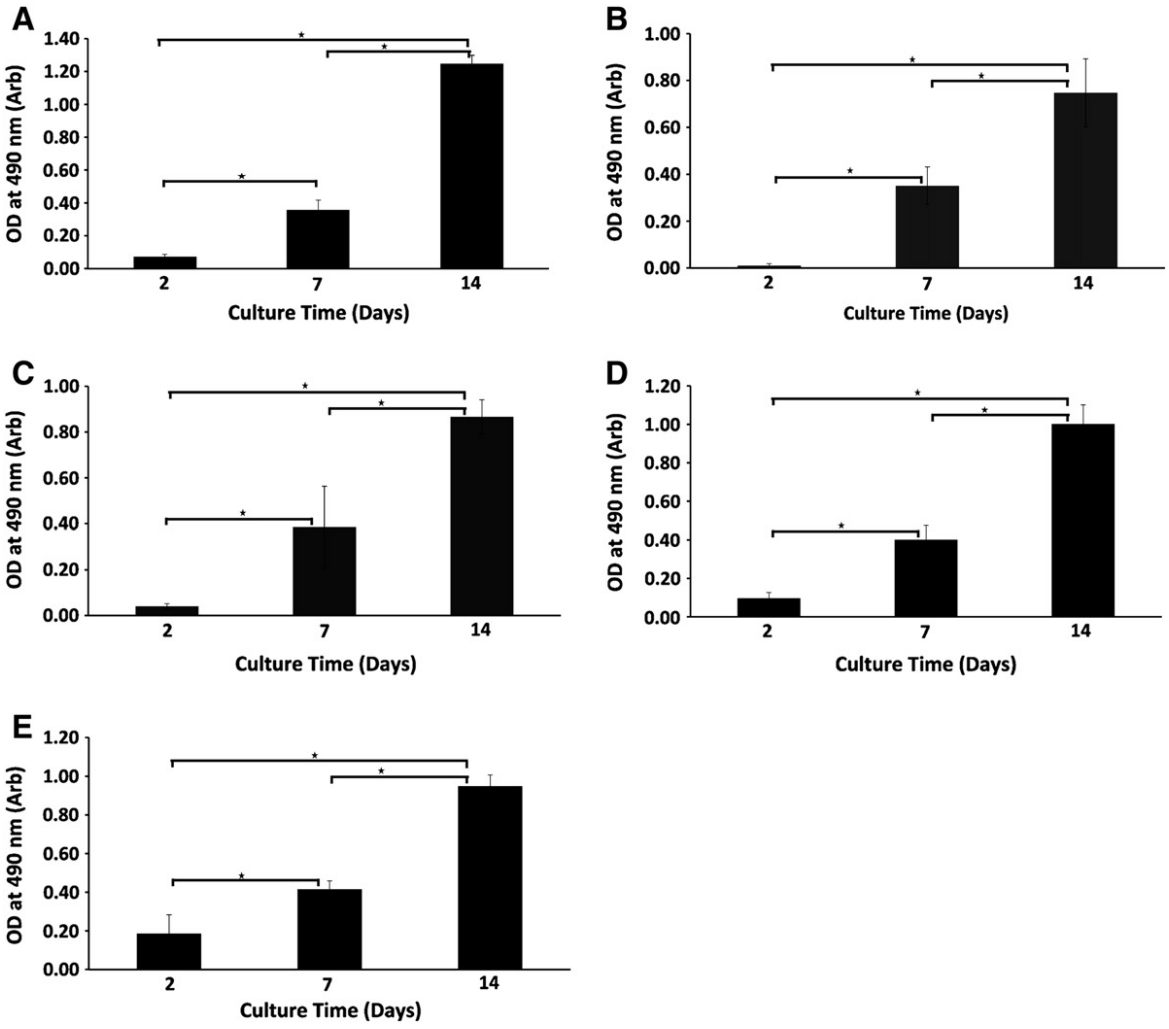

Figure 3.3: Cellular viability assay: MTS test. Comparison of proliferation of cells as determined by MTS assay for 96-well EqMSCs-TCP and EqMSCs-BC scaffolds for 2, 7 and 14 days. Linear responses were observed between cell seeding density and absorbance at 490 nm. Approximately 3.16×10^4 cells/cm^2 seeded on TCP ($R^2 = 0.919$) (A); 3.16×10^4 cells/cm^2 seeded on BC construct ($R^2 = 0.998$) (B); 6.32×10^4 cells/cm^2 seeded on BC construct ($R^2 = 0.991$) (C); 9.48×10^4 cells/cm^2 seeded on BC construct ($R^2 = 0.966$) (D); and 1.26×10^5 cells/cm^2 seeded on BC construct ($R^2 = 0.950$) (E). The results represent the means ± standard deviation with n=3 for each bar; asterisks (*) indicates significant differences at $p<0.05$ between testing conditions as a function of time [106].

To determine the cell quantity appropriate for the *in vitro* study, the linear response between cell number and absorbance at 490 nm were examined for several cell seeding densities of EqMSCs-TCP. In the study, the EqMSCs after 2, 7 and 14 days in culture showed a squared correlation coefficient of 0.998, 0.999, 0.983, 0.968 and 0.995 for approximately 3.16×10^3, 4.74×10^3, 6.32×10^3, 1.58×10^4 and 3.16×10^4 cells/cm^2 seeded on TCP, respectively (Figure 3.4). From the experiment, 3.16×10^4 cells were selected for seeding on TCP because the squared correlation coefficient was strong (0.995). In addition, at least 3.16×10^4 cells/cm^2 were selected for seeding on BC to ensure adequate cell seeding density on the scaffold.

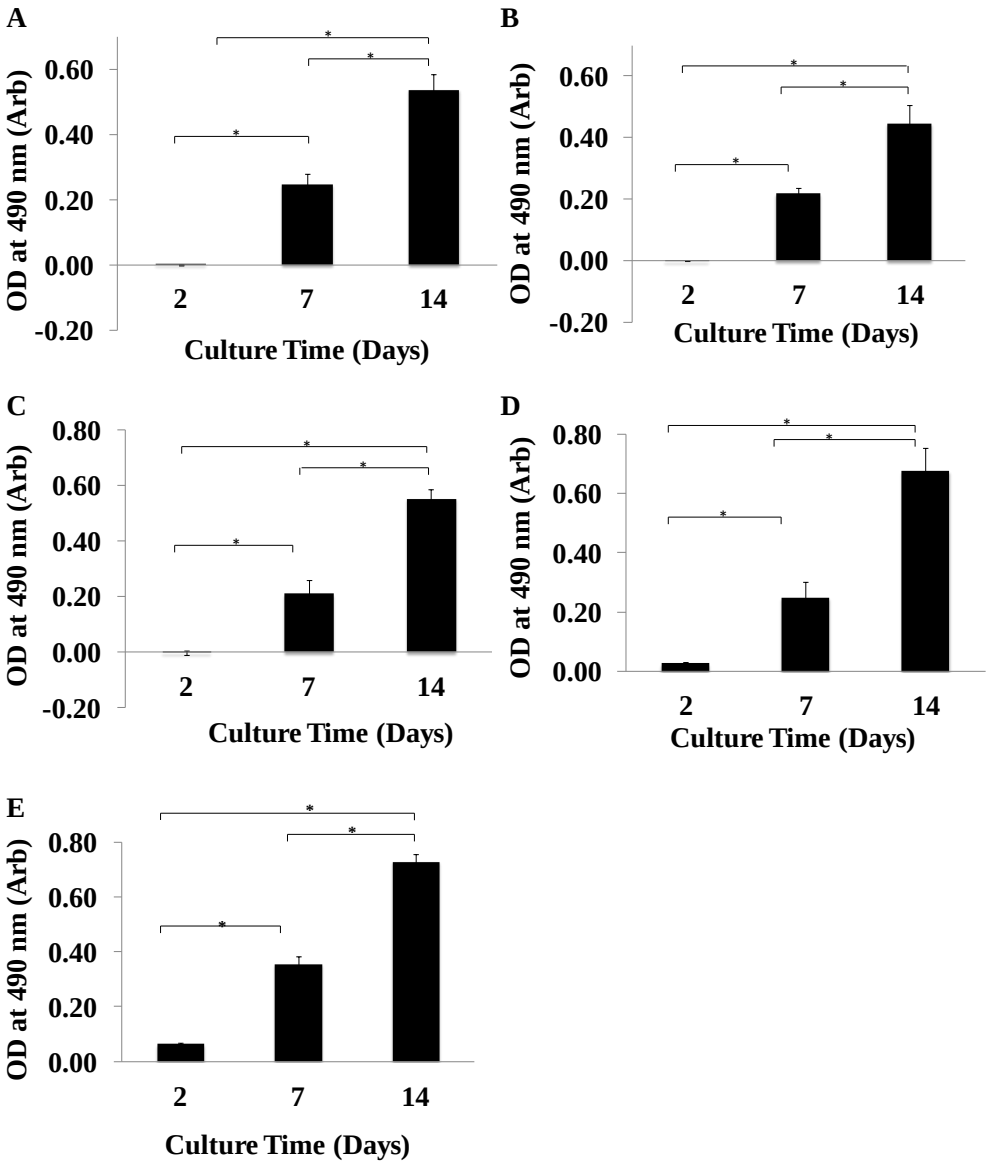

Figure 3.4: Assessment of minimum cell number optimum for *in vitro* study. Comparison of proliferation of cells was performed by MTS assay. EqMSCs were seeded on 96-well TCPs and cultured for 2, 7 and 14 days. The squared correlation coefficient for approximately 3.16×10^3 (A), 4.74×10^3 (B), 6.32×10^3 (C), 1.58×10^4 (D) and 3.16×10^4 cells/cm^2 (E) seeded on TCP were $R^2 = 0.998$, 0.999, 0.983, 0.968 and 0.995, respectively. Asterisks (*) indicates significant differences at $p<0.05$ between testing conditions as a function of time.

Calcein-AM (Calcein acetoxymethyl ester) and PI staining provides a two-color fluorescence cell viability assay that is based on the concurrent determination of live and dead cells with two probes that measure recognized parameters of cell viability – intracellular esterase activity and plasma membrane integrity. Calcein-AM, a non-fluorescent cell permeable compound, converts to the strongly green fluorescent calcein when hydrolyzed by intracellular esterases in live cells and is widely used for determining cell viability since the fluorescence intensity of calcein is proportional to the amount of live cells. Alternatively, PI is excluded by viable cells but can penetrate cell membranes of dying or dead cells, and hence, stains dead cells. Data shows that EqMSCs seeded on BC were viable, grew in population overtime and were well distributed throughout BC compared to EqMSCs seeded on TCP (Figure 3.5).

After 2 days in culture (Figure 3.5), the cells on the BC surface showed a distinct phenotype, with less elongated shapes and a round morphology. Furthermore, by 14 days in culture (Figure 3.5), EqMSCs have a full spread-out morphology on the BC scaffold. Conversely, the cells on the TCP from 2 to 14 days in culture (Figure 3.5) appear to continually maintain a full spread-out appearance. The authors hypothesize that the reason for these dissimilarities in cell phenotype on BC and TCP especially at 2 days in culture is the difference in substrate stiffness. Referring to previous studies using fibroblasts, researchers have demonstrated that cells generate greater traction force and develop a broader and flatter morphology on stiff substrates than they do on soft but equally adhesive surfaces [138]. In this study, these characteristics were observed after 2 days in culture (Figure 3.5) where EqMCs produced traction force and developed a flatter morphology on the stiff TCP with Young's modulus of ~1 GPa [139] and a round morphology on the softer hydrated BC with Young's modulus of 3.0-4.5 KPa [68]. Additionally, researchers have shown that fibroblasts stop their dependence on substrate stiffness when cells become confluent, or when two cells make contact and through mechanosensing use their internal signals to override cell-matrix adhesion complexes leading to cell spreading and eventually

proliferate [140]. These attributes were observed in this study with EqMSCs seeded on BC after 14 days in culture (Figure 3.5), where EqMSCs have ended their dependence on the BC stiffness and by mechanosensing with cell-cell interactions, have attached to and spread-out on the soft BC scaffold.

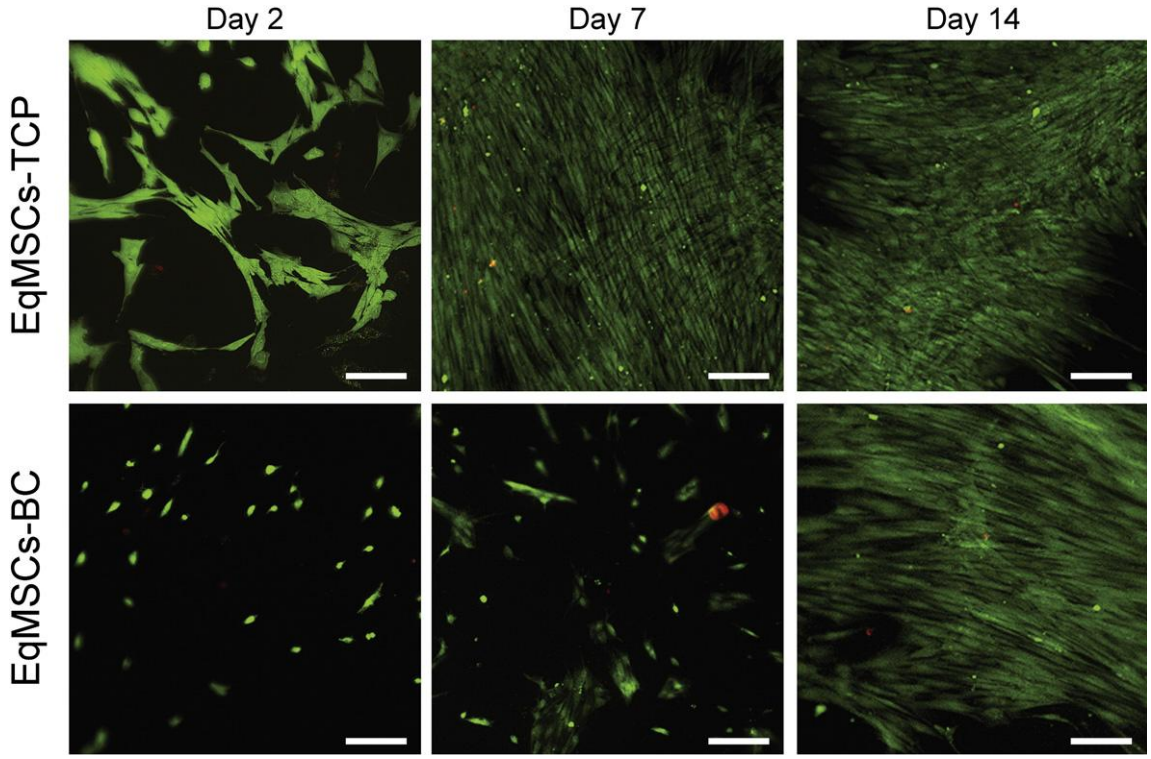

Figure 3.5: Cellular adhesion and cell viability stained with calcein-AM and PI using fluorescent microscopy. Cell viability of EqMSCs-TCP (3.16×10^4 cells/cm^2) and EqMSCs-BC (3.16×10^4 cells/cm^2) after 2, 7 and 14 days in culture. Cells were analyzed by calcein-AM which exhibits green fluorescence and demonstrates live cells and PI which displays red fluorescence and demonstrates dead cells. Fluorescent micrograph showed that overtime the cell adhered to, were viable and proliferation on BC compared to TCP in culture. Scale bar = 50 µm [106].

WGA, a carbohydrate-binding protein, selectively recognizes and binds to N‑acetylglucosamine sugars and sialic acid residues predominantly found on the plasma membrane. The WGA used is conjugated to convert to a strongly red fluorescent to achieve selective and simple staining of the plasma membrane of cells. DAPI is a blue fluorescent stain that has high cell permeability and bind strongly to the A-T rich regions in DNA, where its fluorescence is approximately 20-fold greater than in the non-bound state. Its selectivity for DNA and high cell permeability allows efficient staining of nuclei. Figure 3.6 shows that by 14 days, EqMSCs-BC has grown in population, were fully attached and well distributed throughout BC. By 14 days, WGA staining clearly illustrates the cell membranes of EqMSCs with the fibroblast like morphology customary to EqMSC (Figure 3.6). DAPI staining confirmed large, round nuclei contained in the cell bodies.

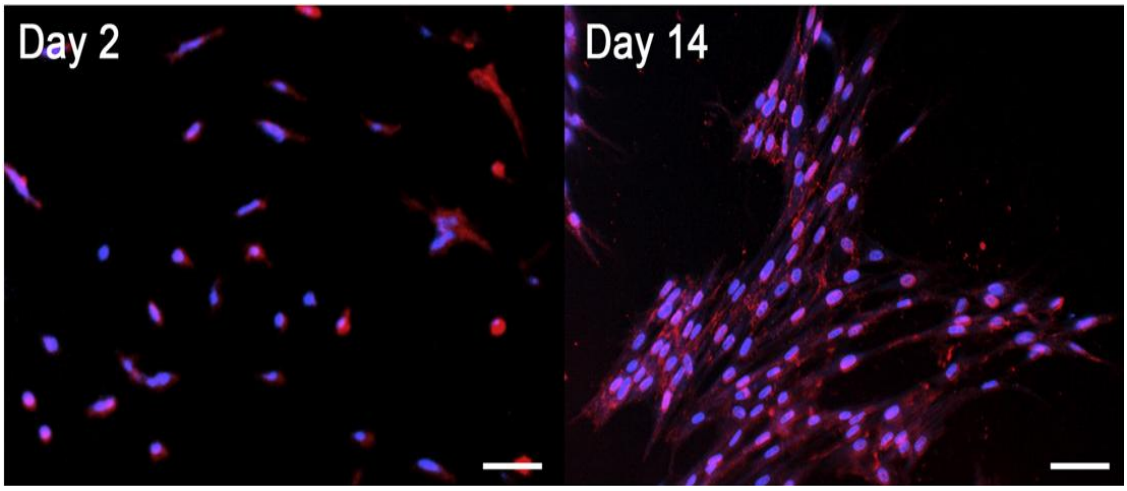

Figure 3.6: Cellular adhesion and morphology with WGA and DAPI staining. Fluorescent micrograph of EqMSCs-BC showing adhesion and morphology of cell membrane stained using WGA and cell nucleus stained using DAPI at 2 and 14 days in culture. Scale bar = 50 μm [106].

3.3.2. Alkaline Phosphatase Staining of Cell

ALP is a stem cell membrane marker and elevated expression of this enzyme is associated with undifferentiated pluripotent stem cell. WGA comparing to ALP, is typically used as a plasma membrane marker and WGA staining suggests the integrity of cells and confirms that the cells are not damaged or dead. ALP and WGA staining patterns demonstrated that EqMSC-BC retain their structure, stem cell-like properties, and confirm that the cells are living (Figure 3.6 and 3.7).

3.3.3. Cell Adhesion and Morphology by Scanning Electron Microscopy

The morphology of EqMSC growing on BC scaffold was assessed using a SEM to examine the shape of the cell and adherence of the cell on BC. A representative SEM micrograph of EqMSC attachment on BC scaffold is illustrated in Figure 3.8. SEM micrograph demonstrated that cell size of EqMSC with fibroblast like morphology to be approximately 200 μm on the BC scaffold (Figure 3.8.B). The cell adhered to the surface of the nanofibrous BC and maintained an extended fibroblast membrane morphology revealing satisfactory cell adhesion on the BC scaffold. Tissue-derived cells are anchorage dependent and must adhere to a solid surface to grow, proliferate and precede to further events including cell migration and differentiation [141]. The MTS assay results (Figure 3.3.B-3.3.E) show that the EqMSC effectively attached on the BC scaffold (Figure 3.8) as indicated by the high cell proliferation. The cell seeding density disparity between Figure 3.8 and Figure 3.5 of EqMSCs-BC at 14 days in culture is due to the higher magnification at which the images in Figure 3.8 were taken and the cells in Figure 3.8 were selectively imaged compared to those in Figure 3.5 (EqMSCs-BC at day 14).

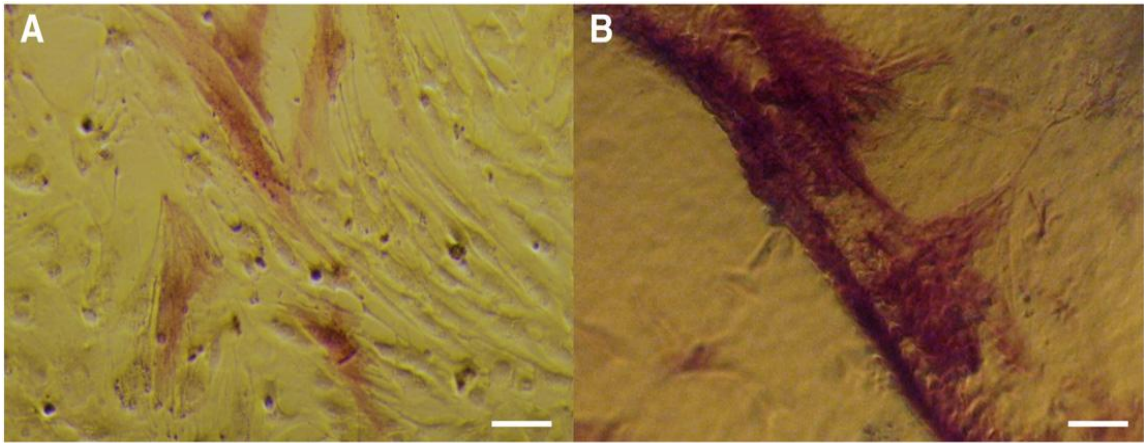

Figure 3.7: ALP activity. Contrast micrograph of ALP staining of EqMSCs-TCP cultured for 12 days (A) and EqMSCs-BC cultured for 14 days (B). Scale bar = 100 µm.

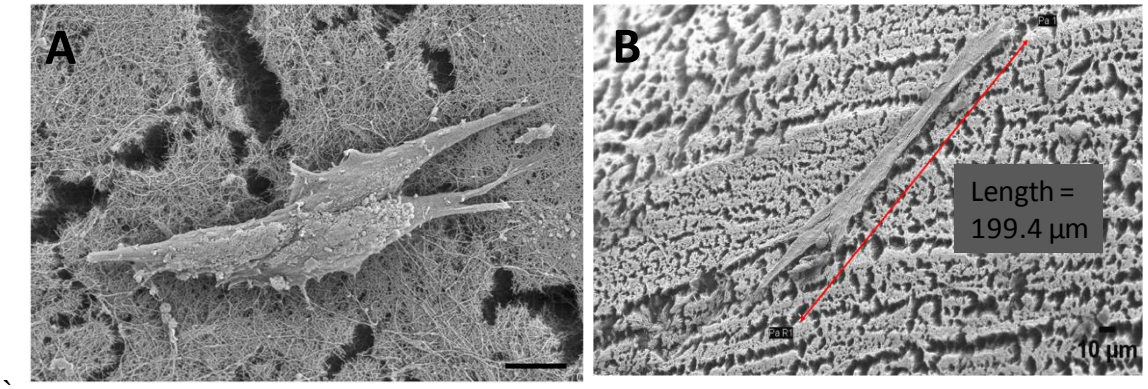

Figure 3.8: Cell adhesion and morphology by SEM. The SEM of EqMSCs attachment to BC scaffold (A). SEM micrograph demonstrated that cell size of EqMSC with fibroblast like morphology to be approximately 200 µm (B). Scale bar = 2 µm (A) and 10 µm (B) [106].

3.3.4. In Vitro differentiation of EqMSCs

To further characterize the EqMSCs, they were induced to differentiate into osteocytes and chondrocytes *in vitro* (Figure 3.9). As demonstrated, the EqMSCs-BC similar to the cells on TCP exhibited the potential to differentiate into a bone and a cartilage cell depending on the induction media. The results support the fact that EqMSCs do not lose their potentials to differentiate when they adhere to BC.

The differentiation of EqMSCs into chondrocytes and osteocytes is one of the key processes for cartilage and bone regeneration, respectively. From a functional perspective, where cell therapy for musculoskeletal hindrances is the ultimate goal, it is fundamental that the cells do not lose or have reduced capacity of differentiation [127]. This study showed that EqMSCs have the capability to differentiate into chondrocytes and osteocytes on the nanofibrous BC, an important characteristic for cartilage and bone regeneration.

This study conducted with native BC showed that EqMSCs can adhere to, are viable, and retain the potential to differentiate into osteocytes and chondrocytes on BC. Although this scaffold seems to hold great promise for future *in vivo* stem-cell based musculoskeletal therapies, further research into chemical modification of BC to enhance cell proliferation and to make it biodegradable seems advantageous. Additional BC modification for future research consideration is embedding and delivering growth factors present in stem cells and native tissue from the scaffold. Delivering growth factors from the BC scaffold has the potential to control and enhance cell growth, stimulate stem cell differentiations, and facilitate regeneration of the damaged native tissues which is advantageous for in vivo applications of the tissue engineered scaffold.

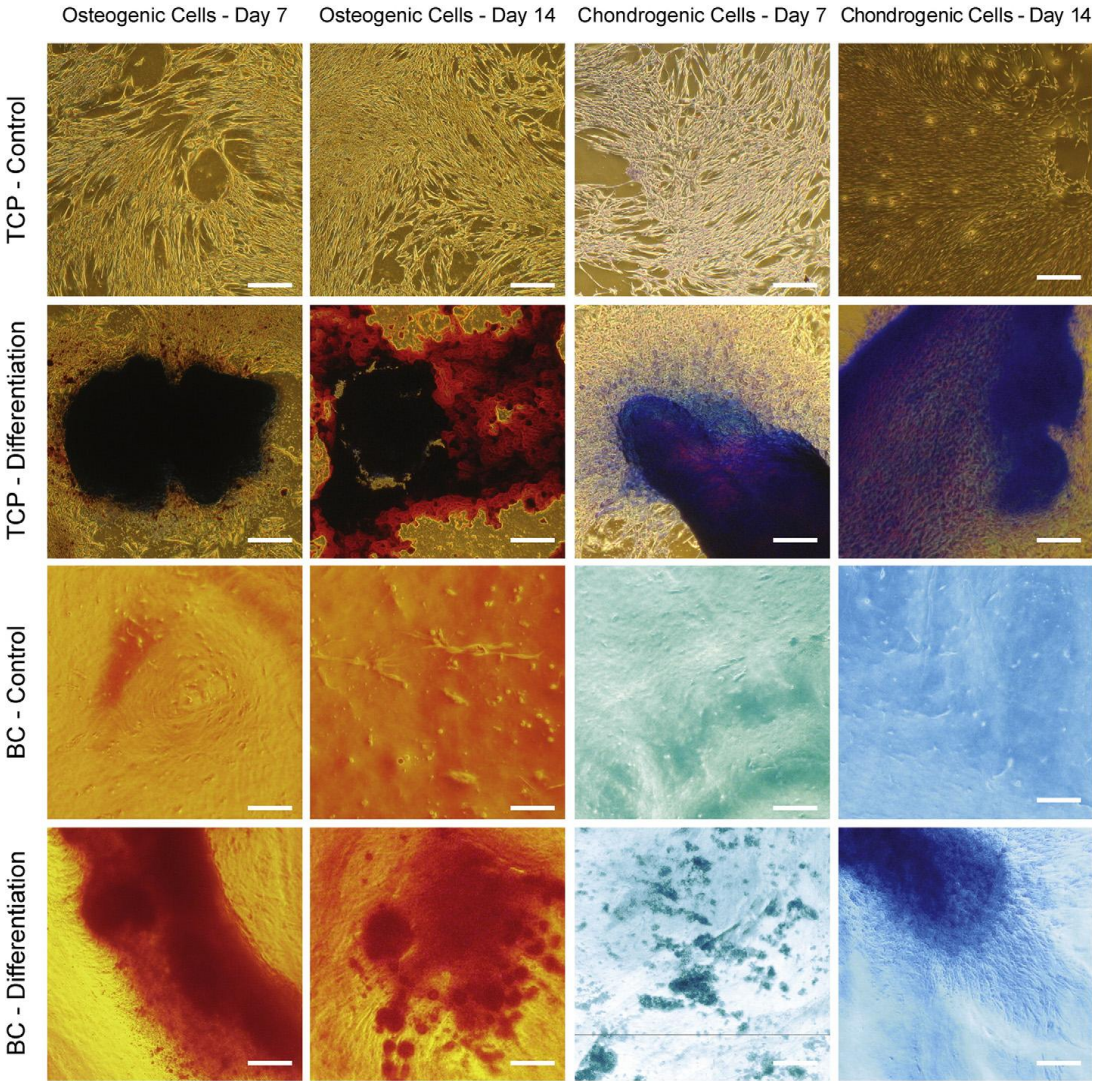

Figure 3.9: Osteogenesis and chondrogenic differentiation capacity of EqMSCs. EqMSCs (1.0 x 10^5 cells/cm^2) were investigated for their *in vitro* trans-differentiation capacity on BC compared to TCP after 7 and 14 days of differentiation. Osteogenesis was induced using the β-glycerophosphate-based method and was demonstrated by the detection of calcium in the mineralized matrix indicated by alizarin red stain shown in the differentiated cells. As shown, non-induced osteogenesis BC controls did not stain positive for alizarin red. Chondrogenesis was induced using the TGFβ1-based method and was indicated by alcian blue staining shown in the differentiated cells. As shown, non-induced chondrogenesis BC controls did not stain positive for alcian blue. Scale bars = 100 µm [106].

3.4. Conclusions

BC, a cost-effective natural hydrogel scaffolds, was successfully prepared and characterized using SEM. The lyophilized scaffold illustrated distinct pore morphology, 32.08 ± 10.85 nm fiber diameters and 254.16 ± 76.65 nm pore sizes.

It was demonstrated that the BC scaffolds were cytocompatible with EqMSCs *in vitro*. The BC scaffolds supported the adhesion, proliferation, osteogenic and chondrogenic differentiation. The cells seeded on the BC scaffolds were viable and possess a high rate of proliferation.

CHAPTER IV
Analysis of Microporous Bacterial Cellulose and Oxidized Microporous Bacterial Cellulose Scaffolds

Native BC is a non-biodegradable and nanoporous natural polysaccharide with promise as a scaffold for tissue engineering due to its biocompatibility. However, for bone and cartilage applications a biodegradable and microporous scaffold is desired to support osteocyte and chondrocyte ingrowth, enable tissue regeneration and resorb over time to be replaced by new osseous and cartilaginous tissues. The ideal biomaterial will be microporous to allow for cell ingrowth and degrade after stimulating new tissue growth. Therefore, in this section, microporous BC (porous BC) was synthesized and chemically modified into degradable microporous BC to make the scaffold more suitable for bone and cartilage tissue engineering. Natural beeswax microspheres were placed in the BC growing culture to prepare microporous BCs. After synthesis and beeswax leaching, microporous BCs with interconnected pores and native BCs were oxidized to make them degradable. BC oxidation was performed using sodium periodate to yield dialdehyde cellulose which degrades in mammalian systems.

Beeswax was characterized for its degradation and melting temperatures. Microporous BC and microporous oxidized BC were synthesized, characterized, and compared to native BC and oxidized BC. Proliferation and viability potential of EqMSCs on oxidized BC, microporous BC and microporous oxidized BC were assessed. The BC scaffolds were also characterized for their ability to support and maintain differentiation of EqMSCs *in vitro* for potential tissue engineering use. The potential for EqMSCs to differentiate into osteocytes and chondrocytes on oxidized BC and microporous oxidized BC were assessed. In this chapter, the results and discussions from the study are presented concurrently in Sections 4.1 - 4.6, and the conclusions are presented in Section 4.7.

4.1. Characterization of Beeswax

4.1.1. Thermal Gravimetric Analysis

The initial weight percent versus temperature thermogravimetric curve for the beeswax is illustrated in Figure 4.1. The thermogravimetric curve shows that in an 100% N_2 atmosphere, the decomposition of impurities in the beeswax occurs at approximately 43°C and 114°C. The weight of the beeswax decreases at approximately 315°C and continue decreasing until all of the material vaporizes at 420°C.

TGA analysis is evidence that beeswax undergoes non-isothermal weight loss (Figure 4.1). Under N_2 atmospheric conditions, the beeswax does not undergo thermal degradation until temperatures greater than approximately 315°C. After 315°C the beeswax material degrades and evaporates until no material remains at 420°C. These results agree with findings from Cheremisinoff [142], and Rivenc and Schilling [143].

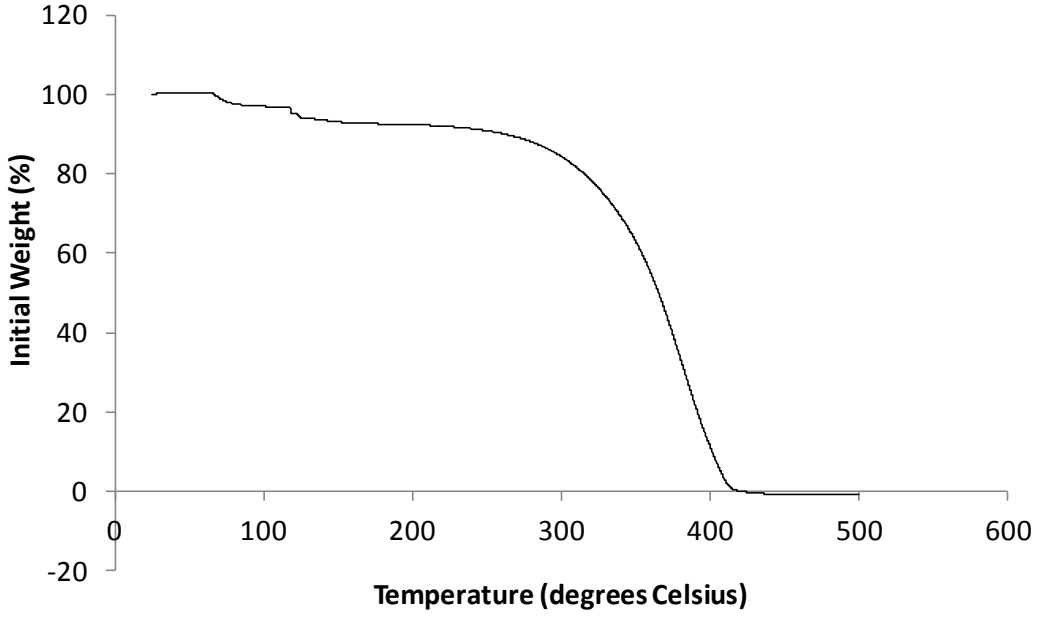

Figure 4.1: Initial weight percent versus temperature thermogravimetric curve of beeswax.

4.1.2. Differential Scanning Calorimetry

The DSC thermogram of beeswax (Figure 4.2) illustrates the melting properties of the wax. The peak melting point of the beeswax was observed in the DSC analysis at 65°C (Figure 4.2).

The DSC thermogram of beeswax indicated a broad thermal transition or phase change of beeswax with the onset of melting at approximately 40°C and an endpoint at approximately 66.2°C (Figure 4.2). One reason for this may be that the various components in the beeswax begin to melt at approximately 40°C and continue melting until the endpoint at approximately 66.2°C. Native beeswax is a heterogeneous material composed primarily of fatty acids, wax esters and various long chain alcohols [144, 145]. The endpoint of the thermal transition of beeswax has been reported to indicate the complete melting of the major components in the wax including fatty acids and wax esters [146].

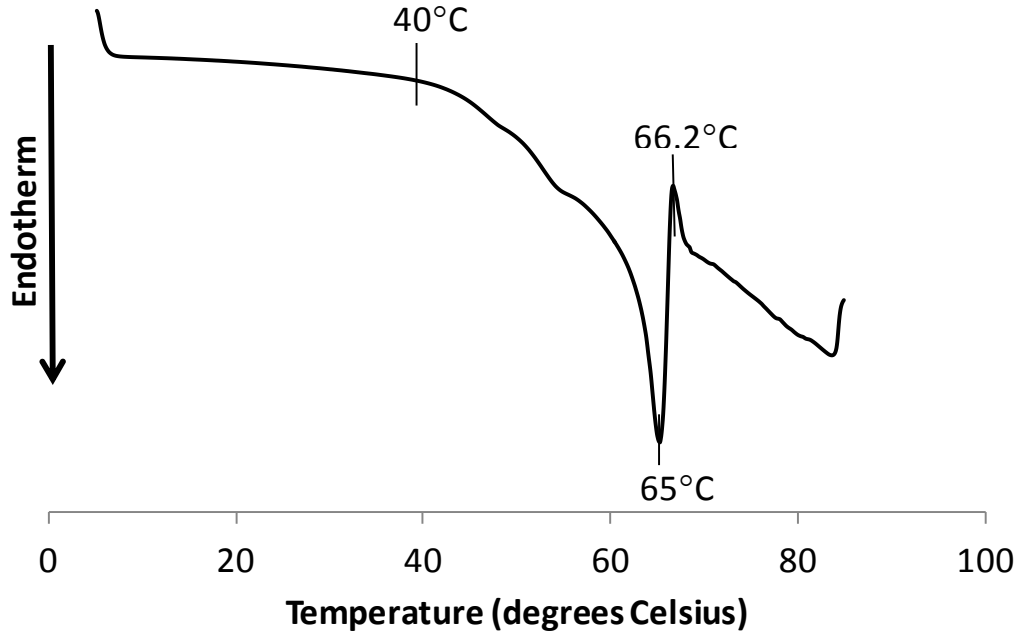

Figure 4.2: DSC heating curve of beeswax.

4.2. Synthesis of Microporous Bacterial Cellulose Scaffolds

Three-dimensional microporous BC scaffolds with interconnected pores were prepared as described in Section 2.2.2. In brief, beeswax microspheres were sintered in TCPs, TCDs and glassware (360 mm L x 200 mm W x 5 mm H), Schramm-Hestrin medium was added to the cultures, and the mixtures were cultured for 14 days under static conditions. Native BCs were synthesized without the addition of beeswax (Section 2.2.1). The cellulose pellicles were then purified following the protocols in Sections 2.2.1 and 2.2.2. Half of the samples were oxidized using the sodium periodate in n-propanol procedure outlined in Section 2.2.5. Overall, four groups of samples were prepared: native BC, oxidized BC, microporous BC, and porous oxidized BC. The terminologies microporous BC and porous BC were used interchangeably throughout this study.

4.2.1. Preparation of Beeswax Microspheres

Beeswax microspheres were fabricated using a dispersion method by adding beeswax melted at 90 °C to 0.5% (g/mL) low molecular weight PVA solution, under constant stirring [110]. DSC (Figure 4.2) and TGA (Figure 4.1) analyses of beeswax shows that the material melts at approximately 65 °C but does not degrade at the use temperature of 90 °C. Therefore, degradation of beeswax was not expected at the in use temperature of 90 °C.

In this study, under controlled mechanical stirring, beeswax microspheres approximately 500 μm or less formed in the dilute PVA solution (Figure 4.3.A, 4.3.B). Phase contrast microscope was used to image and assess the diameter of the produced beeswax microspheres in real-time during their production. It was observed that the size of the beeswax microsphere was dependent on the stirring rate of the solution. Faster stirring rates resulted in beeswax microspheres with smaller diameters and uniform spherical shapes (Figure 4.3.C). Conversely, slower stirring rates resulted in beeswax microspheres with

larger diameters (Figure 4.3.D). Care was taken during the preparation of the beeswax microspheres to control the stirring rate of the solution and limit the production of the beeswax microsphers with undesirable diameters. The beeswax microspheres generated using the PVA solution were washed in DI water and sieved to obtain microspheres with diameters of 500 µm or less. Phase contrast micrograph images of the sieved beeswax microspheres confirmed the spherical shape of the particles and their diameter to be approximately 500 µm or less (Figure 4.3.A, B). Other research groups including Ma and Choi (2001) [110], Backdahl et al (2008) [95], Zaborowska et al (2010) [96], and Bodin et al (2010) [147] have used a similar method to produce paraffin microspheres in dilute PVA solutions.

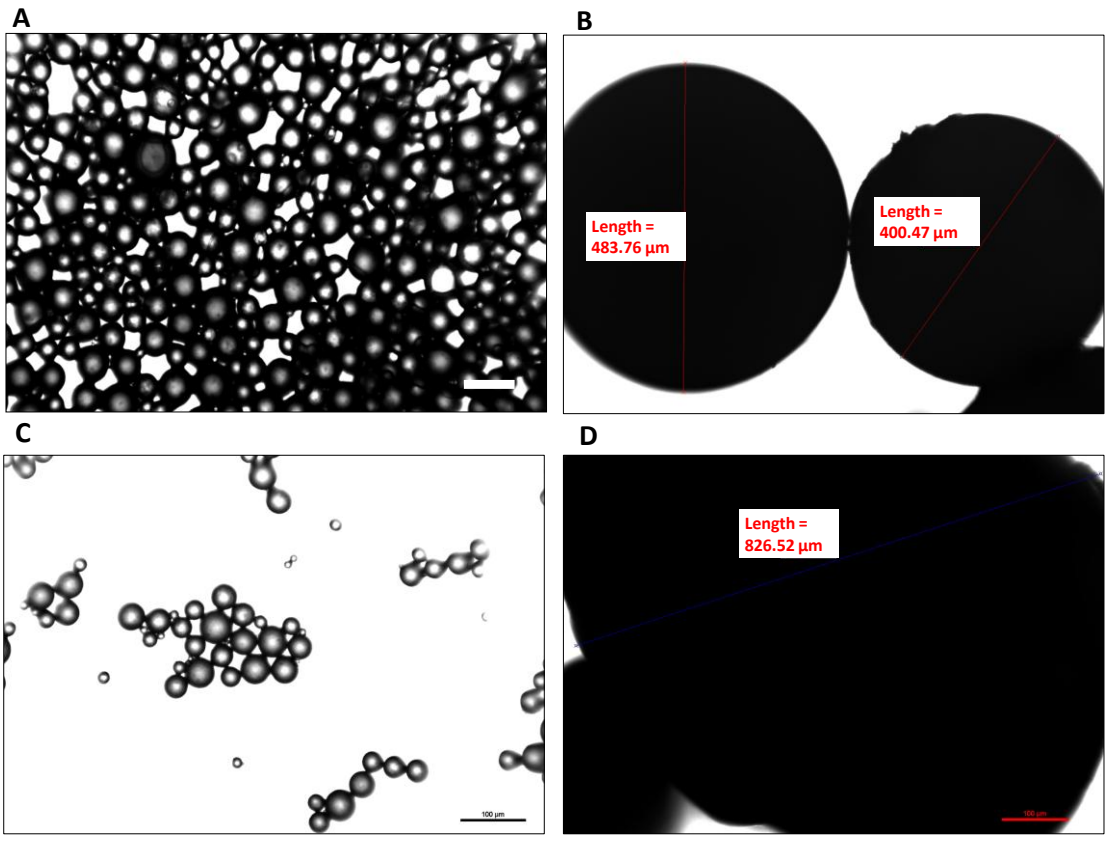

Figure 4.3: Phase contrast microscope images of beeswax microspheres at 5X (A) and 10X (B-D). Scale bar = 1 mm (A) and 100 µm (C, D).

4.2.2. Porosity and Interconnectivity in Microporous Bacterial Cellulose Scaffolds

Sterile beeswax microspheres were sintered at 40 °C prior to cellulose synthesis to bond the microspheres and form a stacked 3D array of particles to ensure cell interconnectivity. During cellulose synthesis, beeswax microspheres floated in the culture medium as a packed mass because of its density (density ~0.96 g/cm^3 [111]) relative to the water-based Schramm-Hestrin Medium (density ~1 g/cm^3), as illustrated in Figure 4.4. Cell interconnectivity became evident after leaching of the beeswax (Figure 4.5.). The pore size of the microporous BC scaffolds were approximately 500 μm or less as demonstrated in real-time assessment using phase contrast microscope (Figure 4.5.B).

Figure 4.4: Photograph of porous BC culture consisting of *Gluconacetobacter sucrofermentans* and beeswax microspheres in Schramm-Hestrin Medium in a 100 mm diameter tissue culture dish. The beeswax microsphers floated in the bacterial medium during culture.

During beeswax leaching and scaffold purification, phase contrast microscope was used to assess the progress of the beeswax removal from the scaffold in real-time. Beeswax residues were visible as dark spots in the microporous BC images (Figure 4.5.A), compared to a microporous BC that had been cleared of beeswax (Figrue 4.5.B). The addition of the beeswax microsphers in the BC culture resulted in a randomly-sized microporous BC scaffold as demonstrated by phase contrast microscope (Figure 4.5.B). Native BC scaffold synthesized without the use of beeswax microspheres and imaged using a phase contrast microscope did not exhibit visible pore structures in the scaffold (Figure 4.5.C). Phase contrast microscope images of native BC confirmed a transparent-like material which lacks micro-pore structures (Figure 4.5.C).

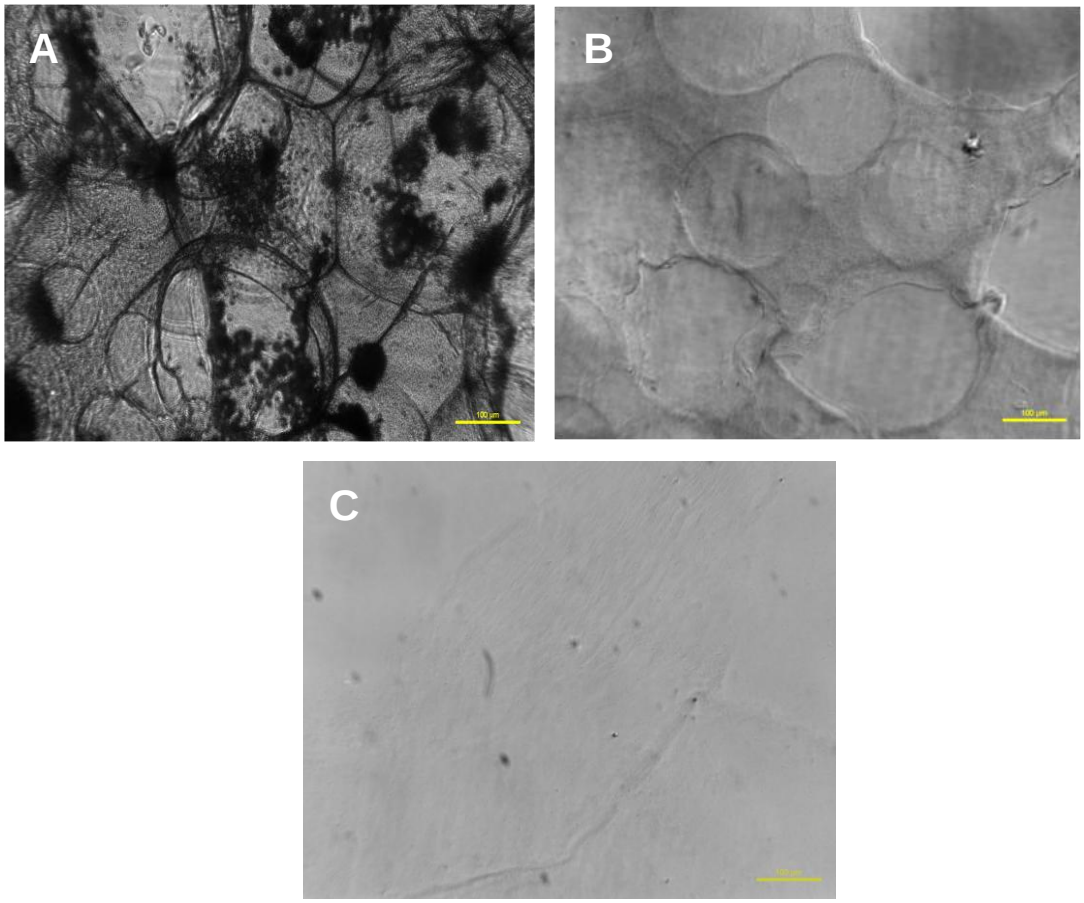

Figure 4.5: Phase contrast microscope images comparing microporous BC after 1 (A) and 15 (B) cyclic washes with Tween 80 and ethanol, and purified native BC synthesized without beeswax (C). Beeswax residues were visible as dark spots in the microporous BC that have undergone 1 cycle of wash (A). There was no visible beeswax particles in microporous BC washed for 15 cycles. Micro-sized pore structures were visible on the microporous BC scaffolds (B) compared to the non-visible pores on the native BC (B). Scale bar = 100 µm.

4.2.3. Oxidation of Bacterial Cellulose Scaffolds

Half of the prepared native (nano-porous, non-porous) and micro-porous BC scaffolds were oxidized using sodium periodate in n-propanol following the procedure outlined in Section 2.2.5. Overall, a total of four groups of BC scaffolds were prepared: native BC, oxidized BC, porous BC, and porous oxidized BC.

Periodate oxidation is an oxidation technique that has been reported to predictably oxidize cellulose into degradable dialdehyde cellulose [94]. During oxidation, free radical side reaction may occur resulting in non-specific chain breakages. These undesirable reactions are diminish with the addition of the free-radical scavenger, n-propanol, during the reaction. Assessment of the scaffolds after oxidation using sodium periodate in n-propanol showed no visible changes in the color and morphology of the BC scaffolds when compared to the non-oxidized native and porous BCs.

The four groups of BC samples initially cultured in 6-well TCPs were weighed under wet (hydrated, never-dried) and dried (lyophilized) conditions (Figure 4.6). Wet weights of the samples showed a significant decrease in the oxidized BC samples compared to the non-oxidized native BC samples (Figure 4.6.A). A similar significant difference was also observed between the wet weights of the porous oxidized BC samples and the non-oxidized porous BC samples (Figure 4.6.A). There were no significant difference between the wet weights of the native BCs and porous BCs (Figure 4.6.A). Both native BC and porous BC were significantly greater in weight compared to the oxidized BC and porous oxidized BC (Figure 4.6.A). Dry weights of the samples only demonstrated a significant decrease between the porous oxidized BC sample and the remaining three groups of samples (Figure 4.6.B). The wet weights of the native BC, oxidized BC, and porous BC showed that there were no significant difference in their weights.

Wet weights of the native and modified BC scaffolds show that periodate oxidation results in changes to the molecular structure of the bacterial cellulose

that reduces its ability to retain water. Dry weights results of scaffolds demonstrate that periodate oxidation did not degrade oxidized BC compared to the native BC and porous BC. In contrast, the dry weight of the porous oxidized BC indicated that periodate oxidation have degraded the sample compared to native BC, oxidized BC and porous BC. It is possible that the inter- and intramolecular hydrogen bonds that allow BC to retain water in its interstitial spaces have been altered by the formation of aldehyde groups in the chemical structure of the oxidized BCs. These alterations in the hydrogen bonding in the oxidized BC scaffolds may have reduced its ability to retain water. It is also possible that creating porous structures and forming aldehyde groups in the bacterial cellulose structure (i.e., porous oxidized BC) affects the integrity of the fibrous network and results in the loss of the cellulose network. Hutchens et al. (2009) have previously reported a similar trend in the significant decrease in wet weights between native BC and oxidized BC scaffolds [68].

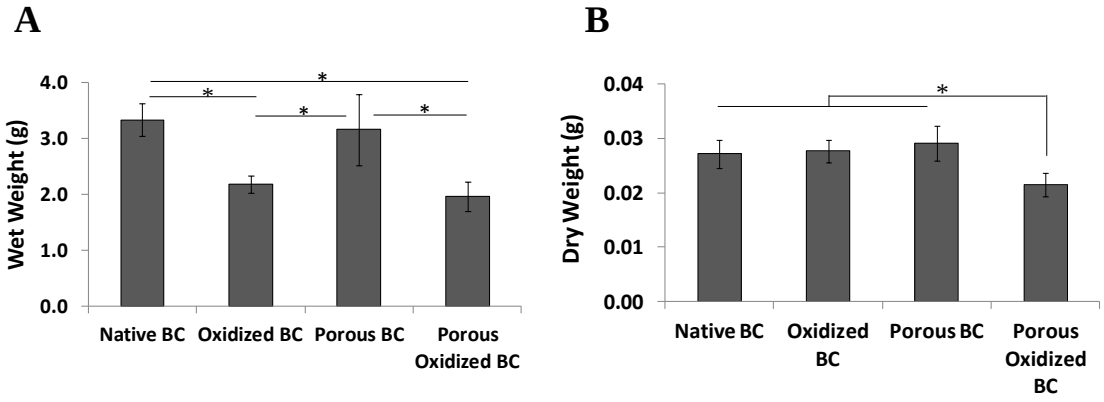

Figure 4.6: Comparison of wet weights (A) and dry weights (B) of native BC, oxidized BC, porous BC, and porous oxidized BC. Asterisks (*) indicates significant differences at $p<0.05$.

4.3. Fourier Transform Infrared Spectroscopy

The chemical structure of the cellulose chain of BC scaffold is shown in Figure 1.7 and the FTIR spectrum of the native BC is presented in Figure 4.7. Each of the FTIR peaks represents a functional chemical group present in the BC structure. Based on the chemical structure of cellulose, the material consists of β-D-glucopyranose units linked together by (1→4)-glycosidic bonds (Figure 1.7), and numerous hydroxyl groups in its network (Figure 1.8). The characteristic FTIR bands of native bacterial cellulose are presented in Table 4.1.

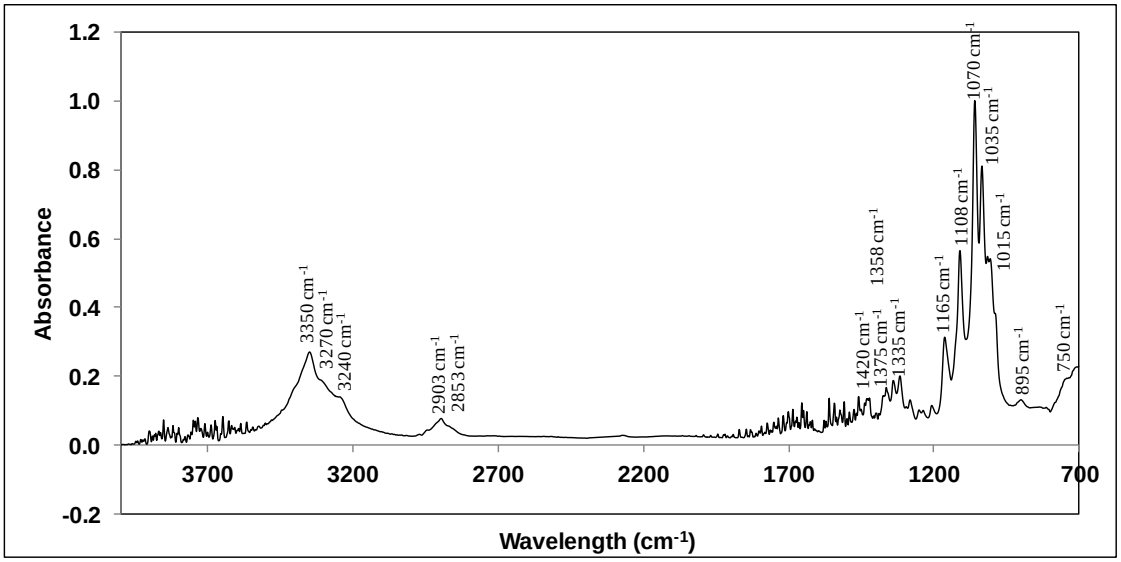

Figure 4.7: FTIR spectrum of native BC. Sample was analyzed in the ATR mode.

Table 4.1: Characteristic FTIR bands of native bacterial cellulose.

Frequency	Relative Intensity	Assignment	Ref.
3350 cm^{-1}	Strong	OH Stretching (associated with intramolecular hydrogen bonding)	[148]
3270 cm^{-1}	Medium	OH Stretching (characteristic of hydroxyl bonding in cellulose structure due to I_β crystalline phase)	[148, 149]
3240 cm^{-1}	Medium	OH Stretching (characteristic of hydroxyl bonding in cellulose structure due to I_α crystalline phase)	[148, 149]
2903 cm^{-1}	Medium	CH Stretching	[149]
2853 cm^{-1}	Medium	CH_2 Symmetric Stretching	[150]
1653 cm^{-1}		Absorbed H_2O	[150]
1420 cm^{-1}	Weak	CH_2 Symmetric Bending	[149]
1375 cm^{-1}	Medium	CH Bending	[149]
1358 cm^{-1}	Medium	CH Bending	[150]
1335 cm^{-1}	Medium	OH In-plane Bending	[150]
1165 cm^{-1}	Strong	Antisymmetric Bridge COC Stretching	[150]
1108 cm^{-1}	Strong	Antisymmetric In-phase Ring Stretching	[149]
1070 cm^{-1}	Strong	Skeletal Vibrations Involving C-O Stretching	[149]
1035 cm^{-1}	Strong	Skeletal Vibrations Involving C-O Stretching	[149, 150]
1015 cm^{-1}	Medium	Skeletal Vibrations Involving C-O Stretching	[150]
895 cm^{-1}	Weak	Antisymmetric Out-of-phase ring stretching	[150]
750 cm^{-1}	Medium	OH Stretching (characteristic of hydroxyl bonding in cellulose structure due to I_α crystalline phase)	[148, 149]

In addition to phase contrast microscopy (Figure 4.5), FTIR was used to validate the removal of the beeswax from the microporous BC scaffolds. FTIR spectra of native BC, porous BC, beeswax, and Tween 80 cleaning agent are illustrated in Figure 4.8. Beeswax displays characteristic peaks at 1149, 1206, 1459, 1463, 1713, and 1735 cm^{-1} which were not observed for the FTIR spectra for the porous BC. The FTIR spectrum for the porous BC was exceedingly comparable to the control native BC spectrum which was synthesized without the addition of beeswax (Figure 4.5). The FTIR spectra for both native BC and porous BC demonstrated distinct dissimilarities from that of the detergent Tween 80, and beeswax, confirming that the detergent and beeswax had been removed from the porous BC following purification (Figure 4.5).

Thorough and complete removal of the beeswax from the porous BC scaffolds was essential in order to ensure scaffold purity and obtain interconnected pore structures for cell growth and migration. Tween 80 is a non-ionic biological detergent that reduces the surface tension of the beeswax by forming miscelles around the microspheres. Tween 80 was used to make the beeswax soluble, and ethanol was used to dry and remove the soluble composites of beeswax and Tween 80. Phase contrast micrograph image (Figure 4.5) and FTIR (Figure 4.8) have confirmed the complete removal of the beeswax following cyclic incubation of the microporous scaffolds in the solution of Tween 80 and 99% ethanol.

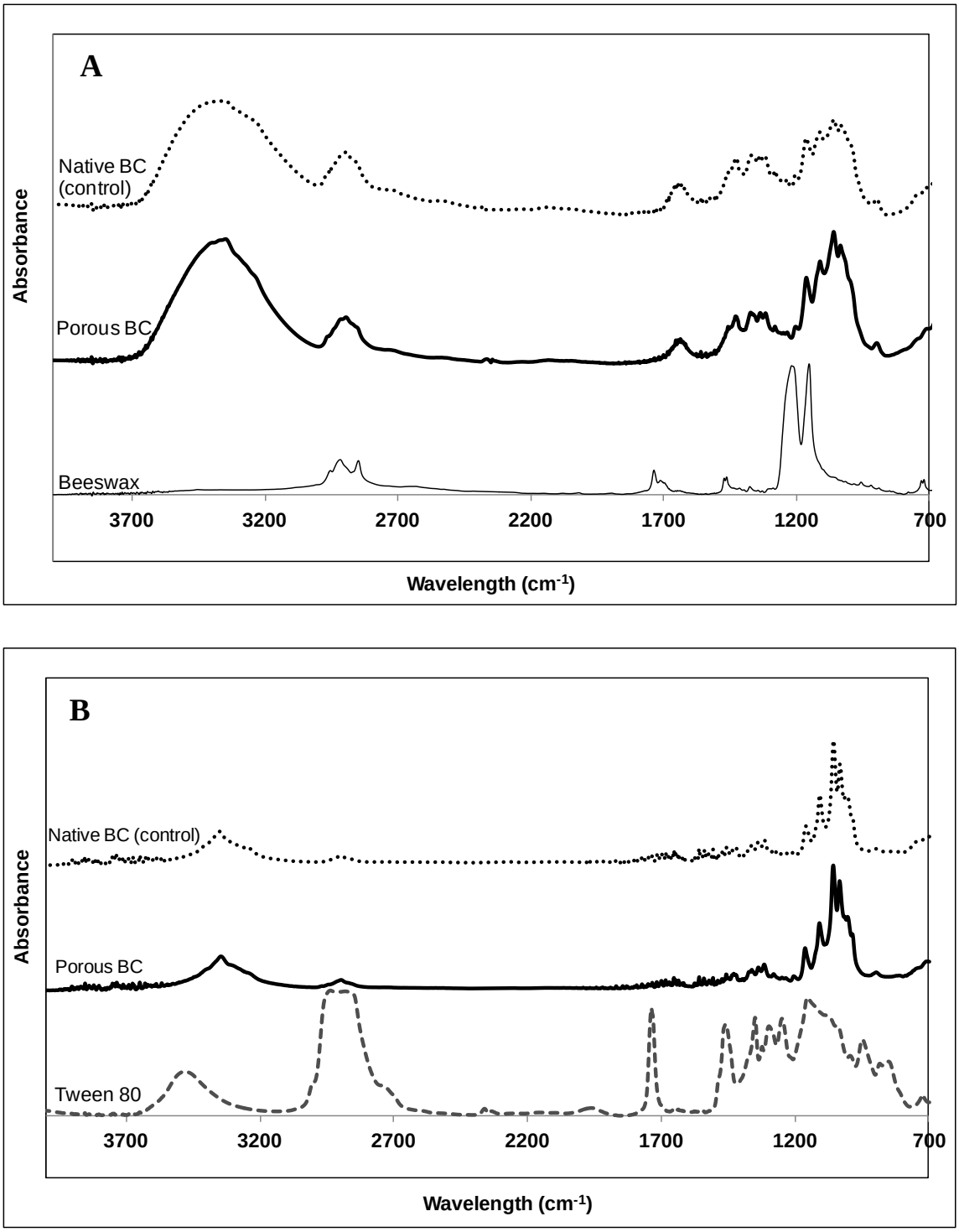

Figure 4.8: FTIR spectra of samples analyzed in standard FTIR mode (A) and ATR mode (B). Spectra of native BC (control) synthesized without beeswax microparticles and porous BC (A, B). Spectra for beeswax (A) and Tween 80 cleaning agent (B) were included for comparison.

The FTIR spectra of native BC, porous BC, oxidized BC, and porous oxidized BC are shown in Figure 4.9. The spectra of the oxidized BC and porous oxidized BC have an absorption band at 1740 cm^{-1} that represents the stretching vibration in the aldehyde carbonyl group formed on the cellulose during periodate oxidation (Figure 4.9). The spectra of oxidized BC and porous oxidized BC also have an absorption band at 1650 cm^{-1} which corresponds to the carbonyl groups associated with hydrogen bonding (Figure 4.9). These absorption peaks are absent in the native BC and porous BC spectra (Figure 4.9), proving that periodate oxidation can transform native BC and porous BC scaffolds into dialdehyde cellulose scaffolds. The absorption peaks at 1740 and 1650 cm^{-1} in the spectra of the BC scaffolds are broad (Figure 4.9). The broad peak at 1740 cm^{-1} in these spectra (Figure 4.9) is attributed to the strong hydrogen bonding in the aldehyde carbonyl group which results in the broadening of the peak [151]. The broad peak at 1650 cm^{-1} in these spectra (Figure 4.9) is attributed to the considerable overlap with the absorption of water at 1653 cm^{-1} [151].

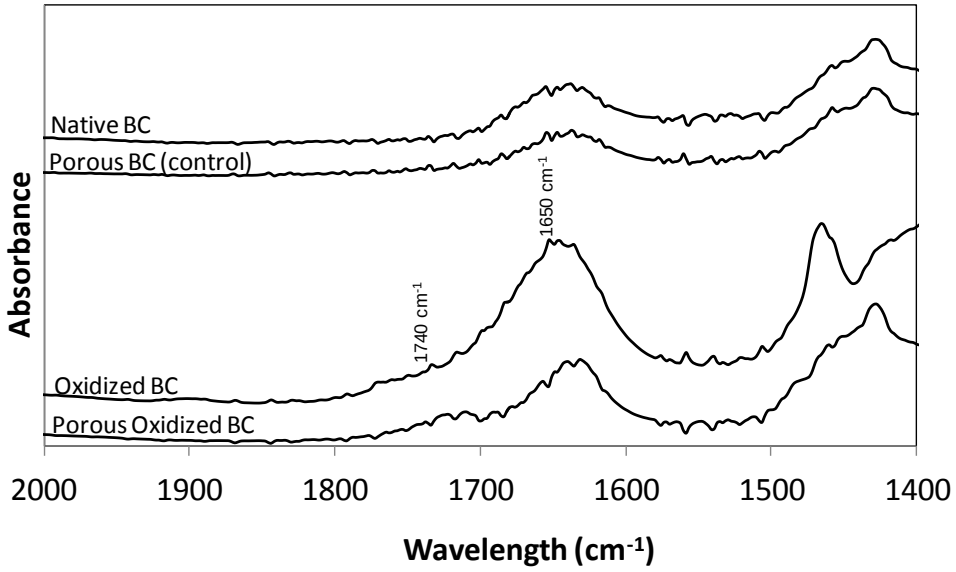

Figure 4.9: FTIR spectra of native BC (control), porous BC (control), oxidized BC, and oxidized porous BC.

4.4. Scanning Electron Microscopy

The formation of beeswax microspheres was further confirmed using SEM (Figure 4.10). In addition to phase contrast microscopy (Figure 4.3), SEM images demonstrate that beeswax microspheres were successfully produced with melted beeswax in a PVA solution (Figure 4.10.A) and the diameter of the microspheres were approximately 500 µm or less (Figure 4.10.B).

The SEM micrograph of microporous BC scaffolds imaged following one cyclic wash with Tween 80 and ethanol confirmed the presence of pore structures as well as beeswax in the scaffold (Figure 4.11). SEM image of the porous BC showed visible signs of beeswax on the surface of the scaffolds (Figure 4.11). Additionally, the SEM image of the porous BC scaffolds did not show cell interconnectivity between the pore structures (Figure 4.11). One cyclic wash of the BC scaffold demonstrate that additional washing was needed to ensure complete removal of the beeswax. It has been demonstrated that in addition to phase contrast microscopy (Figure 4.5.A), SEM can be used to assess the presence of beeswax in the porous BC scaffolds (Figure 4.11).

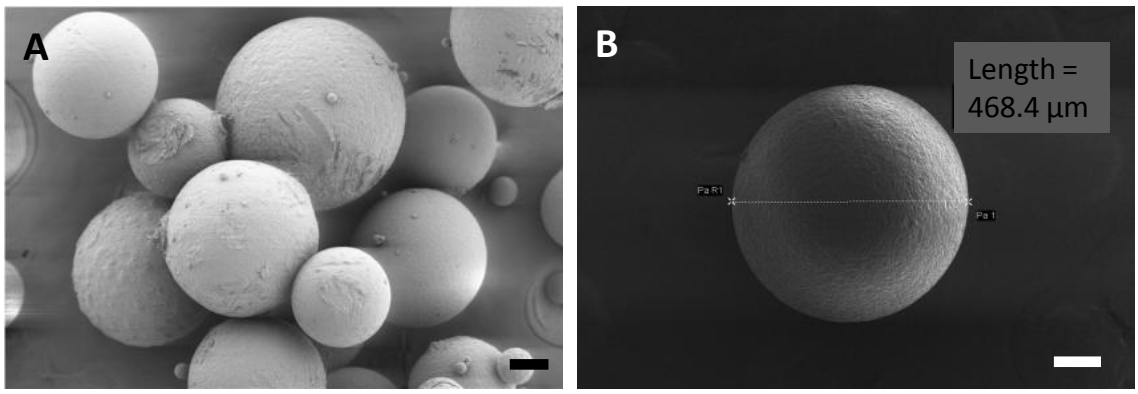

Figure 4.10: SEM images of beeswax microspheres produced with melted beeswax in a PVA solution at 230X (A) and 300X (B). Accelerating voltages of 3 kV (A) and 5 kV (B) were used to image the beeswax microspheres. SEM image demonstrated beeswax microsphere size to be approximately 500 µm or less after sieving (B). Scale bar = 100 µm.

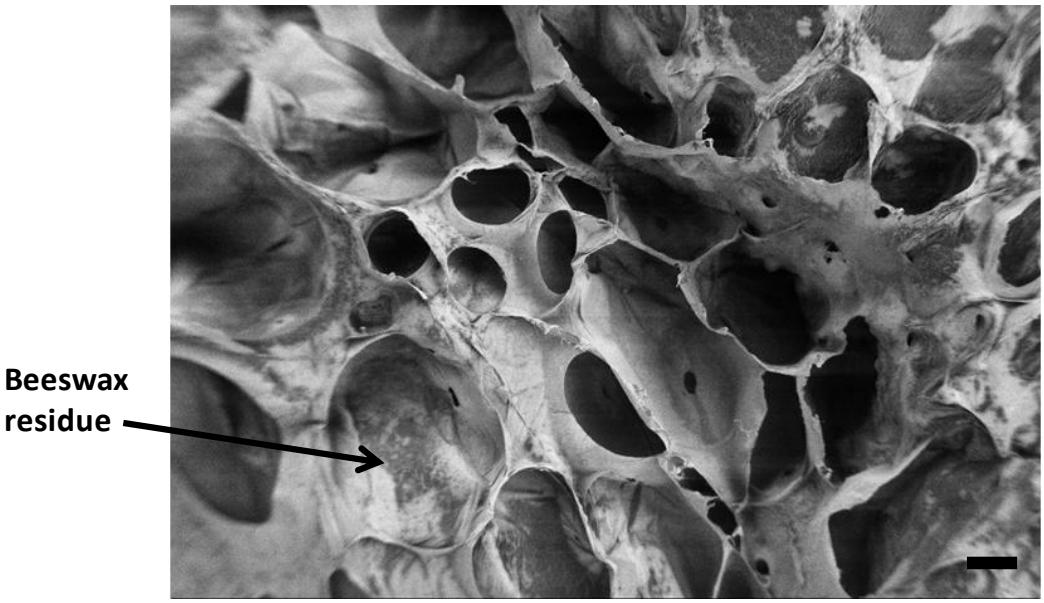

Figure 4.11: SEM image of porous BC after 1 cyclic wash with Tween 80 and ethanol at 200X. A 1.5 kV accelerating voltage was used to image the sample. Beeswax residues were visible in the porous BC that have undergone 1 cycle of wash. Scale bar = 100 µm.

SEM images of purified native BC, oxidized BC, porous BC, and porous oxidized BC are shown in Figure 4.12. The SEM images of porous BC (Figure 4.12.C) and porous oxidized BC (Figure 4.12.D) confirm that the addition of beeswax microspheres in the BC culture successfully resulted in the generation of microporous BC scaffolds. Micro-sized pore structures were visible on the porous BC (Figure 4.12.C) and porous oxidized BC (Figure 4.12.D) scaffolds. Native BC (Figure 4.12.A) and oxidized BC (Figure 4.12.B) scaffolds which were synthesized without the use of beeswax microspheres exhibited submicron-sized pores at the imaging magnification of 300X.

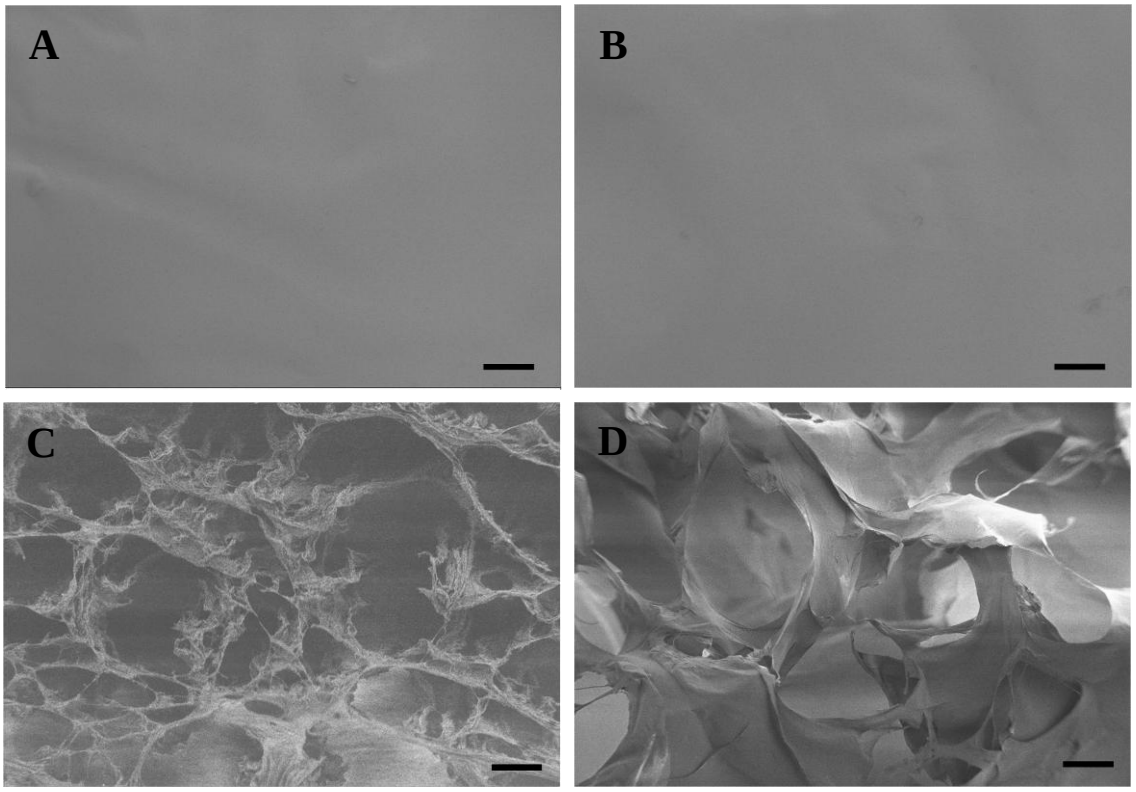

Figure 4.12: SEM images of scaffold pore structure for native BC (A), oxidized BC (B), porous BC (C), and porous oxidized BC (D) at 300X. A 1.5 kV accelerating voltage was used to image the samples. Scale bar = 100 μm.

4.5. Mechanical Testing

The mechanical properties of the native BC, oxidized BC, porous BC, and porous oxidized BC were determined at 5% strain rate to assess the relationship between the native and modified BCs. The engineering stress-strain curves of the hydrated never-dried BC samples are illustrated in Figure 4.13. The ultimate tensile strength, strain at break, and elastic modulus values of the native and modified BC samples calculated from the engineering stress-strain curves are illustrated in Figure 4.14. The results show that oxidation of native BC into oxidized BC significantly affects the ultimate tensile strength and elastic modulus

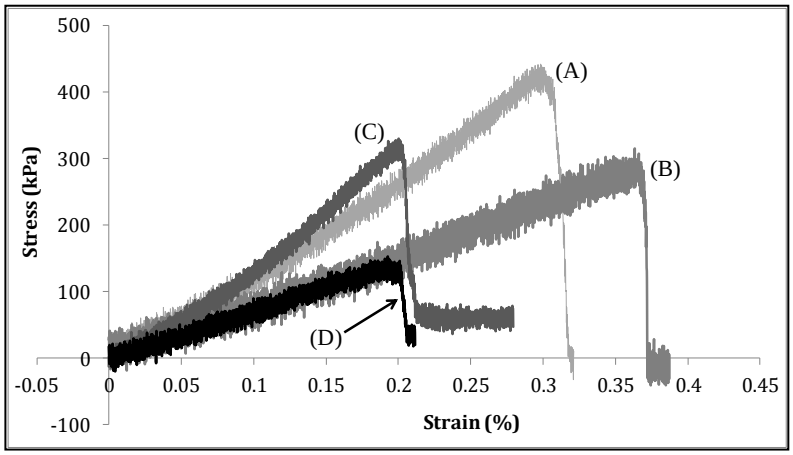

Figure 4.13: Engineering stress-strain curve of native BC (A), oxidized BC (B), porous BC (C), and porous oxidized BC (D).

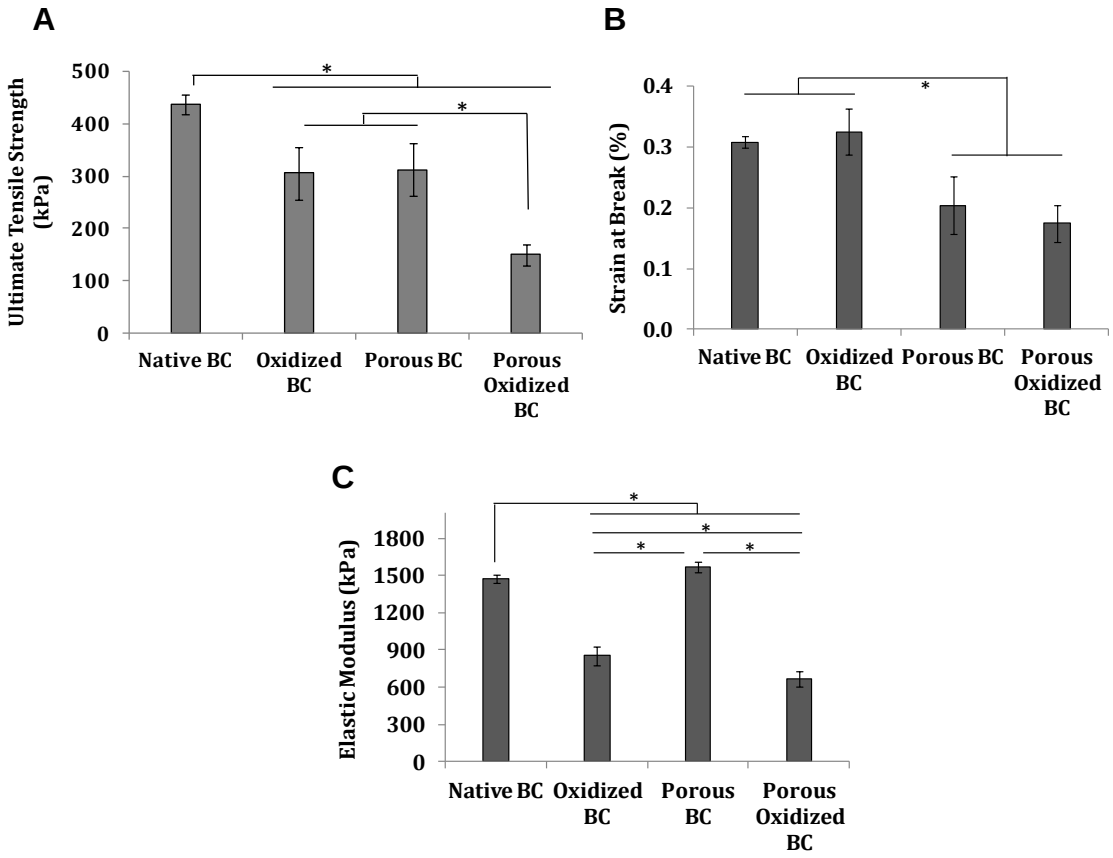

Figure 4.14: Comparison of ultimate tensile strengths (A), strain at breaks (B), and elastic moduli (C) of native BC, oxidized BC, porous BC, and porous oxidized BC. Asterisks (*) indicates significant differences at $p<0.05$.

of the BC scaffold (Figure 4.14.A, C). The ultimate tensile strength of the oxidized BC scaffold is significantly decreased compared to the native BC (Figure 4.14.A). In contrast, the elastic modulus of the oxidized BC scaffold is significantly increased compared to the native BC (Figure 4.14.C). The strain at break of the oxidized BC scaffold is not significantly affected by the periodate oxidation of the scaffold compared to the native BC (Figure 4.14.B).

Compared to native BC, the ultimate tensile strength and strain at break are significantly affected by the introduction of micron-sized pore structures in the native BC (Figure 4.14.A, B). Both the ultimate tensile strength and strain at break are significantly reduced in the porous BC samples in comparison to the native BC (Figure 4.14.A, B). Strain at break and elastic modulus is significantly different in the porous BC compared to the oxidized BC (Figure 4.14.B, C). The strain at break is reduced whilst the elastic modulus is increase in the porous BC compared to the oxidized BC (Figure 4.14.B, C). The ultimate tensile strength of porous BC is not significantly different compared to oxidized BC samples (Figure 414.A).

The ultimate tensile strength and elastic modulus of the porous oxidized BC scaffold is significantly reduced compared to native BC, oxidized BC and porous BC. The strain at break of porous oxidized BC is only significantly reduced compared to native and oxidized BC.

Overall, the data show that oxidation of the native BC (oxidized BC) or introduction of micron-sized pore structures in the native BC (porous BC) causes an approximate 25% decrease in the ultimate tensile strength of the native BC (Figure 4.1.A). Introduction of micron-sized pore structures and oxidation of the scaffold (porous oxidized BC) causes an approximate 75% decrease in the ultimate tensile strength of the native BC (Figure 4.1.A). Oxidation the native BC scaffold (oxidized BC) causes an approximate 40% decrease in the elastic modulus of the native BC (Figure 4.1.C). Micron-sized porous structures and oxidation of the scaffold (porous oxidized BC) causes an approximate 55% decrease in the elastic modulus of the native BC (Figure 4.1.C). Presence of

micron-sized pore structures in the scaffolds (porous BC, porous oxidized BC) causes an approximate 33% decrease in the strain at break of the native BC and oxidized BC scaffolds (Figure 4.1.B).

These results show that oxidation does affect the ultimate tensile strength and elastic modulus of the BC scaffolds, and the micron-sized pore structures in addition to oxidation further affects the ultimate tensile strength, strain at break and elastic modulus of the BC scaffolds. Periodate oxidation which transforms native BC and porous BC scaffolds into dialdehyde cellulose scaffolds may have altered the inter- and intramolecular hydrogen bonding in the cellulose structure and impaired the mechanical properties of the scaffold. Creating porous structures and forming aldehyde groups in the bacterial cellulose structure (i.e., porous oxidized BC) may have also affected the hydrogen bonding of the cellulose structure, the integrity of the fibrous network, and reduced the mechanical properties of the scaffold.

Although, currently, there is no simple mathematical model capable of describing the relationship between mechanical behaviors and porosity in polymeric materials, the porous BC scaffold complied with the power-law theory between mechanical parameters and relative density [152]. The elastic modulus and strength of the BC scaffolds decreased with the increase of porosity, as is evident in Figure 4.14.

The observed average moduli of the native and modified BC scaffolds were approximately 667 – 1472 kPa. This range of moduli is four to five orders of magnitude lower than that of reported human bone [55]. Motherway et al. (2009) previously reported the elastic moduli for the parietal bones of adult human skulls to be approximately 6 – 18 GPa [55]. Although the observed moduli of the BC scaffolds are lower than that of human bone, the scaffold may be best suited for bone and cartilage repair under non-load conditions, such as selected plate bones of the face and skull. The BC scaffolds may also be used as a non-load bearing scaffolds to fill tissue voids resulting from tissue damages, and serve as a matrix for new tissue to attach to during tissue regeneration.

4.6. Characterization of Cell and Bacterial Cellulose Scaffolds

4.6.1. Cellular Adhesion, Viability and Proliferation Assays

MTS assay analysis was performed to determine the viability of EqMSCs seeded on the native and modified BC scaffolds. The MTS assay results of EqMSCs seeded on native BC and its modified composites are shown in Figure 4.15. EqMSCs seeded on the BC scaffolds (Figure. 4.15) demonstrated high growth rates as a function time and represent a high viability and proliferation composition.

As discussed in Section 3.3.1, EqMSCs react with a tetrazolium-based compound in the MTS assay and produce a formazan product. The quantity of these formazan products, measured at the absorbance of 490 nm, is directly proportional to the number of living cells in culture. The results of MTS assay as shown in Figure 4.15 demonstrate that similar to EqMSCs cultured on native BC, EqMSCs seeded on the oxidized BC, porous BC, and porous oxidized BC were able to metabolize MTS into formazon product and have a high rate of proliferation as a function of time.

The results show that EqMSCs seeded on porous oxidized BC had significantly higher proliferation rate after 7 days in culture compared to EqMSCs seeded on native BC, oxidized BC and porous BC (Figure 4.15). Introduction of micron-sized pore structures and oxidation of the scaffold (porous oxidized BC) caused an approximate 100% increase in the proliferation rate of EqMSCs on the scaffold compared to the native BC, oxidized BC, and porous BCs after 7 days in culture (Figure 4.15). Non-degradable modified BCs was observed to not have enhanced the rate of cell proliferation after 7 days in culture (Figure 4.15). Oxidized and porous oxidized BCs enhanced rate of proliferation 1.5-2 folds after 7 days in culture (Figure 4.15).

After day 14 in culture, MTS assay results demonstrate that EqMSCs seeded on native BC had a significantly higher proliferation rate compared to the EqMSCs seeded on the oxidized BC and porous BC scaffolds (Figure 4.15). Approximately 30% increase in proliferation rate of EqMSCs was observed on

the native BC compared to the oxidized BC and porous BC scaffolds after 14 days in culture. Cell staining using calcein-AM and PI was performed following MTS assay analysis to visually assess EqMSCs attachment under these conditions and further analyze the observed proliferation behavior of the cell on the BC scaffolds as demonstrated by the MTS assay results.

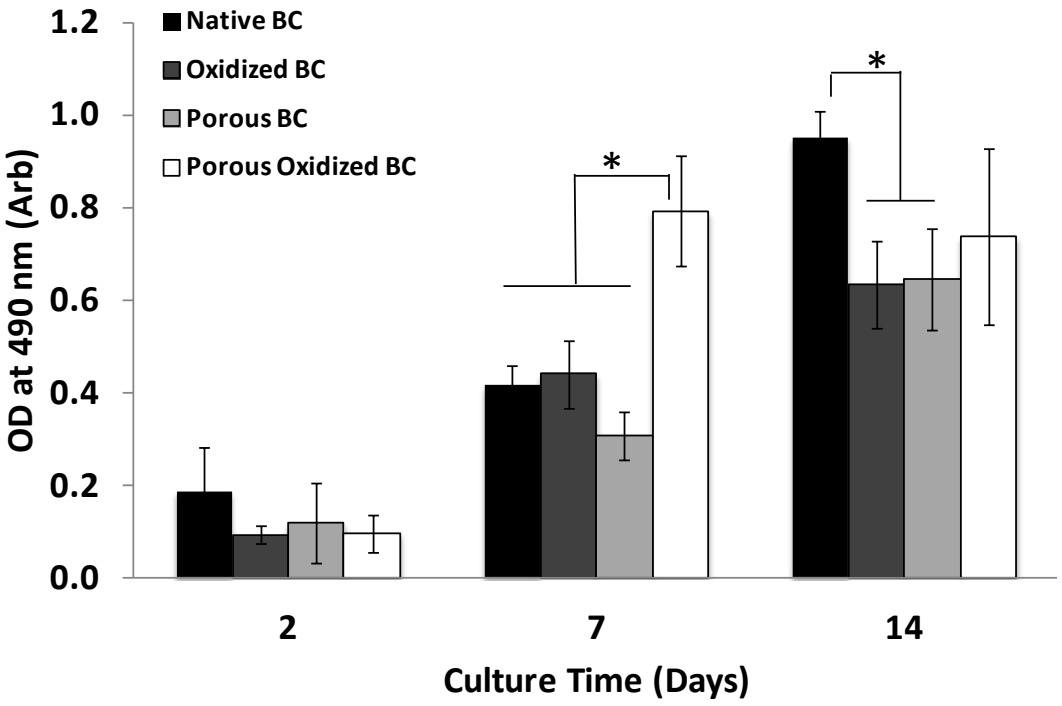

Figure 4.15: Cellular viability assay: MTS test. Comparison of proliferation of cells as determined by MTS assay of EqMSCs (1.26 x 10^5 cells/cm^2) seeded for 2, 7 and 14 days on native BC, porous BC, oxidized BC, and porous oxidized BC. Asterisks (*) indicates significant differences at $p<0.05$.

As discussed in Section 3.3.1, calcein-AM and PI staining provides a two-color fluorescence cell viability and attachment assay of seeded cells. Calcein-AM exhibits green fluorescence and demonstrates live cells, and PI displays red fluorescence and demonstrates dead cells. After 2 days in culture (Figure 4.16.A, 4.17), the cells seeded on the four different forms of BC surfaces showed a distinct phenotype, with less elongated shapes and several displayed a round morphology. The cells seeded on the porous BC, and more specifically porous oxidized BC, appear to have bridged, have attached to, and were proliferating in the BC micropores (Figure 4.16.A).

By 7 days in culture (Figure 4.16.B, 4.17), EqMSCs have a full spread-out morphology on the oxidized BC, porous oxidized BC, and native BC scaffolds. Cells on the porous oxidized BC also appeared to have reached 100% confluency on the scaffold. The full spread-out morphology of the EqMSCs on the porous BC was less pronounced compared to the other BC scaffolds after 7 days in culture (Figure 4.16.B, 4.17).

After 14 days in culture (Figure 4.16.C, 4.17), EqMSCs seeded on the native BC and oxidized BC continued to maintained the full spread-out appearance, demonstrated to have increased in proliferation, and have reached approximately 80-90% confluency on their respected scaffolds. At 14 days in culture (Figure 4.16.C), EqMSCs seeded on the porous oxidized BC appeared to have reduced in confluency compared to 7 days in culture (Figure 4.16.B). The EqMSCs on the porous BC from 2 to 14 days in culture (Figure 4.16.A-C) appear to be viable and continually maintained the less pronounced spread-out morphology on the cellulose scaffold. The cells seeded on the four different forms of scaffolds from 2 to 14 days appear to have a limited number of dead cells, as demonstrated by the PI staining which fluoresced red, compared to live cells which fluoresced green from the calcein-AM stain (Figure 4.16, 4.17).

Figure 4.16: Cellular adhesion and cell viability stained with calcein-AM and PI using fluorescent microscopy. Cell viability of EqMSCs (1.26×10^5 cells/cm^2) seeded for 2 (A), 7 (B), and 14 (C) days on porous BC, oxidized BC, and porous oxidized BC compared to native BC. Cells were analyzed by calcein-AM which exhibits green fluorescence and demonstrates live cells and PI which displays red fluorescence and demonstrates dead cells. Fluorescent micrograph showed that overtime the cell adhered to, were viable and proliferation on the modified BC scaffolds compared to native BC in culture. Scale bar = 100 μm.

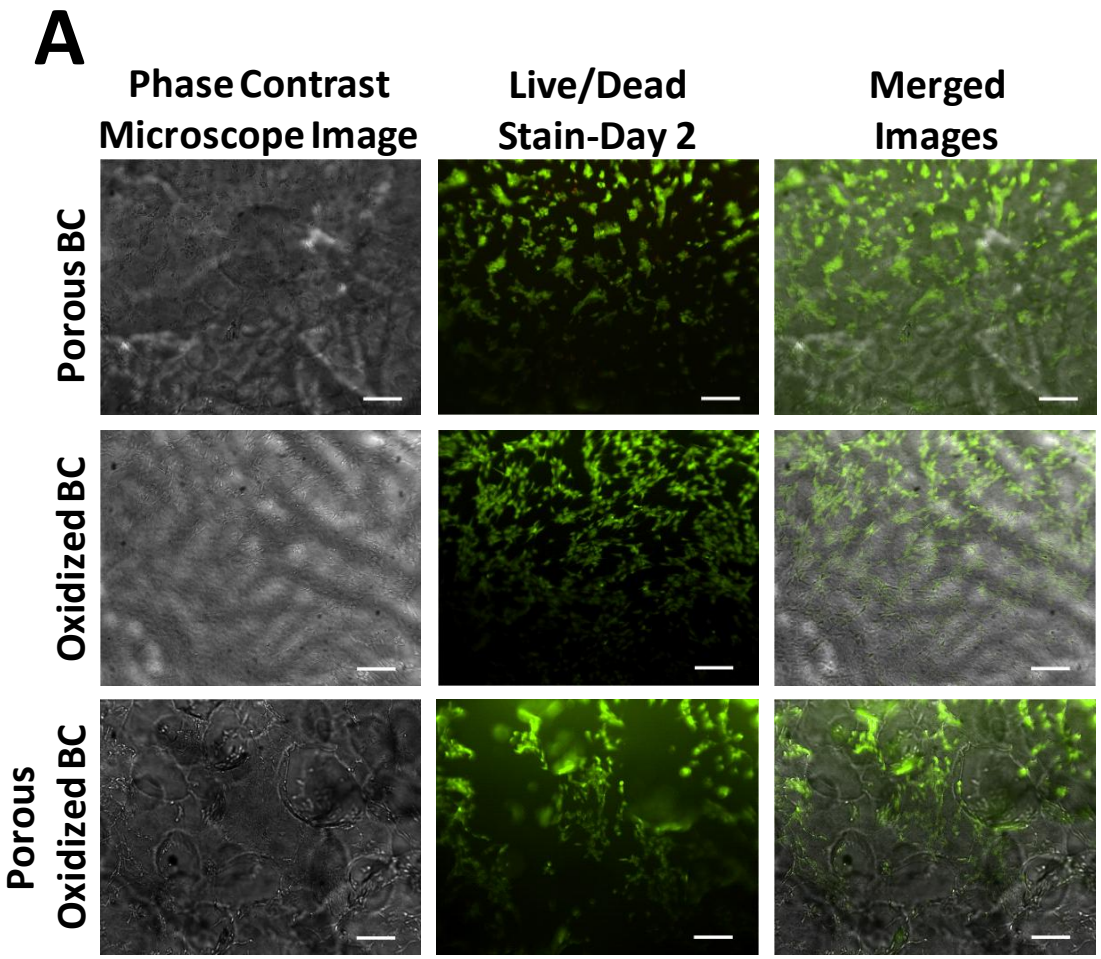

Figure 4.16: Continued.

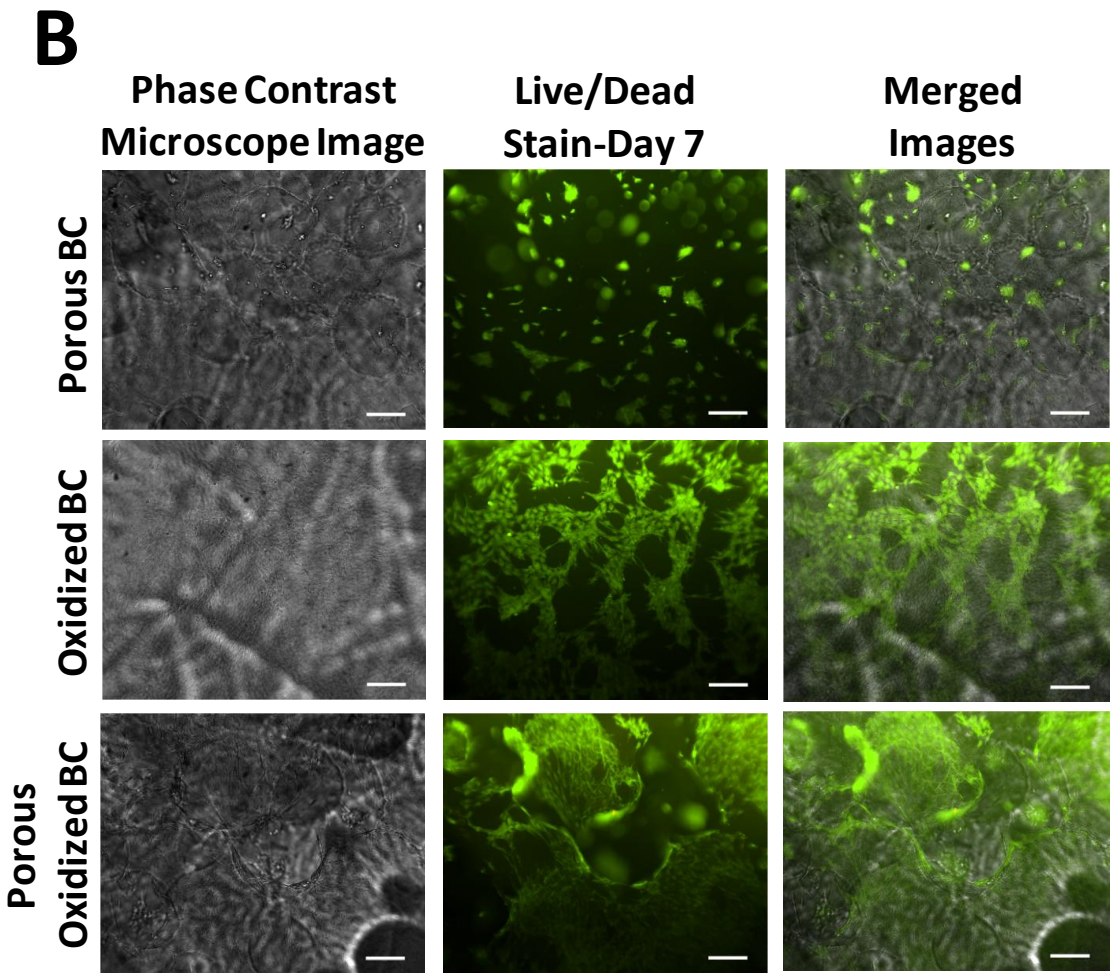

Figure 4.16: Continued.

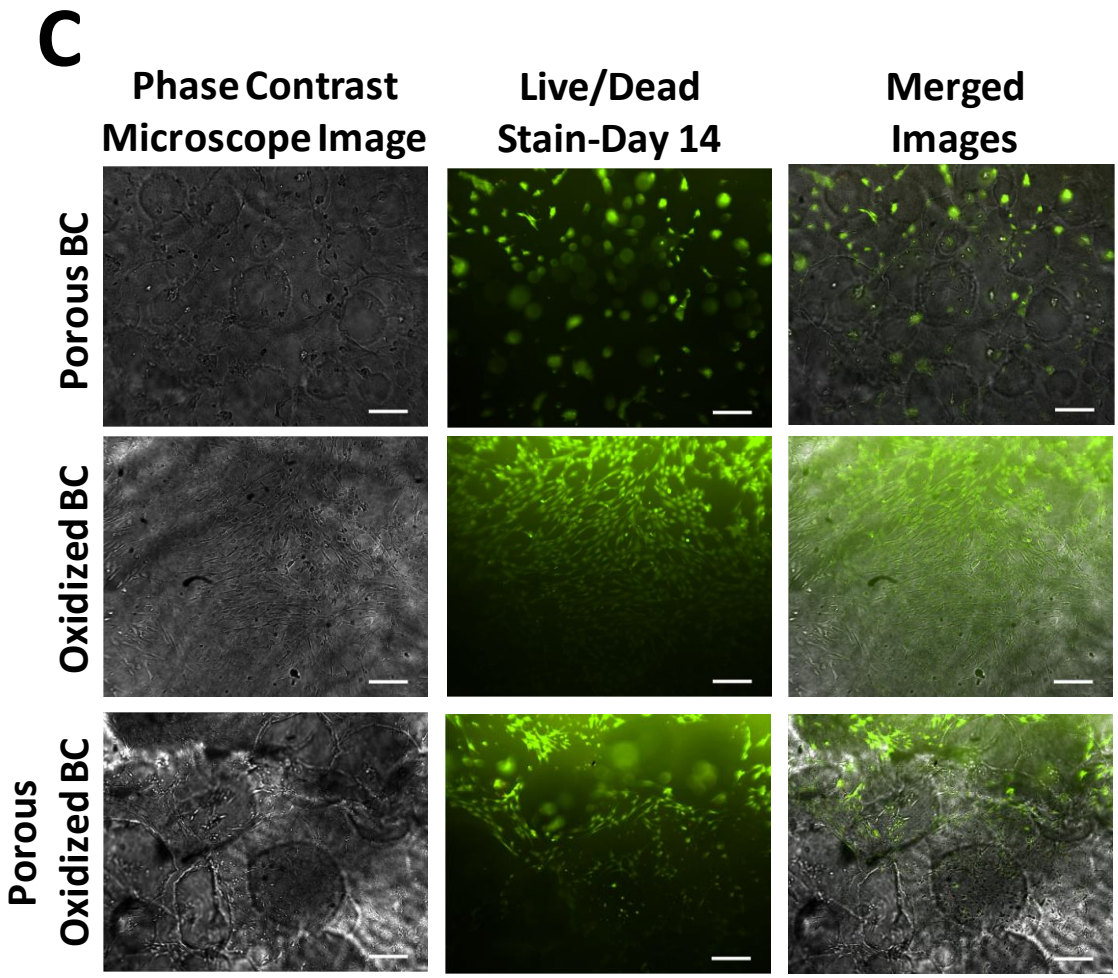

Figure 4.16: Continued.

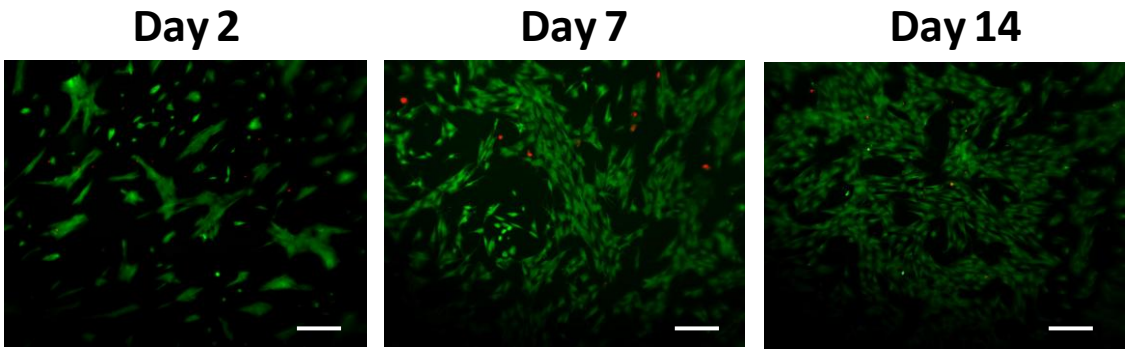

Figure 4.17: Cellular adhesion and cell viability stained with calcein-AM and PI using fluorescent microscopy. Cell viability of EqMSCs (1.26 x 10^5 cells/cm^2) seeded for 2, 7, and 14 days on native BC and analyzed by calcein-AM and PI. Scale bar = 100 µm.

Calcein-AM and PI data shows that the density of seeded EqMSCs on porous BC and oxidized BC (Figure 4.16) were viable, grew in population overtime, and were well distributed throughout the BC compared to EqMSCs seeded on native BC (Figure 4.17). Calcein-AM and PI data shows that EqMSCs seeded on the porous BC (Figure 4.16) performed similarly to the native BC and oxidized BC but its growth overtime was not as visually pronounced compared to these BC scaffolds. This may be because the selected numbers of cells seeded on the porous BC have attached inside the voids in the porous scaffolds consequently constructing them from view. Calcein-AM and PI data also shows that EqMSCs seeded on the porous oxidized BC (Figure 4.16) became 100% confluence after 7 days in culture therefore limiting the area needed by the cells to continue to grow. As a result, the proliferation rate of the cells decreased by 14 days in culture because of the limited area for growth, as indicated in Figure 4.16.C.

Calcein-AM and PI staining observations (Figure 4.16, 4.17) concur with the MTS assay results (Figure 4.15), as discussed. The addition of micro-porosity into the scaffolds increased the surface area available of the EqMSCs to attach to and proliferate. Periodate oxidation which transforms native BC and

porous BC scaffolds into dialdehyde cellulose scaffolds have altered the surface chemistry of the cellulose scaffold. Calcein-AM and PI staining, and MTS assay both confirmed that EqMSCs prefer the combination of micro-porosity and dialdehyde cellulose scaffold because they reached 100% confluency sooner on these scaffolds compared to the three other forms of BC scaffolds while maintaining a full-spread out morphology indicative of contentment with the physical and chemical properties of the material.

4.6.2. In Vitro differentiation of EqMSCs

To further characterize the EqMSCs, they were induced to differentiate into osteocytes and chondrocytes *in vitro* on the oxidized scaffolds (Figure 4.18, 4.19). Because a degradable scaffold is preferred for bone and cartilage tissue engineering, and the EqMSCs demonstrated superior growth on the oxidized BC and porous oxidized BCs (Figure 4.15, 4.16), they were used for the *in vitro* differentiation assessment of the stem cells. As demonstrated, the EqMSCs seeded on the porous oxidized BC scaffolds similar to the cells on the oxidized BC scaffolds exhibited the potential to differentiate into a bone and a cartilage cell depending on the induction media. The results support the fact that EqMSCs do not lose their potentials to differentiate when they adhere to oxidized BC, and porous oxidized BC. Figure 4.18 also confirms that the chondrocytes and osteocytes have bridged and completely covered the micropores of the porous oxidized BC. Selected cells as illustrated in Figure 4.19, differentiated inside of the porous structures of the porous oxidized BC scaffold.

The differentiation of EqMSCs into chondrocytes and osteocytes as previously discussed is one of the key processes for cartilage and bone regeneration, respectively. From a functional perspective, where cell therapy for musculoskeletal hindrances is the ultimate goal, it is fundamental that the cells do not lose or have reduced capacity of differentiation [127]. This study showed that EqMSCs have the capability to differentiate into chondrocytes and

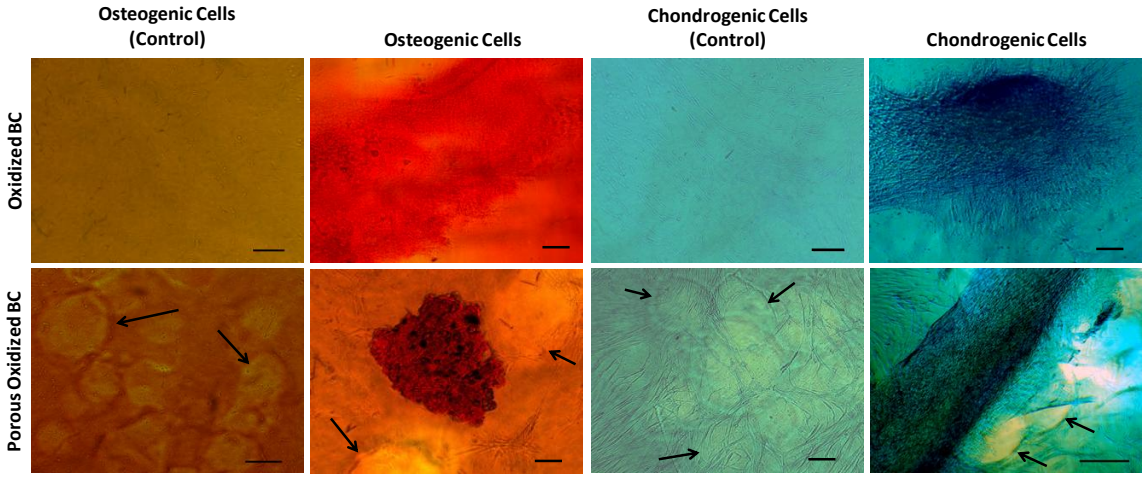

Figure 4.18: Osteogenesis and chondrogenic differentiation capacity of EqMSCs. EqMSCs (5.0 x 10^4 cells/cm^2) were investigated for their *in vitro* trans-differentiation capacity on oxidized BC and porous oxidized BC after 7 days of differentiation. Osteogenesis was demonstrated by the detection of calcium in the mineralized matrix indicated by alizarin red stain shown in the differentiated cells. Chondrogenesis was indicated by alcian blue staining shown in the differentiated cells. Arrows indicate pore structures in the scaffolds. Scale bars = 100 µm.

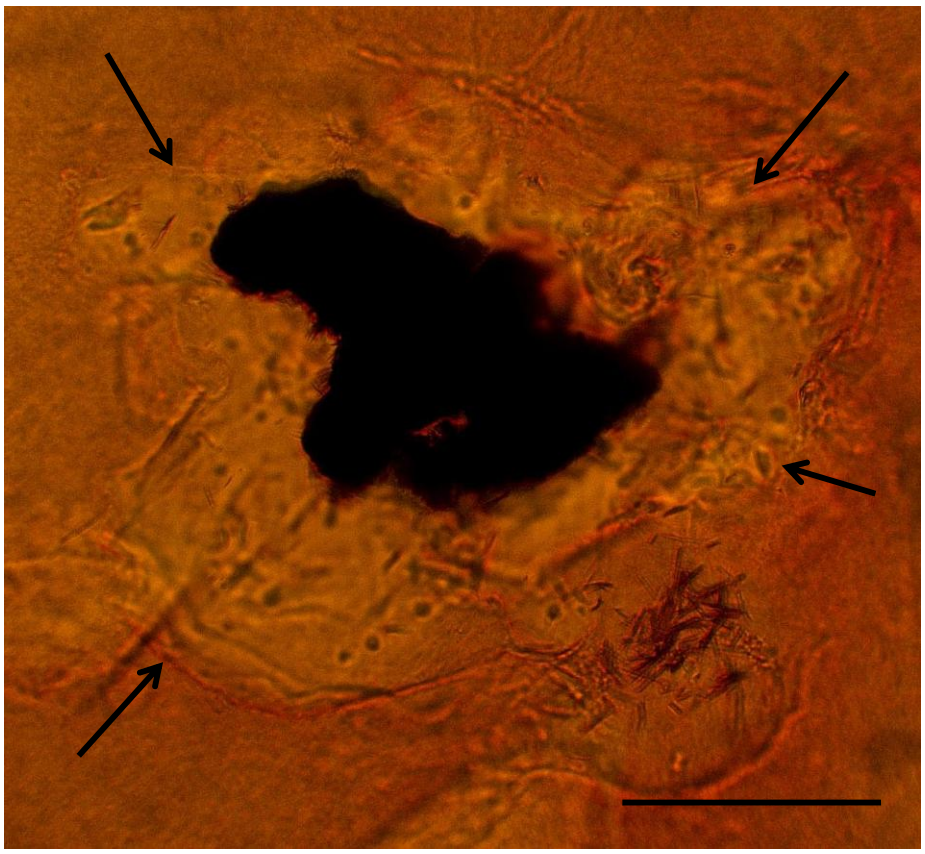

Figure 4.19: Induced osteogenesis differentiation capacity of EqMSCs (5.0 x 10^4 cells/cm^2) seeded on porous oxidized BC after 7 days of differentiation. Contrast micrograph demonstrated that cells positively stained for alizarin red. Micrograph demonstrated the positive differentiation of EqMSCs inside the pore structure of the porous oxidized BC. Arrow indicated pore structure in the scaffolds. Scale bars = 100 µm.

osteocytes on the oxidized BC and porous oxidized BC scaffolds, an important characteristic for cartilage and bone regeneration.

4.6.3. Confocal Microscopy of Seeded EqMSCs

Confocal microscopy was used to examine surface cell attachment profile and distance of cellular penetration into the bulk of oxidized BC and porous oxidized BC scaffolds. Confocal 2D image mapping of EqMSCs adhesion and morphology across the surface of oxidized BC shows that the cells adhered onto the scaffold (Figure 4.20.A) and were at different depths on the scaffold (Figure 4.20.B).

Confocal Z-mapping demonstrated that the cells adhered onto the non-flat surface topography of the oxidized BC scaffold, and not inside the nano-pores of the scaffold (Figure 4.21, 4.22). The different depth profiles measured by the confocal microscope (Figure 4.20.A, 4.21, 4.23) were the change in surface topography of the nano-fibrous oxidized BC, and not depth of cell growth. Confocal microscopy illustrated that the change in surface topography of the oxidized BC is approximately 130 μm in depth.

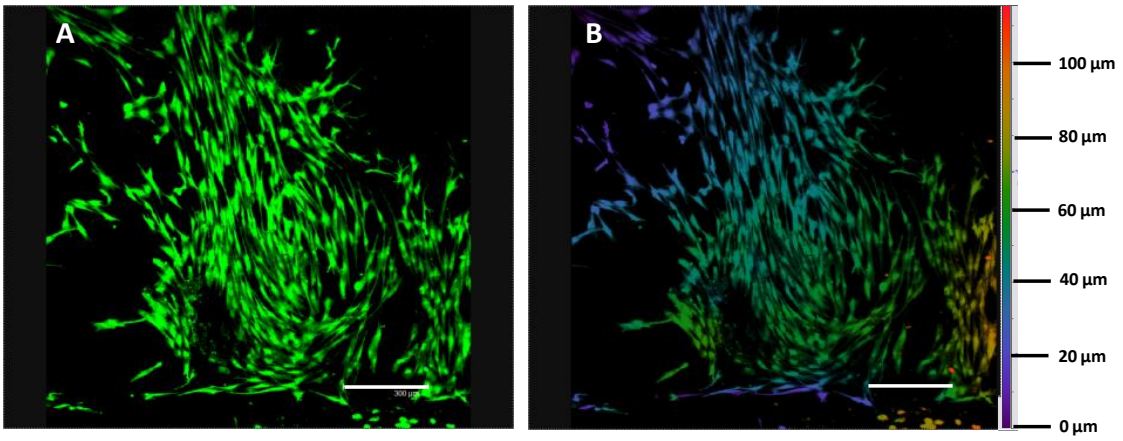

Figure 4.20: Confocol 2D image mapping of EqMSCs adhesion and morphology across the top surface of oxidized BC scaffold. Overlay images from confocol scanning in 2D uni-color format (A) and color-scaled 2D format (B). Scale bar = 300 µm.

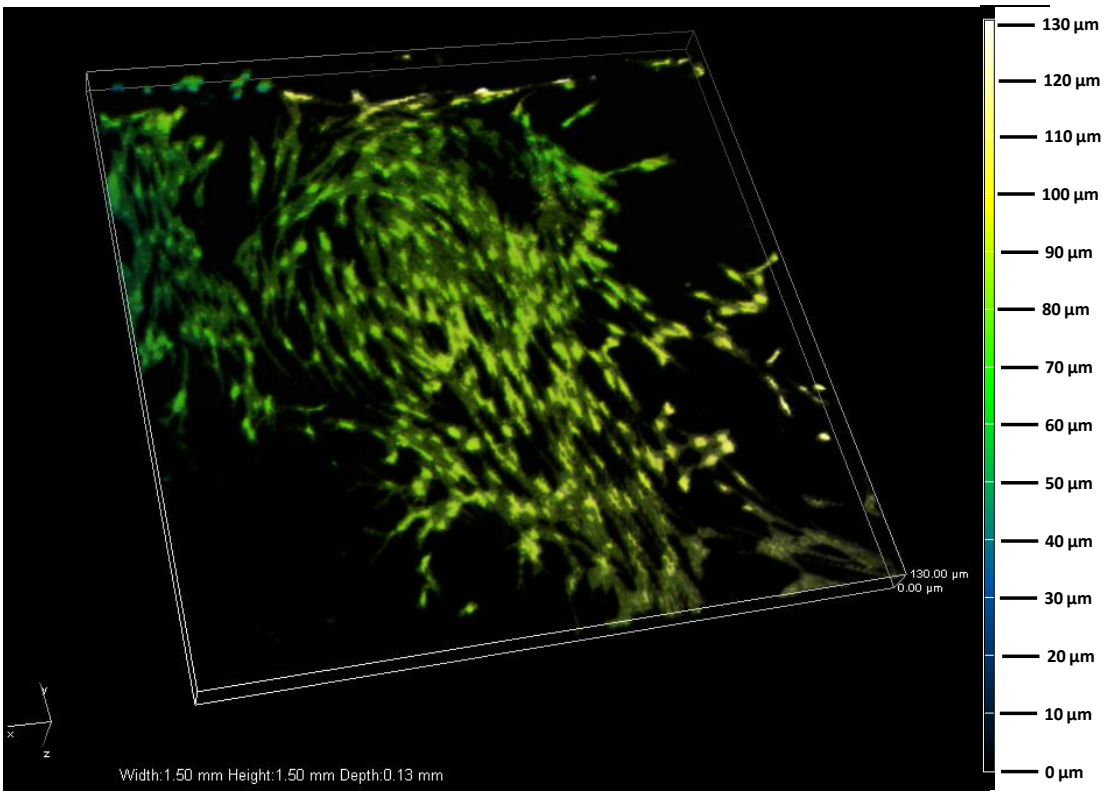

Figure 4.21: Confocol Z-mapping box volume view from the top surface into the bulk of oxidized BC scaffold seeded with EqMSCs.

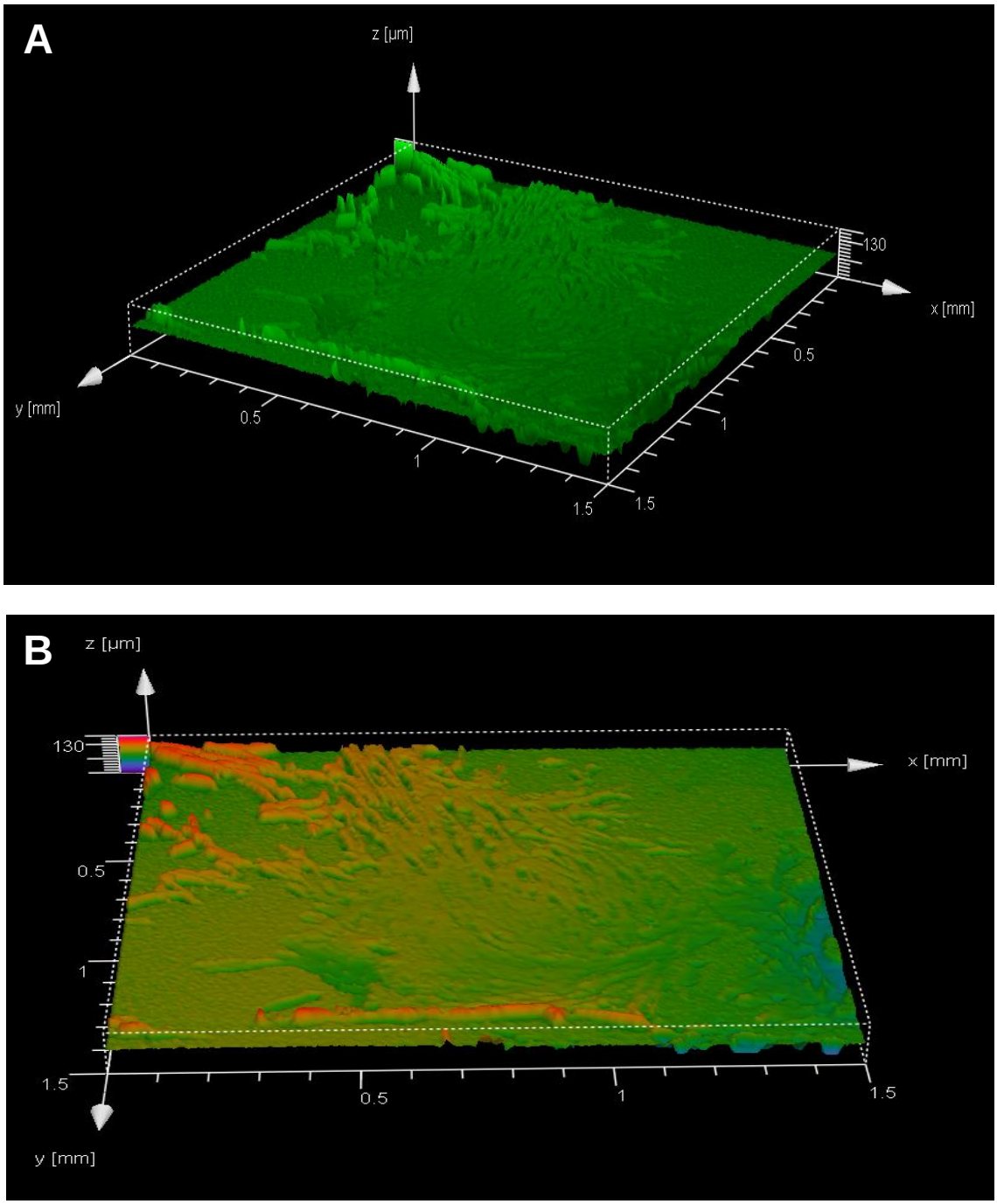

Figure 4.22: Confocol 3D Z-mapping view from the top surface into the bulk of oxidized BC scaffold seeded with EqMSCs. Confocol 3D Z-mapping images in 3D uni-color format (A) and color-scaled 3D format (B). The confocol images demonstrated that cells adhere onto the uneven surface of the scaffold (A, B).

Confocal 2D image mapping of EqMSCs adhesion and morphology across the surface of porous oxidized BC shows that the cells adhered onto the scaffold (Figure 4.23.A) and were at different depths on the scaffold (Figure 4.23.B). As indicated by the arrows in the confocal 2D image mapping images (Figure 4.23), the cells have bridged or completely covered the micro-pores of the porous oxidized BCs.

Confocal Z-mapping demonstrated that the cells adhered onto the surface of the porous-structure of the porous oxidized BC scaffold (Figure 4.24, 4.25). The 160 μm depth measurement in Figure 4.24 and 4.25 is based on the brightest images per scanning series captured by the confocal microscopy. Based on the diameter of the beeswax microspheres used to create the porous structures in the BC scaffolds, the depth of each pore is expected to be approximately 500 μm or less. The absolute limit of depth measurable by confocal microcopy in a biological specimen is 200 μm. The depth of cell in-growth and the pore diameter of the porous oxidized BC specimen are in fact larger than the measurable resolution of the instrument. The 160 μm depth measured by the confocal microscopy image is limited by the measurable resolution of the instrument. Therefore, the actual depth of EqMSCs in-growth on porous oxidized BC may be greater than the 160 μm depth shown using confocal microscopy.

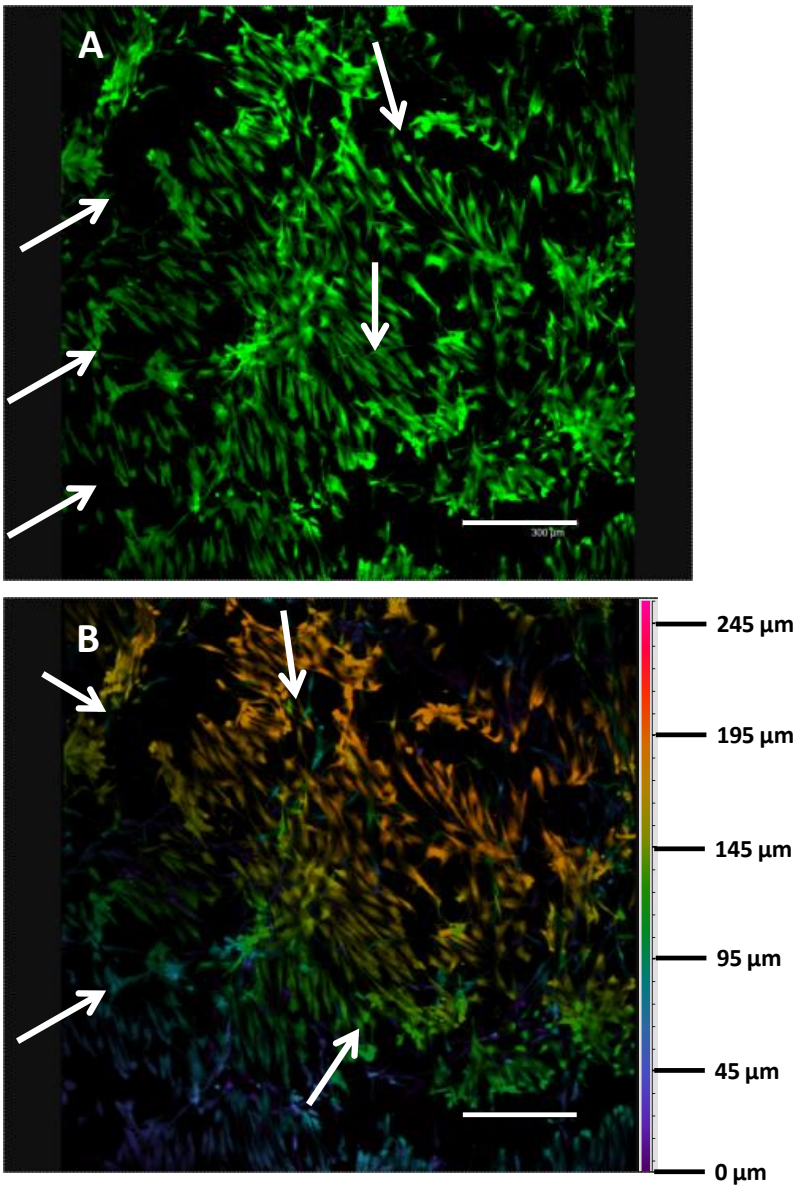

Figure 4.23: Confocol 2D image mapping of EqMSCs adhesion and morphology across the top surface of porous oxidized BC scaffold. Overlay images from confocol scanning in 2D uni-color format (A) and color-scaled 2D format (B). Arrow in images indicated where cells had bridged or completely covered the BC micropores. Scale bar = 300 µm.

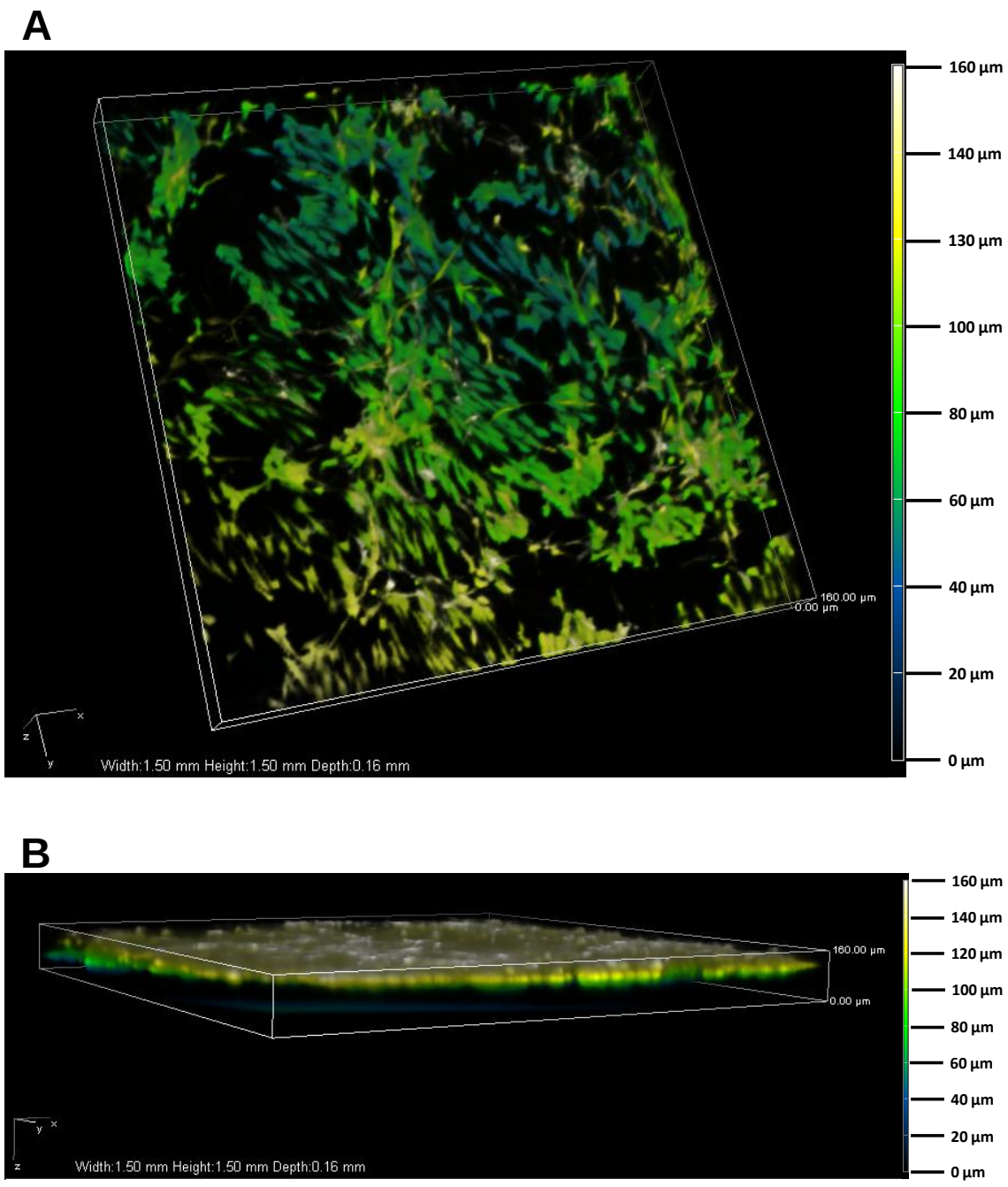

Figure 4.24: Confocol Z-mapping box volume view from the top surface into the bulk of porous oxidized BC scaffold seeded with EqMSCs. Confocol Z-mapping box volume image of cell-scaffold seeded construct from angled view (A) and side view (B).

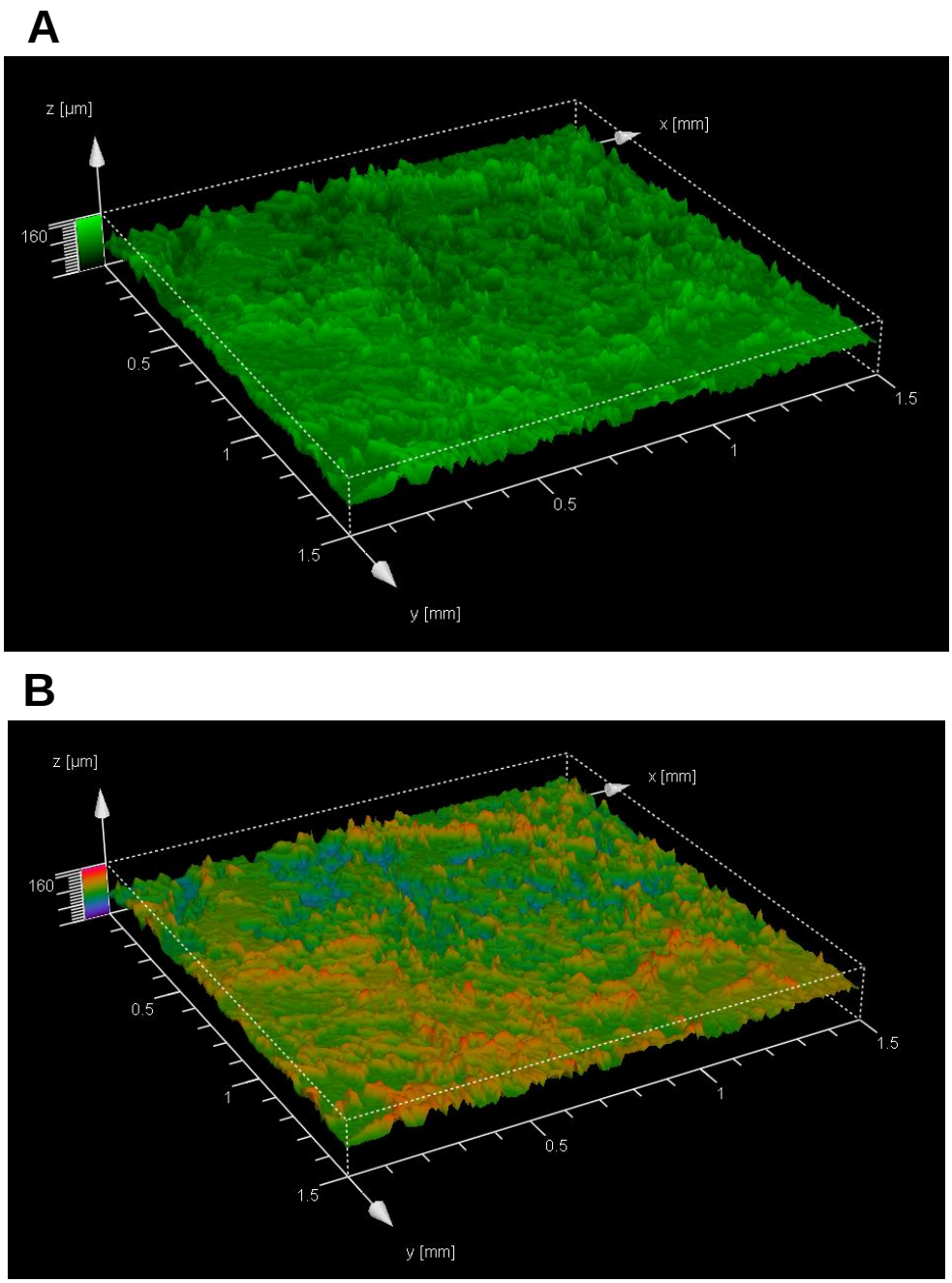

Figure 4.25: Confocol 3D Z-mapping view from the top surface into the bulk of porous oxidized BC scaffold seeded with EqMSCs. Confocol 3D Z-mapping images in 3D uni-color format (A) and color-scaled 3D format (B).

This study conducted with oxidized BC, porous BC, and porous oxidized BC showed that EqMSCs can adhere to, are viable, and retain the potential to differentiate into osteocytes and chondrocytes on the oxidized and porous oxidized BC scaffolds. Although these biodegradable scaffolds seems to hold great promise for future *in vivo* stem-cell based musculoskeletal therapies, further research into chemical modification of BC to mimic the chemistry of the tissues of interest seems advantageous.

4.7. Conclusions

Microporous BC scaffolds with interconnected pores were successfully synthesized by incorporating beeswax microspheres into the growing bacterial culture. The beeswax microspheres were effectively leached out of the produced scaffolds as confirmed by phase contrast microscopy, FTIR and SEM. Both native BC and porous BC were chemically modified into degradable scaffolds using periodate oxidation and n-propanol. Although there were no visible apparent changes to the oxidized BC and porous oxidized BC scaffolds, they both reduced their ability to retain water. The elastic modulus of the modified scaffolds decreased compared to the native BC. Oxidation of the scaffolds was confirmed using FTIR.

It was demonstrated that the modified BC scaffolds were cytocompatible with EqMSCs *in vitro*. The modified BC scaffolds supported the adhesion and proliferation of the EqMSCs. Non-degradable modified BCs did not enhance the rate of cell proliferation after 7 days in culture. Oxidized and porous oxidized BCs enhanced rate of proliferation 1.5-2 folds after 7 days in culture. Oxidized BC and porous oxidized BC supported the osteogenic and chondrogenic differentiation of the EqMSCs. The cells seeded on the modified BC scaffolds were viable and possessed high proliferation rate. Based on these results, the

porous oxidized BC scaffolds appear to have potential as a scaffold for tissue engineering of bone and cartilage.

CHAPTER V
Analysis of Nano-porous and Micro-porous Bacterial Cellulose Scaffolds Chemically Modified with Surface Amination and Surface Carboxylation

In this study, surface amination and carboxylation were completed on native BCs, microporous BCs, and on their oxidized composites. Amination and carboxylation was explored to mimic the amine and carboxylic acid functional groups present in the glycosaminoglycans (GAGs) inherent in cartilage tissue *in vivo*. Amination (primary, tertiary, and quaternary amine) and carboxylation of native BC scaffold were accomplished by chemically modifying the scaffolds with various amine reactants and a carboxylation reactant. The BC composites were characterized using FTIR, SEM, and mechanical testing instrument. The BC composites were also characterized for their ability to support and maintain differentiation of EqMSCs *in vitro* for potential tissue engineering use. The potential for EqMSCs to differentiate into chondrocytes were assessed. The degradation properties were then analyzed by incubating the samples in HEPES buffer (pH 7.4) at 37 °C under static and dynamic conditions. The samples were measured for weight loss while the buffer was analyzed for degradation products.

5.1. Surface Amination and Carboxylation of Bacterial Cellulose Scaffolds

Native BC and porous BCs were synthesized and purified as described in Sections 2.2.1 and 2.2.2, respectively. Surface amination and carboxylation were performed on half of the native BC and porous BC samples as described in Section 2.2.4. Table 5.1 lists the reactants used and the surface functionalities produced on the native BC (i.e., nano-porous BC) and porous BC samples. The reaction scheme for the surface functionalized BC scaffolds is shown in Figure 5.1.

Table 5.1: Reactants used to produce the listed surface functionalities on non-porous and microporous bacterial cellulose samples.

Surface Functionality	Reactant	Non-modified Cellulose	Modified Cellulose
Primary Amine	2-Chloroethylamine hydrochloride (CEA)	Native BC	Aminoethyl BC (AE-BC)
		Microporous BC	Aminoethyl microporous BC (AE Porous BC)
Tertiary Amine	2-Chloro-*N,N*-dimethylethylamine hydrochloride (CDMEA)	Native BC	Dimethyl aminoethyl BC (DMAE-BC)
		Microporous BC	Dimethyl aminoethyl microporous BC (DMAE Porous BC)
Quaternary Amine	Glycidyl trimethyl ammonium chloride (GTMEA)	Native BC	Trimethyl ammonium betahydroxy propyl BC (TMAHP-BC)
		Microporous BC	Trimethyl ammonium betahydroxy propyl microporous BC (TMAHP Porous BC)
Carboxylation	Monochloro acetic acid sodium salt (Na-MCA)	Native BC	Carboxymethyl BC (CM-BC)
		Microporous BC	Carboxymethyl microporous BC (CM Porous BC)

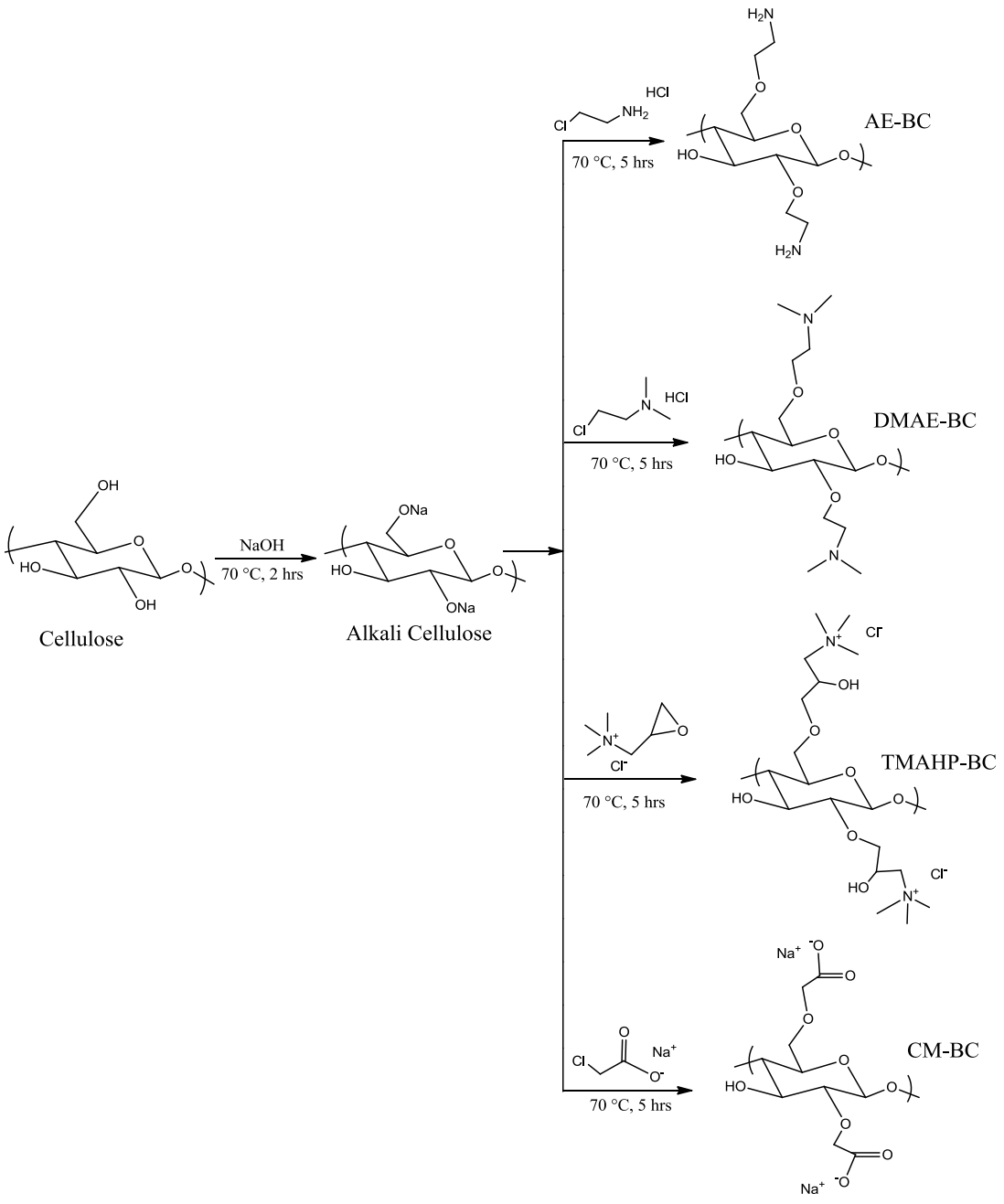

Figure 5.1: Surface functionalization reactions performed on bacterial cellulose.

Amination (primary, tertiary, and quaternary amine) and carboxylation reactions were performed on BC scaffolds.[97, 112]. The surface of the BC scaffold were chemically functionalized with the purpose of creating a biomaterial with the amine and carboxylic acid functional groups present in the GAGs in native cartilage tissue, and to enhance EqMSCs proliferation and differentiation on the biomimetic scaffold for cartilage tissue engineering applications.

GAGs are linear polysaccharides that contain amino sugars. They are covalently attached to proteins that are located on the surface of cells and in native extracellular matrixes such as cartilage [136, 153]. Their role in biological systems is to promote protein interactions, and as a result, they participate in a diverse range of biological activities including cell and tissue growth control, cell adhesion, and sequestering growth factors within matrices [154-156]. GAGs are composed of highly variable repeating disaccharide units with sequences that contain an amino sugar (either N-acetylgalactosamine or N-acetylglucosamine) and an uronic acid (either D-glucuronic or L-iduronic acid). There are five different types of GAGs chains: hyaluronan, chondroitin 4- and/or 6-sulfate, dermatan sulfate, heparan sulfate and/or heparin, and keratan sulfate as illustrated in Figure A.1 in Appendix A [157]. As shown in Figure A.1 in Appendix A, secondary amine and carboxylic acid functional groups are present on the chemical structure of GAGs [157].

In this study, BC scaffolds were modified using primary, tertiary and quaternary amines, and not secondary amines which are prevalent in GAGs. This was the first step to modifying the BC scaffolds with amine surface functionalities. The objective of this research was to produce and assess the performance of primary, tertiary and quaternary amine surface functionalities for possible future studies using more complex modifications.

In brief, chemically modified cellulose scaffolds were prepared using three different reactant concentrations (19.8, 39.6, and 59.4 mM mM) to access their effect on cell behavior. Primary surface amination was performed on native BC to obtain an aminoethyl BC (AE-BC) scaffolds. Tertiary surface amination was

performed on native BC to obtain dimethyl aminoethyl BC (DMAE-BC) scaffolds. Quaternary surface amination was also performed on native BC to obtain trimethyl ammonium betahydroxy propyl BC (TMAHP-BC) scaffolds. Carboxylation surface amination was performed on native BC to obtain carboxymethyl BC (CM-BC) scaffolds. Microporous BCs were chemically modified under the same conditions to obtain aminoethyl microporous BC (AE porous BC), dimethyl aminoethyl microporous BC (DMAE porous BC), trimethyl ammonium betahydroxy propyl microporous BC (TMAHP porous BC), and carboxymethyl microporous BC (CM porous BC).

Half of the chemically functionalized scaffolds were oxidized BC using sodium periodate in n-propanol following the procedure outlined in Section 2.2.5. Table 5.2 lists the acronyms for the surface-functionalized BC samples and their corresponding oxidized samples. The reaction scheme for the surface functionalized BC scaffolds is shown in Figure 5.2. Assessment of the scaffolds after oxidation using sodium periodate in n-propanol showed no visible changes in the color and morphology of the BC scaffolds when compared to the non-oxidized functional BCs.

Table 5.2: Surface-functionalized bacterial cellulose samples and their corresponding oxidized samples.

Surface-functionalized Scaffold	Oxidized and Surface-functionalized Scaffold
Aminoethyl BC (AE-BC)	Aminoethyl oxidized BC (AE-OBC)
Aminoethyl microporous BC (AE Porous BC)	Aminoethyl microporous oxidized BC (AE Porous OBC)
Dimethyl aminoethyl BC (DMAE-BC)	Dimethyl aminoethyl oxidized BC (DMAE-OBC)
Dimethyl aminoethyl microporous BC (DMAE Porous BC)	Dimethyl aminoethyl microporous oxidized BC (DMAE Porous OBC)
Trimethyl ammonium betahydroxy propyl BC (TMAHP-BC)	Trimethyl ammonium betahydroxy propyl oxidized BC (TMAHP-OBC)
Trimethyl ammonium betahydroxy propyl microporous BC (TMAHP Porous BC)	Trimethyl ammonium betahydroxy propyl microporous oxidized BC (TMAHP Porous OBC)
Carboxymethyl BC (CM-BC)	Carboxymethyl oxidized BC (CM-OBC)
Carboxymethyl microporous BC (CM Porous BC)	Carboxymethyl microporous oxidized BC (CM Porous OBC)

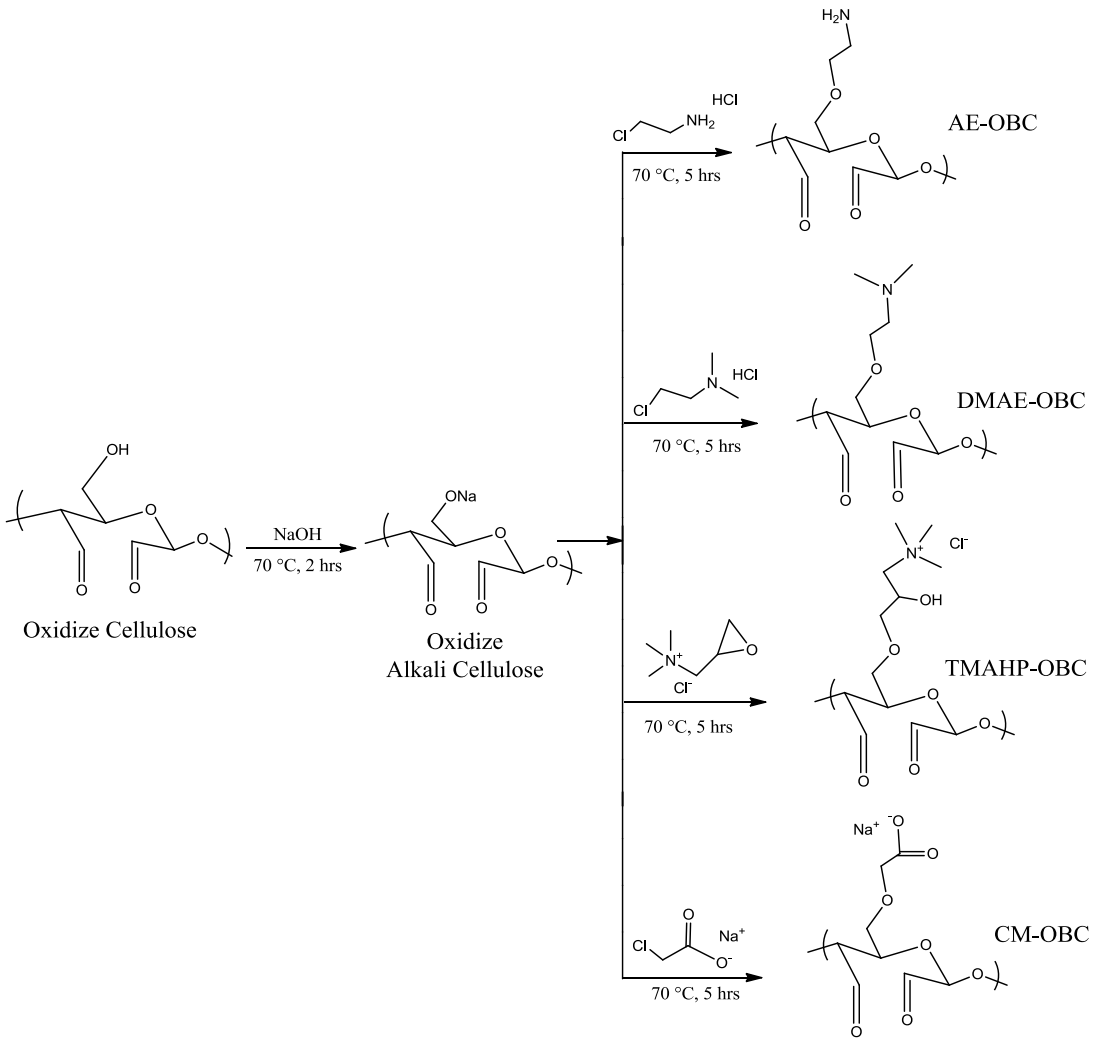

Figure 5.2: Surface functionalization reactions performed on oxidized bacterial cellulose.

Wet (hydrated, never-dried) sample weights of a representative set of samples were measured (Figure 5.3). Wet weights of 39.6 mM TMAHP-BC, 39.6 mM TMAHP OBC, 39.6 mM TMAHP porous BC, and 39.6 mM TMAHP porous OBC showed no significant difference with corresponding sample controls (native BC, oxidized BC, porous BC, and porous oxidized BC) (Figure 5.3). This data indicates that compared to the corresponding sample controls, chemical functionalization reaction did not change the structure of the cellulose and its fundamental ability to retain water. The analysis of the change in wet weight between native BC, oxidized BC, porous BC, and porous oxidized BC has been previously discussed (Section 4.2.3).

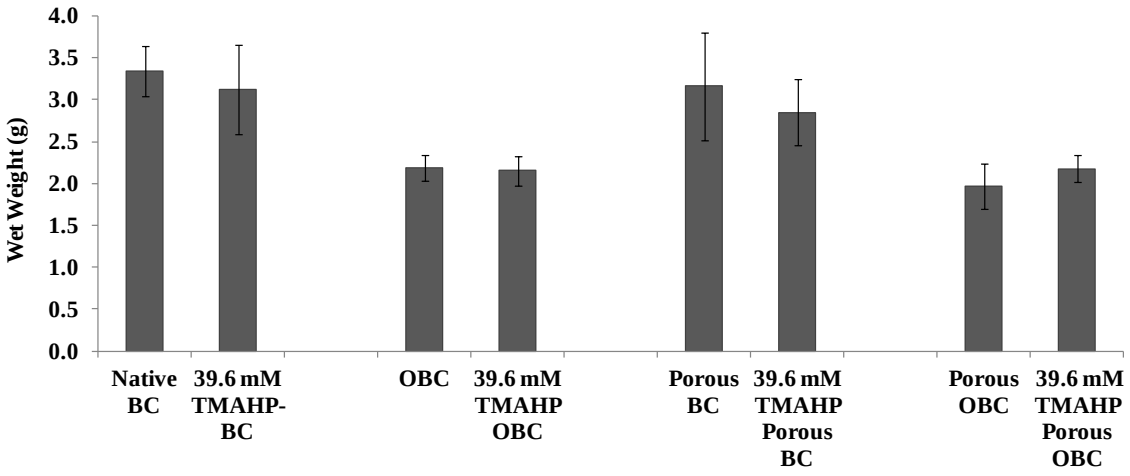

Figure 5.3: Comparison of wet weights of 39.6 mM TMAHP-BC, 39.6 mM TMAHP OBC, 39.6 mM TMAHP porous BC, and 39.6 mM TMAHP porous OBC with corresponding sample controls (native BC, oxidized BC, porous BC, and porous oxidized BC). Asterisks (*) indicates significant differences at $p<0.05$.

5.2. Fourier Transform Infrared Spectroscopy

The chemical structure of the cellulose chain of BC scaffold is shown in Figure 1.7 and the FTIR spectrum of the native BC analyzed in standard FTIR mode is presented in Figure 5.4. FTIR absorption band represent the energy absorbed by the vibration of specific functional groups on the BC structure. Based on the chemical structure of cellulose, it consists of β-D-glucopyranose units linked together by (1→4)-glycosidic bonds (Figure 1.7), and numerous hydroxyl groups in its network (Figure 1.8). The characteristic FTIR bands of native bacterial cellulose corresponding to the spectrum in Figure 5.4 are presented in Table 5.3.

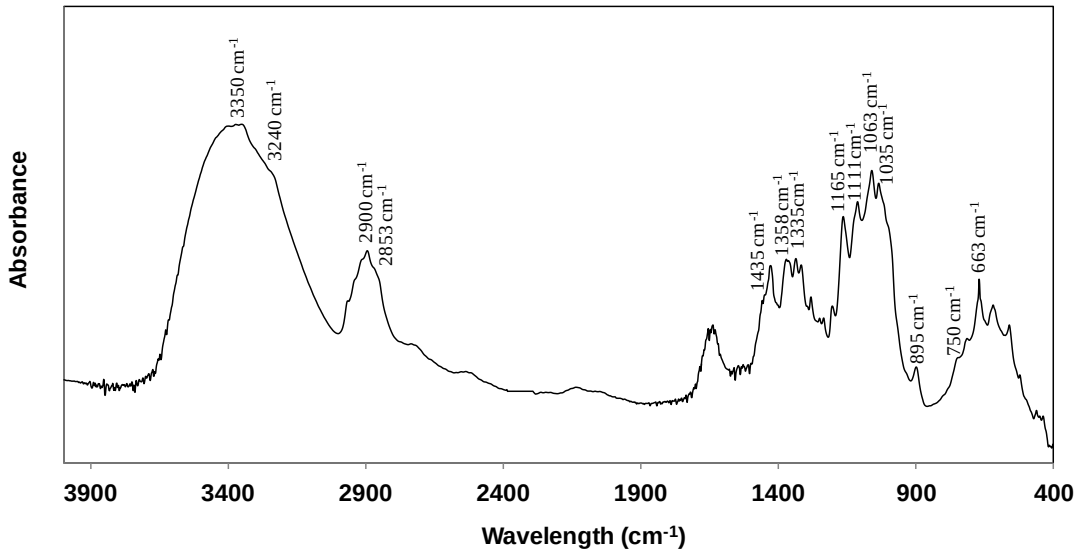

Figure 5.4: FTIR spectra of native bacterial cellulose analyzed in standard FTIR mode.

Table 5.3: Characteristic FTIR bands of native bacterial cellulose.

Frequency	Relative Intensity	Assignment	Ref.
3350 cm^{-1}	Strong	OH Stretching (associated with intramolecular hydrogen bonding)	[148]
3240 cm^{-1}	Medium	OH Stretching (characteristic of hydroxyl bonding in cellulose structure due to I_α crystalline phase)	[148, 149]
2900 cm^{-1}	Medium	CH Stretching	[149]
2853 cm^{-1}	Medium	CH_2 Symmetric Stretching	[150]
1653 cm^{-1}		Absorbed H_2O	[150]
1435 cm^{-1}	Weak	CH_2 Symmetric Bending	[150]
1358 cm^{-1}	Medium	CH Bending	[150]
1335 cm^{-1}	Medium	OH In-plane Bending	[150]
1165 cm^{-1}	Strong	Antisymmetric Bridge COC Stretching	[150]
1111 cm^{-1}	Strong	Antisymmetric In-phase Ring Stretching	[150]
1063 cm^{-1}	Strong	Skeletal Vibrations Involving C-O Stretching	[150]
1035 cm^{-1}	Strong	Skeletal Vibrations Involving C-O Stretching	[149, 150]
895 cm^{-1}	Weak	Antisymmetric Out-of-phase ring stretching	[150]
750 cm^{-1}	Medium	OH Stretching (characteristic of hydroxyl bonding in cellulose structure due to I_α crystalline phase)	[148, 149]
663 cm^{-1}	Medium	OH Out-of-plane Bending	[150]

The FTIR spectra of the AE-BC, DMAE-BC, and TMAHP-BC composites are given in Figure 5.5, 5.6 and 5.7, respectively. FTIR absorption band represent the energy absorbed by the vibration of specific functional groups on the chemically modified BC structure. Based on the chemical structure of surface functionalized cellulose, these chemically modified BC composites should have specific amine functional groups (Figure 5.1). The characteristic FTIR bands of the functional groups containing amines are presented in Table 5.4. The FTIR spectra of the CM-BC composites are given in Figure 5.8. The characteristic FTIR bands of the functional groups containing carboxylation are presented in Table 5.5.

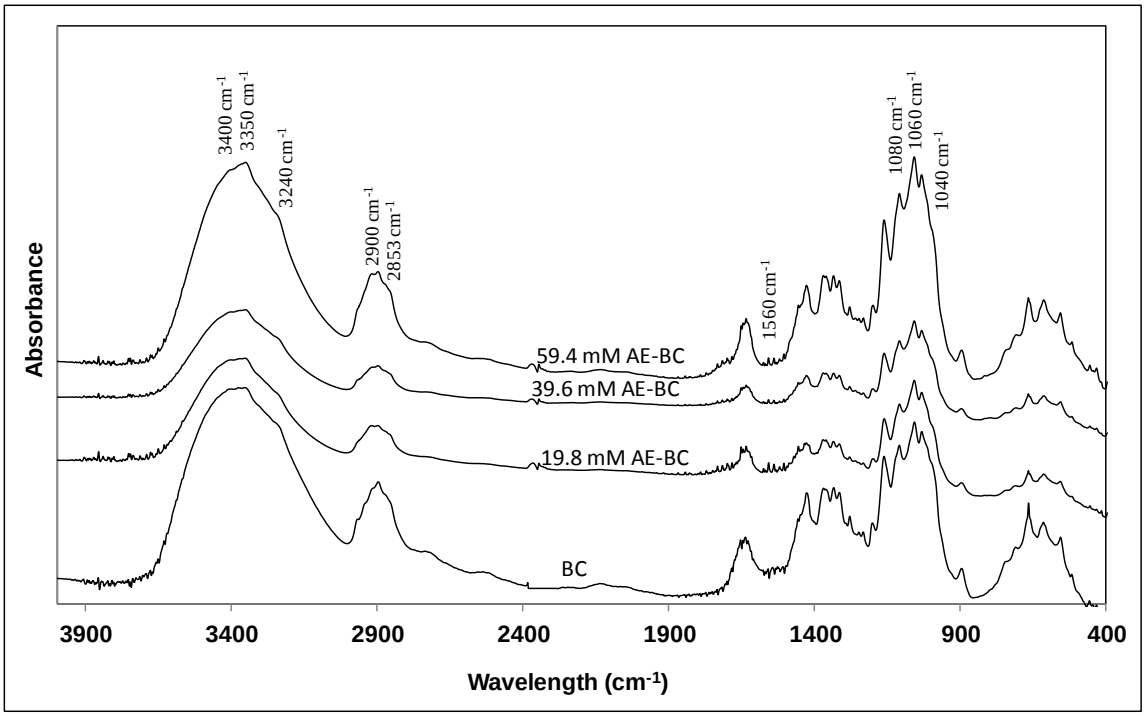

Figure 5.5: FTIR spectra of 19.8, 39.6, and 59.4 mM AE-BC.

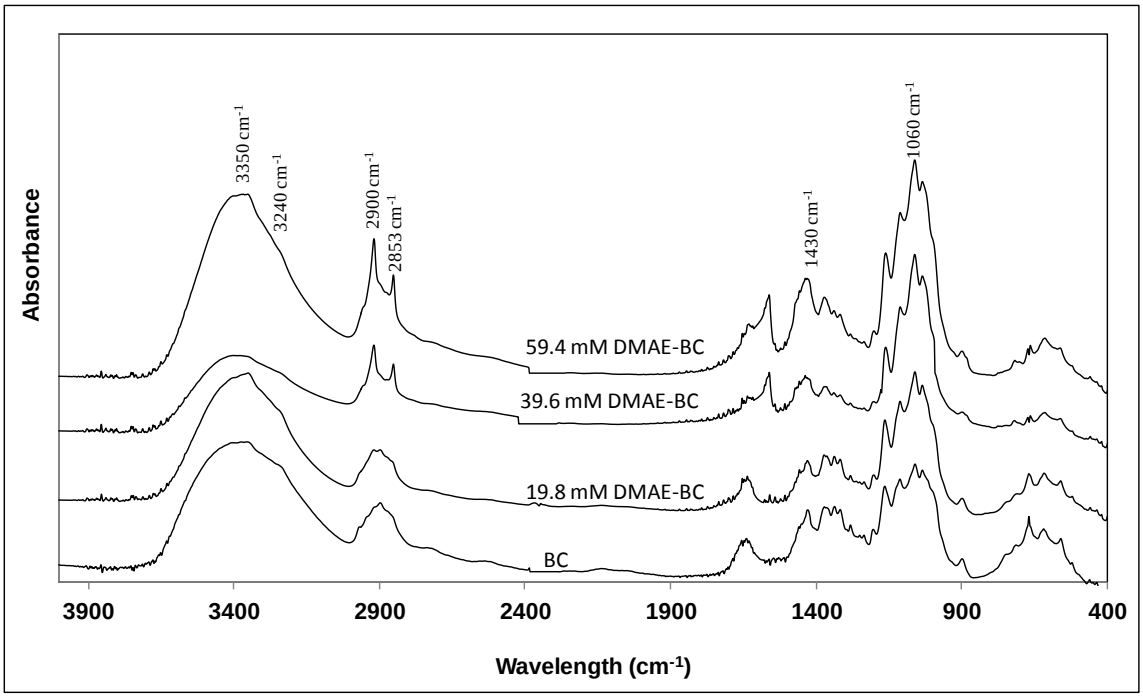

Figure 5.6: FTIR spectra of 19.8, 39.6, and 59.4 mM DMAE-BC.

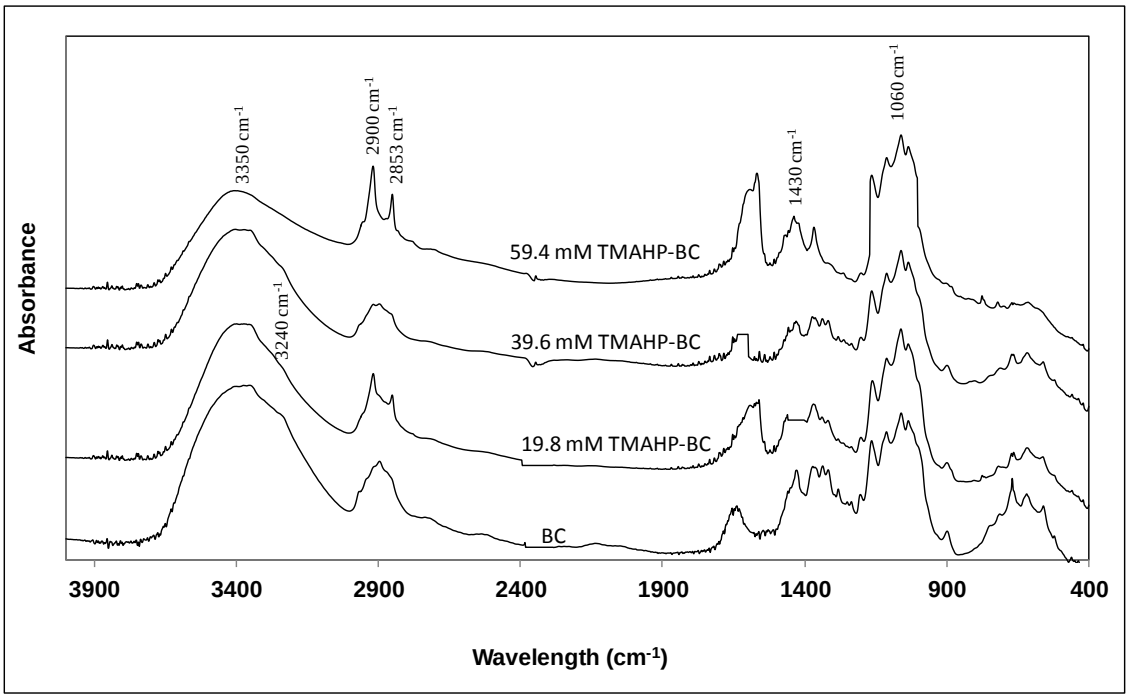

Figure 5.7: FTIR spectra of 19.8, 39.6, and 59.4 mM TMAHP-BC.

Table 5.4: Characteristic FTIR bands of functional groups containing amines.

Frequency	Relative Intensity	Assignment	Ref.
3400 cm^{-1}	Broad	NH Stretching of Primary Amines (Overlaps with OH Stretching)	[151]
3350 cm^{-1}	Strong	OH Stretching (associated with intramolecular hydrogen bonding)	[148]
3240 cm^{-1}	Medium	OH Stretching (characteristic of hydroxyl bonding in cellulose structure due to I_α crystalline phase)	[148, 149]
2900 cm^{-1}	Medium	CH Stretching	[150]
2853 cm^{-1}	Medium	CH_2 Symmetric Stretching	[150]
1650 cm^{-1}	Medium	NH Bending Vibration in Primary Amines	[151]
1560 cm^{-1}	Medium	NH_2 Bending Vibration	[151]
1430 cm^{-1}	Medium	Bending Vibration of CH_3 Group Attached to Nitrogen Atom	[151]
1080 cm^{-1}	Medium	CN Stretching of Primary α-carbon atom in Primary Amines	[151]
1060 cm^{-1}	Medium	CN Stretching in Alkyl Amines	[151]
1040 cm^{-1}	Medium	CN Stretching of Secondary α-carbon in Primary Amines	[151]

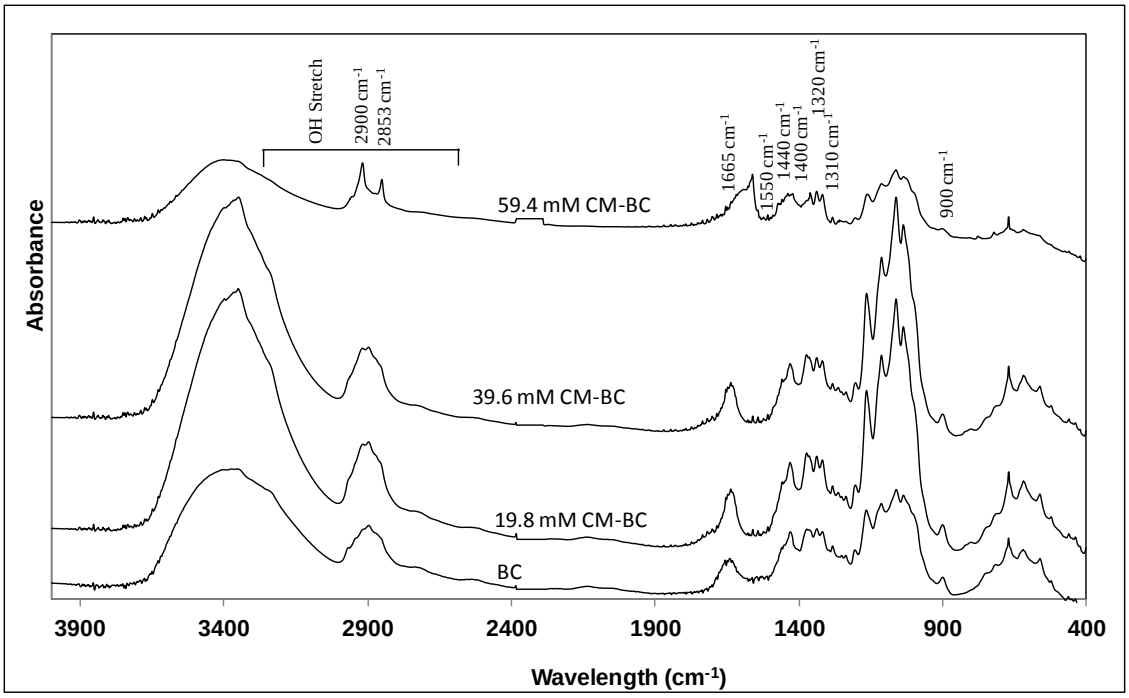

Figure 5.8: FTIR spectra of 19.8, 39.6, and 59.4 mM CM-BC.

Table 5.5: Characteristic FTIR bands of functional groups containing carboxyl groups.

Frequency	Relative Intensity	Assignment	Ref.
3300 - 2500 cm^{-1}	Broad	OH Stretching of COO^- (Overlaps with CH Stretching)	[148]
2900 cm^{-1}	Medium	CH Stretching	[149]
1700 cm^{-1}	Strong	C=O Stretching	[151]
1550 cm^{-1}	Strong	Symmetrical and Anti-symmetrical vibrations of COO^-	[151]
1440 cm^{-1}	Weak	CO Stretching Vibrations or OH In-plane Bending Vibrations	[151]
1400 cm^{-1}	Strong	Symmetrical and Anti-symmetrical vibrations of COO^-	[151]
1320 cm^{-1}	Strong	CO Stretching	[151]
1310 cm^{-1}	Strong	CO Stretching Vibrations or OH In-plane Bending Vibrations	[151]
900 cm^{-1}	Medium	OH Out-of-plane Bending	[151]

The absorbances of the amine peaks were graphed against the concentration of BCs with surface amination (Figure 5.9.A-5.9.C). The absorbances of the carboxyl peaks were also graphed against the concentration of the surface functionalized CM-BC composites (Figure 5.9.D). The absorbances were normalized by dividing the amine or carboxyl peak absorbance by the CH cellulose peak absorbance at 2900 cm^{-1}. This CH peak was used because its absorbance is constant in all the samples given that the amount of cellulose in the composites is constant. The increase in absorbance correlates to the increased of concentration of amine groups (Figure 5.9) or carboxyl groups (Figure 5.10) as governed by the Beer-Lambert Law [158]. Even though the intensity of the amine absorption peaks increase with the concentration of amine, the absorbance of the amine peaks demonstrate some scattering (Figure 5.9). The variation present in samples that have demonstrated scattering may be attributed to minor differences in the amount of material in the KBr pellets.

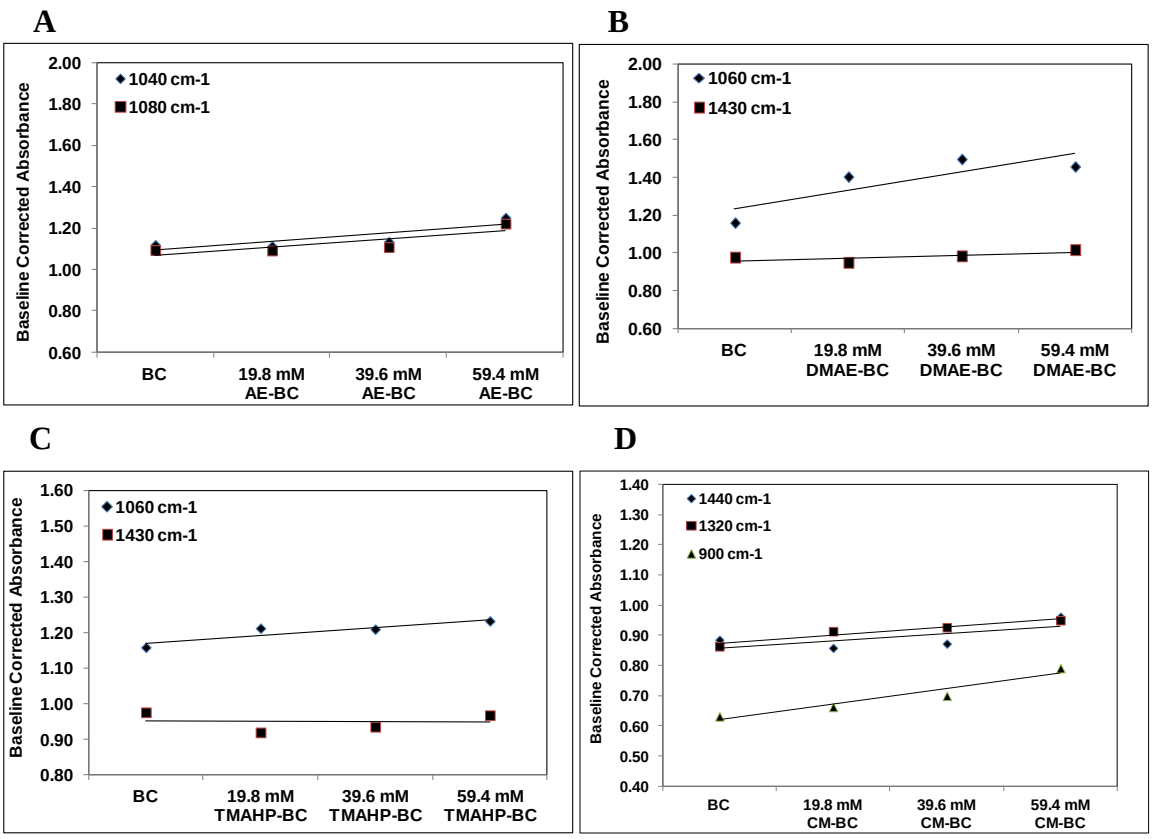

Figure 5.9: Graph of amine peak absorbance versus concentration of BCs with surface amination (A, B, C). Graph of carboxylic peak absorbance versus concentration of surface functionalized CM-BCs (D).

The FTIR spectra of porous BC (control) and a representative set of porous functional composites are illustrated in Figure 5.10. The chemical spectra of the porous functional composites were comparable to their corresponding nano-porous functional sample composites (Figure 5.5-5.8). This data indicates that compared to the corresponding nano-porous functional sample composites (Figure 5.5- 5.8), porosity did not change the chemical structure of the porous functional composites.

The FTIR spectra of OBC (control), porous OBC (control) and a representative set of oxidized functional composites (39.6 mM TMAHP OBC and

39.6 mM TMAHP porous OBC) are illustrated in Figure 5.11. The spectra of the oxidized BC and porous oxidized BC have an absorption band at 1740 cm^{-1} that represents the stretching vibration in the aldehyde carbonyl group formed on the cellulose during periodate oxidation (Figure 5.11). The 39.6 mM TMAHP OBC and the 39.6 mM TMAHP porous OBC spectra also have this absorption band (Figure 5.11) confirming that periodate oxidation converted these scaffolds into dialdehyde cellulose. Oxidized BC and porous oxidized BC have an absorption band at 1650 cm^{-1} which corresponds to the carbonyl groups associated with hydrogen bonding (Figure 5.11). This absorption peak is present in the spectra of 39.6 mM TMAHP OBC and 39.6 mM TMAHP porous OBC (Figure 5.11), proving that periodate oxidation can transform 39.6 mM TMAHP BC and 39.6 mM TMAHP porous BC scaffolds into dialdehyde cellulose scaffolds. The absorption peaks identified at 1740 and 1650 cm^{-1} in Figure 5.11 are broad. The broad peak at 1740 cm^{-1} in these spectra (Figure 5.11) is attributed to the strong hydrogen bonding in the aldehyde carbonyl group which results in the broadening of the peak [151]. The broad peak at 1650 cm^{-1} in these spectra (Figure 5.11) is attributed to the considerable overlap with the absorption of water at 1653 cm^{-1} [151].

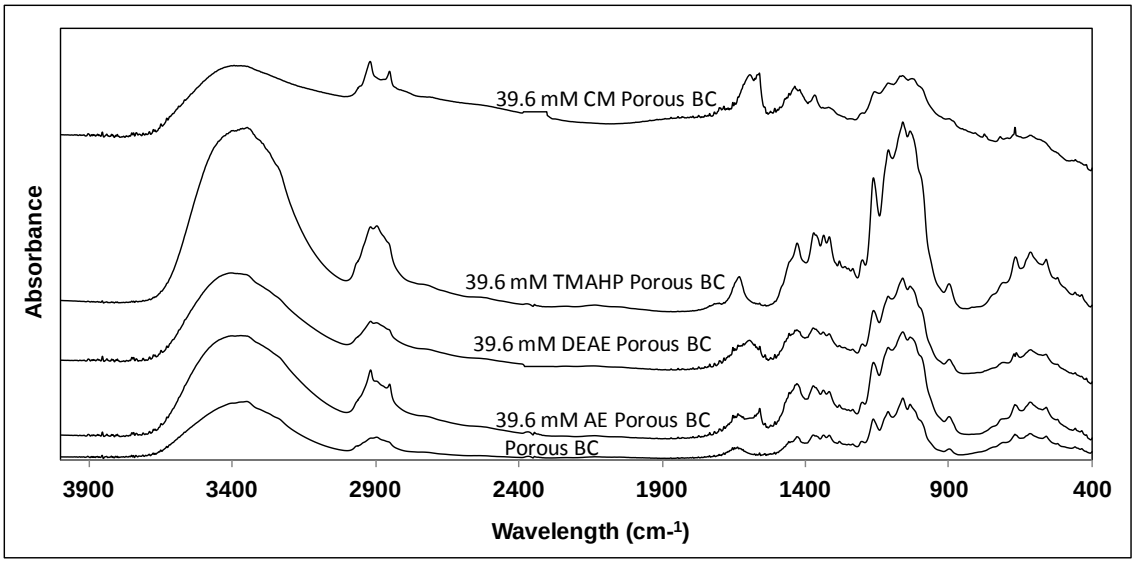

Figure 5.10: FTIR spectra of porous BC and porous surface functionalized BCs.

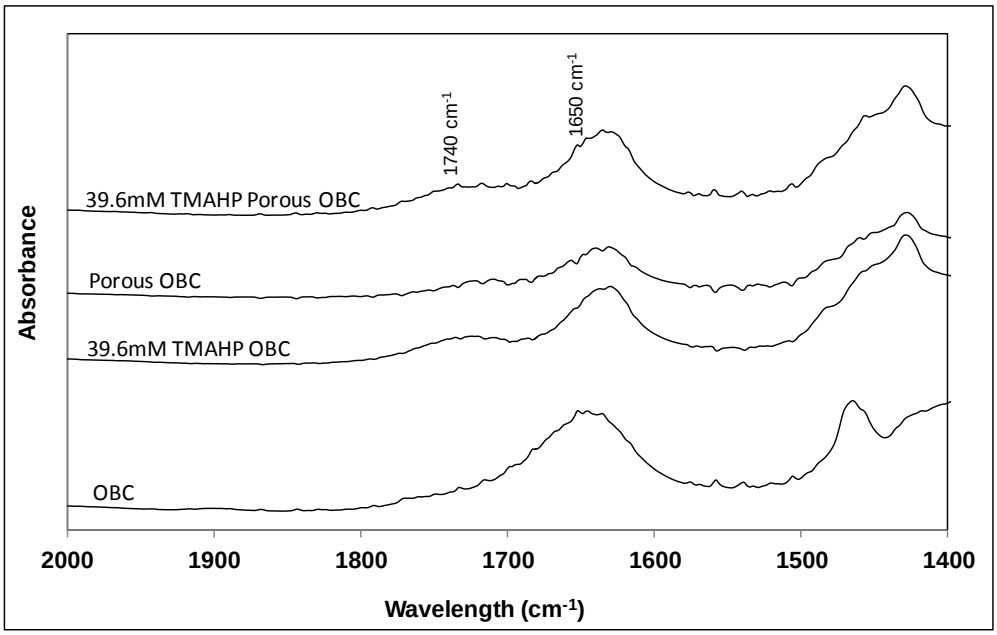

Figure 5.11: FTIR spectra of OBC, 39.6 mM TMAHP OBC, porous OBC and 39.6 mM TMAHP Porous OBC.

5.3. Scanning Electron Microscopy

SEM images of surface functionalized BC composites (Figure 5.12), surface functionalized porous BCs composites (Figure 5.13), and their corresponding controls (native BC, OBC, porous BC, and porous OBC) are shown. SEM images demonstrate that compared to native BC (Figure 5.12.A), amination and carboxylation of the BC scaffolds did not affect the nano-fibrous and nano-porous structures of the sub-micron BC scaffolds (Figure 5.12.B-E). SEM images also confirm that compared to the non-functionalized scaffolds (Figure 5.13.A, C, E, G), amination (Figure 5.13.B, F), and amination and oxidation of the BC scaffolds (Figure 5.13.D, H) did not affect the morphology of the BC structure. No morphological changes were observed between the chemically functionalized BC scaffolds and the non-functionalized BC scaffolds.

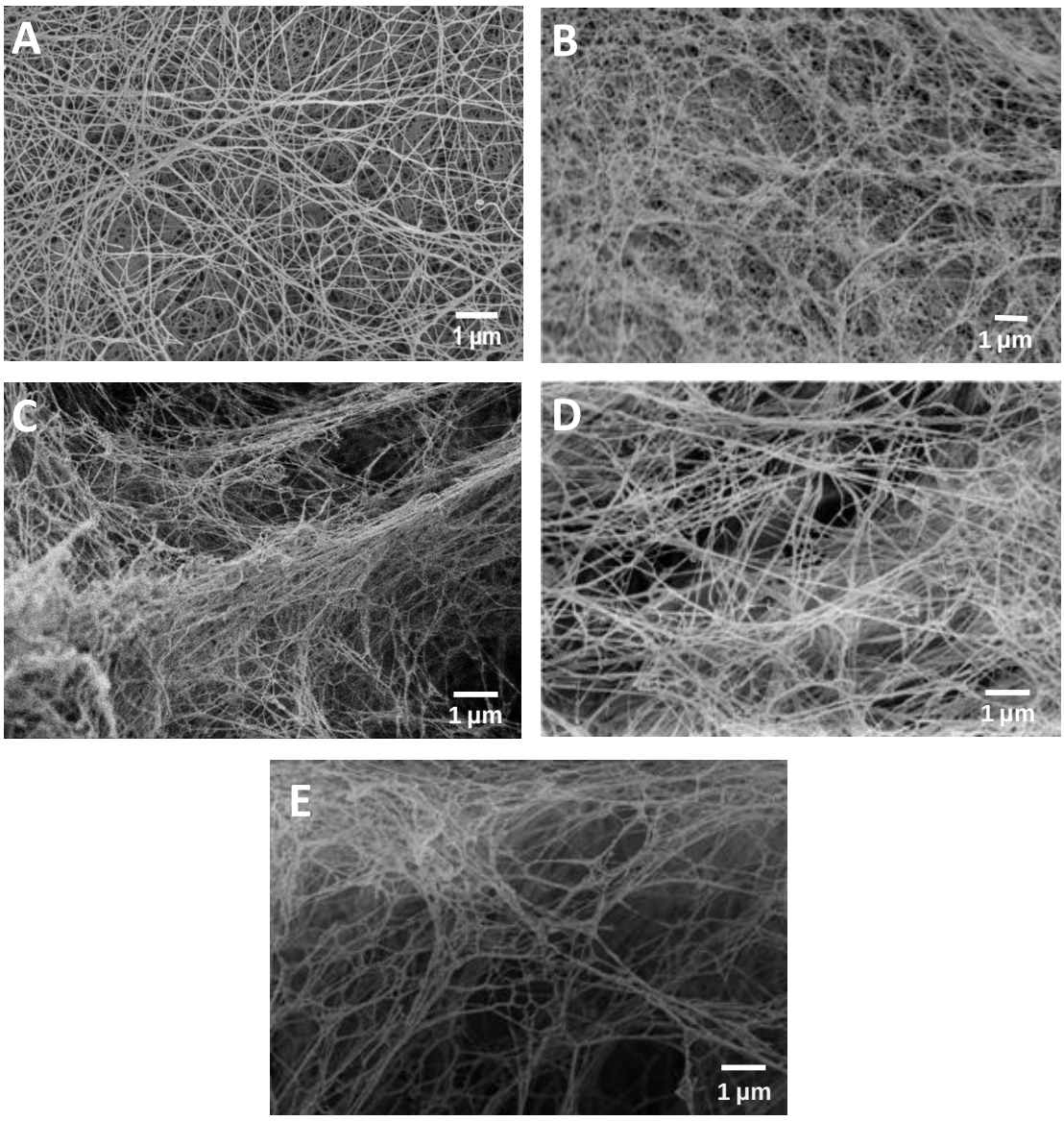

Figure 5.12: SEM images of native BC (A), 39.6 mM AE-BC (B), 39.6 mM DMAE-BC (C), 39.6 mM TMAHP-BC (D), and 39.6 mM CM-BC (E) at 20000X. Accelerating voltages of 5 kV (A, D), 2 kV (C) and 2.5 kV (E) were used to image the samples. Scale bar = 1 µm.

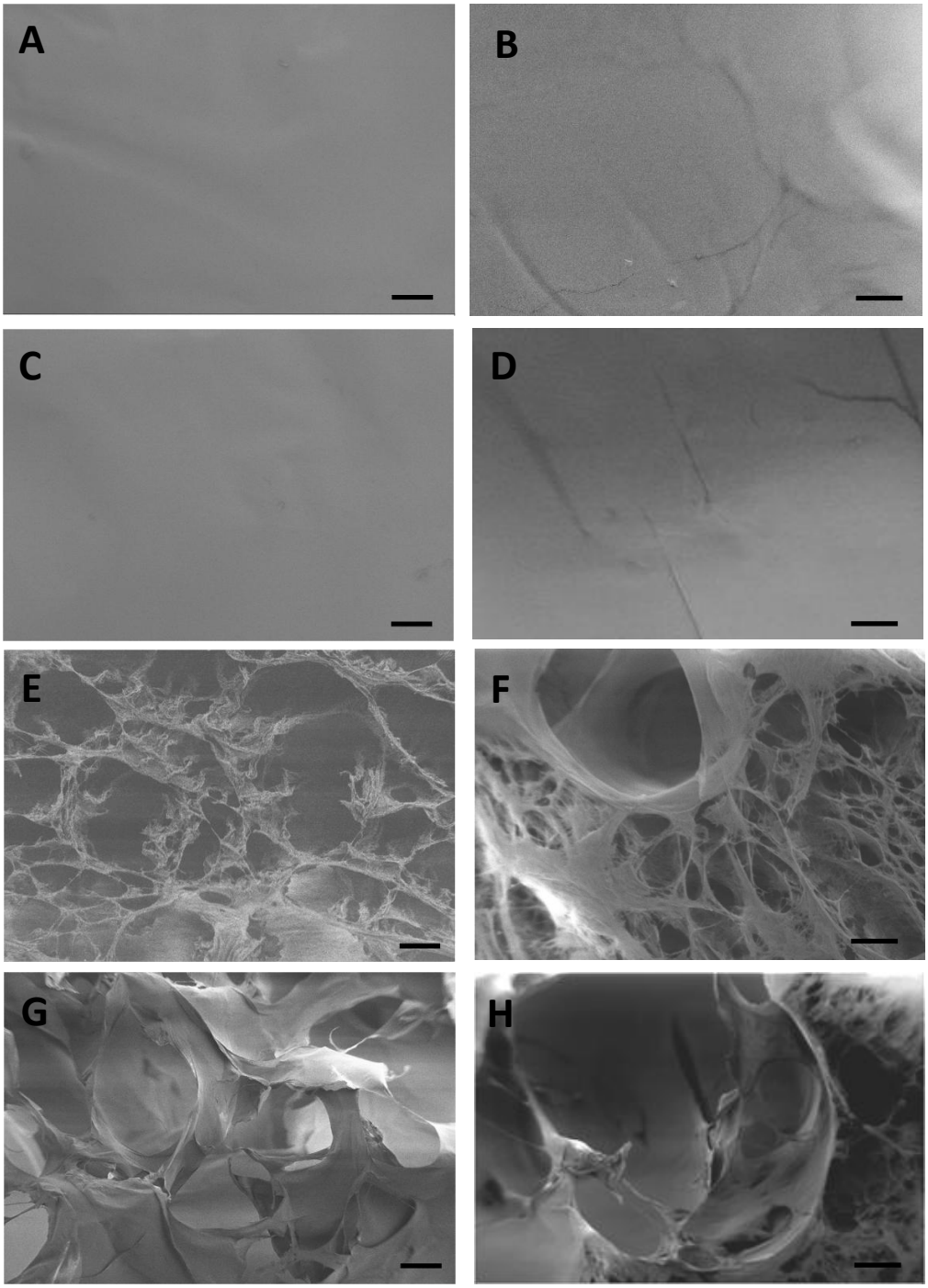

Figure 5.13: SEM images of native BC (A), 39.6 mM TMAHP-BC (B), OBC (C), 39.6 mM TMAHP OBC (D), porous BC (E), 39.6 mM TMAHP porous BC (F), porous OBC (G), and 39.6 mM TMAHP porous OBC (H) at 300X. Accelerating voltages of 1.5 kV (A, C, E, G, H), 2 kV (B, D), and 10 kV (F) were used to image the samples. Scale bar = 100 μm.

5.4. Mechanical Testing

The mechanical properties of representative surface functionalized BC composites, surface functionalized porous BCs composites, and their corresponding controls (native BC, OBC, porous BC, and porous OBC) were determined at 5% strain rate to assess the relationship between the non-functionalized and functionalized BCs. The engineering stress-strain curves of the hydrated never-dried BC samples are illustrated in Figure 5.14. The ultimate tensile strength, strain at break, and elastic modulus values of the native and modified BC samples calculated from the engineering stress-strain curves are illustrated in Figure 5.15.

The results show that the chemical modification significantly decreased the ultimate tensile strength and elastic modulus of the 39.6 mM TMAHP porous OBC compared to porous oxidized BC (Figure 5.15). Similar changes in mechanical properties were observed with the 39.6 mM TMAHP porous BC compared to porous BC results (Figure 5.15). The elastic modulus of the 39.6 mM TMAHP OBC significantly decreased compared to OBC (Figure 5.15). All the functionalized scaffolds demonstrated a significant increase in their strain at break (%) compared to their corresponding non-functionalized BC scaffolds (Figure 5.15). The chemical reactions performed to functionalize the surface structures of the BC scaffolds may have altered inter- and intramolecular hydrogen bonding in the cellulose structure, resulting in the impairment of scaffold's mechanical properties.

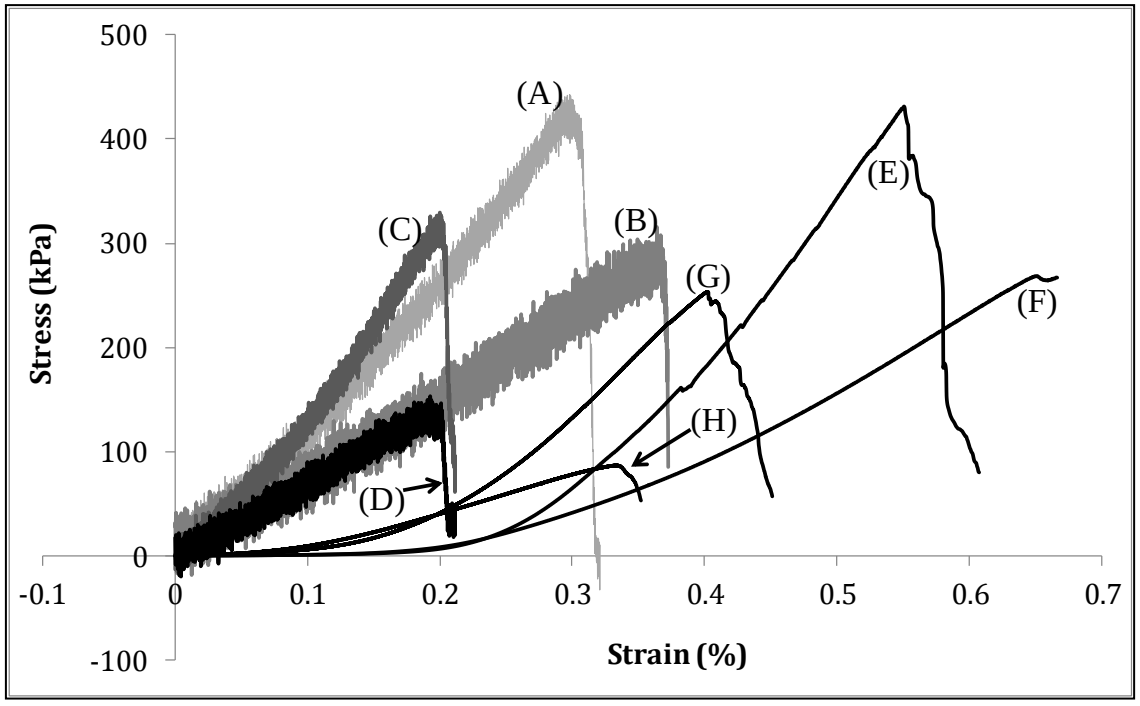

Figure 5.14: Engineering stress-strain curve of native BC (A), oxidized BC (B), porous BC (C), porous oxidized BC (D), 39.6 mM TMAHP-BC (E), 39.6 mM TMAHP OBC (F), 39.6 mM TMAHP porous BC (G), and 39.6 mM TMAHP porous OBC (H).

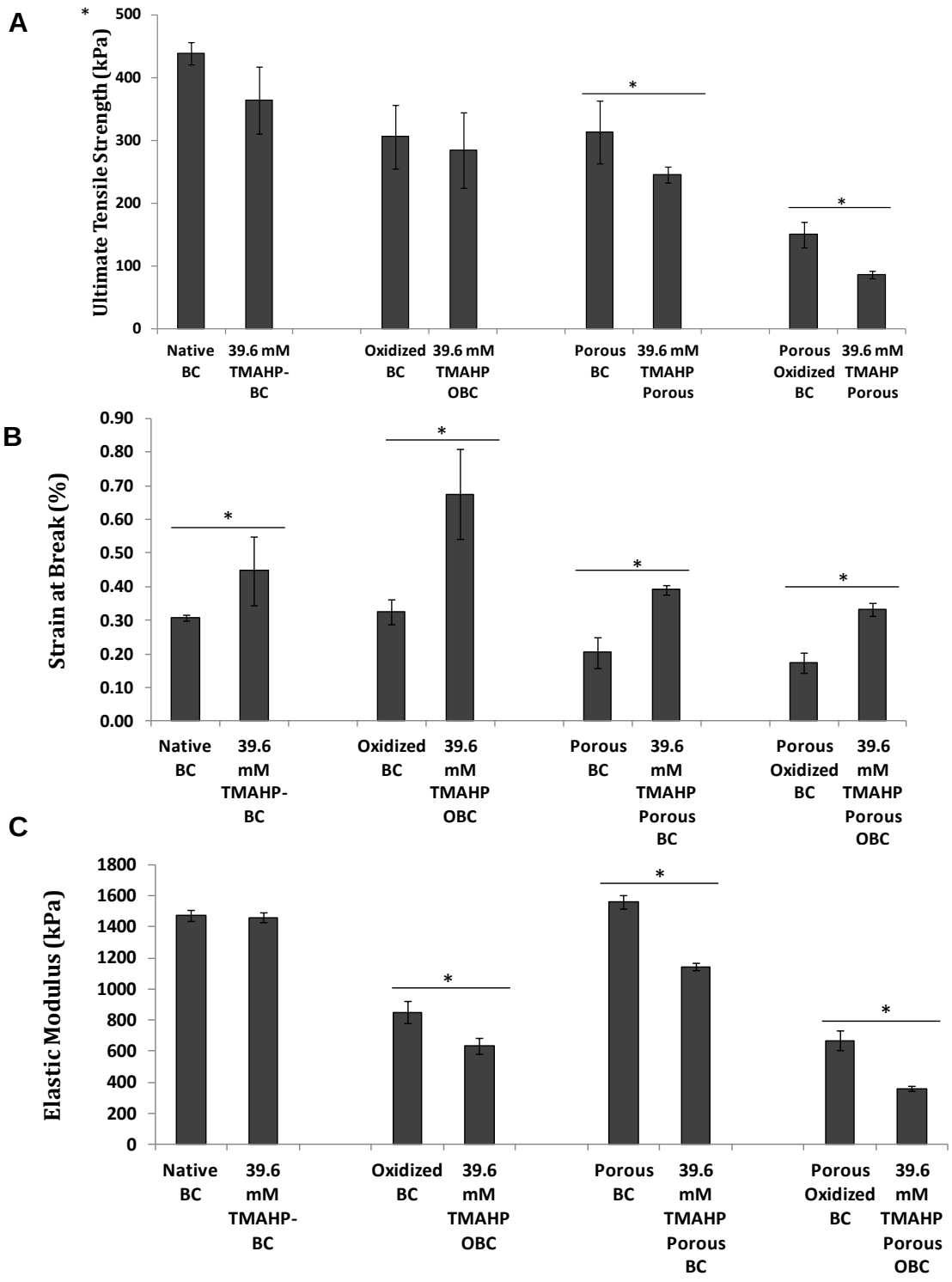

Figure 5.15: Comparison of ultimate tensile strengths (A), strain at breaks (B), and elastic moduli of native BC, oxidized BC, porous BC, porous oxidized BC, and TMAHP-BC and its composites. Asterisks (*) indicates significant differences at $p<0.05$.

5.5. Characterization of Cell and Bacterial Cellulose Scaffolds

5.5.1. Cellular Adhesion, Viability and Proliferation Assays

MTS assay analysis was performed to determine the viability of EqMSCs seeded on the chemically functionalized BC scaffolds. Cell staining using calcein-AM and PI was also performed to visually assess the EqMSCs attachment under the same conditions. The MTS assay results of EqMSCs seeded on functionalized non-porous BC are shown in Figure 5.16. Calcein-AM and PI staining results of the EqMSCs seeded on these functionalized non-porous BC scaffolds are illustrated in Figure 5.17-5.20. From 2 to 14 days in culture, the cells seeded on the four different forms of functionalized non-porous scaffolds (AE-BC, DMAE-BC, TMAHP-BC and CM-BC), appear to have demonstrated high proliferation rates as a function time and represent a high viability and proliferation (Figure 5.16, 5.17-5.20).

Figure 5.16: Cellular viability assay: MTS test. Comparison of proliferation of cells as determined by MTS assay for EqMSCs (1.26×10^5) seeded on AE-BC (A), DMAE-BC (B), TMAHP-BC (C), and CM-BC (D) scaffolds functionalized at various concentrations for 2, 7 and 14 days. Asterisks (*) indicates significant differences at $p<0.05$.

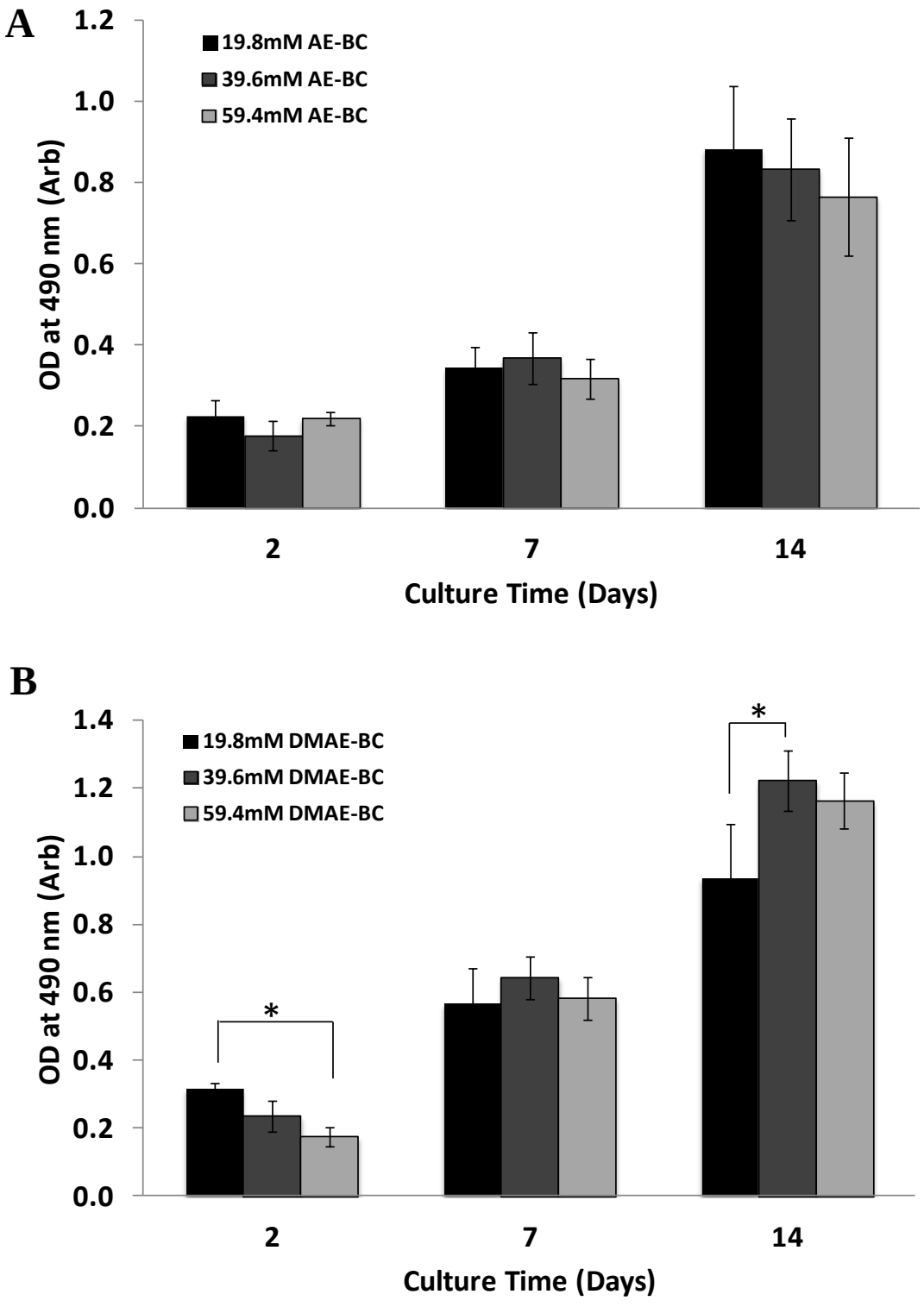

Figure 5.16: Continued.

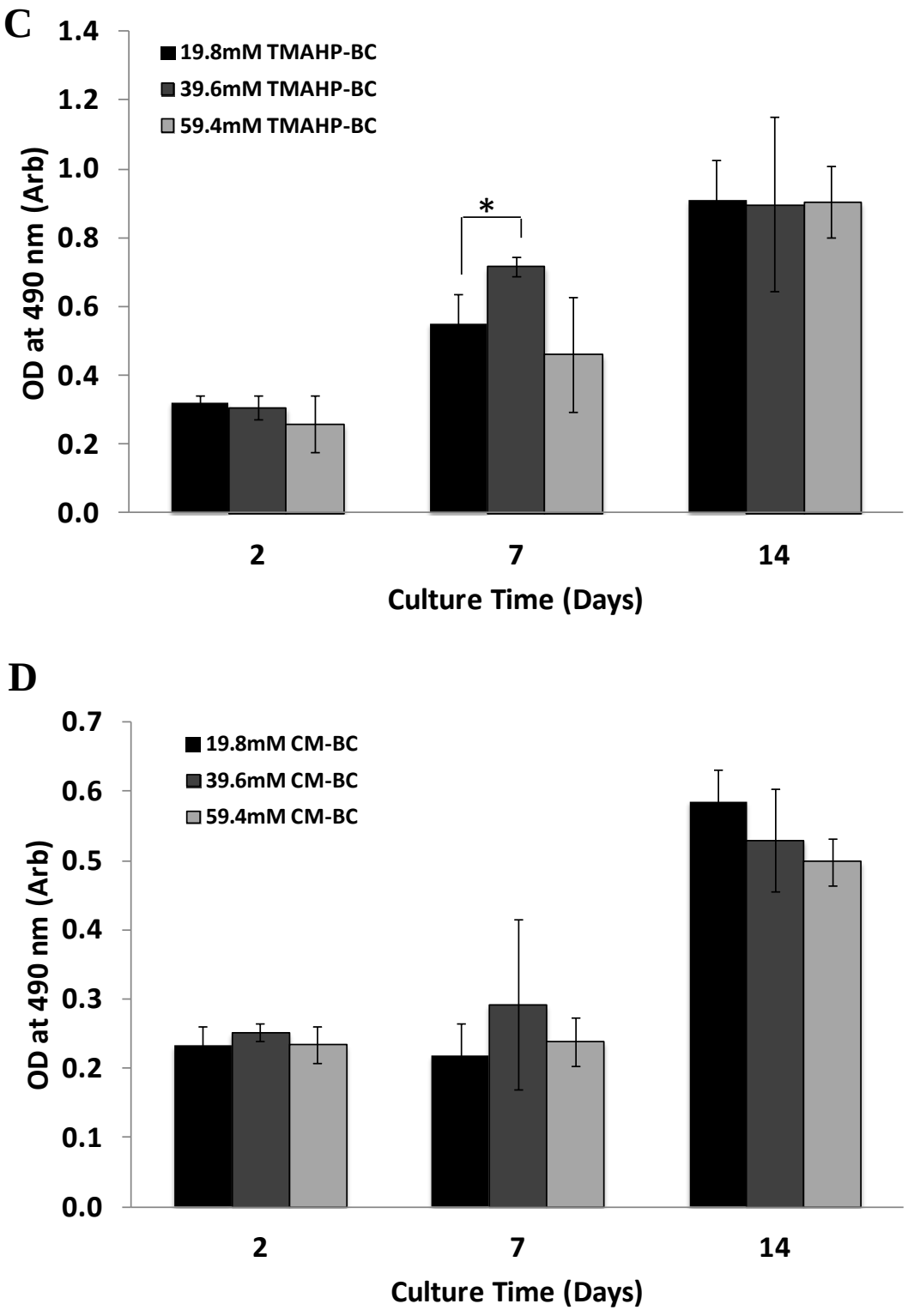

Figure 5.16: Continued.

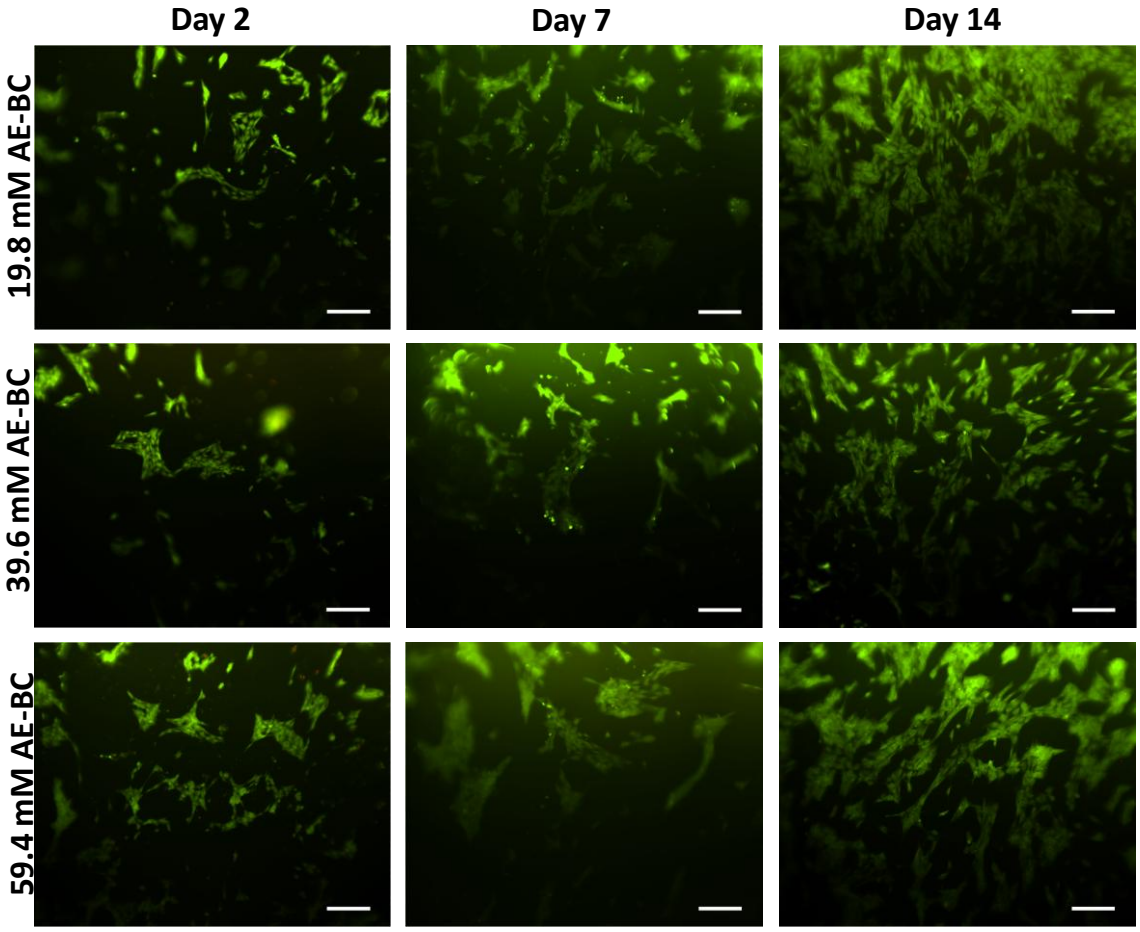

Figure 5.17: Cellular adhesion and cell viability stained with calcein-AM and PI using fluorescent microscopy. Cell viability of EqMSCs (1.26×10^5 cells/cm^2) seeded for 2, 7, and 14 days on the AE-BC functionalized scaffolds. Cell viability of EqMSCs were analyzed by calcein-AM which exhibits green fluorescence and demonstrates live cells and PI which displays red fluorescence and demonstrates dead cells. Scale bar = 100 µm.

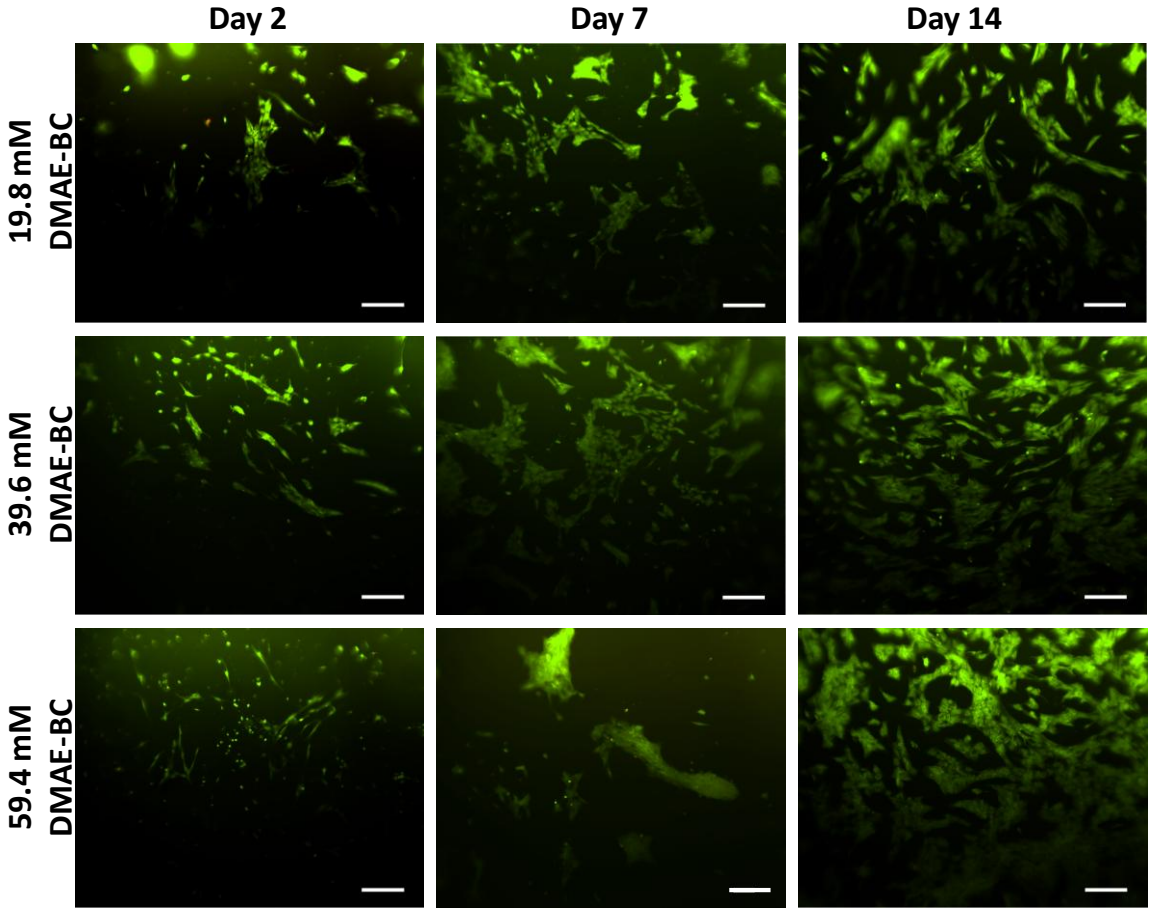

Figure 5.18: Cellular adhesion and cell viability stained with calcein-AM and PI using fluorescent microscopy. Cell viability of EqMSCs (1.26×10^5 cells/cm^2) seeded for 2, 7, and 14 days on the DMAE-BC functionalized scaffolds. Scale bar = 100 µm.

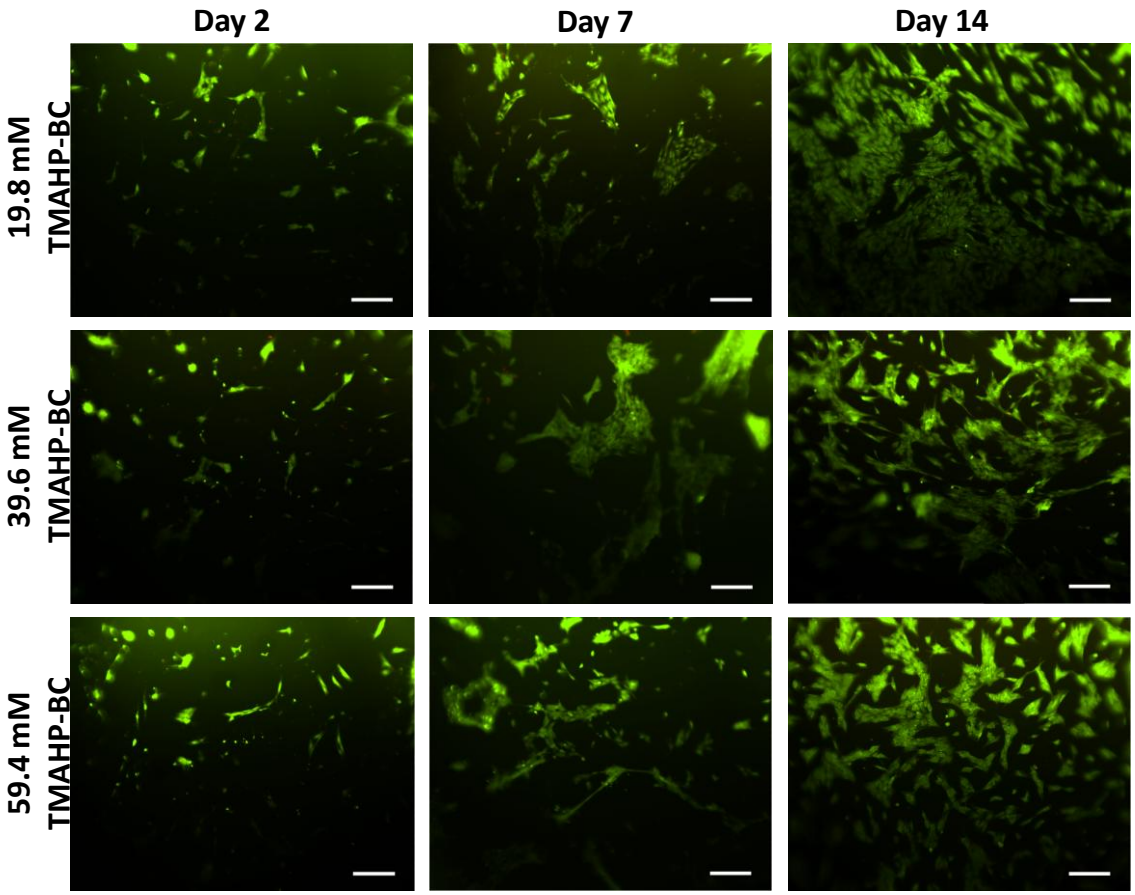

Figure 5.19: Cellular adhesion and cell viability stained with calcein-AM and PI using fluorescent microscopy. Cell viability of EqMSCs (1.26×10^5 cells/cm^2) seeded for 2, 7, and 14 days on the TMAHP-BC functionalized scaffold. Scale bar = 100 μm.

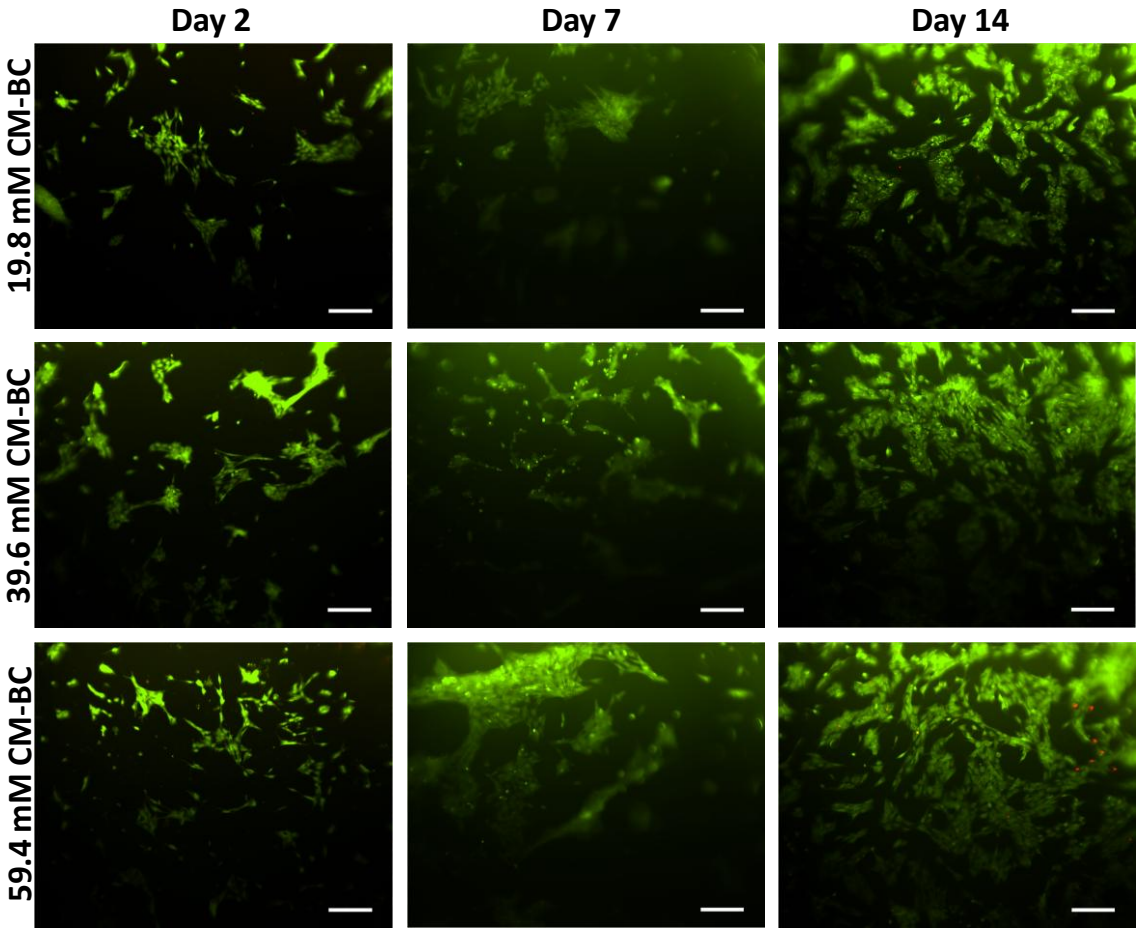

Figure 5.20: Cellular adhesion and cell viability stained with calcein-AM and PI using fluorescent microscopy. Cell viability of EqMSCs (1.26 x 10^5 cells/cm^2) seeded for 2, 7, and 14 days on the CM-BC functionalized scaffold. Scale bar = 100 µm.

The EqMSCs response on the surface functionalized non-porous BC scaffolds show that that cell proliferation and attachment between the chemically modified scaffolds were primarily comparable (Figure 5.16-5.20). A previous study performed by Watanabe et al. (1993) reported that cell proliferation of genetically engineered Chinese hamster ovary cells were significantly greater on 39.6 mM TMAHP-BC compared to DMAE-BC, AE-BC, CM-BC, and native BC [97]. Following the findings from Watanabe et al. (1993) [97], porous BC scaffolds were functionalized at a concentration of 39.6 mM for cell proliferation and attachment studies.

MTS assay analysis was performed to determine the viability of EqMSCs seeded on the chemically functionalized porous BC scaffolds. Cell staining using calcein-AM and PI was also performed to visually assess the EqMSCs attachment under the same conditions. The MTS assay results of EqMSCs seeded on functionalized porous BC are shown in Figure 5.21. Calcein-AM and PI staining results of the EqMSCs seeded on these functionalized porous BC scaffolds are illustrated in Figure 5.22.

From 2 to 7 days in culture, the cells seeded on the four different forms of functionalized porous scaffolds (AE-BC, DMAE-BC, TMAHP-BC and CM-BC), appear to have demonstrated high growth rates as a function time and represent a high viability and proliferation composition (Figure 5.21). However, after 7 days in culture, the morphology of the cells on the functional porous scaffolds was different (Figure 5.21.B). EqMSCs appeared to have a greater number of cells with the pronounced spread-out morphology on the 39.6 mM TMAHP porous BC scaffold. Due to the optimal cell morphology observed on the 39.6 mM TMAHP porous BC scaffold, 39.6 mM TMAHP BC and 39.6 mM TMAHP porous BCs were selected for oxidation and further cell culture assessment, to determine the optimum surface functionality for the biomimetic cartilage tissue engineering scaffold.

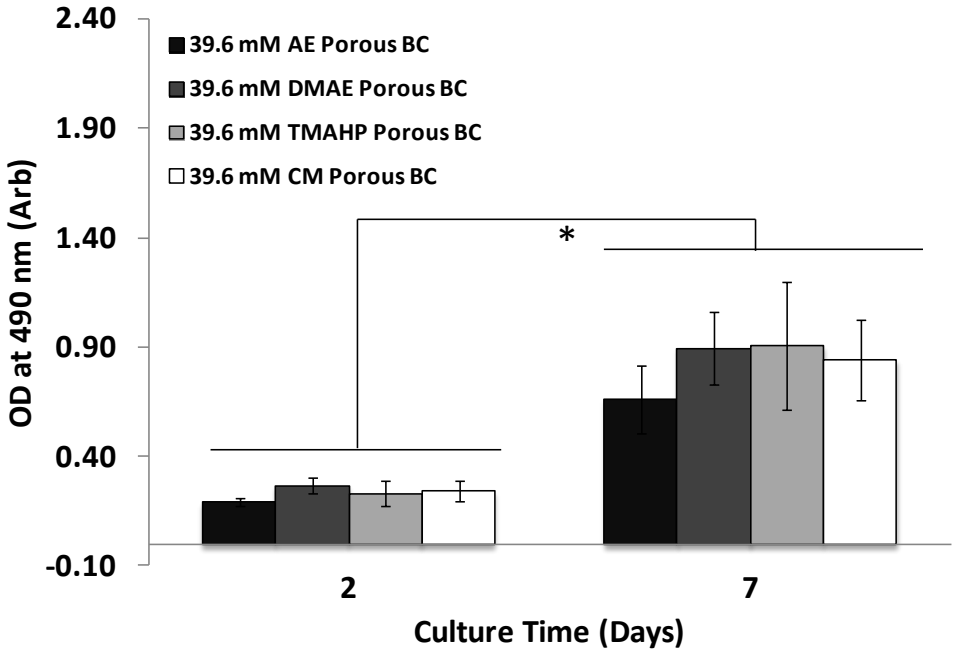

Figure 5.21: Cellular viability assay: MTS test. Comparison of proliferation of cells as determined by MTS assay for EqMSCs (1.26×10^5) seeded on 39.6 mM AE porous BC, 39.6 mM DMAE porous BC, 39.6 mM TMAHP porous BC, and 39.6 mM porous CM-BC scaffolds for 2 and 7 days. Asterisks (*) indicates significant differences at $p<0.05$.

Figure 5.22: Cellular viability assay: MTS test. Comparison of proliferation of cells as determined by MTS assay for EqMSCs (1.26×10^5) seeded on 39.6 mM AE porous BC, 39.6 mM DMAE porous BC, 39.6 mM TMAHP porous BC, and 39.6 mM CM porous BC scaffolds for 2 (A) and 7 (B) days. Scale bar = 100 μm.

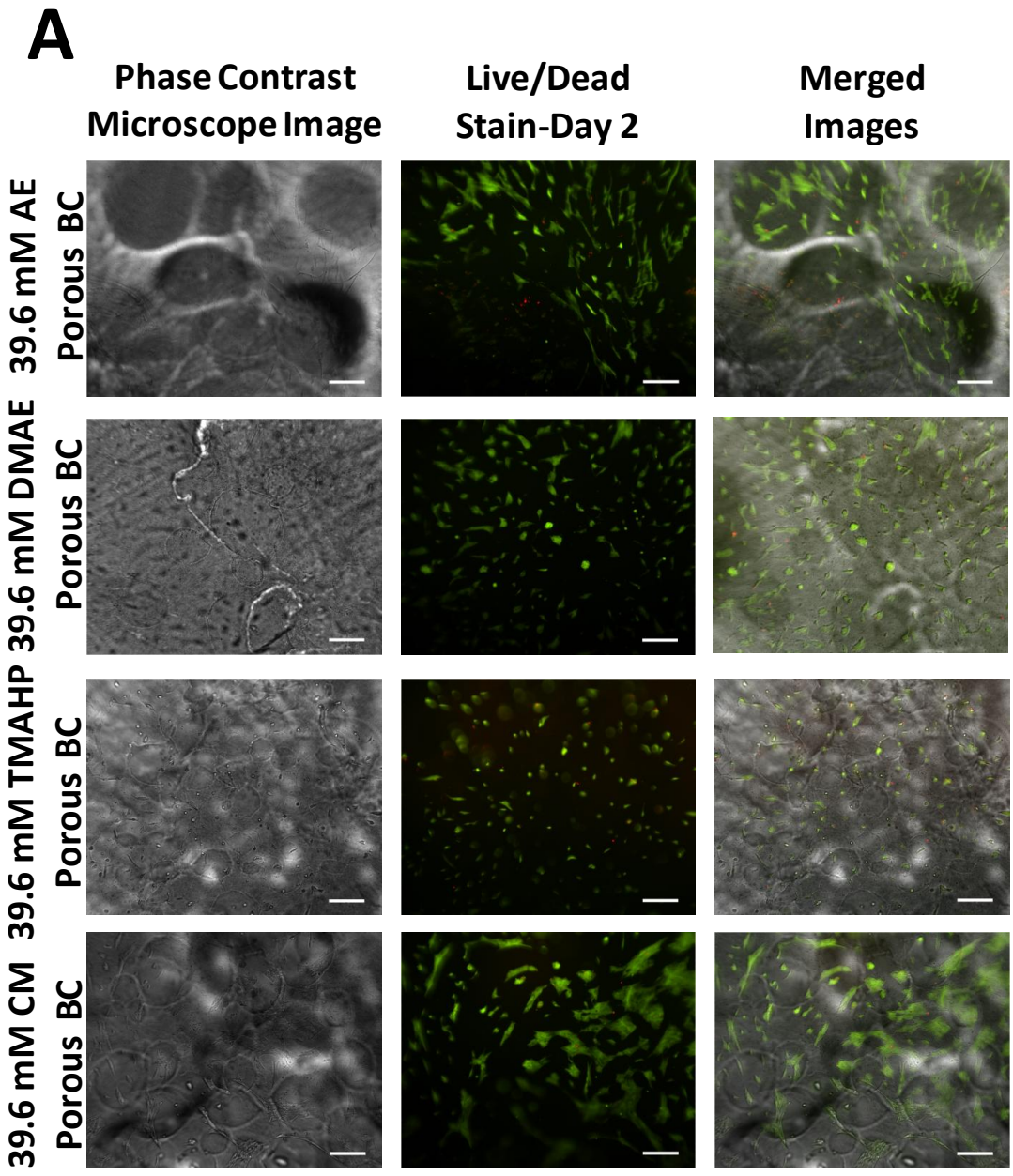

Figure 5.22: Continued.

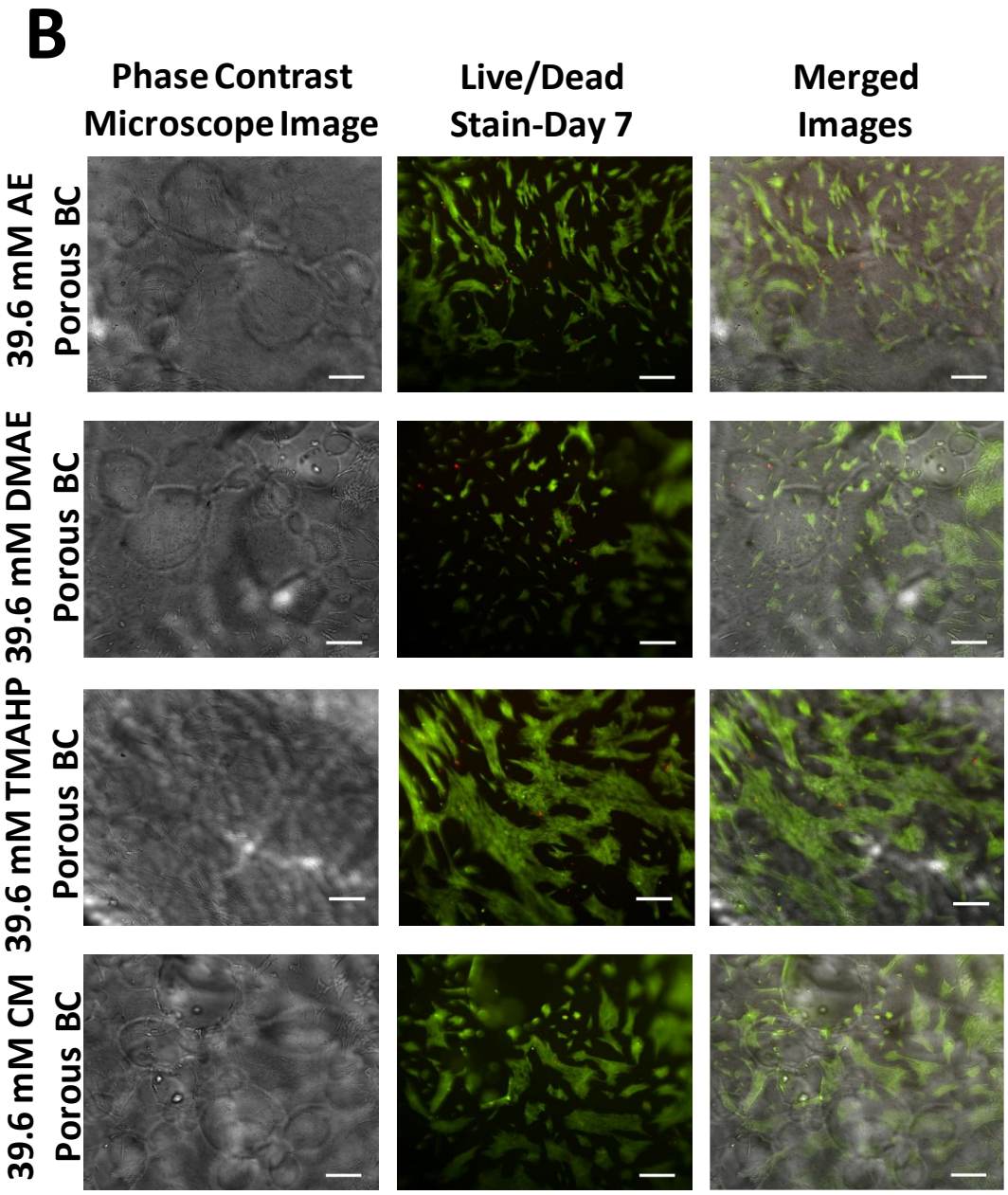

Figure 5.22: Continued.

MTS assay analysis was performed to determine the viability of EqMSCs seeded on 39.6 mM TMAHP OBC and 39.6 mM TMAHP porous OBCs scaffolds. Cell staining using calcein-AM and PI was also performed to visually assess the EqMSCs attachment on these scaffolds. The MTS assay results of EqMSCs seeded on functionalized porous OBC are shown in Figure 5.23. Calcein-AM and PI staining results of the EqMSCs seeded on these functionalized porous OBC scaffolds are illustrated in Figure 5.24.

From 2 to 7 days in culture, the cells seeded on the 39.6 mM TMAHP OBC and 39.6 mM TMAHP porous OBCs scaffolds, appear to have demonstrated high viability and proliferation rates as a function time (Figure 5.23). After 7 days in culture, the EqMSCs appeared to have proliferated overtime and have demonstrated the pronounced spread-out morphology on both forms of scaffold composites (Figure 5.24).

.

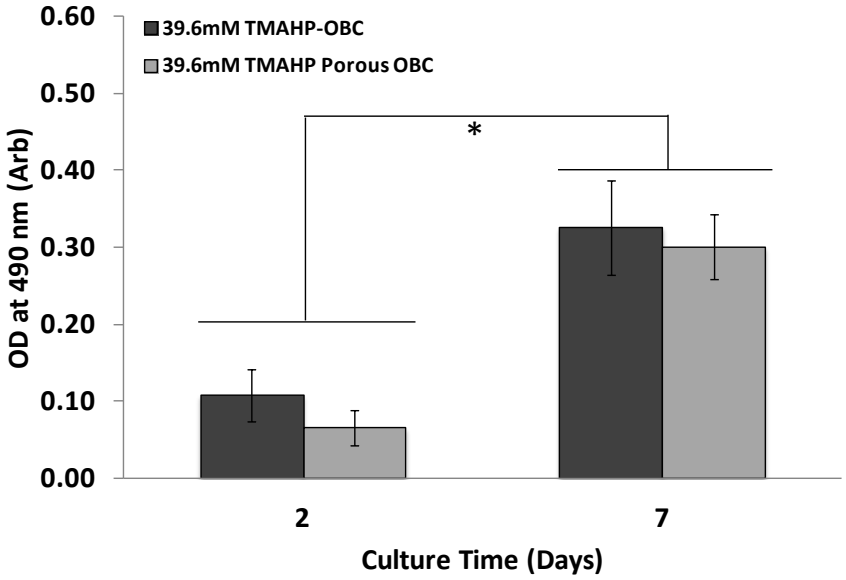

Figure 5.23: Cellular viability assay: MTS test. Comparison of proliferation of cells as determined by MTS assay for EqMSCs (1.26×10^5) seeded on 39.6 mM TMAHP OBC and 39.6 mM TMAHP porous OBC scaffolds for 2 and 7 days. Asterisks (*) indicates significant differences at $p<0.05$.

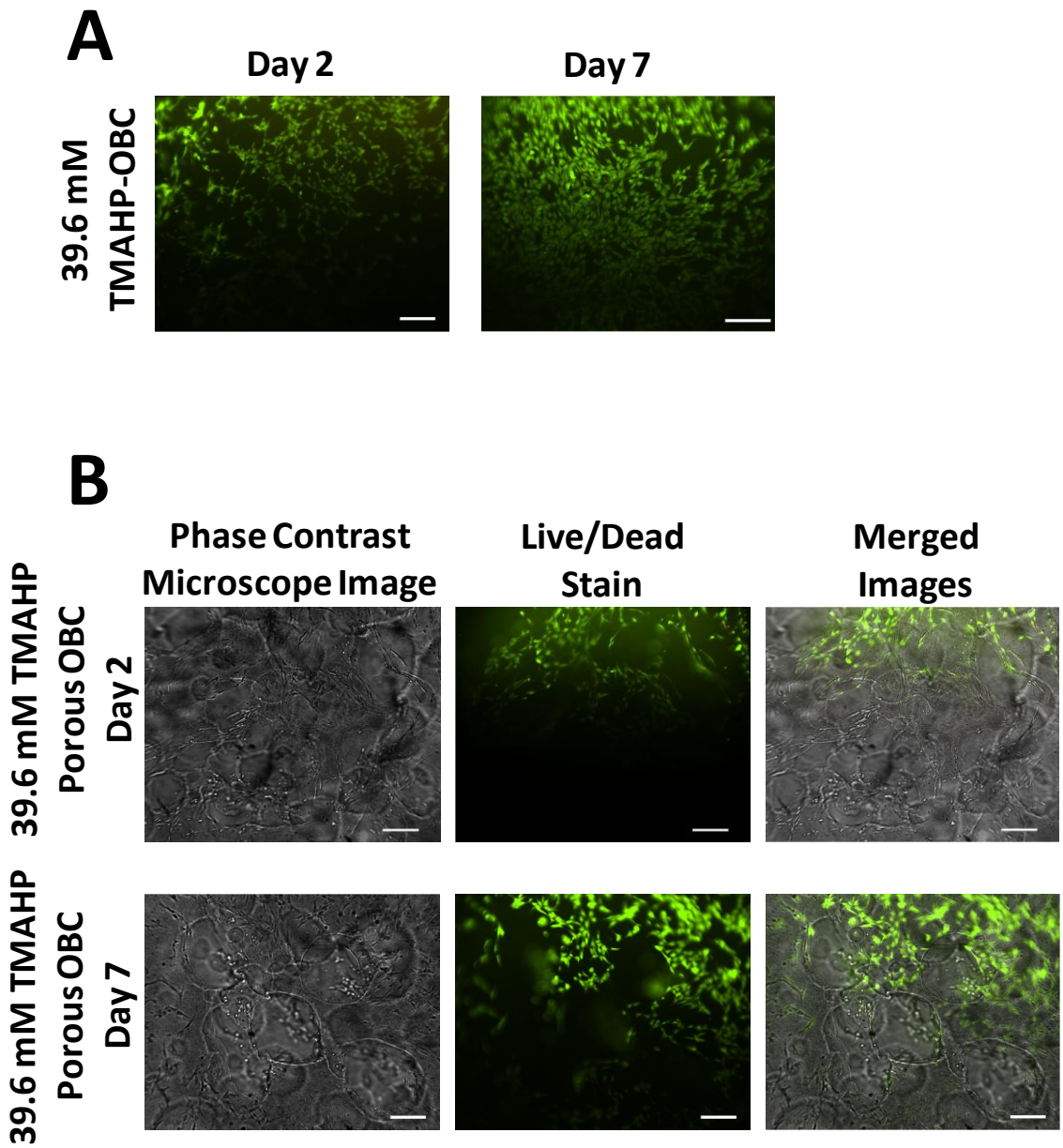

Figure 5.24: Cellular adhesion and cell viability stained with calcein-AM and PI using fluorescent microscopy. Cell viability of EqMSCs (1.26 x 10^5 cells/cm^2) seeded for 2 and 7 days on 39.6 mM TMAHP OBC (A) and 39.6 mM TMAHP porous OBC scaffolds (B). Scale bar = 100 μm.

5.5.2. In Vitro differentiation of EqMSCs

To further characterize the EqMSCs, they were induced to differentiate into chondrocytes *in vitro* on the 39.6 mM TMAHP OBC and 39.6 mM TMAHP porous OBC scaffolds (Figure 5.25). These scaffolds were used for the differentiation study because a degradable scaffold is preferred for cartilage tissue engineering and these combinations of oxidized BC and porous oxidized BCs were systematically selected from their performance as previously described (Section 5.5.1). The 39.6 mM TMAHP OBC and 39.6 mM TMAHP porous OBC scaffolds were used for the *in vitro* differentiation assessment of the stem cells. As demonstrated, the EqMSCs seeded on the 39.6 mM TMAHP porous OBC scaffold similar to the cells on the 39.6 mM TMAHP OBC scaffold exhibited the potential to differentiate into a cartilage cell with the use of the induction media. The results support the fact that EqMSCs do not lose their potentials to differentiate when they adhere to 39.6 mM TMAHP OBC and 39.6 mM TMAHP porous OBC. Figure 5.25 also confirms that the chondrocytes have bridged and completely covered the micropores of the porous oxidized BC.

The differentiation of EqMSCs into chondrocytes as previously discussed is one of the key processes for cartilage regeneration. From a functional perspective, where cell therapy for musculoskeletal hindrances is the ultimate goal, it is fundamental that the cells do not lose or have reduced capacity of differentiation [127]. This study showed that EqMSCs have the capability to differentiate into chondrocytes on the 39.6 mM TMAHP OBC and 39.6 mM TMAHP porous OBC scaffolds, an important characteristic for cartilage regeneration.

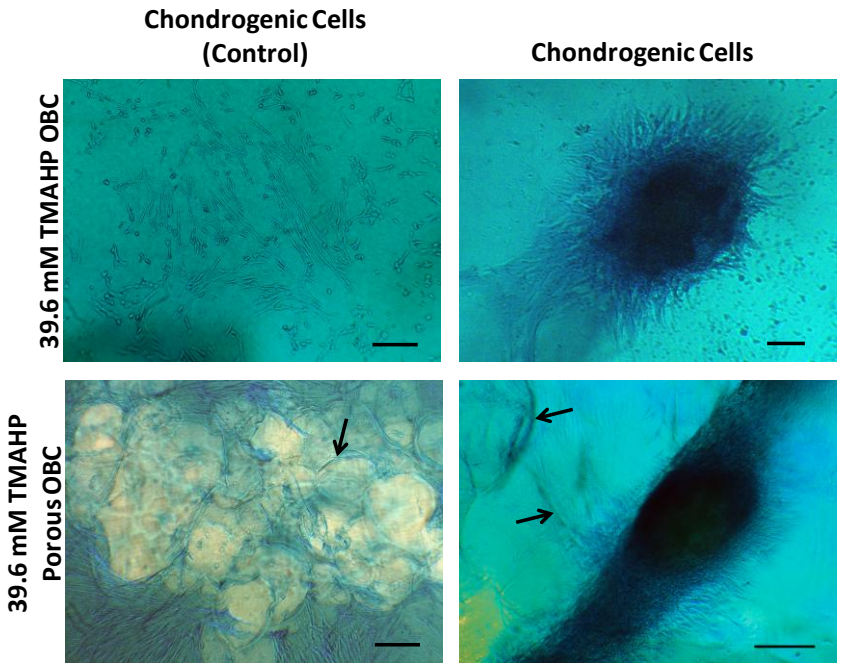

Figure 5.25: Chondrogenic differentiation capacity of EqMSCs (5.0 x 10^4 cells/cm^2) on 39.6 mM TMAHP OBC and 39.6 mM TMAHP porous OBC scaffolds after 7 days of differentiation. Chondrogenesis was induced using the TGFβ1-based method and was indicated by alcian blue staining shown in the differentiated cells. As shown, non-induced chondrogenesis BC controls did not stain positive for alcian blue. Arrows indicate pore structures in the scaffolds. Scale bars = 100 μm.

5.6. In Vitro Degradation Study of Oxidized Bacterial Cellulose Scaffolds

The degradation of BC samples were performed as described in Section 2.4 [68]. The samples analyzed for the degradation study include native BC, OBC, porous BC, porous OBC, 39.6 mM TMAHP OBC and 39.6 mM TMAHP porous OBC scaffolds. The samples were incubated in HEPES buffer at 37 °C for 14 days under static and dynamic incubations. During the incubation period, the supernatants were monitored using a UV-Vis spectrophotometer. After 14 days of incubations, the samples were rinsed, lyophilized and weighed.

Corresponding BC samples which did not undergo the degradation process were lyophilized and weighted for comparison.

After 14 days of static and dynamic incubation, the oxidized, porous, and porous oxidized BC composites lost significant mass compared to their native BC scaffold (Figure 5.26). It was observed that mechanical disruptions in the form of shaking significantly affected the weight loss of the oxidized, porous, and porous oxidized BC scaffolds incubated under dynamic conditions (Figure 5.26). The results also show that mechanical disruptions in the form of sample handling may have contributed to the significant weight loss of the oxidized, porous, and porous oxidized BC scaffolds and their functionalized composites, which were incubated under static conditions (Figure 5.26).

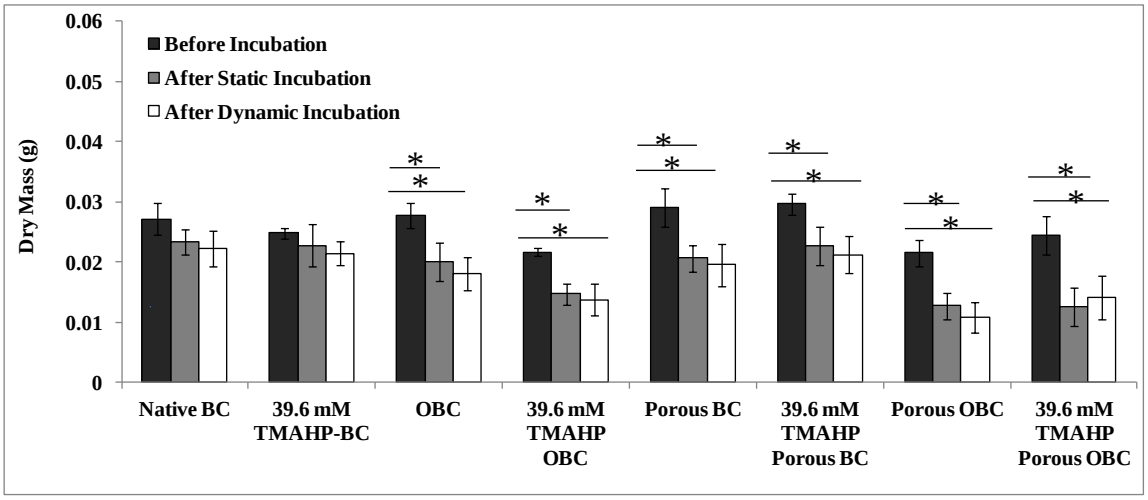

Figure 5.26: Comparison of sample masses before and after incubation in low salt HEPES buffer (pH 7.4) in static and dynamic conditions. Samples analyzed include native BC, OBC, porous BC, porous OBC, 39.6 mM TMAHP-BC, 39.6 mM TMAHP OBC, 39.6 mM TMAHP Porous BC, and 39.6 mM TMAHP Porous OBC. Asterisks (*) indicates significant differences at $p<0.05$.

Dialdehyde cellulose has been proposed to degrade into 2,4-dihydroxybutyric acid, glycolic acid and carbohydrate (Figure 5.27) [159]. Previously, it has been demonstrated that dialdehyde degradation products including 2,4-dihydroxybutyric acid, glycolic acid and carbohydrate can be directly measured using UV-visible spectrophotometry (UV-VIS) [68]. The carbonyl groups present in 2,4- dihydroxybutyric acid, and glycolic acid in the degrading cellulose product have been proposed to absorb at 240 nm. Enzymatic hydrolysis and acid hydrolysis have been proposed to absorb at 260 nm during the degradation of the biological material indicative of cellulose fiber release as a result of physical disruption of scaffold.

In this study, the supernatants of the samples under static and dynamic agitation were measured at 240 and 260 nm every 2 days using UV-Vis and the results are shown in Figure 5.28-5.31. The results show compared to all the analyzed samples, OBC, porous OBC, 39.6 mM TMAHP porous OBC and 39.6 mM TMAHP porous OBC released a high concentration of the degradation product (Figure 5.28-5.31). Native BC and 39.6 mM TMAHP-BC released low levels of the detectable degradation products (Figure 5.28-5.31).

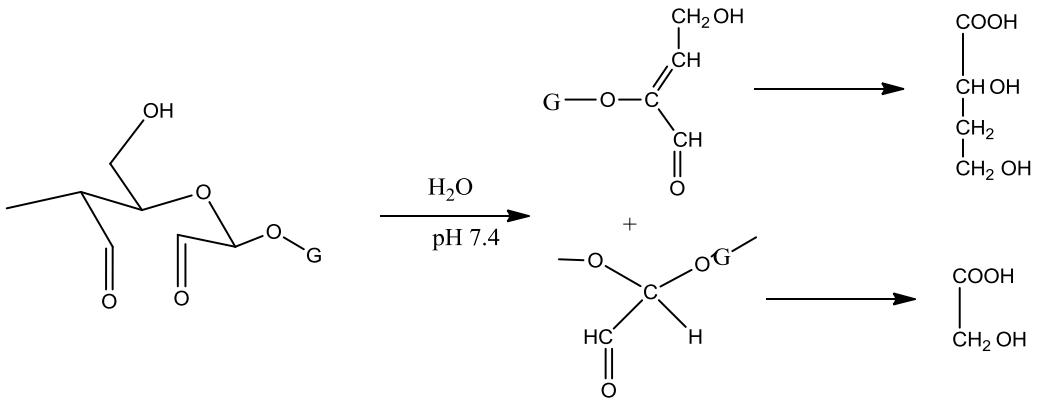

Figure 5.27: Proposed degradation mechanism of dialdehyde cellulose into 2,4-dihydroxybutyric acid and glycolic acid [159].

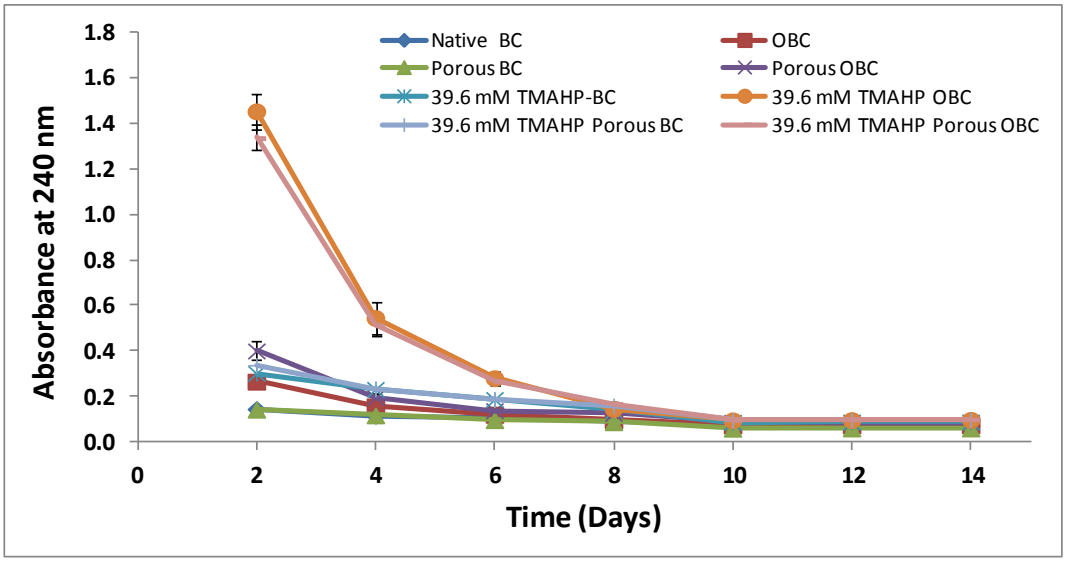

Figure 5.28: Absorbance versus time of HEPES supernatant of static samples at 240 nm. Comparison of native BC, OBC, porous BC, porous OBC, 39.6 mM TMAHP-BC, 39.6 mM TMAHP OBC, 39.6 mM TMAHP Porous BC, and 39.6 mM TMAHP Porous OBC.

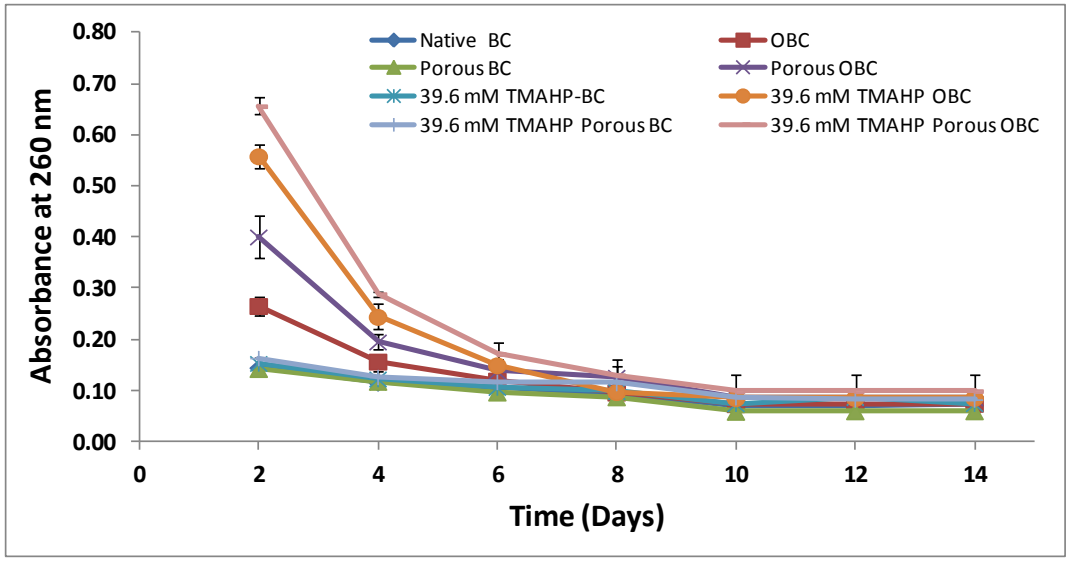

Figure 5.29: Absorbance versus time of HEPES supernatant of static samples at 260 nm. Comparison of native BC, OBC, porous BC, porous OBC, 39.6 mM TMAHP-BC, 39.6 mM TMAHP OBC, 39.6 mM TMAHP Porous BC, and 39.6 mM TMAHP Porous OBC.

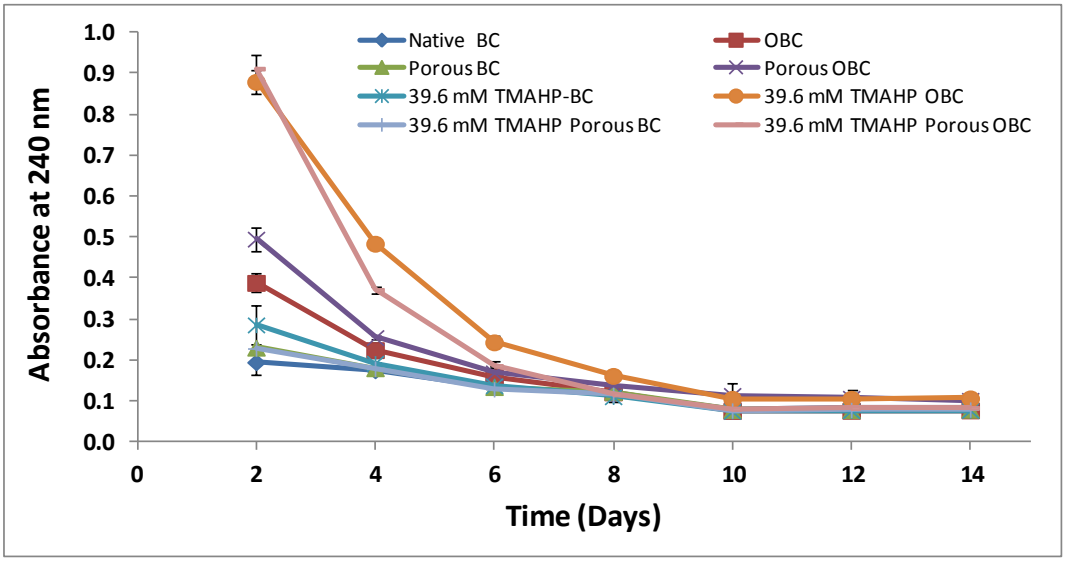

Figure 5.30: Absorbance versus time of HEPES supernatant of dynamic samples at 240 nm. Comparison of native BC, OBC, porous BC, porous OBC, 39.6 mM TMAHP-BC, 39.6 mM TMAHP OBC, 39.6 mM TMAHP Porous BC, and 39.6 mM TMAHP Porous OBC.

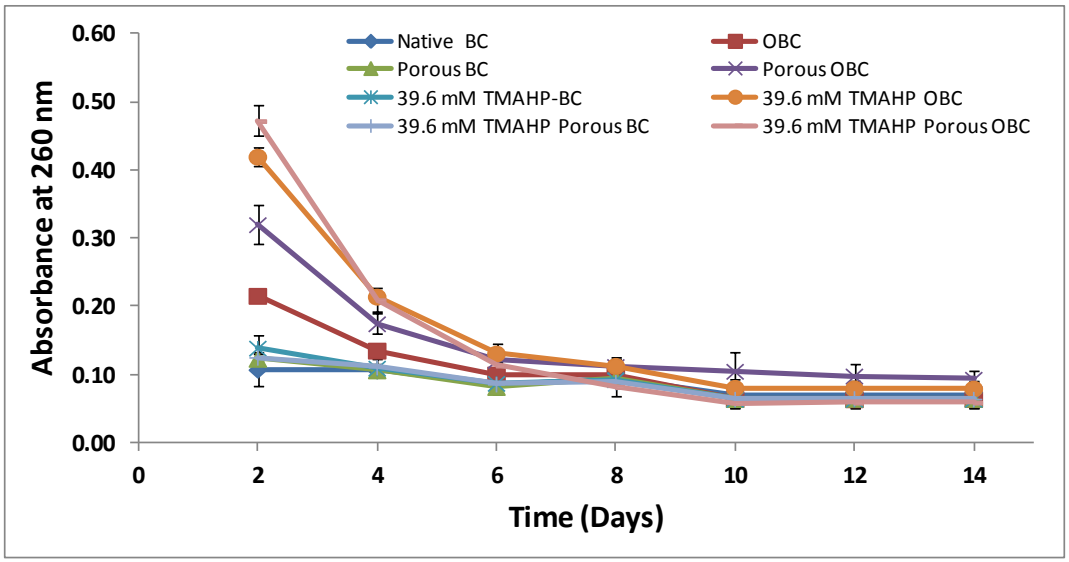

Figure 5.31: Absorbance versus time of HEPES supernatant of dynamic samples at 260 nm. Comparison of native BC, OBC, porous BC, porous OBC, 39.6 mM TMAHP-BC, 39.6 mM TMAHP OBC, 39.6 mM TMAHP Porous BC, and 39.6 mM TMAHP Porous OBC.

5.7. Conclusions

Surface amination and carboxylation were successfully performed on nano-porous and micro-porous BC scaffolds as confirmed by FTIR. SEM imaging confirmed that surface amination and carboxylation did not affect the morphology of the BC scaffolds.

It was demonstrated that the chemically functionalized BC scaffolds were cytocompatible with EqMSCs *in vitro*. The chemically functionalized scaffolds supported the adhesion and proliferation of EqMSCs. The 39.6 mM TMAHP oxidized BC and 39.6 mM TMAHP porous oxidized BC supported chondrogenic differentiation. The cells seeded on the chemically functionalized BC scaffolds were viable and proliferated on the scaffolds. Based on these results, the 39.6 mM TMAHP porous oxidized BC scaffold appear to have potential as a scaffold for tissue engineering of cartilage.

CHAPTER VI
Analysis of Nano-porous and Micro-porous Calcium-Deficient Hydroxyapatite Bacterial Cellulose Scaffolds and their Oxidized Composites

In this study, nano-porous BC and micro-porous BC scaffolds were mineralized with calcium-deficient hydroxyapatite to produce different amounts of CdHAP in the BC composites. BC mineralization was performed by incubating the scaffolds in solutions of calcium chloride and sodium phosphate dibasic. The resulting BC composites were characterized using FTIR, SEM and mechanical testing instrument. The BC composites were also characterized for their ability to support and maintain differentiation of EqMSCs *in vitro* for potential tissue engineering use. The potential for EqMSCs to differentiate into osteocytes were assessed. The degradation properties were then analyzed by incubating the samples in HEPES buffer (pH 7.4) at 37 °C under static and dynamic conditions. The samples were measured for weight loss while the buffer was analyzed for degradation products.

6.1. Mineralization of Bacterial Cellulose with Varying Concentrations of Calcium and Phosphate Solutions

Native BC (nano-porous BC) and microporous BCs (porous BCs) were synthesized and purified as described in Sections 2.2.1 and 2.2.2, respectively. Half of the prepared native and porous BCs were oxidized and purified following the procedure outlined in Section 2.2.5 [69]. Half of the oxidized and non-oxidized scaffolds were mineralized following the procedure in Section 2.2.6. Briefly, cellulose pellicles were suspended in 1.0 mM $CaCl_2$ under agitation in an orbital shaker for 24 h (23 °C), rinsed briefly in DI water, and then transferred to 0.6mM Na_2HPO_4 under agitation for another 24 h (23 °C) to obtain CdHAP (CdHAP-1). Two additional groups of CdHAP synthesis were performed on the BCs using the combination of 2.5 mM $CaCl_2$/1.5 mM Na_2HPO_4 (CdHAP-2) and 5

mM $CaCl_2$/3.0 mM Na_2HPO_4 (CdHAP-3) under the same conditions. Native BC and porous BC scaffolds that had not undergone oxidation and mineralization were used as controls

6.2. Fourier Transform Infrared Spectroscopy

The FTIR spectra of the BC composites (BC-CdHAP-1, BC-CdHPAP-2, BC-CdHAP-3) and their corresponding oxidized BC composites (OBC-CdHAP-1, OBC-CdHPAP-2, OBC-CdHAP-3) are shown in Figure 6.1. The FTIR spectra of the porous BC composites (porous BC-CdHAP-1, porous BC-CdHPAP-2, porous BC-CdHAP-3) and their corresponding porous oxidized BC composites (porous OBC-CdHAP-1, porous OBC-CdHPAP-2, porous OBC-CdHAP-3) are shown in Figure 6.2. Phosphate, a component of CdHAP, had been identified to have four phosphate vibrational modes: v_1 symmetric stretching mode, v_2 symmetric bending mode, v_3 antisymmetric stretching mode, and v_4 out-of-plane bending mode [160]. The characteristic absorption bands of CdHAP are illustrated in Table 6.1.

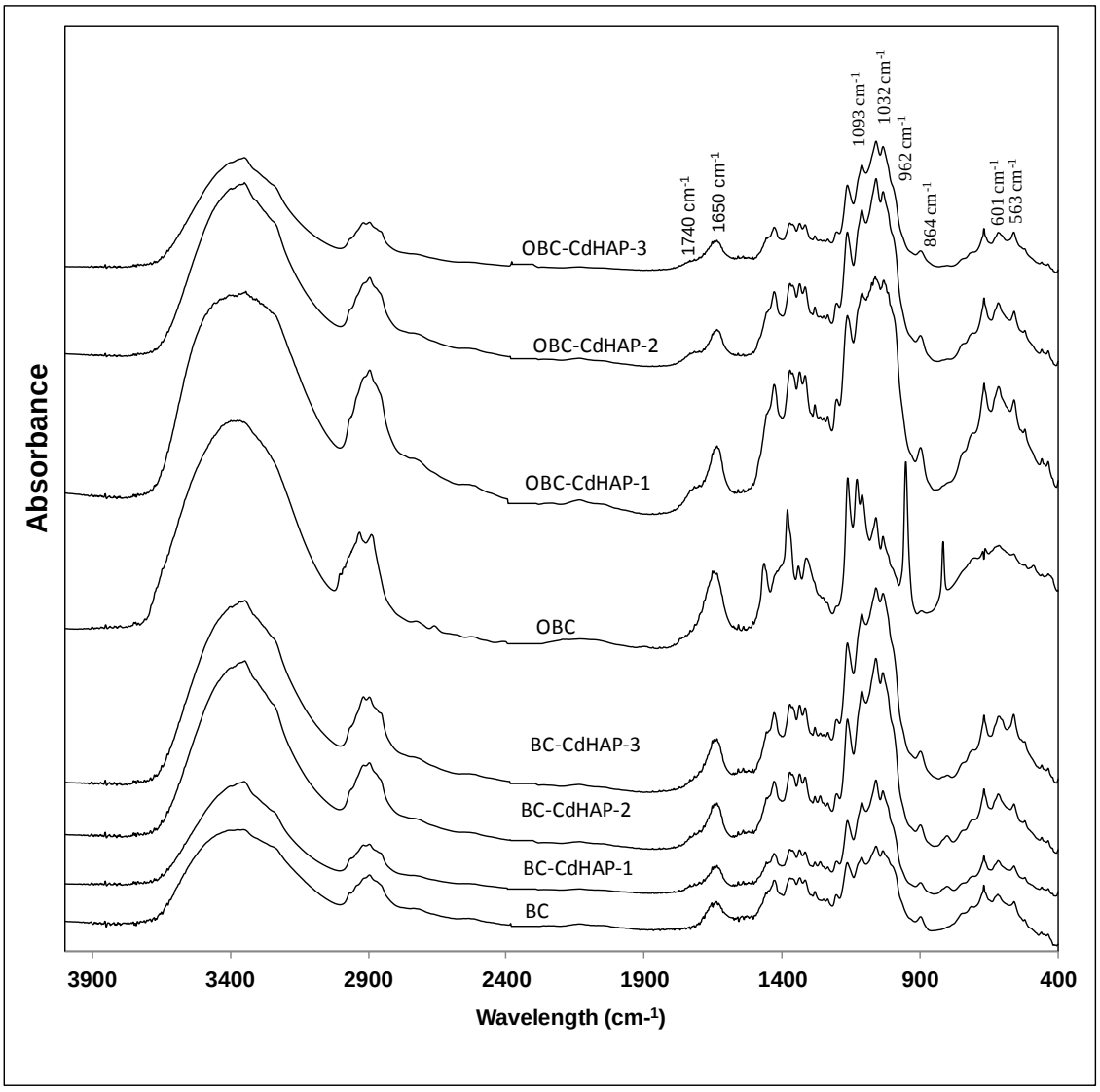

Figure 6.1: FTIR spectra of BC-CdHAP composites.

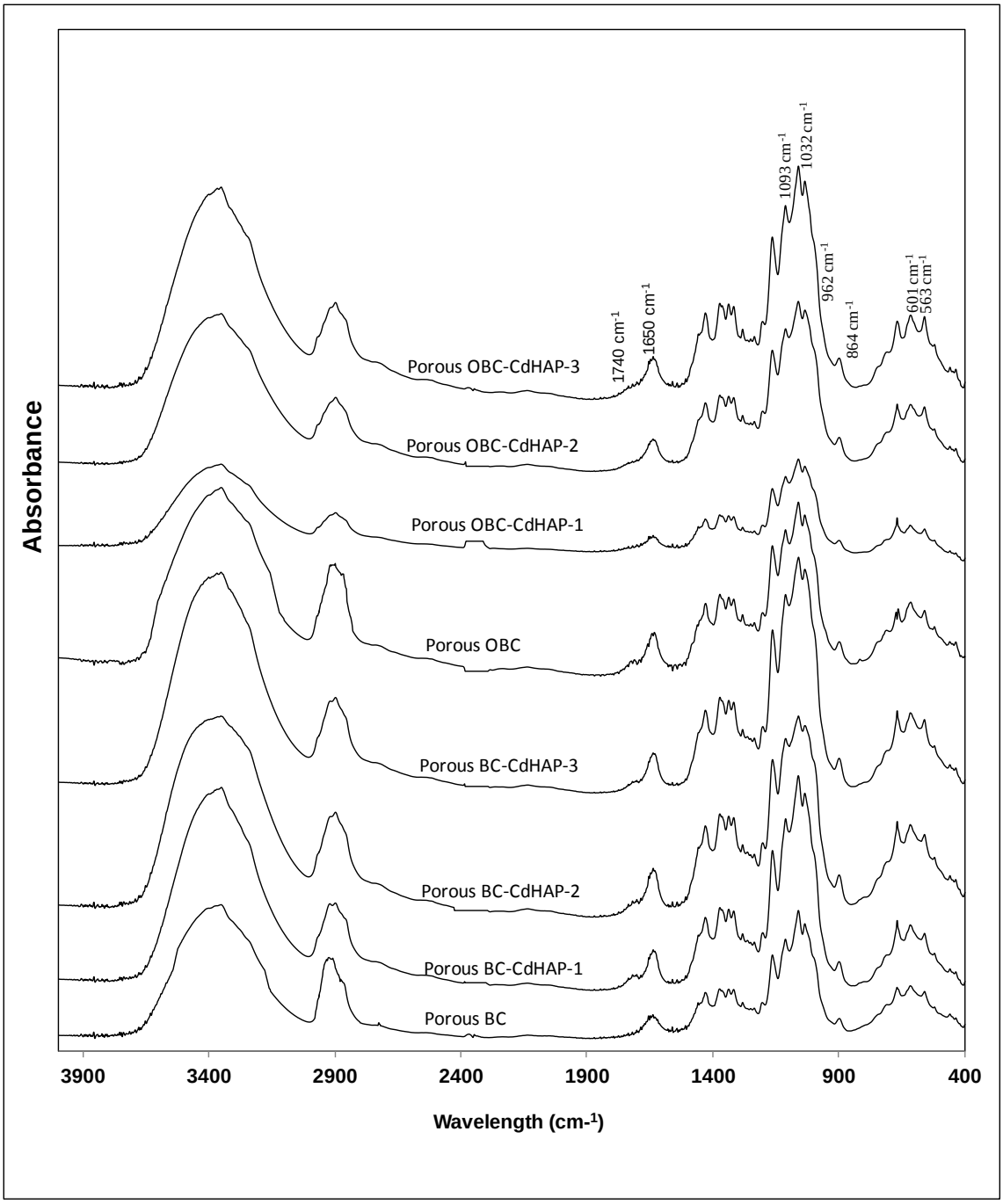

Figure 6.2: FTIR spectra of porous BC-CdHAP composites.

Table 6.1: Characteristic FTIR bands of calcium-deficient hydroxyapatite.

Frequency	Relative Intensity	Assignment	Ref.
3567 cm^{-1}	Strong	OH Stretching (Overlaps with Absorbed H_2O)	[161]
3400 cm^{-1}	Broad	Absorbed H_20	[161]
1653 cm^{-1}		Absorbed H_2O	[150]
1093 cm^{-1}	Strong	Phosphate (PO_4^{-3}) v_3 vibrational mode	[161]
1032 cm^{-1}	Strong	Phosphate (PO_4^{-3}) v_3 vibrational mode	[161]
962 cm^{-1}	Medium	Phosphate (PO_4^{-3}) v_1 vibrational mode	[161]
864 cm^{-1}	Weak	Hydrogen Phosphate (PO_4^{-2}) vibrational mode	[162]
601 cm^{-1}	Strong	Phosphate (PO_4^{-3}) v_4 vibrational mode	[161]
563 cm^{-1}	Strong	Phosphate (PO_4^{-3}) v_4 vibrational mode	[150, 161]

The absorbances of the phosphate peaks were graphed against the concentration of BC-CdHAP composition (Figure 6.3.A), OBC-CdHAP composition (Figure 6.3.B.), porous BC-CdHAP composition (Figure 6.4.A), and porous OBC-CdHAP composition (Figure 6.4.B). The absorbances were normalized by dividing the phosphate absorbance by the CH cellulose peak absorbance at 2900 cm^{-1}. This CH peak was used because its absorbance is constant in all the samples given that the amount of cellulose in the composites is constant. The increase in absorbance correlates to the increase in hydroxyapatite concentration as governed by the Beer-Lambert Law [158]. Even though the intensity of the phosphate absorption peaks increase with the concentration of hydroxyapatite, the absorbance of the *v*3 modes demonstrate increased scatter compared to the *v*1 and *v*4 vibrational modes (Figure 6.3, 6.4). The variation present in the *v*3 modes may be due to the antisymmetric stretching of the dipole, and the variation in band absorbance may also be attributed to minor differences in the amount of material in the KBr pellets.

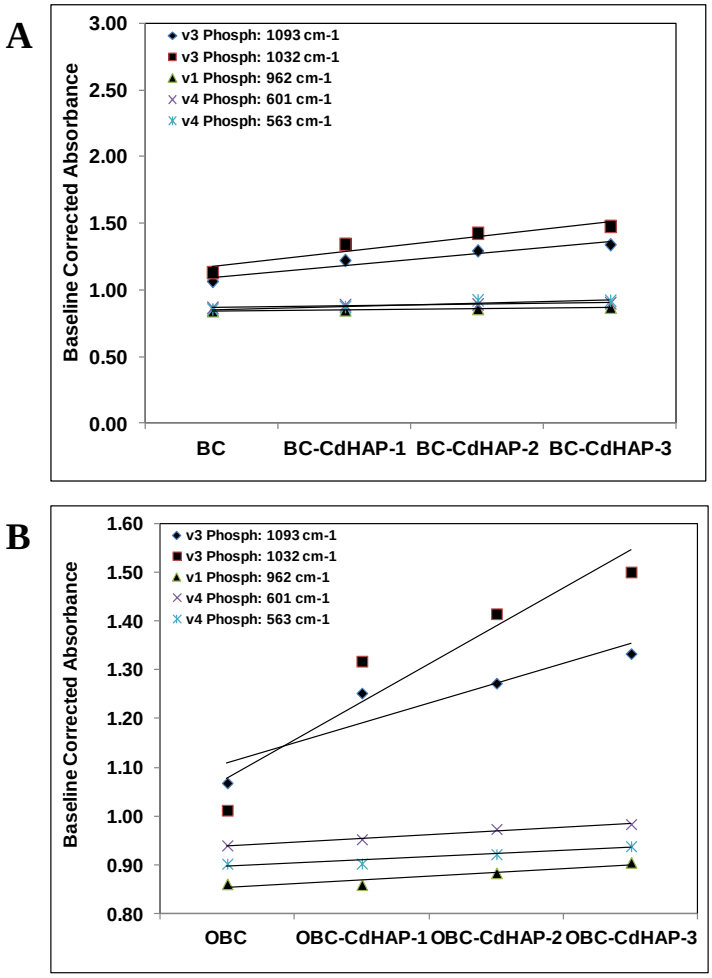

Figure 6.3: Graph of phosphate peak absorbance versus BC-CdHAP composites (A) and OBC-CdHAP composites (B).

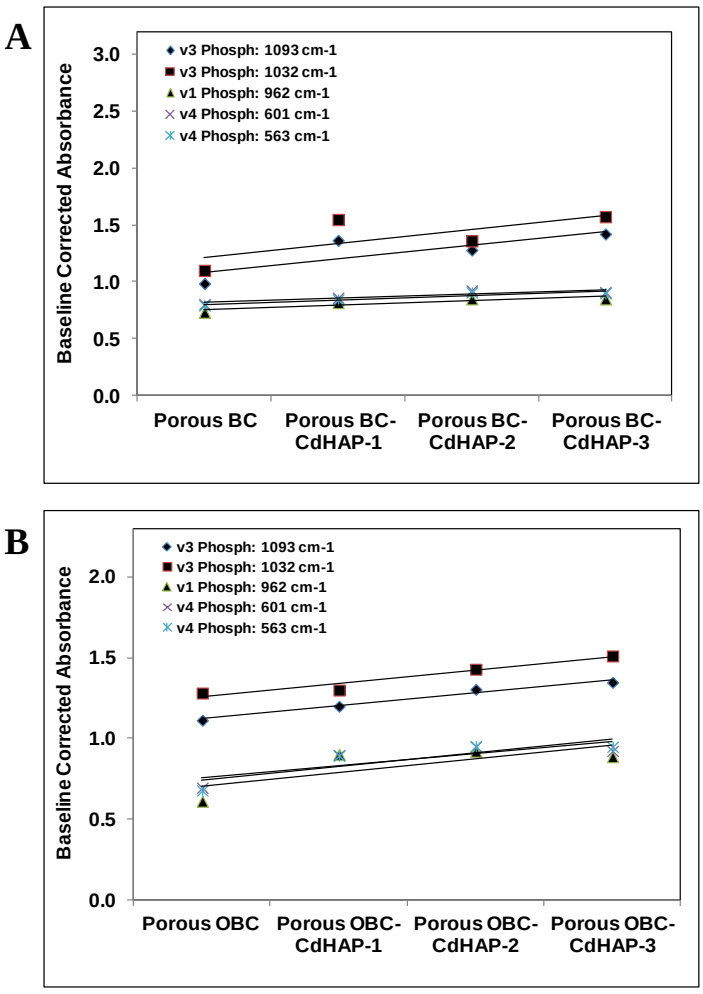

Figure 6.4: Graph of phosphate peak absorbance versus porous BC-CdHAP composites (A) and porous OBC-CdHAP (B) composites.

6.3. Scanning Electron Microscopy

SEM images of the BC composites and their corresponding OBC composites are illustrated in Figures 6.5, 6.6, and 6.7. The highest concentration of the hydroxyapatite deposition was observed on the BC-CdHAP-3 and OBC-CdHAP-3 scaffolds (Figure 6.5-6.7). The sizes of the irregularly-shaped hydroxyapatite clusters were observed to be approximately 1μm or less in length (Figure 6.7). At lower magnification (Figure 6.5), the hydroxyapatite clusters in the scaffold matrixes appeared to have deposited mostly uniformly on the scaffolds as solid particles. At higher magnifications (Figure 6.6, 6.7), hydroxyapatite appeared to have deposited heterogeneously in the matrices as irregularly-shaped crystallites. SEM images of porous OBC composites are shown in Figure 6.8. SEM images demonstrated that the scaffolds maintained their porous structures after deposition of CdHAP into the scaffolds (Figure 6.8). Hutchens et al. (2006, 2009) have used a similar method to mineralized BC and oxidized BC scaffolds [68, 69]. The authors used X-ray diffraction to confirm that these hydroxyapatite clusters are indeed CdHAP.

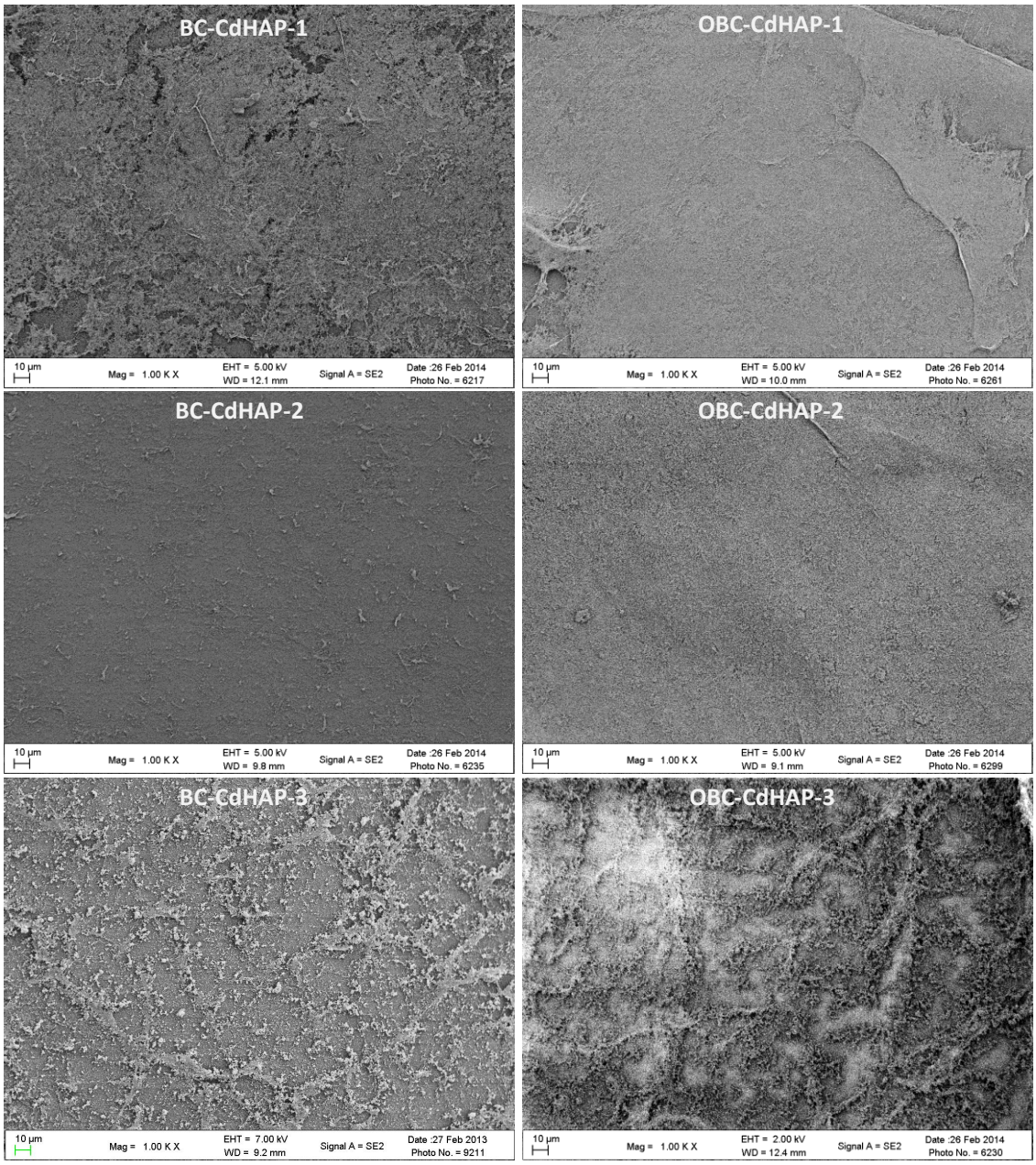

Figure 6.5: SEM images of BC-CdHAP-1, BC-CdHAP-2, BC-CdHAP-3, OBC-CdHAP-1, OBC-CdHAP-2, and OBC-CdHAP-3 at 1000X.

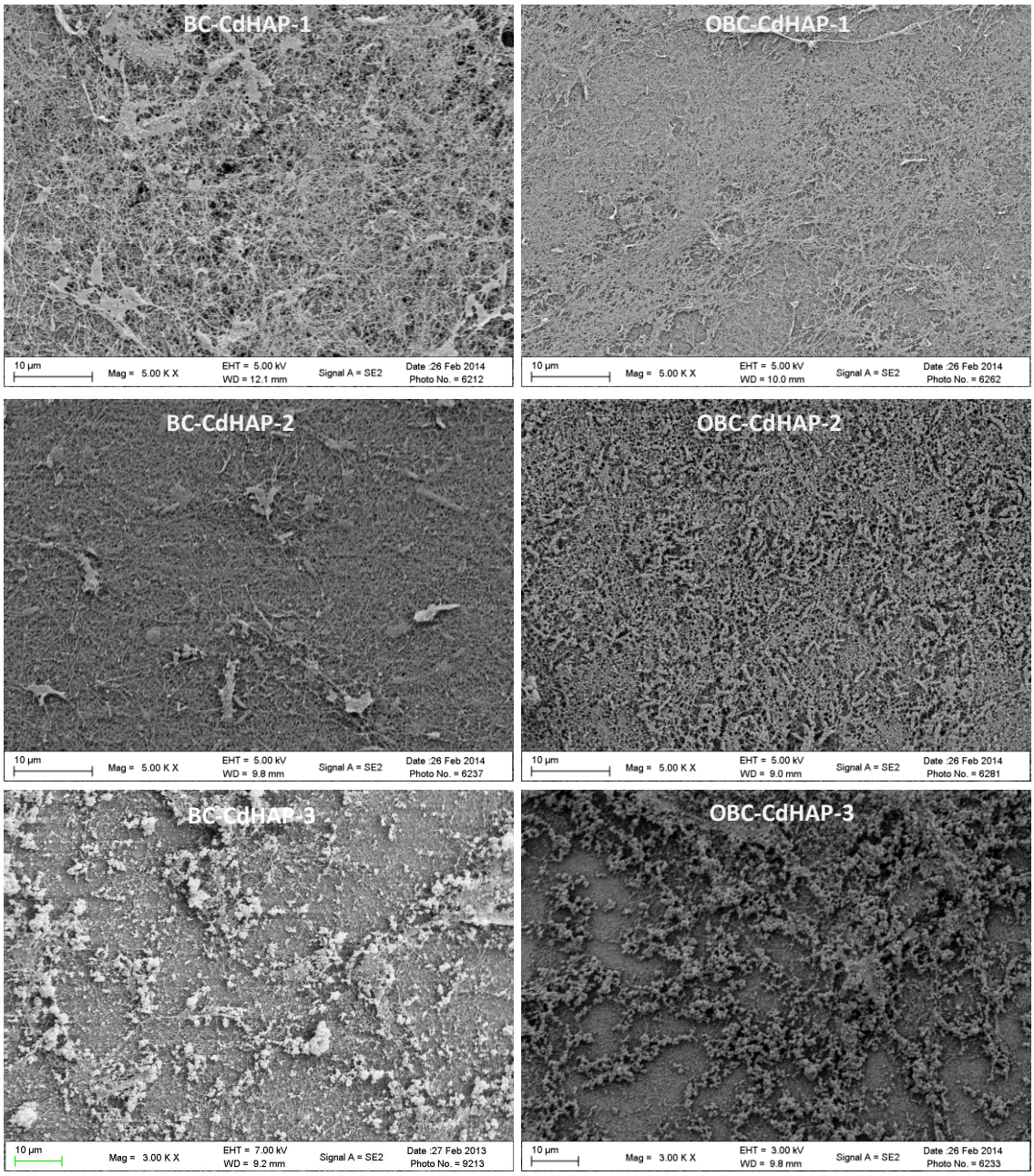

Figure 6.6: SEM images of BC-CdHAP-1, BC-CdHAP-2, BC-CdHAP-3, OBC-CdHAP-1, OBC-CdHAP-2, and OBC-CdHAP-3 at 5000X

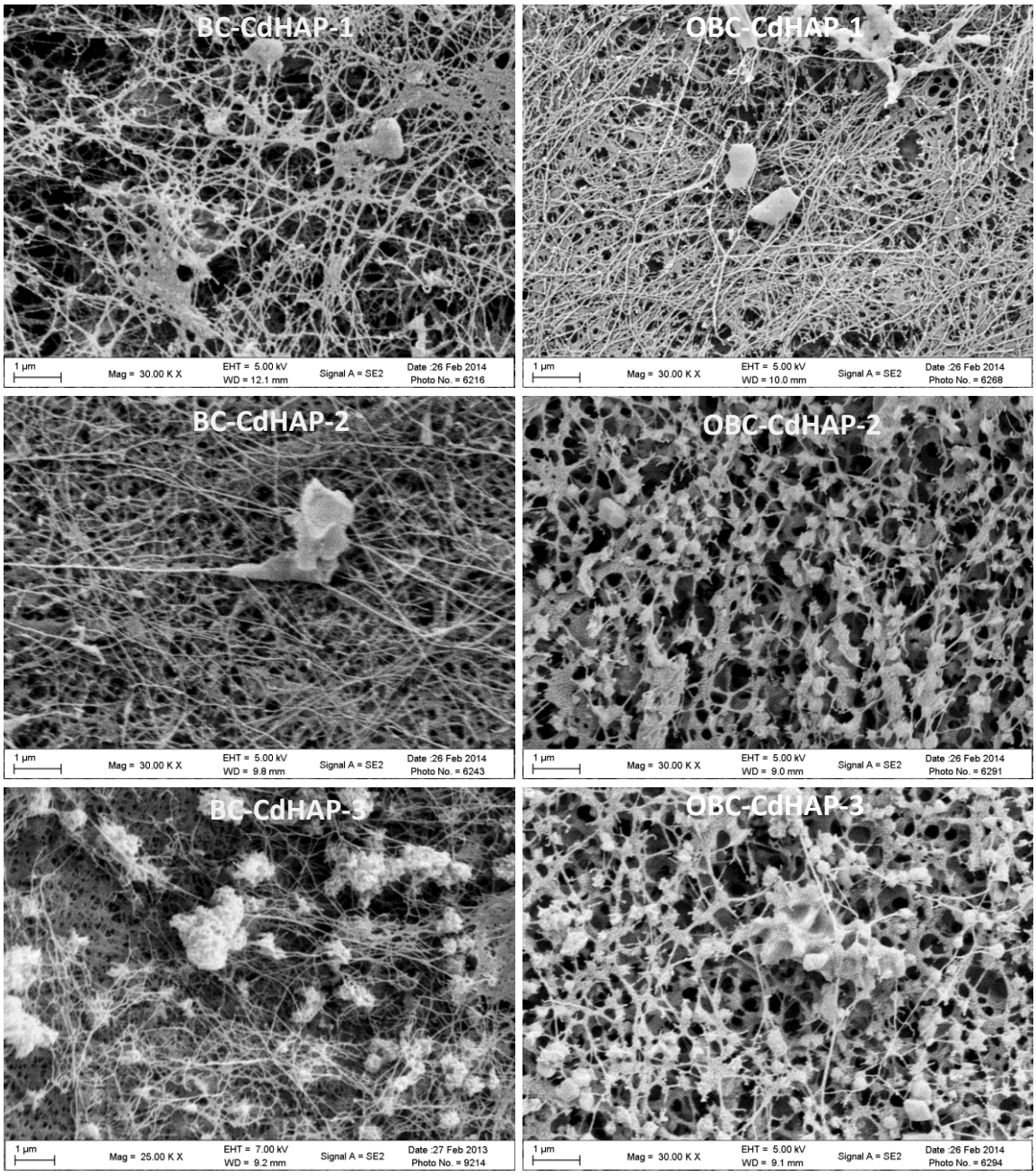

Figure 6.7: SEM images of BC-CdHAP-1, BC-CdHAP-2, BC-CdHAP-3, OBC-CdHAP-1, OBC-CdHAP-2, and OBC-CdHAP-3 at 25000-30000X.

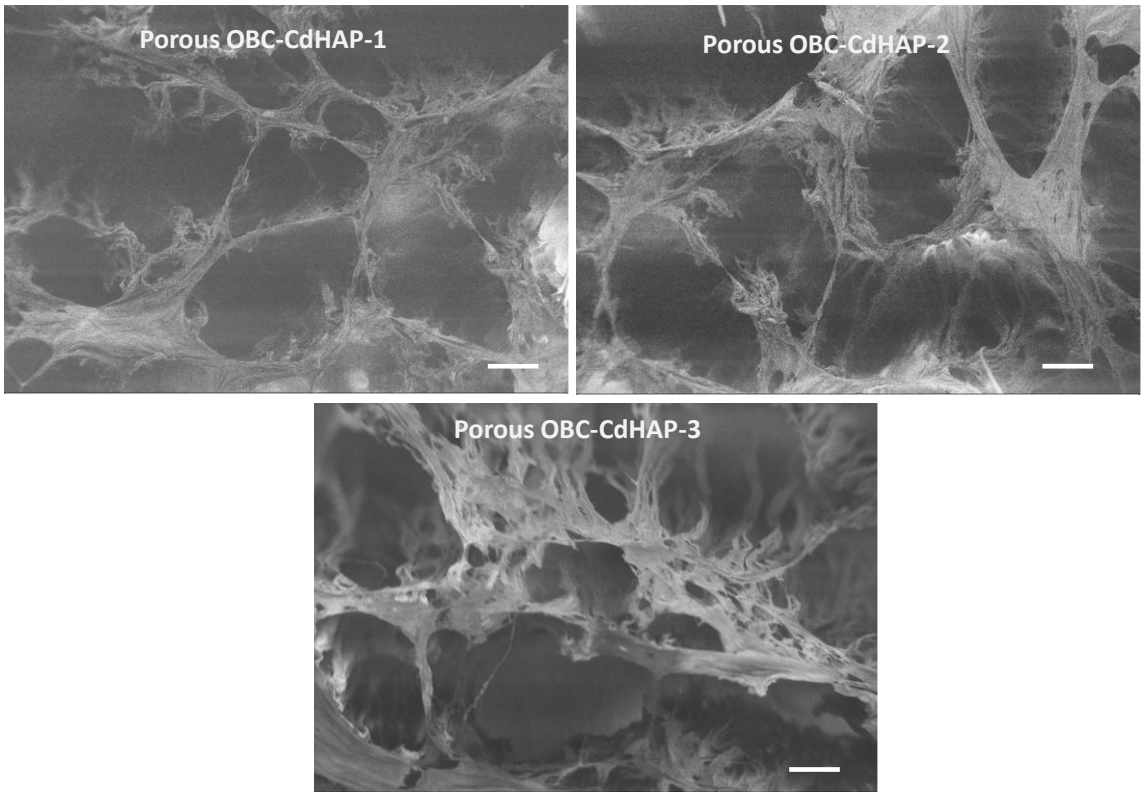

Figure 6.8: SEM images of porous OBC-CdHAP-1 (A), porous OBC-CdHAP-2 (B), porous BC-OCdHAP-3 (C).

6.4. Mechanical Testing

The mechanical properties of a representative sample group, BC-CdHAP-3 composites, and their corresponding controls (native BC, OBC, porous BC, and porous OBC) were determined at 5% strain rate to assess the relationship between the non-mineralized and mineralized BCs. The engineering stress-strain curves of the hydrated never-dried BC composite samples are illustrated in Figure 6.9. The ultimate tensile strength, strain at break, and elastic modulus values of the non-mineralized and mineralized BC samples calculated from the engineering stress-strain curves are illustrated in Figure 6.10.

The results show that the CdHAP mineralization significantly decreased the ultimate tensile strength for all the BC composites (Figure 6.10.A). Strain at break for BC-CdHAP-3 was significantly decrease compared to native BC (Figure 6.10.B). The elastic modulus of the OBC-CdHAP-3, porous BC-CdHAP-3, and porous OBC-CdHAP-3 significantly decreased compared to their non-mineralized BC scaffolds (Figure 6.11). Hydroxyapatite mineralization of the BC scaffolds appeared to have altered inter- and intramolecular hydrogen bonding in the cellulose structure, resulting in the impairment of scaffold's mechanical properties.

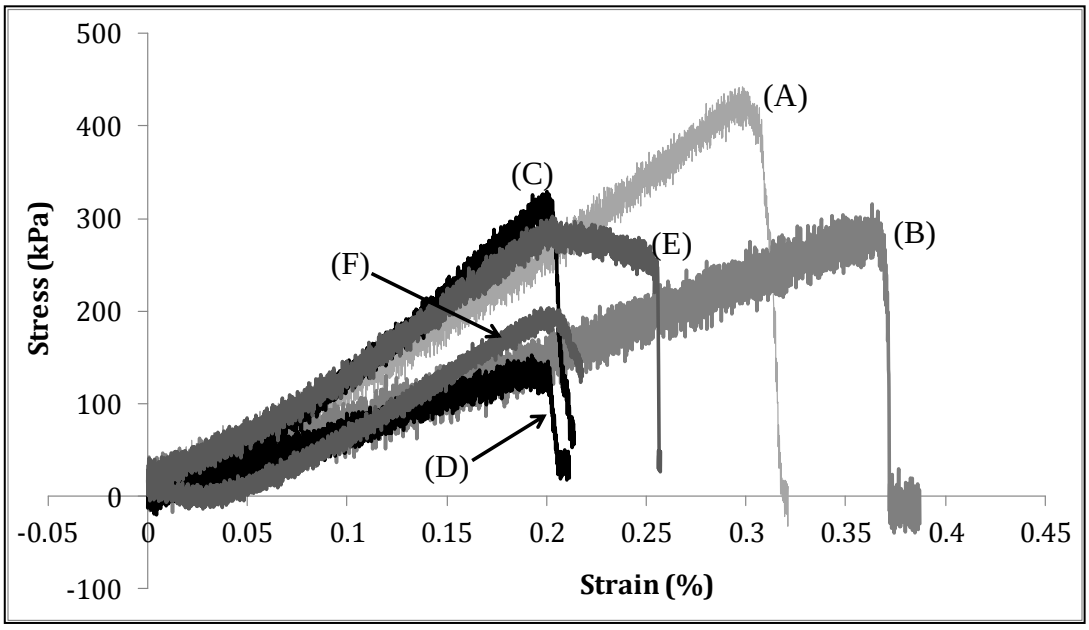

Figure 6.9: Engineering stress-strain curve of native BC (A), oxidized BC (B), porous BC (C), porous oxidized BC (D), BC-CdHAP-3 (E), and porous BC-CdHAP-3 (F).

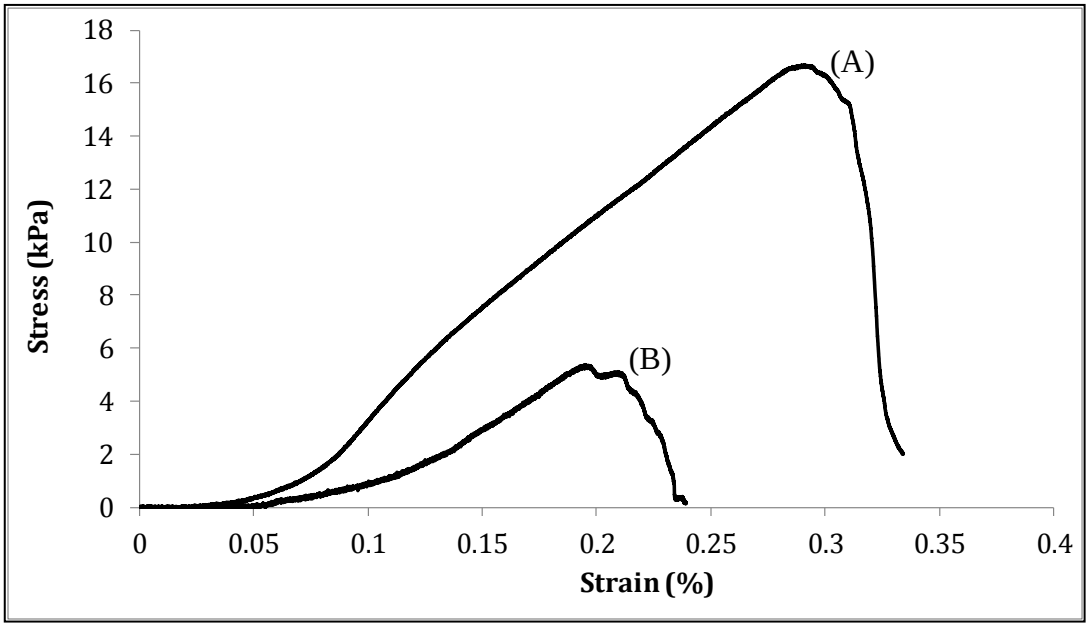

Figure 6.10: Engineering stress-strain curve of OBC-CdHAP-3 (A), and porous OBC-CdHAP-3 (B).

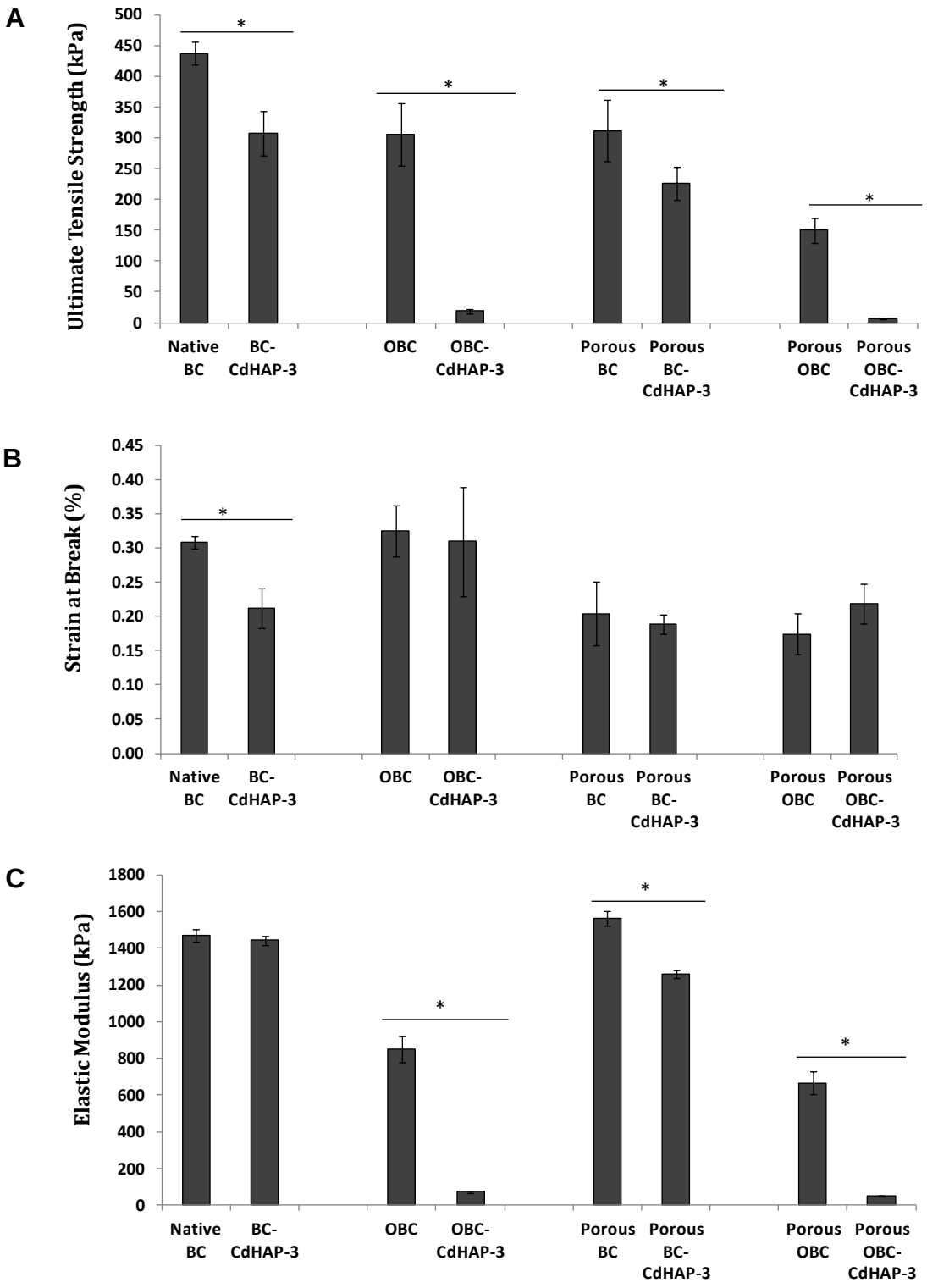

Figure 6.11: Comparison of ultimate tensile strengths (A), strain at breaks (B), and elastic moduli of native BC, BC-CdHAP-3 and their composites. Asterisks (*) indicates significant differences at $p<0.05$.

6.5. Characterization of Cell and Bacterial Cellulose Scaffolds

6.5.1. Cellular Adhesion, Viability and Proliferation Assays

MTS assay analysis was performed to determine the viability of EqMSCs seeded on the non-porous BC-CdHAP composite scaffolds and porous BC-CdHAP composite scaffolds. Cell staining using calcein-AM and PI was also performed to visually assess the EqMSCs attachment under the same conditions. The MTS assay results of EqMSCs seeded on the BC-CdHAP composites are shown in Figure 6.12. Calcein-AM and PI staining results of the EqMSCs seeded on these non-porous BC-CdHAP composite scaffolds are illustrated in Figure 6.13-6.16. From 2 to 14 days in culture, the cells seeded on the BC-CdHAP composite scaffolds appeared to have demonstrated non-linear proliferation rates as a function time compared to their non-mineralized controls.

The results showed that after 2 days in culture, EqMSCs seeded on porous OBC-CdHAP scaffolds had a full spread-out morphology on the scaffolds compared to EqMSCs seeded on the other mineralized BC scaffolds (Figure 6.16.A). By 7 days in the culture, the EqMSCs appeared to have reached 100% confluency on the porous OBC-CdHAP scaffolds (Figure 6.16.B). By 14 days in culture, the EqMSCs appeared to be dying due to thelack of surface area for the cells to grow (Figure 6.16.C).

Figure 6.12: Cellular viability assay: MTS test. Comparison of proliferation of cells as determined by MTS assay for EqMSCs (1.26×10^5) seeded on native BC (A), OBC (B), porous BC (C), porous OBC (D) scaffolds and their composites for 2, 7 and 14 days. Asterisks (*) indicates significant differences at $p<0.05$.

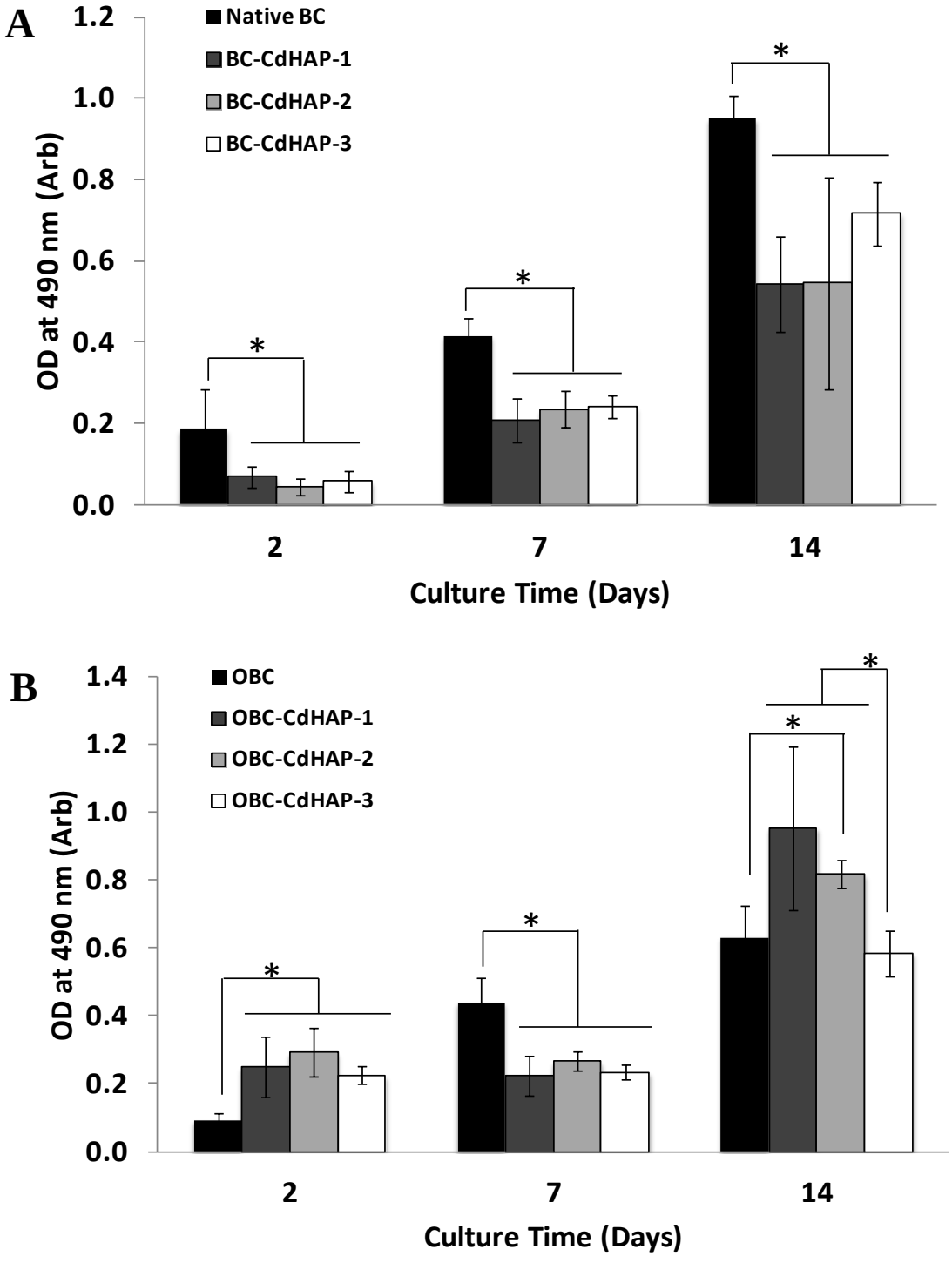

Figure 6.12: Continued.

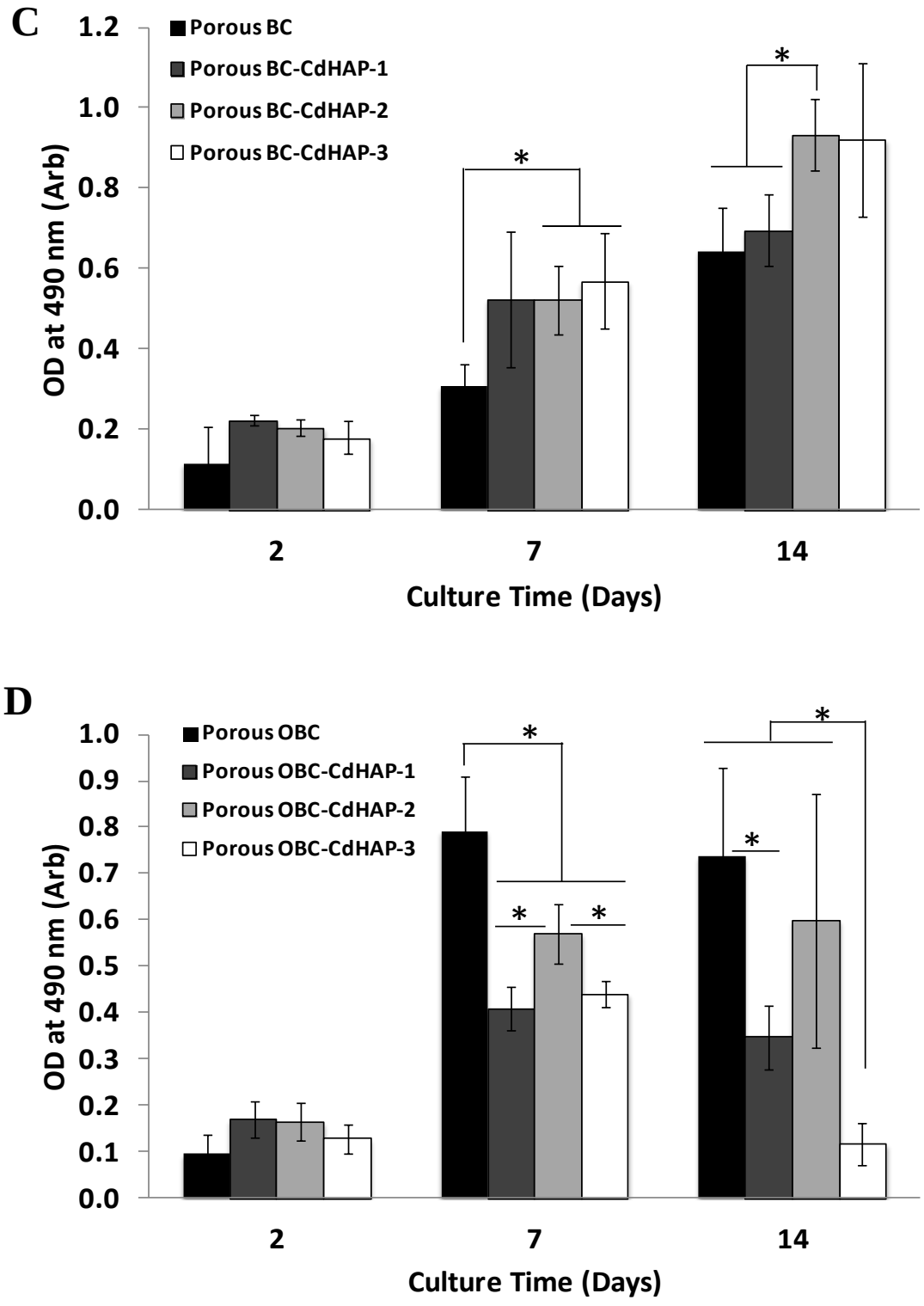

Figure 6.12: Continued.

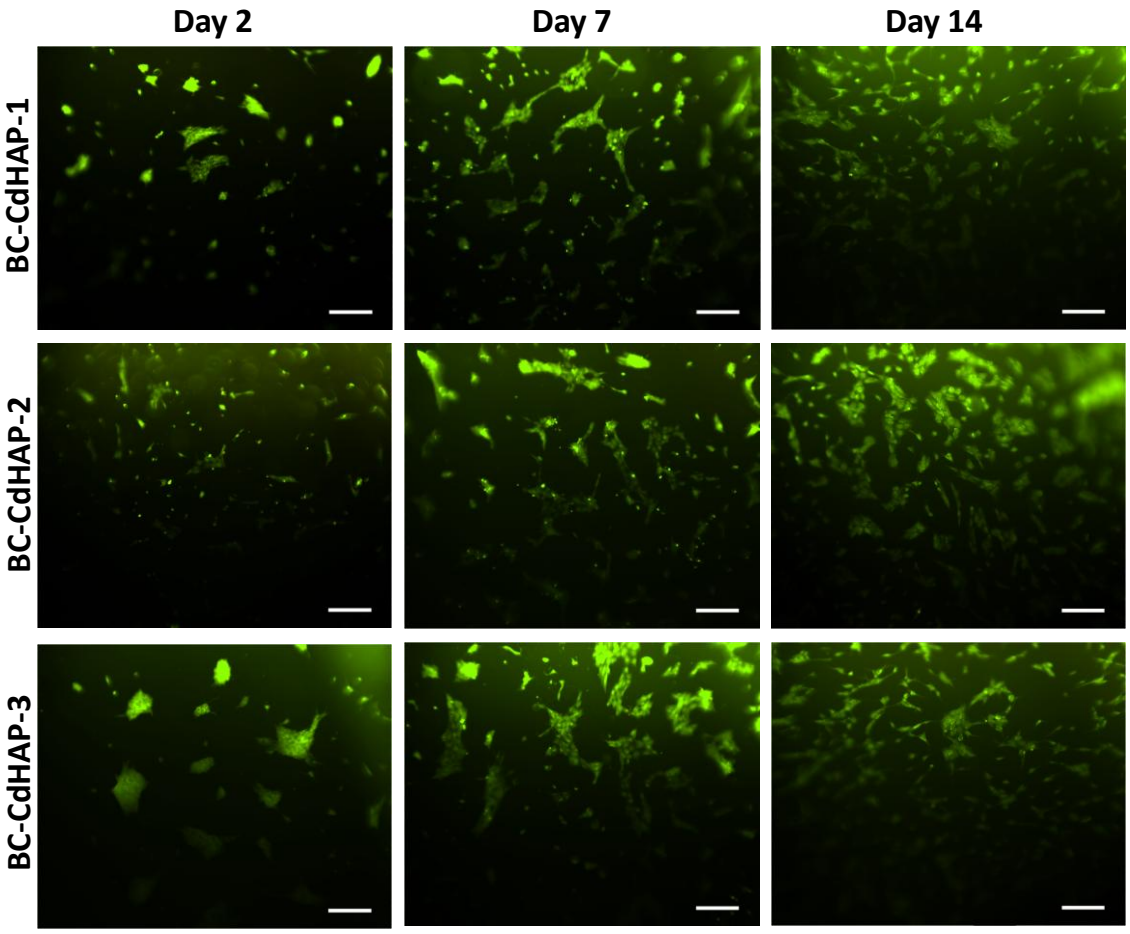

Figure 6.13: Cellular adhesion and cell viability stained with calcein-AM and PI using fluorescent microscopy. Cell viability of EqMSCs (1.26 x 10^5 cells/cm^2) seeded for 2, 7, and 14 days on BC-CdHAP-1, BC-CdHAP-2, and BC-CdHAP-3, scaffolds. Cell viability of EqMSCs were analyzed by calcein-AM which exhibits green fluorescence and demonstrates live cells and PI which displays red fluorescence and demonstrates dead cells. Scale bar = 100 µm.

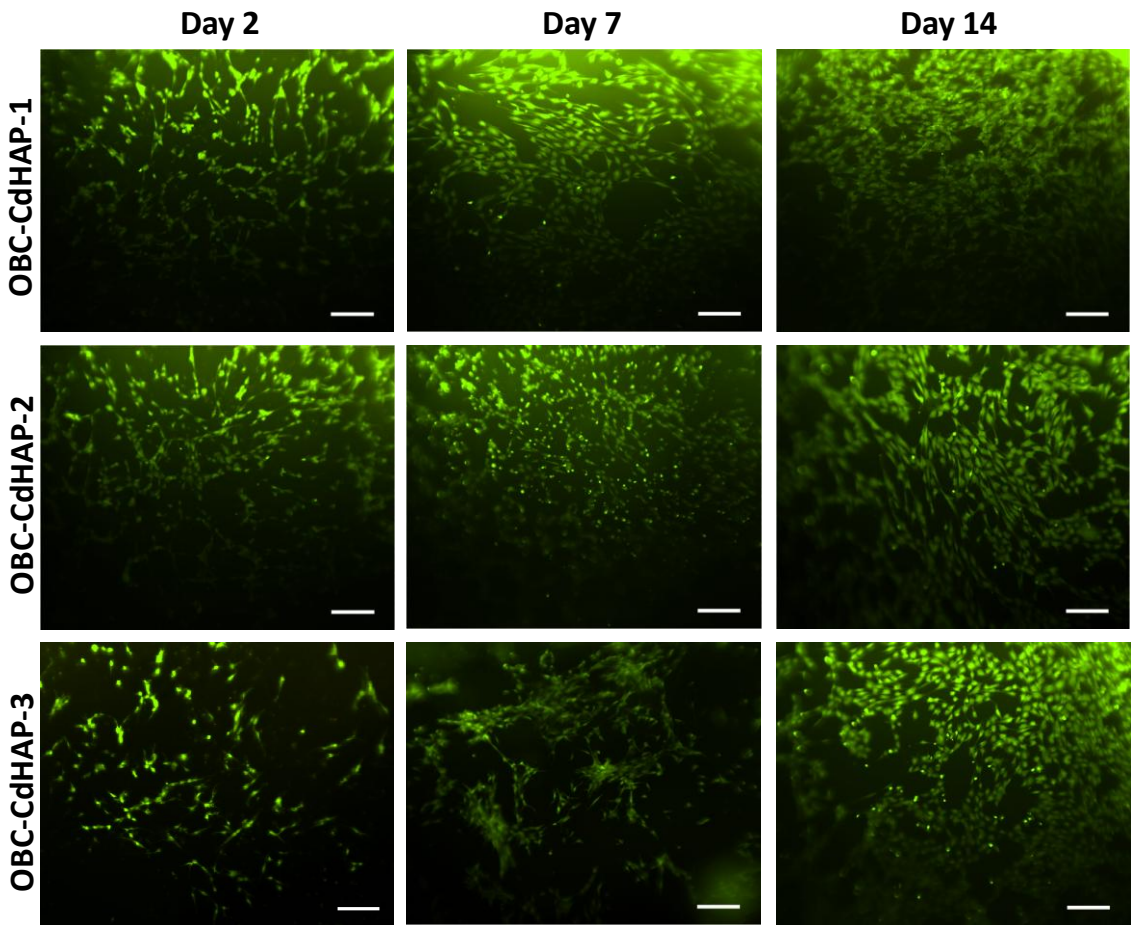

Figure 6.14: Cellular adhesion and cell viability stained with calcein-AM and PI using fluorescent microscopy. Cell viability of EqMSCs (1.26×10^5 cells/cm^2) seeded for 2, 7, and 14 days on OBC-CdHAP-1, OBC-CdHAP-2, and OBC-CdHAP-3 scaffolds. Scale bar = 100 µm.

Figure 6.15: Cellular adhesion and cell viability stained with calcein-AM and PI using fluorescent microscopy. Cell viability of EqMSCs (1.26×10^5 cells/cm^2) seeded for 2 (A), 7 (B), and 14 (C) days on porous BC-CdHAP-1, porous BC-CdHAP-2, and porous BC-CdHAP-3, scaffolds.

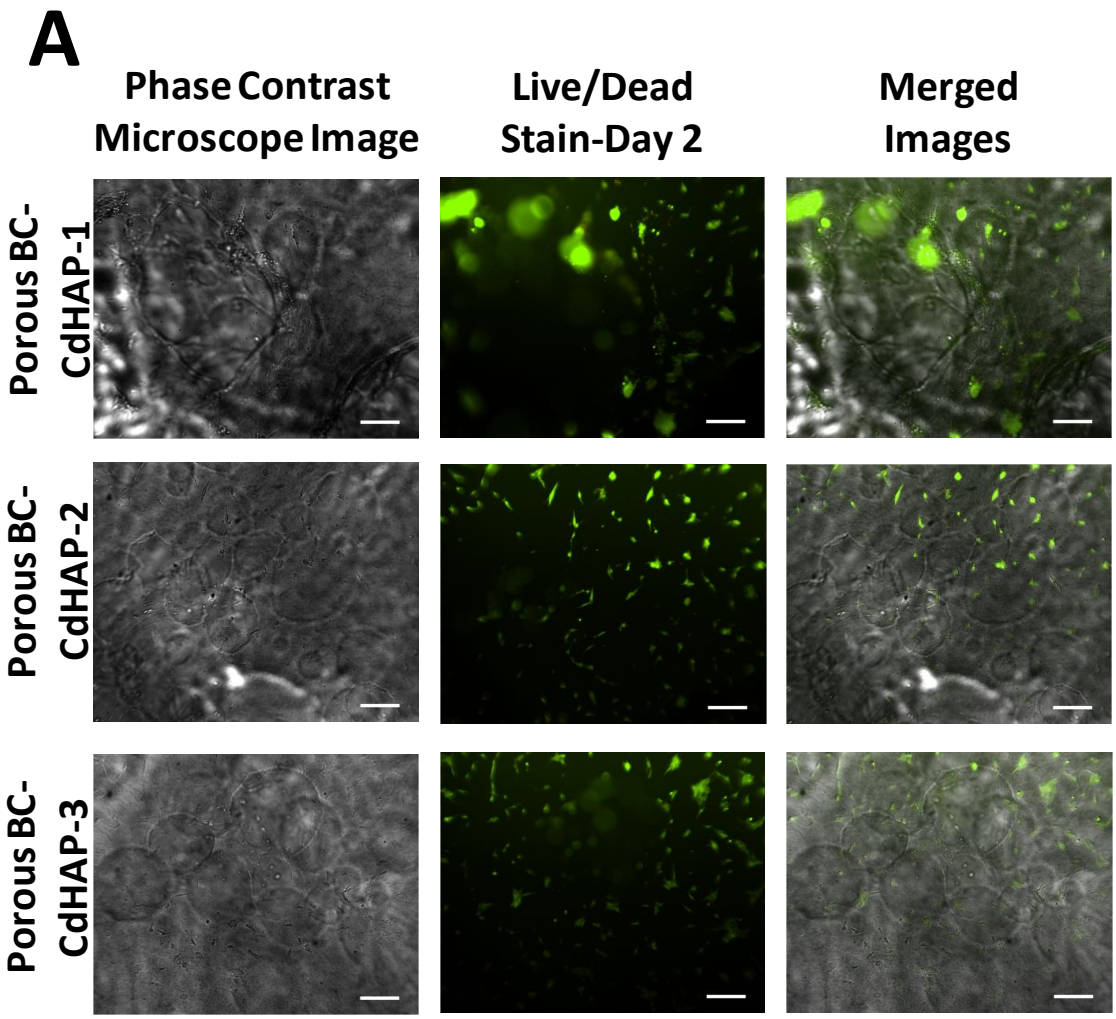

Figure 6.15: Continued.

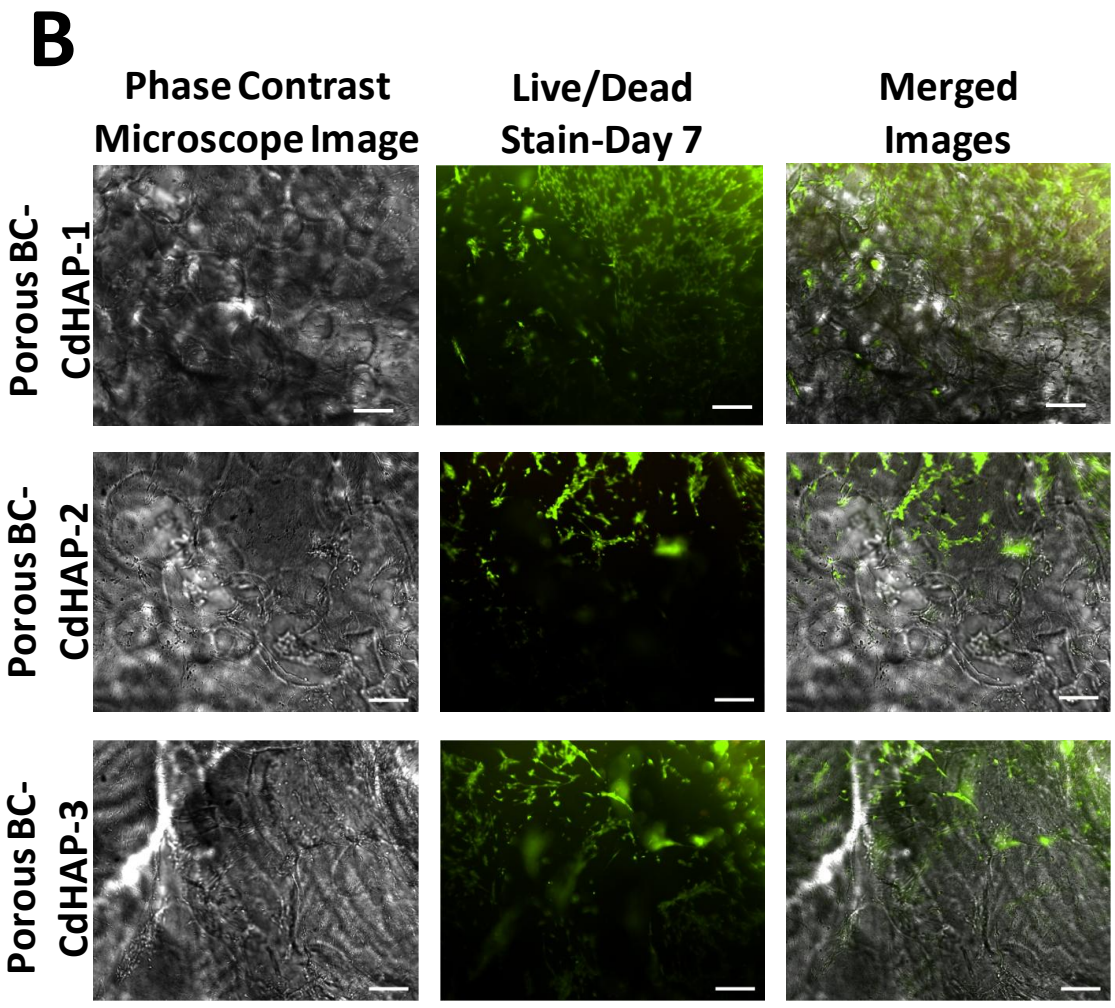

Figure 6.15: Continued.

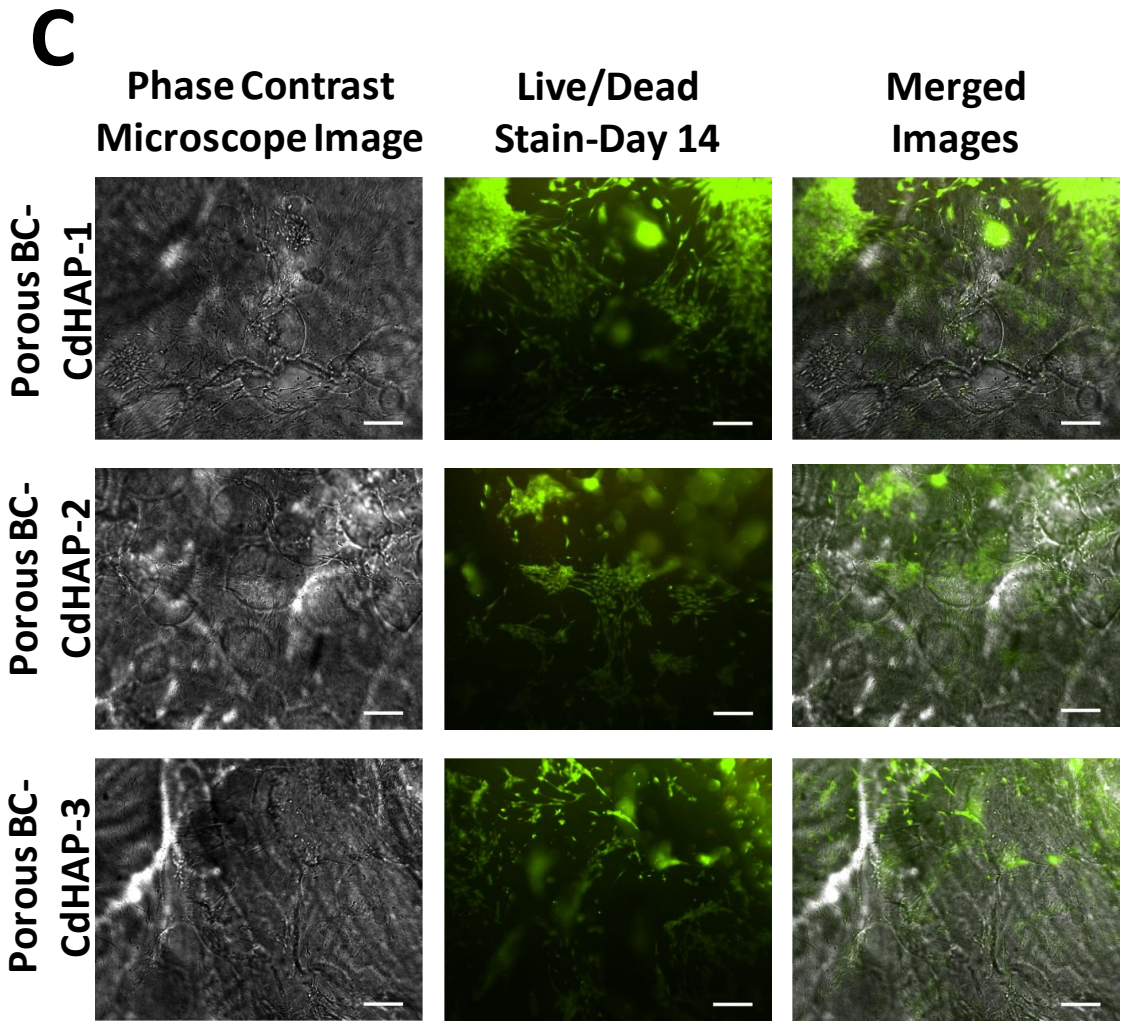

Figure 6.15: Continued.

Figure 6.16: Cellular adhesion and cell viability stained with calcein-AM and PI using fluorescent microscopy. Cell viability of EqMSCs (1.26×10^5 cells/cm^2) seeded for 2 (A), 7 (B), and 14 (C) days on porous OBC-CdHAP-1, porous OBC-CdHAP-2, and porous OBC-CdHAP-3, scaffolds.

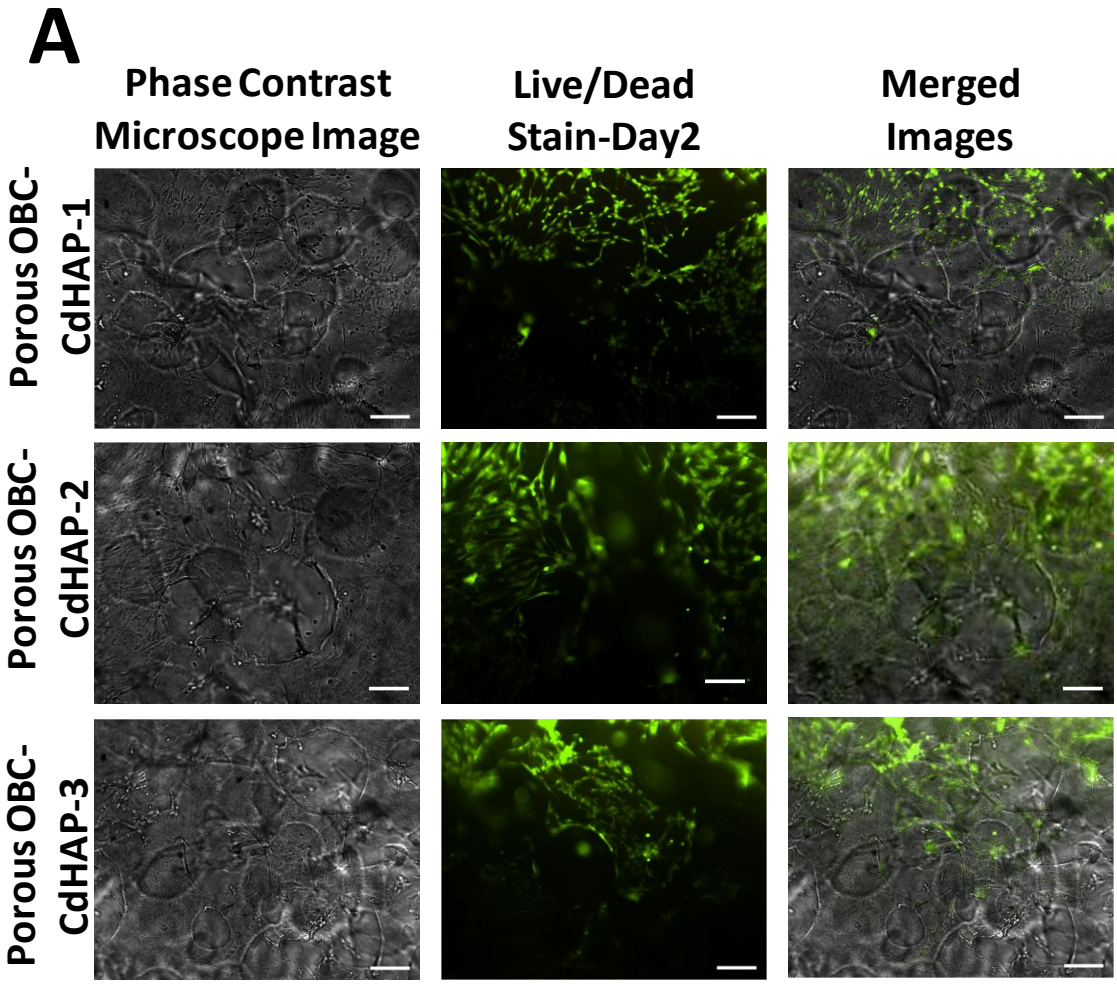

Figure 6.16: Continued.

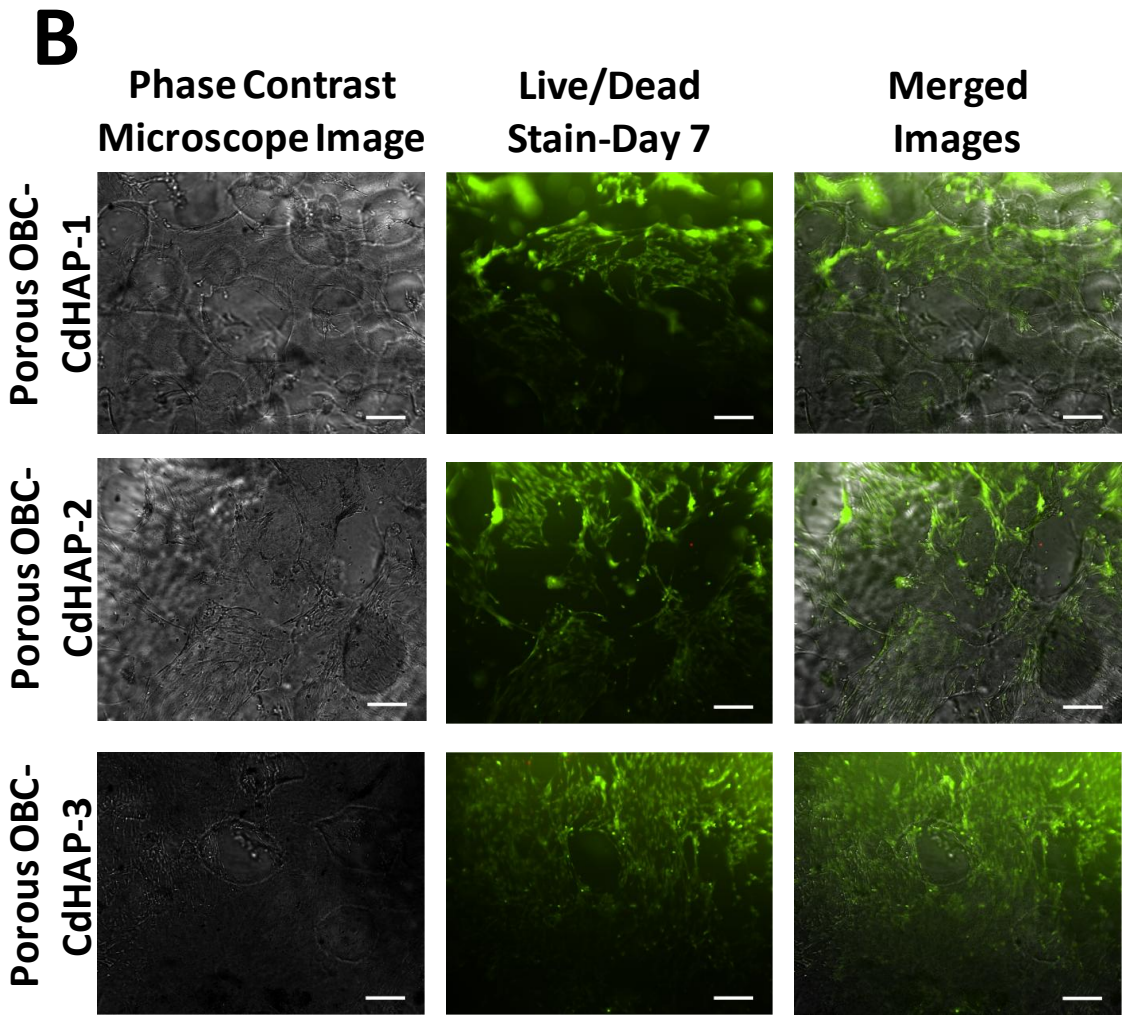

Figure 6.16: Continued.

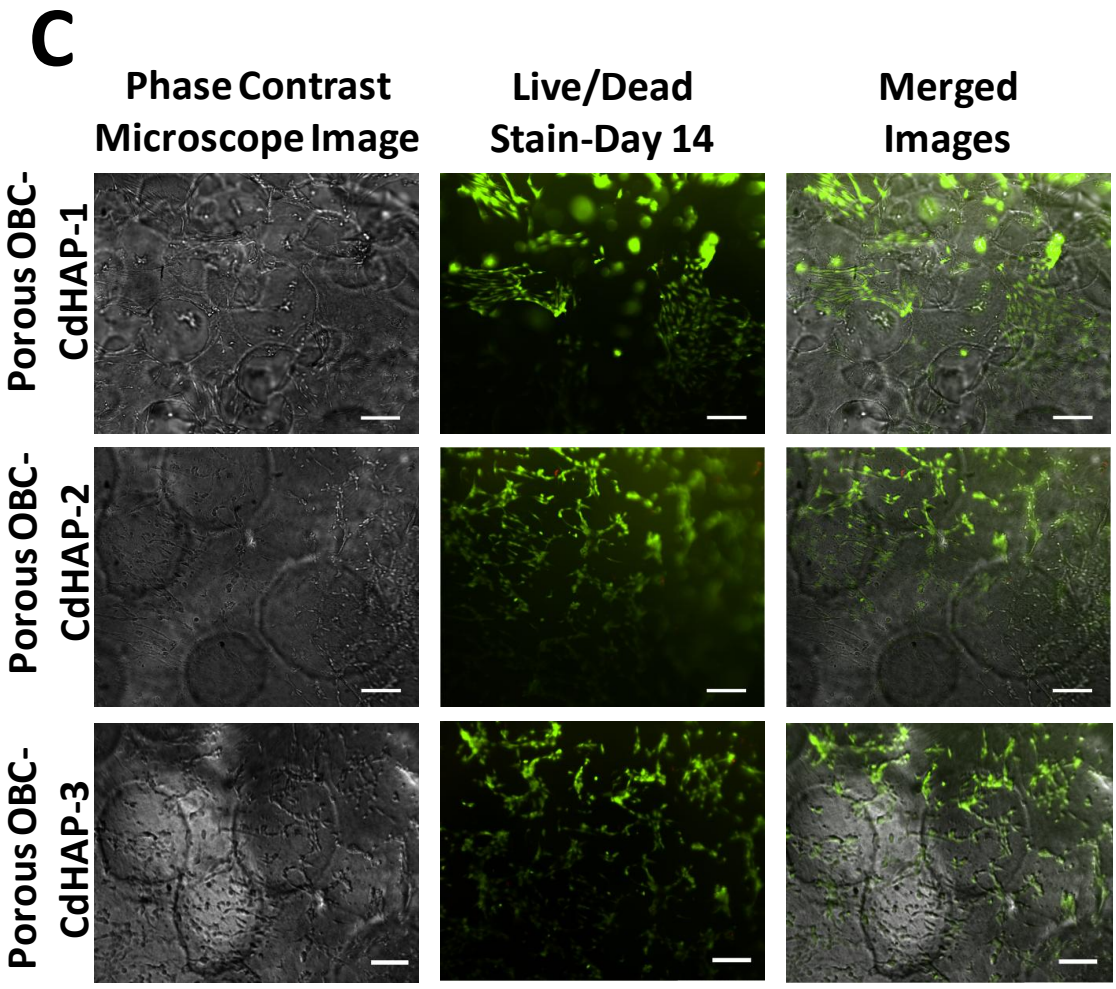

Figure 6.16: Continued.

6.5.2. In Vitro differentiation of EqMSCs

To further characterize the EqMSCs, they were induced to differentiate into osteocytes *in vitro* on the OBC-CdHAP-3 and porous OBC-CdHAP-3 scaffolds (Figure 6.17). Because a degradable scaffold is preferred for bone tissue engineering, and the EqMSCs demonstrated superior growth on the OBC-CdHAP-3 and porous OBC-CdHAP-3 (Figure 6.16.A, B), they were used for the *in vitro* differentiation assessment of the stem cells. As demonstrated, the EqMSCs seeded on the OBC-CdHAP-3 scaffolds similar to the cells on the porous OBC-CdHAP-3 exhibited the potential to differentiate into a bone with the use of induction media (Figure 6.17). Cells seeded on the porous OBC-CdHAP-3 completely transformed into a large calcified mass on the surface of the scaffold on the scaffold when induced with differentiation media (Figure 6.17). The cells seeded on the control scaffolds (without induction media) also differentiated into osteocytes although not to the same extend as the induced cell-scaffold system (Figure 6.17). The results support the fact that EqMSCs do not lose their potentials to differentiate when they adhere to OBC-CdHAP-3, and porous OBC-CdHAP-3. Figure 6.17 also confirms that the osteocytes have bridged and completely covered the micro-pores of the porous OBC-CdHAP-3. Alizarin red staining of BC scaffolds mineralized with CdHAP may result in non-specific staining of the calcium in the hydroxyapatite minerals. In Figure 6.17, the EqMSCs stained red compared to the substrates which stained orange. The orange color of the substrates in Figure 6.17 is attributed to the non-specific staining of the calcium in these CdHAP bacterial cellulose composite scaffolds.

The differentiation of EqMSCs into osteocytes as previously discussed is one of the key processes for bone regeneration. From a functional perspective, where cell therapy for musculoskeletal hindrances is the ultimate goal, it is fundamental that the cells do not lose or have reduced capacity of differentiation [127]. This study showed that EqMSCs have the capability to differentiate into osteocytes on the OBC-CdHAP-3 and porous OBC-CdHAP-3 scaffolds, an important characteristic for cartilage and bone regeneration.

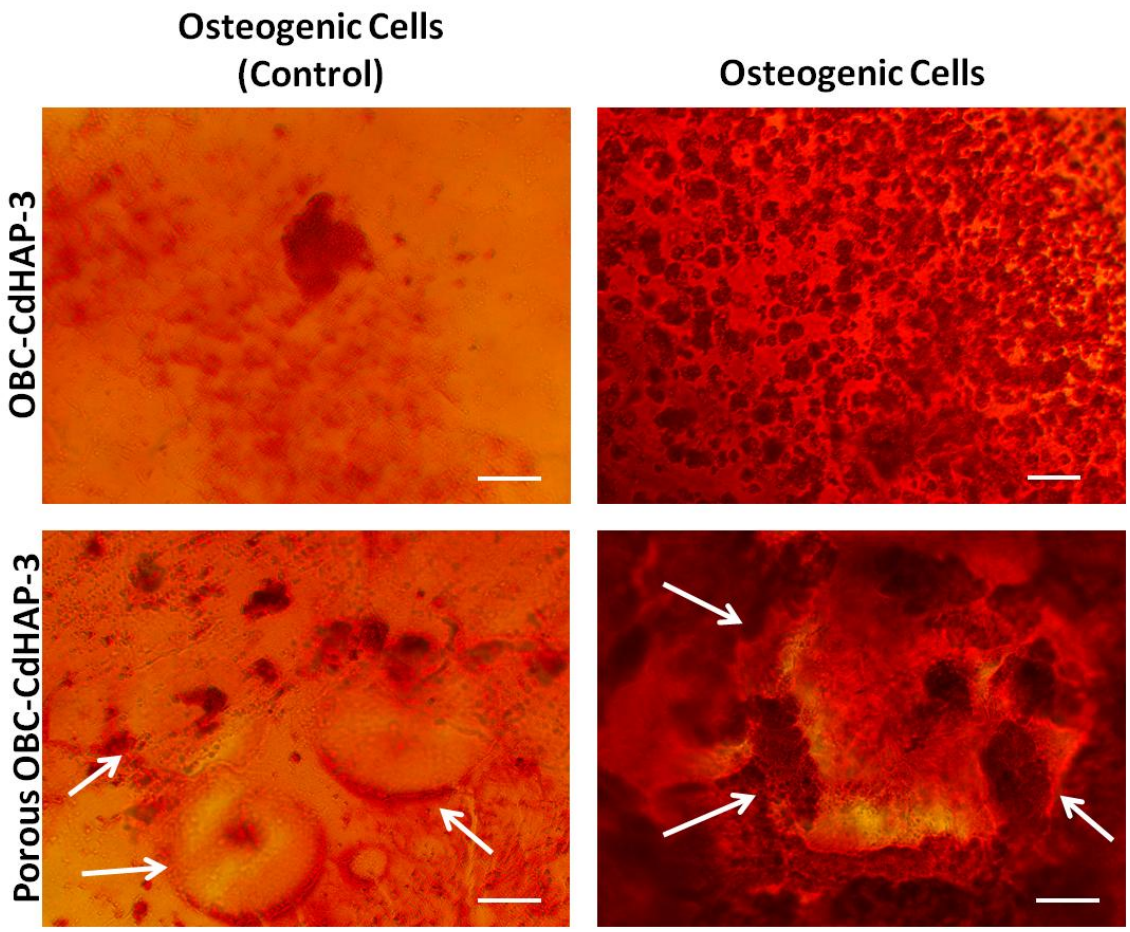

Figure 6.17: Osteogenesis differentiation capacity of EqMSCs. EqMSCs (5.0 x 10^4 cells/cm^2) were investigated for their *in vitro* trans-differentiation capacity on OBC-CdHAP-3 and porous OBC-CdHAP-3 after 7 days of differentiation. Osteogenesis was demonstrated by the detection of calcium in the mineralized matrix indicated by alizarin red stain shown in the differentiated cells. Arrows indicate pore structures in the scaffolds. Scale bars = 100 μm.

6.6. In Vitro Degradation Study of Oxidized Bacterial Cellulose Scaffolds

The degradation of BC-CdHAP sample composites were performed as described in Section 2.4 [68]. The samples analyzed for the degradation study include BC-CdHAP-3, OBC-CdHAP-3, porous BC-CdHAP-3, porous OBC-CdHAP-3, and their control scaffolds (native BC, OBC, porous BC, porous OBC). The samples were incubated in HEPES buffer at 37 °C for 14 days under static and dynamic incubations. During the incubation period, the supernatants were monitored using a UV-Vis spectrophotometer. After 14 days of incubations, the samples were rinsed, lyophilized and weighed. Corresponding BC samples which did not undergo the degradation process were lyophilized and weighted for comparison.

After 14 days of static and dynamic incubation, OBC, porous BC, and porous OBC scaffolds lost significant mass compared to their non-incubated BC samples (Figure 6.18). Compared to the non-mineralized BC samples, no significant change in the masses of the BC-CdHAP sample composites were observed. It was observed that mechanical disruptions in the form of shaking significantly affected the weight loss of the oxidized, porous, and porous oxidized BC scaffolds incubated under dynamic conditions (Figure 6.18). The results also show that mechanical disruptions in the form of sample handling may have contributed to the significant weight loss of the oxidized, porous, and porous oxidized BC scaffolds incubated under static conditions (Figure 6.18).

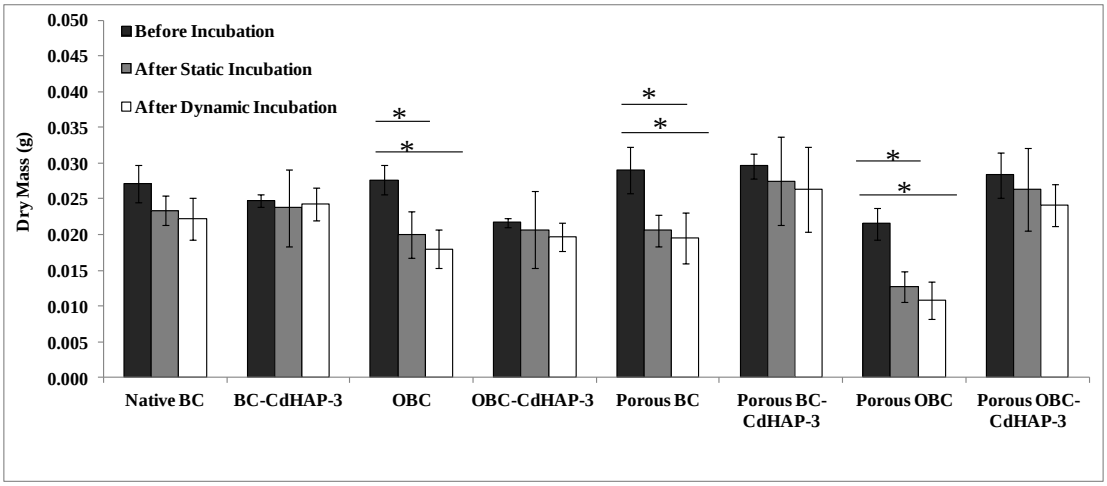

Figure 6.18: Comparison of sample masses before and after incubation in low salt HEPES buffer (pH 7.4) in static and dynamic conditions. Asterisks (*) indicates significant differences at $p<0.05$.

Dialdehyde cellulose has been proposed to degrade into 2,4-dihydroxybutyric acid, glycolic acid and carbohydrate (Figure 5.27) [159]. Previously, it has been demonstrated that dialdehyde degradation products including 2,4- dihydroxybutyric acid, glycolic acid and carbohydrate can be directly measured using UV-visible spectrophotometry (UV-VIS) [68]. The carbonyl groups present in 2,4- dihydroxybutyric acid, and glycolic acid in the degrading cellulose product have been proposed to absorb at 240 nm. Enzymatic hydrolysis and acid hydrolysis have been proposed to absorb at 260 nm during the degradation of the biological material indicative of cellulose fiber release as a result of physical disruption of scaffold.

In this study, the supernatants of the samples under static and dynamic agitation were measured at 240 and 260 nm every 2 days using UV-Vis and the results are shown in Figure 6.23-6.26. The results show compared to all the analyzed samples, OBC and porous OBC released a high concentration of the degradation product up to day 10 of the study for the static and dynamic studies (Figure 6.19-6.22). Under dynamic incubation, OBC-CdHAP and porous OBC-CdHAP samples released detectable degradation products (Figure 6.19-6.22).

Native BC and 39.6 mM TMAHP-BC released low levels of the detectable degradation products (Figure 6.19-6.22). .

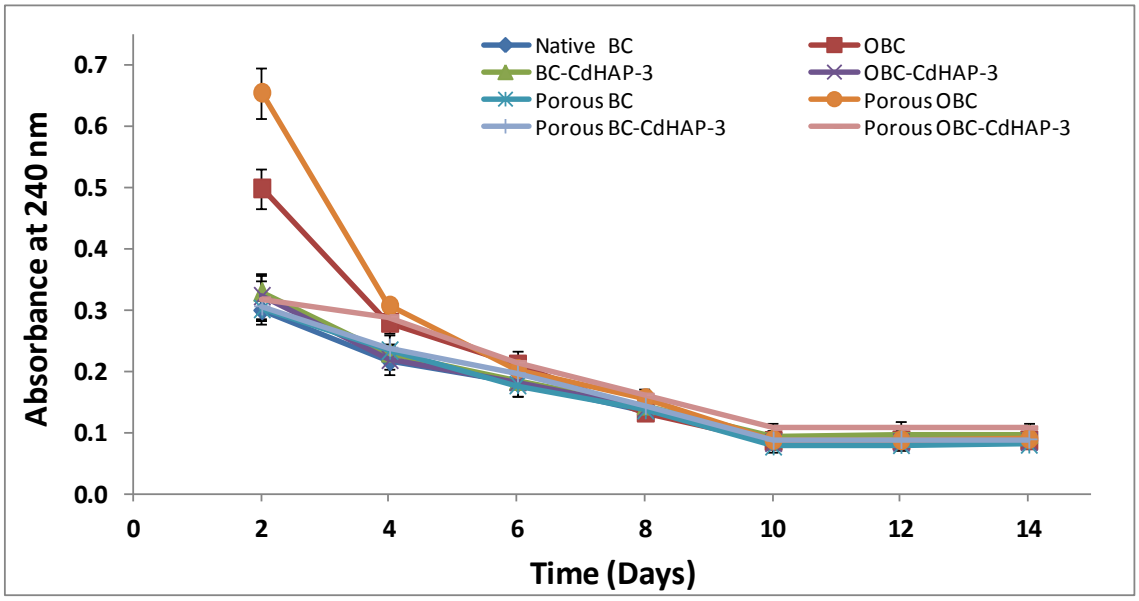

Figure 6.19: Absorbance versus time of HEPES supernatant of static samples at 240 nm. Comparison of native BC, OBC, BC-CdHAP-3, OBC-CdHAP-3, porous BC, porous OBC, porous BC-CdHAP-3, and porous OBC-CdHAP-3.

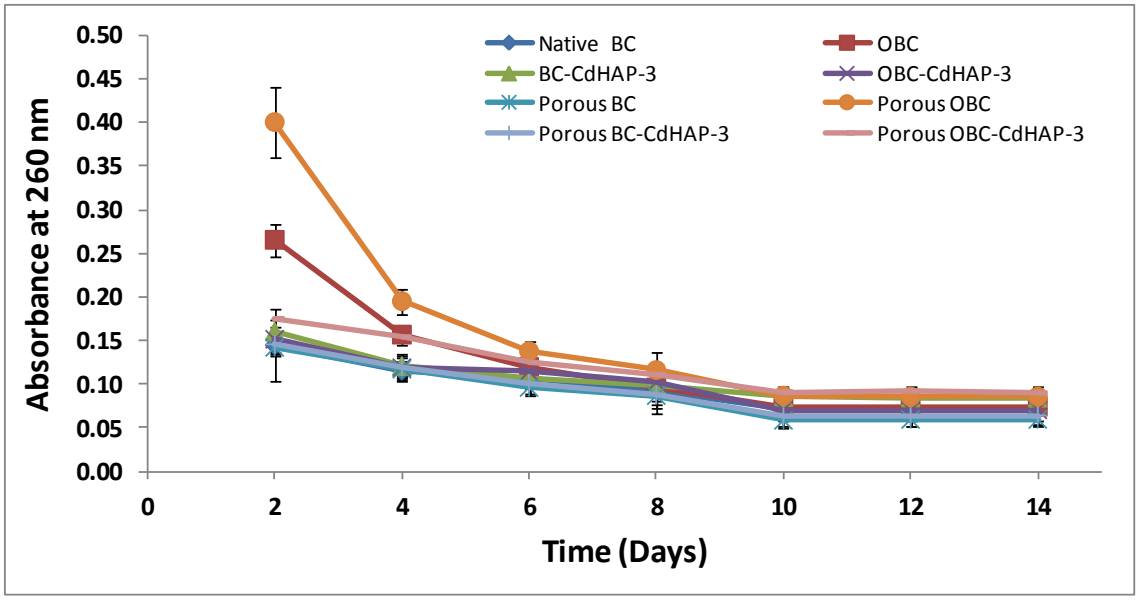

Figure 6.20: Absorbance versus time of HEPES supernatant of static samples at 260 nm. Comparison of native BC, OBC, BC-CdHAP-3, OBC-CdHAP-3, porous BC, porous OBC, porous BC-CdHAP-3, and porous OBC-CdHAP-3.

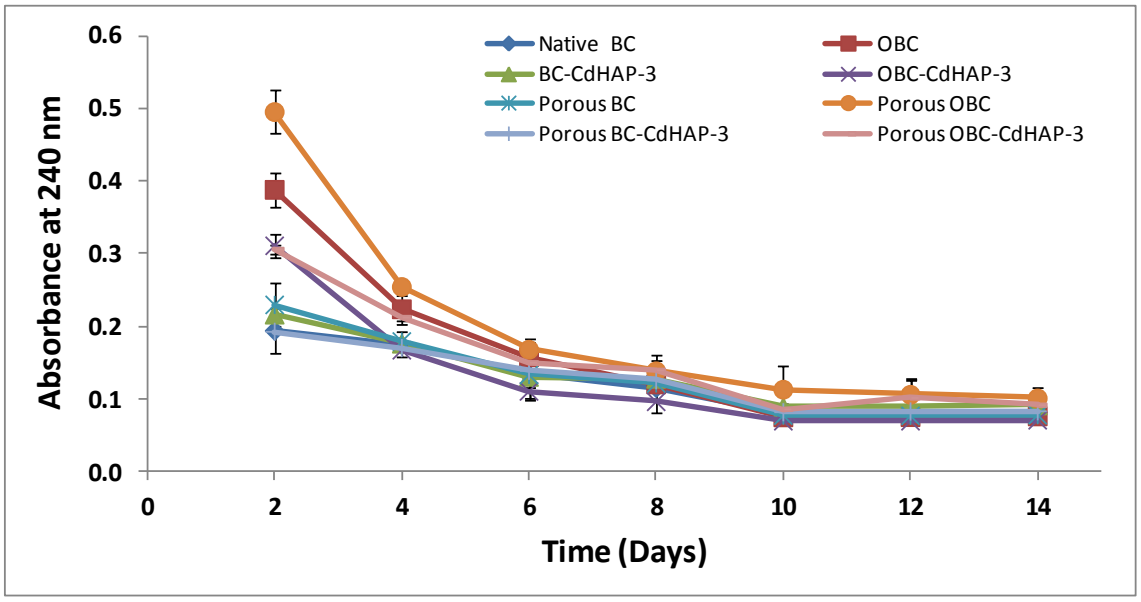

Figure 6.21: Absorbance versus time of HEPES supernatant of dynamic samples at 240 nm. Comparison of native BC, OBC, BC-CdHAP-3, OBC-CdHAP-3, porous BC, porous OBC, porous BC-CdHAP-3, and porous OBC-CdHAP-3.

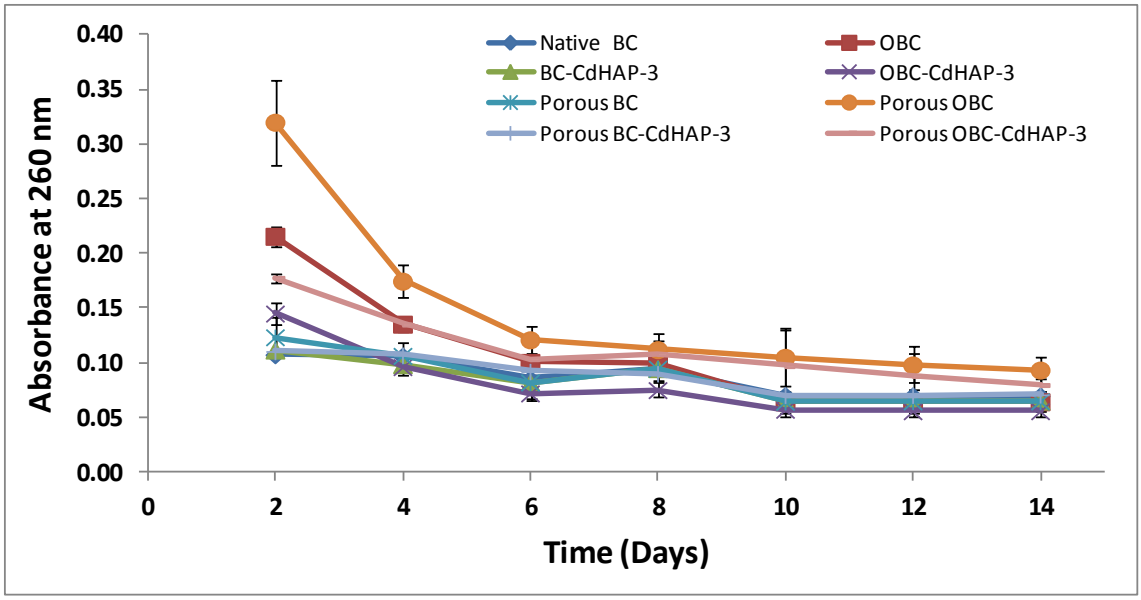

Figure 6.22: Absorbance versus time of HEPES supernatant of dynamic samples at 260 nm. Comparison of native BC, OBC, BC-CdHAP-3, OBC-CdHAP-3, porous BC, porous OBC, porous BC-CdHAP-3, and porous OBC-CdHAP-3.

6.7. Conclusions

In this study, CdHAP mineralization was successfully performed on nano-porous and micro-porous BC scaffolds as confirmed by FTIR. SEM micrographs confirmed that at lower magnification, the hydroxyapatite clusters in the scaffold matrixes appeared to have deposited mostly uniformly on the scaffolds as solid particles. However, at higher magnifications, SEM micrographs confirmed that hydroxyapatite deposited heterogeneously in the matrices as irregularly-shaped crystallites. Hydroxyapatite mineralization of the BC scaffolds appeared to have altered inter- and intramolecular hydrogen bonding in the cellulose structure, resulting in the impairment of scaffold's mechanical properties, more specifically scaffold strength and modulus.

The porous, oxidized and mineralized BC scaffold was cytocompatible with EqMSCs *in vitro*. The porous, oxidized and mineralized BC scaffold as well as the oxidized and mineralized BC scafold supported the adhesion, proliferation

and osteogenic differentiation of EqMSCs. The cells seeded on the oxidized and mineralized BC scaffolds were viable and proliferated on the scaffold. Based on these results, the porous, oxidized and mineralized BC scaffold appear to have potential as a scaffold for tissue engineering of bone.

CHAPTER VII
Analysis of Tubular-Shaped Bacterial Cellulose Scaffolds and its Composites

The objective of this study was to generate and characterize the morphological, cellular response and mechanical properties of biodegradable and mineralized BC-TS of varying diameters. BC-TS and its mineralized composites were developed to mimic the highly aligned collagen nanofibers and hydroxyapatite crystal structures inherent in native bone tissue. The biocompatible gel-like BC-TS was synthesized using the bacterium *Gluconacetobacter sucrofermentans* under static culture in oxygen-permeable silicone tubes. The BC-TS scaffolds were modified using periodate oxidation to yield biodegradable scaffolds. Additionally, CdHAP was deposited in the scaffolds to mimic native bone tissues. The mechanical and morphological properties of the resulting BC-TS and its composites were characterized in addition to their ability to support and maintain EqMSCs growth *in vitro*. Selected results from this study were published in the *Materials Research Society Symposium Proceedings* [107]. An invention disclosure application has also been filed for this technology.

7.1. Synthesis of Tubular-shaped Bacterial Cellulose Scaffold and its Composites

BC-TS was cultured on the inside surface (Figure 7.1.A) and on the outside surface (Figure 7.1.B) of silicone tubes as described in Section 2.2.3. After the inoculation of the bacterial culture, meshes of cellulose began to form within two to three days on the inside surface or on the outside surface of the silicone tubes, depending on the culture set-up. After 14 days of culture, a mass of cellulose in the shape of a tube forms on the surface of the silicone tube in culture as illustrated with the culture set-up consisting of bacterial medium on the

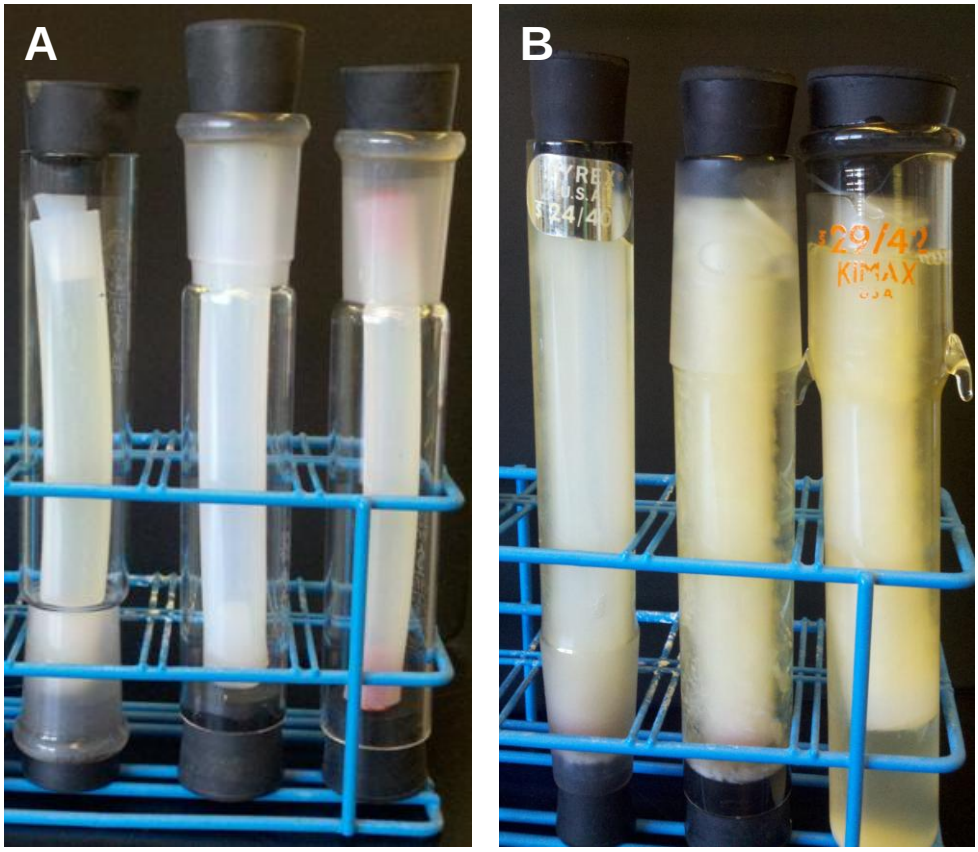

Figure 7.1: BC-TS culture consisting of bacterial culture on the inside surface (A) and on the outside surface (B) of silicone tubes.

outside surface of silicone tubes (Figure 7.1.B). The synthesized BC-TSs were harvested and then purified following the protocols in Section 2.2.3.

Four different sizes of BC-TS samples were successfully generated in oxygen-permeable silicone tubes inoculated with *Gluconacetobacter sucrofermentans* in a Schramm and Hestrin medium. BC-TS scaffolds synthesized on the inner surface of the 6.35 mm ID silicone tubes produced unbounded, swollen gelatinous scaffolds with 8.3 mm diameter and 1.6 mm thickness (Figure 7.2.A, Figure 7.3). BC-TS scaffolds synthesized on the outer surface of the 6.35 mm ID silicone tubes produced unbounded scaffolds with 20

mm diameter and 1.0 mm thickness (Figure 7.2.C, Figure 7.3). Therefore, the diameter of the scaffolds produced on the inner surface of the 6.35 mm ID silicone tubes were significantly smaller (Figure 7.2.A, Figure 7.3) than those produced on the outer surface of the equivalent size tube (Figure 7.2.C, Figure 7.3). Similar increase in scaffold diameter and decrease in thickness were observed with the BC-TS scaffolds synthesized on the inner surface of the 9.525 mm ID silicone tubes (13.5 mm water swollen diameter, 1.1 mm thickness) (Figure 7.2.B, Figure 3) compared to the outer surface of the equivalent tube size (24.2 mm water swollen diameter, 0.7 mm thickness) (Figure 7.2.D, Figure 3).

The oxidation of BC-TS (OBC-TS) was performed using sodium periodate as described in Section 2.2.5. CdHAP minerals were deposited within the unmodified BC-TS (BC-TS-CdHAP) and oxidized BC-TS (OBC-TS-CdHAP) by suspending the samples in 5.0 mM $CaCl_2$ solution followed by incubation in 3.0 mM Na_2HPO_4 solution to obtain CdHAP as described in Section 2.2.6.

Figure 7.2: Photographs of BC-TS scaffolds synthesized on the inside surface (A) and on the outside surface (C) of 6.35 mm ID silicone tubes. Photographs of BC-TS scaffolds synthesized on the inside surface (B) and on the outside surface (D) of the 9.525 mm ID silicone tubes. Insert is the top view image (E) of the four sizes of BC-TS hydrogels synthesized using silicone tubes.

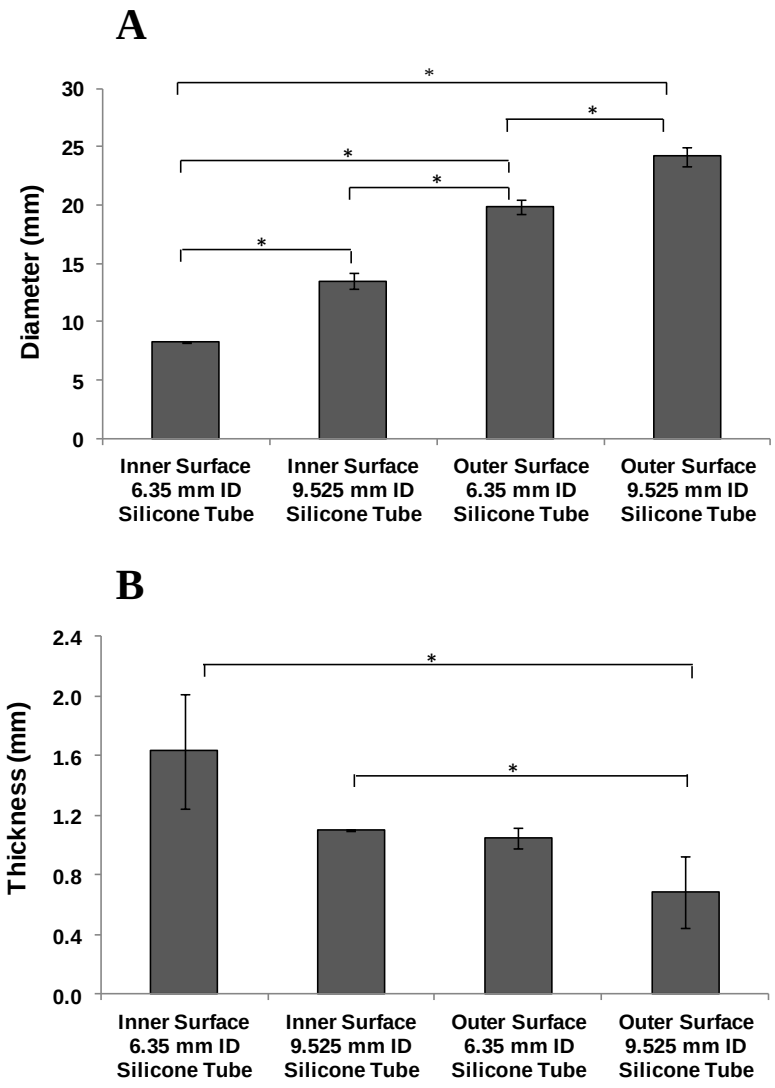

Figure 7.3: Diameter (A) and thickness (B) comparison of BC-TSs synthesized on the inside surface and on the outside surface of 6.35 mm and 9.525 mm silicone tubes. Asterisks (*) indicates significant differences at $p<0.05$.

7.2. Scanning Electron Microscopy

SEM images of the 8.3 mm BC-TS produced under various treatments demonstrated that aligned cellulose fibers were successfully generated in the scaffolds (Figure 7.4, 7.5.). SEM images of the BC-TS before (Figure 7.4.A) and after (Figure 7.4.B) periodate oxidation showed that the scaffolds maintained their morphological integrity of the nanofibers during the chemical reaction. CdHAP ceramics were successfully deposited in the non-oxidized scaffold (Figure 7.4.C) and oxidized scaffold (Figure 7.4.D) as illustrated in the SEM images.

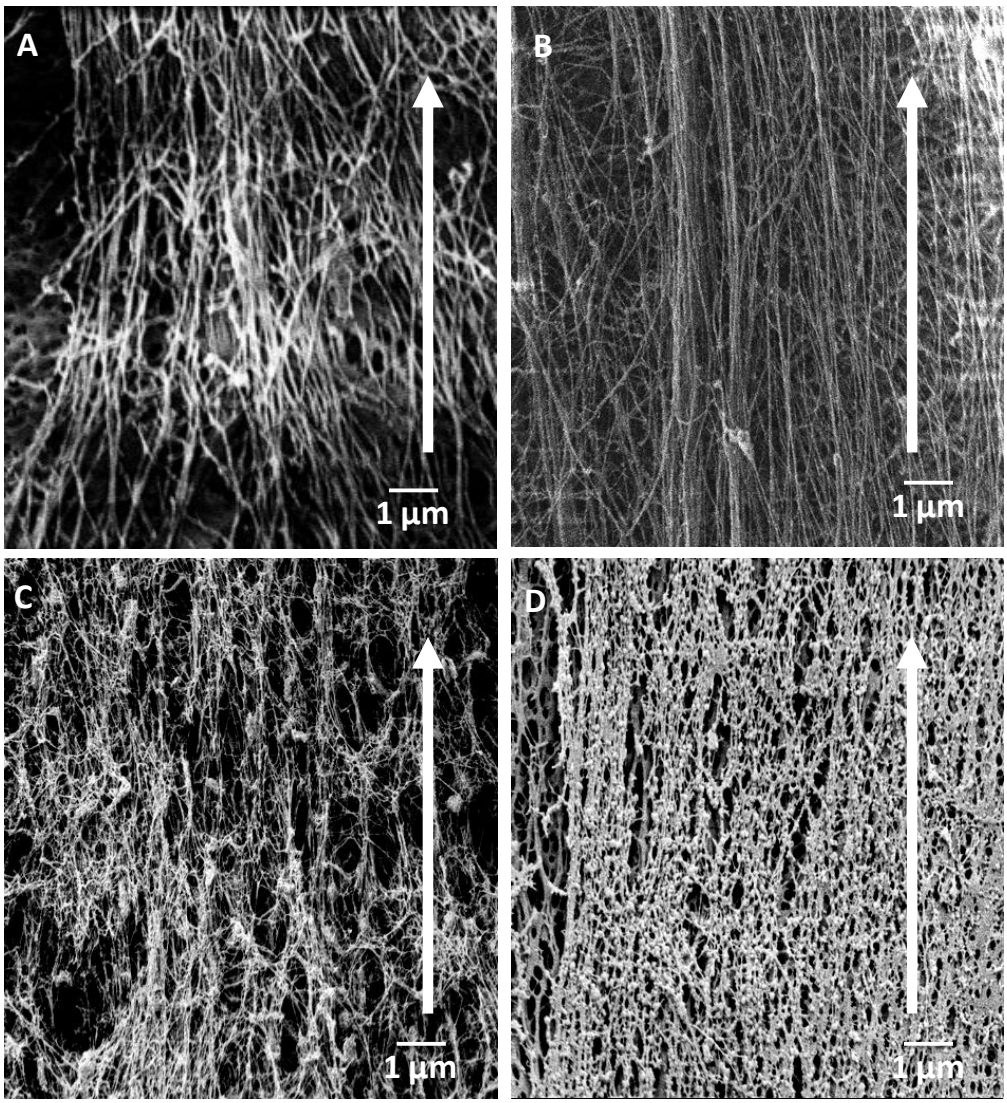

Figure 7.4: SEM images of 8.3 mm diameter BC-TS prepared using various treatments. SEM images of BC-TS (A), OBC-TS (B), BC-TS-CdHAP (C) and OBC-TS-CdHAP. Arrows indicate the direction of the longitudinal axis of the silicone tube during scaffold synthesis.

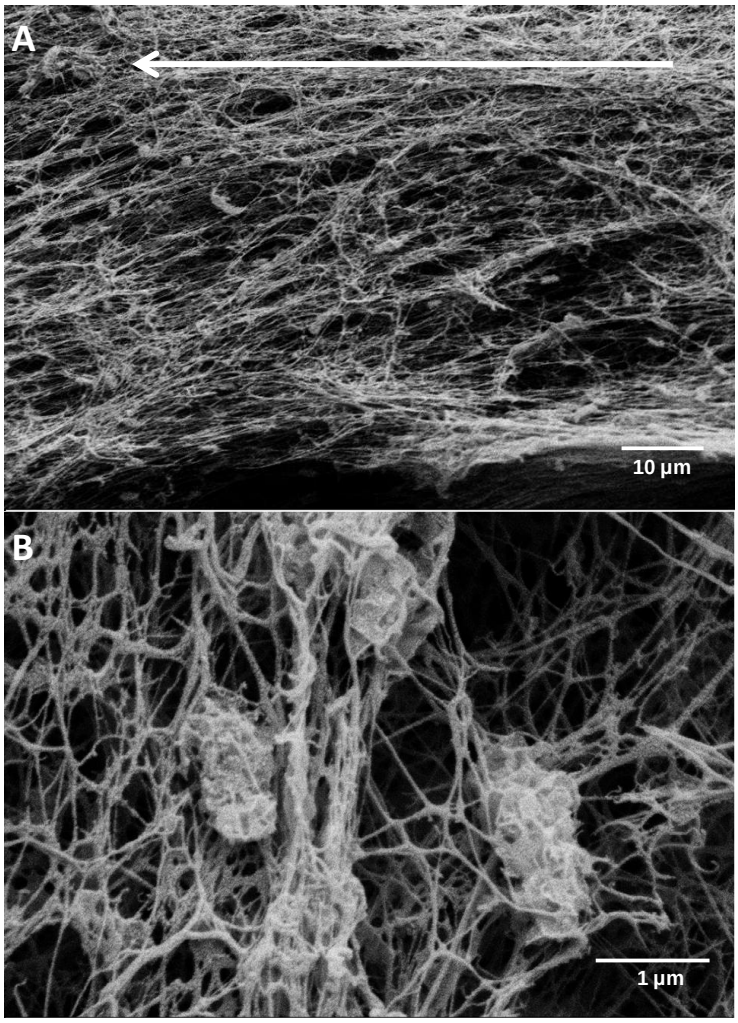

Figure 7.5: SEM images of 8.3 mm diameter BC-TS-CdHAP at 5000X (A) and 50000X. Arrows indicate the direction of the longitudinal axis of the silicone tube during scaffold synthesis.

7.3. Mechanical Testing

The mechanical properties 8.3 mm diameter BC-TS and its composites were determined at 5% strain. The ultimate tensile strength, strain at break, and elastic modulus values of the cellulose samples following lengthwise and breadthwise elongation and calculated from the engineering stress-strain curves are illustrated in Figure 7.6.

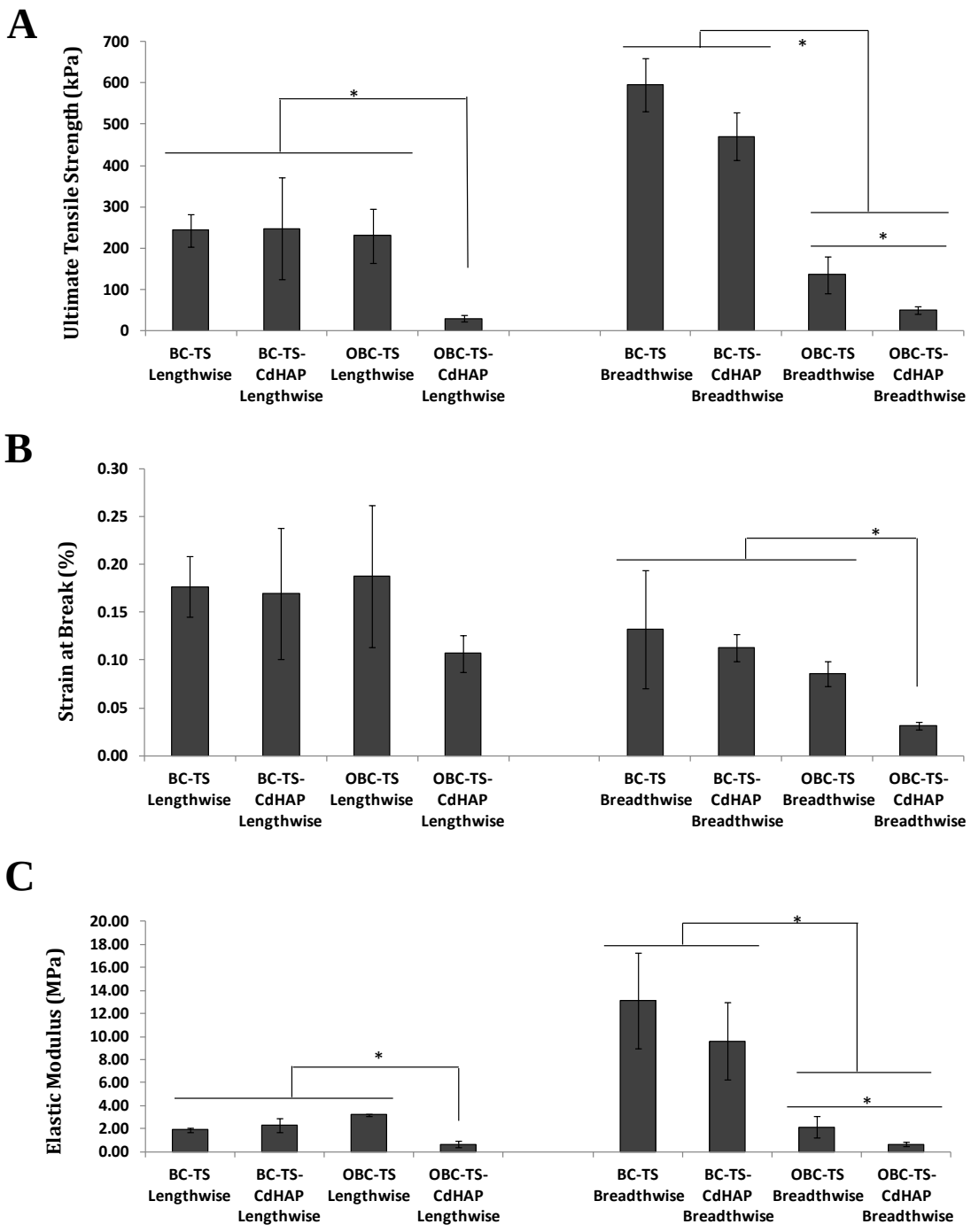

Figure 7.6: Comparison of ultimate tensile strengths (A), strain at breaks (B), and elastic moduli of 8.3 mm diameter BC-TS and its composites following lengthwise and breadthwise elongation.

7.4. Characterization of Cell and Tubular-shaped Bacterial Cellulose Scaffolds

7.4.1. Cellular Adhesion, Viability and Proliferation Assays

MTS assay analysis was performed to determine the viability of EqMSCs on the tubular BC and its composites. MTS assay analysis results of EqMSCs seeded on the tubular BC and its composites are shown in Figure 7.7. EqMSCs seeded on OBC-TS and OBC-TS-CdHAP showed a significant increase compared to BC-TS and BC-TS-CdHAP after the first days in culture. EqMSCs seeded on the scaffolds proliferated during the culture period. Furthermore, the stem cells demonstrated an increased proliferation rate during the two days in culture signifying that the cells were viable and proliferating on the scaffolds.

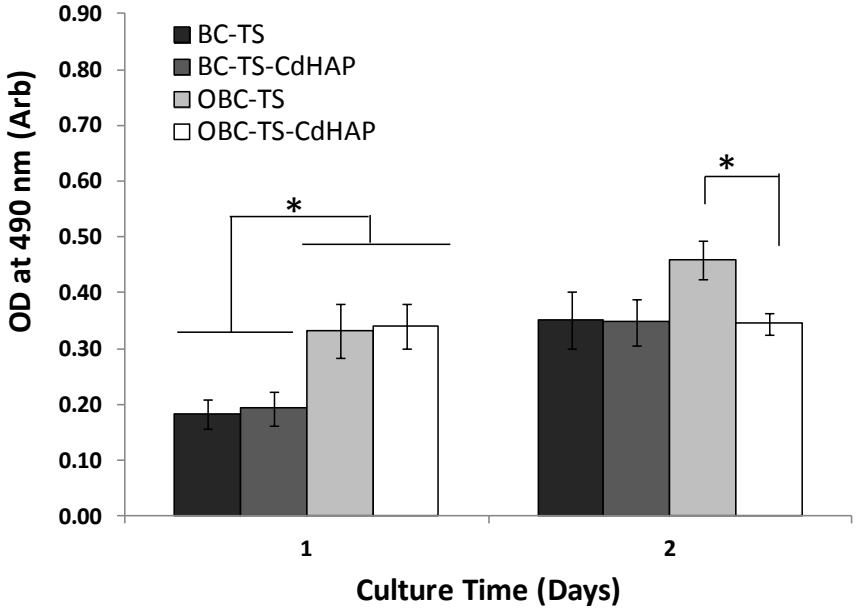

Figure 7.7: Cellular viability assay: MTS test. Comparison of proliferation of cells as determined by MTS assay for EqMSCs seeded on BC-TS, OBC-TS, BC-TS-CdHAP and OBC-TS-CdHAP scaffolds for 1 and 2 days ($p<0.05$).

Calcein-AM and PI staining was performed to visualize the viability of the cells on the scaffolds. After 1 day in culture (Figure 7.8), the cells on all the tubular BC scaffolds were viable. Compared to the non-oxidized BC scaffolds, the cells on the oxidized scaffolds (Figure 7.8.B, D) showed a more distinct mesenchymal stem cell phenotype of fully spread-out morphology on the scaffolds due to the chemistry and morphology of the scaffolds. The cells on the non-oxidized scaffolds (Figure 7.8.A, C) showed less elongated shapes and their morphology was round. We had previously illustrated that up to day 7 in culture, EqMSCs seeded on non-oxidized BC are round in shape (Figure 3.5). Additionally, EqMSCs do proliferate over time and by day 7 and day 14 demonstrated the full spread-out morphology on non-oxidized BCs (Figure 3.5).

As previously discussed, WGA, a carbohydrate-binding protein, selectively recognizes and binds to N‑acetylglucosamine sugars and sialic acid residues predominantly found on the plasma membrane. The WGA used is conjugated to convert to a strongly red fluorescent to achieve selective and simple staining of the plasma membrane of cells. DAPI is a blue fluorescent stain that has high cell permeability and bind strongly to the A-T rich regions in DNA, where its fluorescence is approximately 20-fold greater than in the non-bound state. Its selectivity for DNA and high cell permeability allows efficient staining of nuclei. Figure 7.9 shows that over a period of 24 h (1, 6, 12 and 24 h), EqMSCs-BC grows in population, were fully attached and well distributed throughout OBC-TS and OBC-TS-CdHAP. By 24 h, WGA staining clearly illustrates the cell membranes of EqMSCs with the fibroblast like morphology customary to EqMSC (Figure 7.9) on both oxidized BC-TS scaffolds. However, the non-oxidized BC-TS scaffolds maintained round morphology by 24 h in culture. DAPI staining confirmed large, round nuclei contained in the cell bodies. WGA/DAPI staining (Figure 7.9) confirms the MTS assay results (Figure 7.7) and the calein-AM/PI staining results (Figure 7.8) demonstrating that the EqMSC prefers the dialdehyde cellulose chemistry (i.e., OBC-TS and OBC-TS-CdHAP) upon cell seeding compared to non-oxidized cellulose.

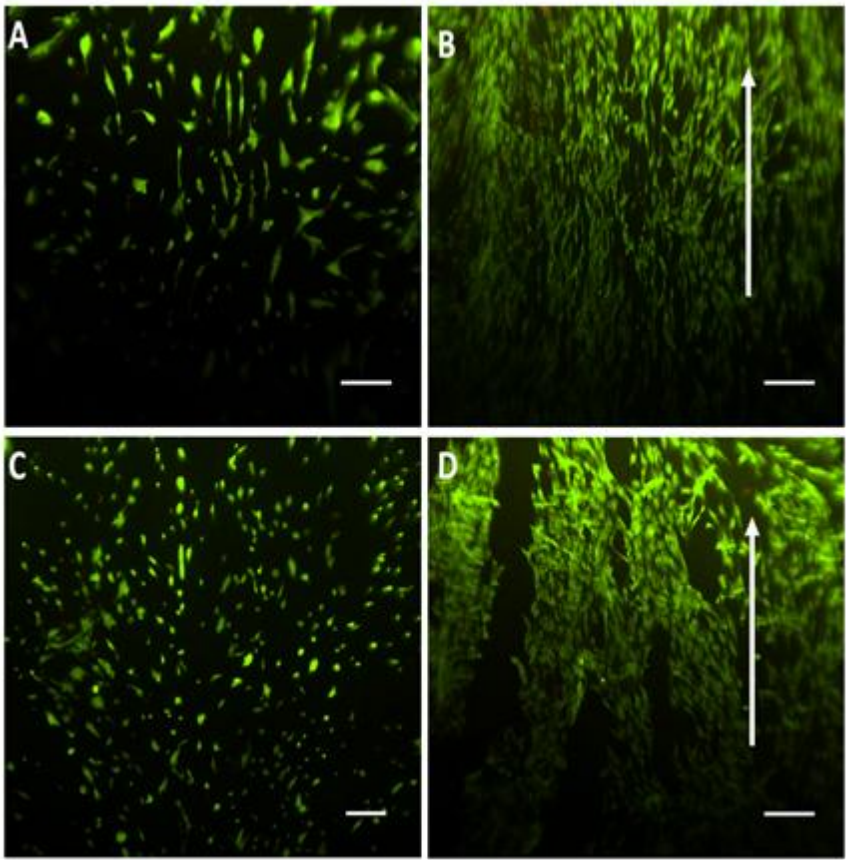

Figure 7.8: Cellular adhesion and cell viability stained with calcein-AM and PI using fluorescent microscopy. Cell viability of EqMSCs seeded on BC-TS (A), OBC-TS (B), BC-TS-CdHAP (C) and OBC-TS-CdHAP (D) after 1 day in culture. Cells were analyzed by calcein-AM which exhibits green fluorescence and demonstrates live cells and PI which displays red fluorescence and demonstrates dead cells. Fluorescent micrographs showed that the cells were viable on the scaffolds. Arrows in image show the aligned direction in which the cells grew following the orientation of the cellulose fibers of tubular BC. Scale bar = 100 µm..

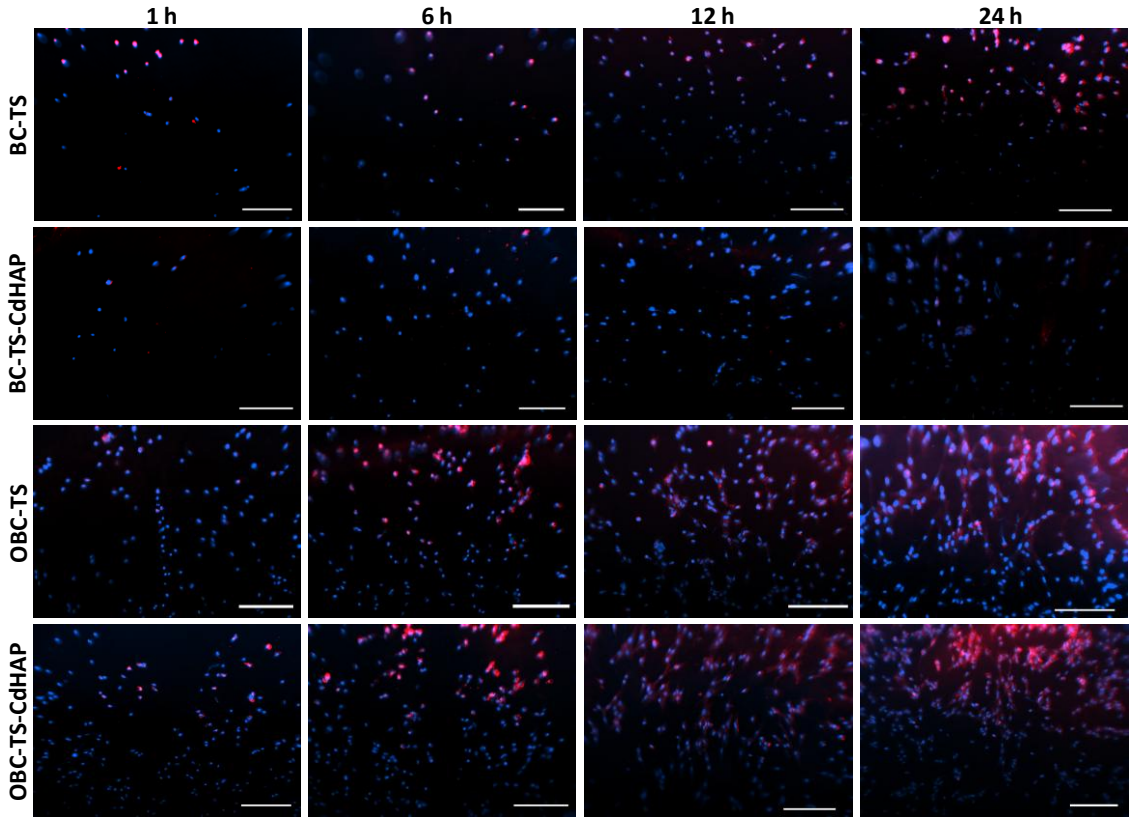

Figure 7.9: Cellular adhesion and morphology with WGA and DAPI staining. Fluorescent micrograph of EqMSCs-BC (7.9 x 10^4 cells/cm^2) showing adhesion and morphology of cell membrane stained using WGA and cell nucleus stained using DAPI at 1, 6, 12 and 24 h in culture. Scale bar = 100 µm

7.4.2. In Vitro differentiation of EqMSCs

EqMSCs successfully differentiated into osteocytes on the tubular BC scaffolds in vitro (Figure 7.10). The cells exhibited the potential to differentiate into bone cells on the induction media as indicated by the detection of calcium in the differentiated cells (Figure 7.10.E-7.10.H). These results show that BC-TS and its composites enable EqMSCs adhesion, proliferation and differentiation into osteocytes.

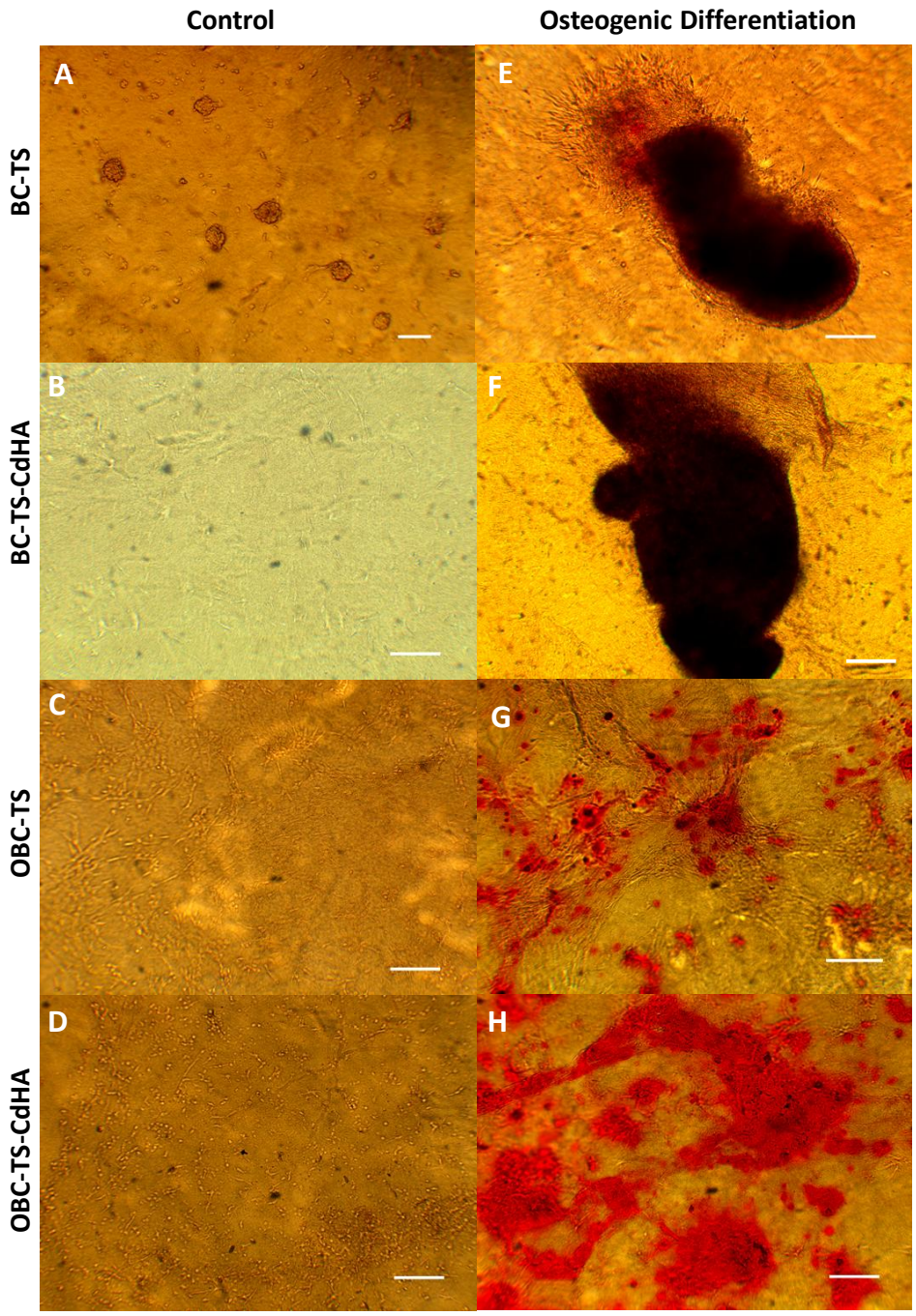

Figure 7.10: Osteogenesis differentiation capacity of EqMSCs on the tubular BC and its composites after 8 days of in vitro differentiation. Osteogenesis was induced using the β-glycerophosphate-based method and was demonstrated by the detection of calcium in the mineralized matrix indicated by alizarin red stain shown in E, F, G and H (A, B, C and D: non-induced controls). Scale bars = 100 µm.

7.5. Conclusions

Tubular-shaped BC is a natural nanofiber hydrogel scaffold that was successfully prepared, and the scaffold and its composites were characterized using SEM. The lyophilized tubular-shaped BC and its composites illustrated aligned nanofibrous morphology. It was demonstrated that the tubular-shaped BC scaffold and its composites were cytocompatible with EqMSCs *in vitro*. Tubular-shaped BC scaffolds and its composites supported the adhesion, proliferation and osteogenic differentiation of EqMSCs. It was shown that oxidation of the cellulose and aligned fiber morphology enhanced cell adhesion after 24 h. Tubular-shaped BC scaffolds and its composites are promising alternative scaffolds for bone tissue engineering. Based on these results, the oxidized, porous, and mineralized tubular-shaped BC scaffolds appear to have potential as a scaffold for tissue engineering of bone.

CHAPTER VIII
Future Studies

The multidisciplinary field of tissue engineering applies the principles of biology and engineering to develop tissue substitutes to restore, maintain, or improve the function of diseased or damaged mammalian tissues. This interdisciplinary effort in tissue development is promising because it includes the contributions of pertinent scientists and engineers, and may prove to offer the solution concerning the limited regenerative capacity and unsatisfactory treatment options currently available for bone and cartilage tissue replacements. Following the tissue engineering technique, appropriate cells such as stem cells are used to engineer biomaterial support scaffolds. These cell-based biomaterial scaffolds are delivered to injured sites to facilitate regeneration without causing immune responses. Biomaterials are largely designed to mimic the properties of the native extracellular matrix (ECM) it will replace in addition to supporting cell growth, and the process of new tissue formation [11]. However, there are several additional characteristic that are recommended for bone and cartilage biomaterial scaffolds such as biocompatibility, porosity and pore interconnectivity, biodegradability, ability to modify surface properties, and ability to design and shape the biomaterial in 3D [163].

In this dissertation research, the natural biomaterial scaffold BC was designed and shown to meet most of the recommended biomaterial properties including *in vitro* biodegradability and biocompatibility, porosity and pore interconnectivity, ability to chemically functionalize BC scaffolds surface to mimic bone or cartilage tissues, and ability to produce tubular-shaped or 3D BC scaffolds. For future studies, *in vivo* tissue graft studies using these BC-stem cell therapies in animal models is recommended in order to fully understand their *in vivo* biocompatibility, degradability, and potential to enable bone and cartilage tissue regenerations [164, 165]. Cartilage and bone wound studies can be

conducted using surgically created osteochondral defects in possible rabbit animal models [164] and bone defects in rat models [165]. From the work in Chapters 4 and 5, porous oxidized BC or 39.6 mM TMAHP porous OBC scaffolds is recommended for use in the *in vivo* studies regarding cartilage tissue engineering. From the work in Chapters 4 and 6, porous oxidized BC or porous oxidized and mineralized BC is recommended for use in the *in vivo* studies concerning bone tissue engineering. The formation of new cartilage and bone in the defect areas, biocompatibility, and biodegradability of the composites can be evaluated using histology immunohistochemistry [164, 165].

Besides *in vivo* assessment of the BC scaffolds engineered in this dissertation, additional BC modification for future research consideration is grafting growth factors present in stem cells and native tissue on BC scaffolds. Delivering growth factors from the BC scaffold has the potential to control and enhance cell growth, stimulate stem cell differentiations, and facilitate regeneration of the damaged native tissues which is advantageous for in vivo applications of the tissue engineered scaffold.

An ideal future study following the surface modification study in Chapter 5 is surface functionalization of the BC scaffold using secondary amines which are prevalent in GAGs. Such a study will reveal the true performance of stem cells on BC scaffolds modified with amine functionalities similar to those in native cartilage tissue.

REFERENCES

[1] Marolt D, Knezevic M, Novakovic GV. Bone tissue engineering with human stem cells. Stem Cell Res Ther. 2010;1:10-20.
[2] Palsson BO, Bhatia SN. Tissue Engineering. Upper Saddle River: Pearson Prentice Hall Bioengineering; 2004.
[3] National-Collaborating-Centre-for-Chronic-Conditions. Osteoarthritis: National clinical guideline for care and management in adults. London: Royal College of Physicians of London; 2008.
[4] Henson F, Getgood A. The use of scaffolds in musculoskeletal tissue engineering. Open Orthop J. 2011;5:261-6.
[5] Revell CM, Athanasiou KA. Success rates and immunologic responses of autogenic, allogenic, and xenogenic treatments to repair articular cartilage defects. Tissue Eng Part B Rev. 2009;15:1-15.
[6] Nandi SK, Roy S, Mukherjee P, Kundu B, De DK, Basu D. Orthopaedic applications of bone graft & graft substitutes: a review. Indian J Med Res. 2010;132:15-30.
[7] Awad HA, Wickham MQ, Leddy HA, Gimble JM, Guilak F. Chondrogenic differentiation of adipose-derived adult stem cells in agarose, alginate, and gelatin scaffolds. Biomaterials. 2004;25:3211-22.
[8] Langer R, Vacanti JP. Tissue Engineering. Science. 1993;260:920-6.
[9] Mooney DJ, Mikos AG. Growing new organs. Sci Am. 1999;280:60-5.
[10] Vacanti CA, Vacanti JP. Bone and cartilage reconstruction with tissue engineering approaches. Otolaryngol Clin North Am. 1994;27:263-76.
[11] Olson JL, Atala A, Yoo JJ. Tissue Engineering: Current Strategies and Future Directions. Chonnam Med J. 2011;47:1-13.
[12] Arnhold SJ, Goletz I, Klein H, Stumpf G, Beluche LA, Rohde C, et al. Isolation and characterization of bone marrow–derived equine mesenchymal stem cells. Am J Vet Res. 2007;68:1095-105.
[13] Pittenger MF, Mackay AM, Beck SC, Jaiswal RK, Douglas R, Mosca JD, et al. Multilineage Potential of Adult Human Mesenchymal Stem Cells. Science. 1999;284:143-7.
[14] Pittenger MF, Mbalaviele G, Black M, Mosca JD, Marshak DR. Mesenchymal stem cells. In: Koller MR, Palsson BO, Masters JRW, editors. Human cell culture Volume V: Primary mesenchymal cells. Dordrecht: Kluwer Academic Publishers; 2001. p. 189-207.
[15] Bryant PJ, Schwartz PH. Stem Cells. In: Monroe KR, Miller RB, Tobis J, editors. Fundamentals of the stem cell debate: The scientific, religious, ethical and political issues. Berkeley: University of California Press; 2008.
[16] Costa-Pinto AR, Correlo VM, Sol PC, Bhattacharya M, Charbord P, Delorme B, et al. Osteogenic Differentiation of Human Bone Marrow Mesenchymal Stem Cells Seeded on Melt Based Chitosan Scaffolds for Bone Tissue Engineering Applications. Biomacromolecules. 2009;10:2067-73.
[17] Stewart MC, Stewart AA. Mesenchymal Stem Cells: Characteristics, Sources, and Mechanisms of Action. Veterinary Clinics of North America-Equine Practice. 2011;27:243-61.

[18] Scott CT. Stem cell now: From the experiment that shook the world to the new politics of life. New York: Pi Press; 2006.
[19] Morrison SJ, Kimble J. Asymmetric and symmetric stem-cell divisions in development and cancer. Nature 2006;441 1068-74.
[20] He S, Nakada D, Morrison SJ. Mechanisms of stem cell self-renewal. Annu Rev Cell Dev Biol. 2009;25:377-406.
[21] Wikenheiser-Brokamp KA. Rb family proteins differentially regulate distinct cell lineages during epithelial development. Development. 2004;131 4299-310.
[22] Caplan AI. Mesenchymal stem cells. In: Lanza R, Gearhart J, Hogan B, Melton D, Pedersen R, Thomas ED, et al., editors. Essentials of stem cell biology 2nd Ed. 2 ed. Amsterdam: Academic Press; 2009. p. 243-8.
[23] Jung S-Y, Ko Y-J, Jang H-S, Kang S-W, Park J-H. The effect of carrier for BMP-2 delivery on histological aspects of tissue-engineered bone. Tissue Eng Regen Med. 2013;10:341-6.
[24] Wikesjö UM, Polimeni G, Qahash M. Tissue engineering with recombinant human bone morphogenetic protein-2 for alveolar augmentation and oral implant osseointegration: experimental observations and clinical perspectives. Clin Implant Dent Relat Res. 2005;7:112-9.
[25] Lee K, Silva EA, Mooney DJ. Growth factor delivery-based tissue engineering: general approaches and a review of recent developments. J R Soc Interface. 2011 8:153-70.
[26] Fakhry M, Hamade E, Badran B, Buchet R, Magne D. Molecular mechanisms of mesenchymal stem cell differentiation towards osteoblasts. World J Stem Cells. 2013;5:136-48.
[27] Bukka P, McKee MD, Karaplis AC. Molecular regulation of osteoblast differentiation. In: Bronner F, Farach-Carson MC, editors. Bone Formation. London, UK: Springer-Verlag; 2004. p. 1-17.
[28] Karperien M, Roelen B, Poelmann R, Gittenberger-deGroot A, Hiercck B, DeRuiter M, et al. Morphogenesis, generation of tissue in the embryo. In: Van Blitterswijk C, Thomsen P, Lindahl A, Hubbell J, Williams DF, Cancedda R, et al., editors. Tissue Engineering. London, UK: Elsevier Academic Press; 2008. p. 27-72.
[29] Martin I, Padera RF, Vunjak-Novakovic G, Freed LE. In vitro differentiation of chick embryo bone marrow stromal cells into cartilaginous and bone-like tissues. Journal of Orthopaedic Research. 1998;16:181-9.
[30] Huang CYC, Reuben PM, D'Ippolito G, Schiller PC, Cheung HS. Chondrogenesis of human bone marrow-derived mesenchymal stem cells in agarose culture. Anatomical Record Part a-Discoveries in Molecular Cellular and Evolutionary Biology. 2004;278A:428-36.
[31] Mauck RL, Yuan X, Tuan RS. Chondrogenic differentiation and functional maturation of bovine mesenchymal stem cells in long-term agarose culture. Osteoarthritis and Cartilage. 2006;14:179-89.
[32] Huang WB, Carlsen B, Wulur I, Rudkin G, Ishida K, Wu B, et al. BMP-2 exerts differential effects on differentiation of rabbit bone marrow stromal cells grown in two-dimensional and three-dimensional systems and is required for in vitro bone formation in a PLGA scaffold. Experimental Cell Research. 2004;299:325-34.

[33] Williams CG, Kim TK, Taboas A, Malik A, Manson P, Elisseeff J. In vitro chondrogenesis of bone marrow-derived mesenchymal stem cells in a photopolymerizing hydrogel. Tissue Engineering. 2003;9:679-88.
[34] Liao HT, Chen CT, Chen JP. Osteogenic Differentiation and Ectopic Bone Formation of Canine Bone Marrow-Derived Mesenchymal Stem Cells in Injectable Thermo-Responsive Polymer Hydrogel. Tissue Engineering Part C-Methods. 2011;17:1139-49.
[35] Wang XJ, Huang H, Yang F, Xia LG, Zhang WJ, Jiang XQ, et al. Ectopic study of tissue-engineered bone complex with enamel matrix proteins, bone marrow stromal cells in porous calcium phosphate cement scaffolds, in nude mice. Cell Proliferation. 2011;44:274-82.
[36] Ranera B, Lyahyai J, Romero A, Vázquez FJ, Remacha AR, Bernal ML, et al. Immunophenotype and gene expression profiles of cell surface markers of mesenchymal stem cells derived from equine bone marrow and adipose tissue. Vet Immunol Immunopathol. 2011;144:147-54.
[37] Advisory Committee Meeting: Cellular, Tissue and Gene Therapies Advisory Committee; 2005.
[38] Paris DBBP, Stout TAE. Equine embryos and embryonic stem cells: Defining reliable markers of pluripotency. Theriogenology. 2010;74:516-24.
[39] Goodrich LR, Hidaka C, Robbins PD, Evans CH, Nixon AJ. Genetic modification of chondrocytes with insulin-like growth factor-1 enhances cartilage healing in an equine model. J Bone Joint Surg Br. 2007;89 B:672-85.
[40] Smith RK, Korda M, Blunn GW, Goodship AE. Isolation and implantation of autologous equine mesenchymal stem cells from bone marrow into the superficial digital flexor tendon as a potential novel treatment. Equine Vet J. 2003;35:99-102.
[41] Koch TG, Berg LC, Betts DH. Concepts for the clinical use of stem cells in equine medicine. Can Vet J. 2008;49:1009–17.
[42] Seo J-p, Tanabe T, Tsuzuki N, Haneda S, Yamada K, Furuoka H, et al. Effects of bilayer gelatin/β-tricalcium phosphate sponges loaded with mesenchymal stem cells, chondrocytes, bone morphogenetic protein-2, and platelet rich plasma on osteochondral defects of the talus in horses. Res Vet Sci. 2013;95:1210-6.
[43] Tsuzuki N, Seo JP, Haneda S, Yamada K, Furuoka H, Tabata Y, et al. Bioengineered osteochondral precursor for treatment of osteochondritis dissecans in a Thoroughbred filly. Aust Vet J. 2013;91:411-5.
[44] McDuffee LA, Pack L, Lores M, Wright GM, Esparza-Gonzalez B, Masaoud E. Osteoprogenitor Cell Therapy in an Equine Fracture Model. Vet Surg. 2012;41:773-83.
[45] Figueroa RJ, Koch TG, Betts DH. Osteogenic differentiation of equine cord blood multipotent mesenchymal stromal cells within coralline hydroxyapatite scaffolds in vitro. Vet Comp Orthopaed 2011;24:354-62.
[46] Kopesky PW, Lee HY, Vanderploeg EJ, Kisiday JD, Frisbie DD, Plaas AHK, et al. Adult equine bone marrow stromal cells produce a cartilage-like ECM mechanically superior to animal-matched adult chondrocytes. Matrix Biol. 2010;29:427-38.
[47] Kisiday JD, Kopesky PW, Evans CH, Grodzinsky AJ, McIlwraith CW, Frisbie DD. Evaluation of adult equine bone marrow- and adipose-derived progenitor cell chondrogenesis in hydrogel cultures. J Orthop Res. 2008;26:322-31.

[48] Raabe O, Shell K, Fietz D, Freitag C, Ohrndorf A, Christ HJ, et al. Tenogenic differentiation of equine adipose-tissue-derived stem cells under the influence of tensile strain, growth differentiation factors and various oxygen tensions. Cell Tissue Res. 2013;352:509-21.
[49] Youngstrom DW, Barrett JG, Jose RR, Kaplan DL. Functional Characterization of Detergent-Decellularized Equine Tendon Extracellular Matrix for Tissue Engineering Applications. Plos One. 2013;8.
[50] Cui D, Daley W, Naftel JP, Lynch JC, Haines DE, Yang G, et al. Atlas of Histology: With Functional and Clinical Correlations. 1st ed. Philadelphia: Wolters Kluwer Health/Lippincott Williams & Wilkins; 2011.
[51] Ross MH, Pawlina W. Histology: A Text and Atlas. 6th ed. Baltimore: Wolters Kluwer Health/Lippincott Williams & Wilkins; 2011.
[52] Tortora GJ, Grabowski SR. Principles of Anatomy and Physiology. 10th ed. New York: John Wiley & Sons, Inc.; 2003.
[53] Bigg HF, Rowan AD, Barker MD, Cawston TE. Activity of matrix metalloproteinase-9 against native collagen types I and III. FEBS J. 2007;274:1246-55.
[54] Discher DE, Mooney DJ, Zandstra PW. Growth Factors, Matrices, and Forces Combine and Control Stem Cells. Science. 2009;324:1673-7.
[55] Motherway JA, Verschueren P, Van der Perre G, Sloten JV, Gilchrist MD. The mechanical properties of cranial bone: The effect of loading rate and cranial sampling position. J Biomech. 2009;42:2129-35.
[56] Martini FH, Nath JL, Bartholomew EF. Fundamentals of anatomy and physiology. 9th ed. Upper Saddle River, NJ: Pearson Education; 2011.
[57] Fontana J, De Souza A, Fontana C, Torriani I, Moreschi J, Gallotti B, et al. *Acetobacter* cellulose pellicle as a temporary skin substitute. Appl Biochem Biotechnol. 1990;24-25:253-64.
[58] TenHuisen KS, Brown PW. Formation of calcium-deficient hydroxyapatite from α-tricalcium phosphate. Biomaterials. 1998;19:2209-17.
[59] Akkouch A, Zhang Z, Rouabhia M. Engineering bone tissue using human dental pulp stem cells and an osteogenic collagen-hydroxyapatite-poly(ʟ-lactide-co-ε-caprolactone) scaffold. J Biomater Appl. 2013.
[60] Chen JN, Chen HA, Li P, Diao HJ, Zhu SY, Dong L, et al. Simultaneous regeneration of articular cartilage and subchondral bone in vivo using MSCs induced by a spatially controlled gene delivery system in bilayered integrated scaffolds. Biomaterials. 2011;32:4793-805.
[61] Chen JP, Chang YS. Preparation and characterization of composite nanofibers of polycaprolactone and nanohydroxyapatite for osteogenic differentiation of mesenchymal stem cells. Colloids and Surfaces B-Biointerfaces. 2011;86:169-75.
[62] Jeong KI, Kim SG, Moon SY, Oh JS, Jo JH, Lim HS, et al. Experimental Study of Osseointegration and Stability of Intentionally Exposed Hydroxyapatite Coating Implants. J Korean Assoc Maxillofac Plast Reconstr Surg. 2012;34:12-6.
[63] Maniatopoulos C, Sodek J, Melcher AH. Bone formation in vitro by stromal cells obtained from bone marrow of young adult rats. Cell and Tissue Research. 1988;254:317-30.

[64] Oliveira JM, Rodrigues MT, Silva SS, Malafaya PB, Gomes ME, Viegas CA, et al. Novel hydroxyapatite/chitosan bilayered scaffold for osteochondral tissue-engineering applications: Scaffold design and its performance when seeded with goat bone marrow stromal cells. Biomaterials. 2006;27:6123-37.
[65] Wahl DA, Czernuszka JT. Collagen-hydroxyapatite composites for hard tissue repair. Eur Cell Mater. 2006;11:43-56.
[66] Blokhuis TJ, Termaat MF, den Boer FC, Patka P, Bakker FC, Haarman HJTM. Properties of calcium phosphate ceramics in relation to their in vivo behavior. J Trauma. 2000;48:179-86.
[67] Park J, Lakes RS. Biomaterials: An introduction. 3rd ed. New York, NY: Springer; 2007.
[68] Hutchens S, Benson R, Evans B, Rawn C, O'Neill H. A resorbable calcium-deficient hydroxyapatite hydrogel composite for osseous regeneration. Cellulose. 2009;16:887-98.
[69] Hutchens SA, Benson RS, Evans BR, O'Neill HM, Rawn CJ. Biomimetic synthesis of calcium-deficient hydroxyapatite in a natural hydrogel. Biomaterials. 2006;27:4661-70.
[70] Klein CPAT, Driessen AA, de Groot K, van den Hooff A. Biodegradation behavior of various calcium phosphate materials in bone tissue. J Biomed Mater Res A. 1983;17:769
[71] Gregoire M, Orly J, Menanteau J, Heughebaert M, Kerebel B. In vitro interactions between calcium phosphate biomaterials and human fibroblastic cells. II Incidences on the behavior of cultured gingival cells. In: De Putter C, editor. Implant Materials in Biofunction. Amsterdam: Elsevier Science; 1988. p. 215.
[72] Jansen JA, De Wijn JR, Wolters-Lutgerhorst JML, Van Mullem PJ. Ultrastructural Study of Epithelial Cell Attachment to Implant Materials. J Dent Res. 1985;64:891-6.
[73] Van Blitterswijk CA, Kuijpers W, Daems WT, Grote JJ. Epithelial Reactions to Hydroxyapatite: An in Vivo and in Vitro Study. Acta Oto-laryngologica. 1986;101:231-41.
[74] van Blitterswijk CA, Hesseling SC, Grote JJ, Koerten HK, de Groot K. The biocompatibility of hydroxyapatite ceramic: A study of retrieved human middle ear implants. J Biomed Mater Res. 1990;24:433-53.
[75] Jarcho M, Kay JF, Gumaer KI, Doremus RH, Drobeck HP. Tissue, cellular, and subcellular events at a ceramic hydroxyaptite bone interface. J Bioeng. 1977;1:79-92.
[76] Nery EB, Lynch KL, Hirthe WM, Mueller KH. Bioceramic Implants in Surgically Produced Infrabony Defects. Periodontology. 1975;46:328-47.
[77] Winter M, Griss P, de Groot K, Tagai H, Heimke G, van Dijk HJA, et al. Comparative histocompatibility testing of seven calcium phosphate ceramics. Biomaterials. 1981;2:159
[78] Klawitter JJ, Hulbert SF. Application of porous ceramics for the attachment of load bearing orthopedic applications. J Biomed Mater Res Symp. 1971;2:161.
[79] Signs SA, Bajpai PKV, Pantano CG. In vitro Dissolution of Synthos Ceramics in an Acellular Physiological Environment. Biomater Med Dev Artif Organs. 1979;7:183-90.
[80] Bhaskar SN, Brady JM, Getter L, Grower F, Driskell T. Biodegradable Ceramic Implants in Bone. Oral Surg. 1971;32:336-46.

[81] Levin MP, Getter L, Cutright DE, Bhaskar SN. Biodegradable Ceramic in Periodontal Defects. Oral Surg. 1974;38:344-50.
[82] Cameron HU, MacNab I, Pillar RM. Evaluation of a Biodegradable Ceramic. J Biomed Muter Res 1977;11:179-85.
[83] Bielecki S, Krystoynowicz A, Turkiewicz M, Kalinowska H. Bacterial cellulose. In: Vandamme EJ, De Baets S, Steinb A, editors. Biopolymers: Vol 5, Polysaccharides I, Polysaccharides from Prokaryotes. Weinham: Wiley; 2001. p. 37–46.
[84] Hutchens S. Synthesis and Initial Characterization of a Calcium-Deficient Hydroxyapatite-Bacterial Cellulose Composite. Knoxville: The University of Tennessee - Knoxville; 2004.
[85] White DG, Brown Jr. RM. Prospects for the commercialization of the biosynthesis of microbial cellulose. In: Schuerch C, editor. Cellulose and Wood – Chemistry and Technology. New York: Wiley; 1989. p. 573-90.
[86] Czaja WK, Young DJ, Kawecki M, Brown RM. The Future Prospects of Microbial Cellulose in Biomedical Applications. Biomacromolecules. 2006;8:1-12.
[87] Helenius G, Bäckdahl H, Bodin A, Nannmark U, Gatenholm P, Risberg B. In vivo biocompatibility of bacterial cellulose. J Biomed Mater Res A. 2006;76A:431-8.
[88] Nishi Y, Uryu M, Yamanaka S, Watanabe K, Kitamura N, Iguchi M, et al. The structure and mechanical properties of sheets prepared from bacterial cellulose. Journal of Mater Sci. 1990;25:2997-3001.
[89] Fang B, Wan Y-Z, Tang T-T, Gao C, Dai K-R. Proliferation and osteoblastic differentiation of human bone marrow stromal cells on hydroxyapatite/bacterial cellulose nanocomposite scaffolds. Tissue Eng Part A. 2009;15:1091-8.
[90] Kucharzewski M, Slezak A, Franek A. Topical treatment of non-healing venous leg ulcers by cellulose membrane. Phlebologie. 2003;32:138-69.
[91] Klemm D, Schumann D, Udhardt U, Marsch S. Bacterial synthesized cellulose — artificial blood vessels for microsurgery. Prog Polym Sci. 2001;26:1561-603.
[92] Hutchens SA, León RV, O'Neill HM, Evans BR. Statistical analysis of optimal culture conditions for Gluconacetobacter hansenii cellulose production. Lett Appl Microbiol. 2007;44:175-80.
[93] Svensson A, Nicklasson E, Harrah T, Panilaitis B, Kaplan DL, Brittberg M, et al. Bacterial cellulose as a potential scaffold for tissue engineering of cartilage. Biomaterials. 2005;26:419-31.
[94] Nevell TP. Oxidation. In: Histler RL, editor. Methods in carbohydrate chemistry. New York: Academic Press; 1963. p. 164–89.
[95] Bäckdahl H, Esguerra M, Delbro D, Risberg B, Gatenholm P. Engineering microporosity in bacterial cellulose scaffolds. J Tissue Eng Regen Med. 2008;2:320-30.
[96] Zaborowska M, Bodin A, Bäckdahl H, Popp J, Goldstein A, Gatenholm P. Microporous bacterial cellulose as a potential scaffold for bone regeneration. Acta Biomater. 2010;6:2540-7.
[97] Watanabe K, Eto Y, Takano S, Nakamori S, Shibai H, Yamanaka S. A new bacterial cellulose substrate for mammalian cell culture. Cytotechnology. 1993;13:107-14.
[98] Nevell TP. Oxidation of cellulose. In: Nevell TP, Zeronian SH, editors. Cellulose chemistry and its applications. New York: Ellis Horwood Limited; 1985. p. 243-65.

[99] Guarino V, Urciuolo F, Alvarez-Perez MA, Mele B, Netti PA, Ambrosio L. Osteogenic differentiation and mineralization in fibre-reinforced tubular scaffolds: theoretical study and experimental evidences. J R Soc Interface. 2012;9:2201-12.
[100] Ustundag CB, Kaya F, Kamitakahara M, Kaya C, Ioku K. Production of tubular porous hydroxyapatite using electrophoretic deposition. J Ceram Soc Jpn. 2012;120:569-73.
[101] Berner A, Boerckel JD, Saifzadeh S, Steck R, Ren J, Vaquette C, et al. Biomimetic tubular nanofiber mesh and platelet rich plasma-mediated delivery of BMP-7 for large bone defect regeneration. Cell Tissue Res. 2012;347:603-12.
[102] Kim B-S, Kang HJ, Lee J. Improvement of the compressive strength of a cuttlefish bone-derived porous hydroxyapatite scaffold via polycaprolactone coating. J Biomed Mater Res B. 2013;101:1302-9.
[103] Wang J, Wan Y, Huang Y. Immobilisation of heparin on bacterial cellulose-chitosan nano-fibres surfaces via the cross-linking technique. IET Nanobiotechnol 2012 6:52-7.
[104] Putra A, Kakugo A, Furukawa H, Gong JP, Osada Y. Tubular bacterial cellulose gel with oriented fibrils on the curved surface. Polymer. 2008;49:1885-91.
[105] Lyu S, Huang C, Yang H, Zhang X. Electrospun fibers as a scaffolding platform for bone tissue repair. J Orthop Res. 2013;31:1382-9.
[106] Favi PM, Benson RS, Neilsen NR, Hammonds RL, Bates CC, Stephens CP, et al. Cell proliferation, viability, and in vitro differentiation of equine mesenchymal stem cells seeded on bacterial cellulose hydrogel scaffolds. Mater Sci Eng C Mater Biol Appl. 2013;33:1935-44.
[107] Favi PM, Dhar MS, Neilsen NR, Benson RS. Proliferation and osteogenic differentiation of mesenchymal stem cells on biodegradable calcium-deficient hydroxyapatite tubular bacterial cellulose composites. (In Press). In: MRS, editor. Mater Res Soc Symp Proc. Boston, MA: Materials Research Society; 2013.
[108] Schramm M, Hestrin S. Factors affecting Production of Cellulose at the Air/ Liquid Interface of a Culture of Acetobacter xylinum. J Gen Microbiol. 1954;11:123-9.
[109] Evans BR, O'Neill HM, Malyvanh VP, Lee I, Woodward J. Palladium-bacterial cellulose membranes for fuel cells. Biosens Bioelectron. 2003;18:917-23.
[110] Ma PX, Choi J-W. Biodegradable Polymer Scaffolds with Well-Defined Interconnected Spherical Pore Network. Tissue Eng. 2001;7:23-33.
[111] Hossain ME, Ketata C, Mann H, Islam MR. SEM-based structural and chemical analysis of paraffin wax and beeswax for petroleum applications J Charact Dev Novel Mater. 2009;1:21-38.
[112] Peterson EA, Sober HA. Chromatography of Proteins. I. Cellulose Ion-exchange Adsorbents. J Am Chem Soc. 1956;78:751-5.
[113] Smith WF. Foundations of materials science and engineering. 2nd ed. Columbus: McGraw-Hill, Inc.; 1993.
[114] Dulbecco R, Vogt M. Plaque formation and isolation of pure lines with poliomyelitis viruses. J Exp Med. 1954;99:167-82.
[115] Buttafoco L, Kolkman NG, Engbers-Buijtenhuijs P, Poot AA, Dijkstra PJ, Vermes I, et al. Electrospinning of collagen and elastin for tissue engineering applications. Biomaterials. 2006;27:724.

[116] Neal RA, McClugage III SG, Link MC, Sefcik LS, Ogle RC, Botchwey EA. Laminin nanofiber meshes that mimic morphological properties and bioactivity of basement membranes. Tissue Eng Part C. 2009;15:11-21.
[117] Yang J, Shi G, Bei J, Wang S, Cao Y, Shang Q, et al. Fabrication and surface modification of macroporous poly(L-lactic acid) and poly(L-lactic-co-glycolic acid) (70/30) cell scaffolds for human skin fibroblast cell culture. J Biomed Mater Res. 2002;62:438-46.
[118] Chalmers JM, Everall NJ. Vibrational spectroscopy. In: Hunt BJ, James MI, editors. Polymer characterization. London, UK: Blackie Academic and Professional; 1993.
[119] Carraher Jr. CE. Carraher's Polymer Chemistry. 8th ed. Boca Raton: CRC Press; 2011.
[120] Moeur HP, Pinnell RP. Use of the Disposable IR Card in the Organic Chemistry Laboratory. J Chem Educ. 1996;73:371.
[121] Graf RT, Koenig JL, Ishida H. Comparison of FT-IR transmission, spectral reflectance and attenuated total reflectance spectra of polymers. In: Ishida H, editor. Fourier transform infrared charracterization of polymers. New York: Plenum Press; 1987.
[122] Garton A. Infrared Spectroscopy of Polymer Blends: Composites and Surfaces. 1st ed. Munich Hanser Publishers; 1992.
[123] Wetton RE. Thermal analysis. In: Hunt BJ, James MI, editors. Polymer characterization. London, UK: Blackie Academic and Professional; 1993.
[124] ASTM. Standard test method for transition temperatures and enthalpies of fusion and crystallization of polymers by differential scanning calorimetry. ASTM D3418-08. West Conshohocken, PA: ASTM International; 2008.
[125] Askeland D, Fulay P. The science and engineering of materials. 5th ed. Stamford, CT: Cengage Learning; 2006.
[126] ASTM. Standard test method for tensile properties of thin plastic sheeting. ASTM D882-09. West Conshohocken, PA: ASTM International; 2009.
[127] Bourzac C, Smith LC, Vincent P, Beauchamp G, Lavoie JP, Laverty S. Isolation of equine bone marrow-derived mesenchymal stem cells: a comparison between three protocols. Equine Vet J. 2010;42:519-27.
[128] Dhar M, Neilsen N, Beatty K, Eaker S, Adair H, Geiser D. Equine peripheral blood-derived mesenchymal stem cells: Isolation, identification, trilineage differentiation and effect of hyperbaric oxygen treatment. Equine Vet J. 2012;44:600-5.
[129] Nordestgaard BG, Rostgaard J. Critical-point drying versus freeze drying for scanning electron microscopy: a quantitative and qualitative study on isolated hepatocytes. J Microsc. 1985;137:189-207.
[130] Karande TS, Ong JL, Agrawal CM. Diffusion in Musculoskeletal Tissue Engineering Scaffolds: Design Issues Related to Porosity, Permeability, Architecture, and Nutrient Mixing. Annals of Biomedical Engineering. 2004;32:1728-43.
[131] Yang S, Leong K-F, Du Z, Chua C-K. The Design of Scaffolds for Use in Tissue Engineering. Part I. Traditional Factors. Tissue Engineering. 2001;7:679-89.
[132] Bäckdahl H, Helenius G, Bodin A, Nannmark U, Johansson BR, Risberg B, et al. Mechanical properties of bacterial cellulose and interactions with smooth muscle cells. Biomaterials. 2006;27:2141-9.

[133] Dominici M, Le Blanc K, Mueller I, Slaper-Cortenbach I, Marini FC, Krause DS, et al. Minimal criteria for defining multipotent mesenchymal stromal cells. The International Society for Cellular Therapy position statement. Cytotherapy. 2006;8:315-7.
[134] Shapiro HM. Practical flow cytometry. 4th ed. Hoboken: John Wiley & Sons, Inc.; 2003.
[135] Mafi P, Hindocha S, Mafi R, Griffin M, Khan WS. Adult Mesenchymal Stem Cells and Cell Surface Characterization - A Systematic Review of the Literature. Open Orthop J 2011;5:253-60.
[136] Garg HG, Warren CD, Siebert JW. Chemistry of scarring. In: Garg HG, Longaker MT, editors. Scarless wound healing. New York: Dekker; 2000. p. 1-22.
[137] Barltrop JA, Owen TC, Cory AH, Cory JG. 5-(3-carboxymethoxyphenyl)-2-(4,5-dimethylthiazolyl)-3-(4-sulfophenyl)tetrazolium, inner salt (MTS) and related analogs of 3-(4,5-dimethylthiazolyl)-2,5-diphenyltetrazolium bromide (MTT) reducing to purple water-soluble formazans As cell-viability indicators. Bioorg Med Chem Lett. 1991;1:611-4.
[138] Lo CM, Wang HB, Dembo M, Wang YL. Cell movement is guided by the rigidity of the substrate. Biophys J. 2000;79:144-52.
[139] Paszek MJ, Boettiger D, Weaver VM, Hammer DA. Integrin Clustering Is Driven by Mechanical Resistance from the Glycocalyx and the Substrate. PLoS Comput Biol. 2009;5:e1000604.
[140] Yeung T, Georges PC, Flanagan LA, Marg B, Ortiz M, Funaki M, et al. Substrate stiffness on cell morphology, cytoskeletal structure, and adhesion. Cell Motil Cytoskeleton. 2005;60:24-34.
[141] Saltzman WM, Kyriakides TR. Cell interactions with polymers. In: Lanza R, Langer R, Vacanti JP, editors. Principles of tissue engineering. 3rd ed. Amsterdam: Elsevier Science; 2007. p. 279–96.
[142] Cheremisinoff NP. Advanced Polymer Processing Operations. Westwood, NJ: Noyes Publications; 1998.
[143] Rivenc R, Schilling MR. Comparative Study of Three Different Kinetic Models Applied to the Ageing of Archaeological Beeswax Used as a Paint Medium. J Therm Anal Calorim. 2008;93:245.
[144] Tulloch AP. The composition of beeswax and other waxes secreted by insects. Lipids 1969;5:247-58.
[145] Tulloch AP. Beeswax: Structure of the esters and their component hydroxy acids and diols. . Chem Phys Lipids. 1971;6:235-65.
[146] Buchwald R, Breed MD, Greenberg AR. The thermal properties of beeswaxes: unexpected findings. J Exp Biol. 2008;211:121-7.
[147] Bodin A, Bharadwaj S, Wu S, Gatenholm P, Atala A, Zhang Y. Tissue-engineered conduit using urine-derived stem cells seeded bacterial cellulose polymer in urinary reconstruction and diversion. Biomaterials. 2010;31:8889e901.
[148] Salmen L, Akerholm M, Hinterstoisser B. Two-dimensional Fourier transform infrared spectroscopy applied to cellulose and paper. In: Dumitriu S, editor. Polysaccharides structural diversity and functional versatility. 2nd ed. 2005: Marcel Dekker; 2005. p. 159-87.

[149] Kondo T. Hydrogen bonds in cellulose and cellulose derivatives. In: Dumitriu S, editor. Polysaccharides: Structural diversity and functional versatility. New York: Marcel Dekker, Inc.; 1998. p. 131-72.
[150] Marchessault RH, Sundarajan PR. Cellulose. In: Aspinall GO, editor. The Polysaccharides Volume 21983. p. 11-95.
[151] Bellamy LJ. The infrared spectra of complex molecules. 3rd ed. London, UK: Chapman and Hall; 1975.
[152] Pan Z, Ding J. Poly(lactide-co-glycolide) porous scaffolds for tissue engineering and regenerative medicine. Interface Focus. 2012;2:366-77.
[153] Berry DA. Glycosaminoglycan regulation of cell function [PhD]. Cambridge: Massachusetts Institute of Technology; 2005.
[154] Antonio JDS, Iozzo RV. Glycosaminoglycans: Structure and Biological Functions. eLS: John Wiley & Sons, Ltd; 2001.
[155] Handel TM, Johnson Z, Crown SE, Lau EK, Sweeney M, Proudfoot AE. Regulation of protein function by glycosaminoglycans - as exemplified by chemokines. Annu Rev Biochem2005. p. 385-410.
[156] Hudalla GA, Koepsel JT, Murphy WL. Surfaces That Sequester Serum-Borne Heparin Amplify Growth Factor Activity. Adv Mater. 2011;23:5415-8.
[157] Berg JM, Tymoczko JL, Stryer L. Biochemistry. 7th ed. New York: W. H. Freeman; 2010.
[158] Coleman MM, Painter PC. Infrared analysis. In: Simon GP, editor. Polymer characterization techniques and their application to blends. Oxford, UK: Oxford University Press; 2003. p. 155-90.
[159] Richards GN. Alkaline degradation. In: Histler RL, editor. Methods in carbohydrate chemistry. New York: Academic Press; 1963. p. 154-64.
[160] Martens W, Frost RL. An infrared spectroscopic study of the basic copper phosphate minerals: corneite, libethenite, and pseudomalachite. American Mineralogist. 2003;88:37-46.
[161] Rehman I, Bonfield W. Characterization of hydroxyapatite and carbonated apatite by photo acoustic FTIR spectroscopy. J Mat Sci: Mat in Med. 1997;8:1-4.
[162] Wilson RM, Elliott JC, Dowker SEP, M. R-LL. Rietveld refinements and spectroscopic studies of the structure of Ca-deficient apatite. Biomaterials. 2005;26:1317-27.
[163] Lee H, Chung HJ, Park TG. Design principles in biomaterials and scaffolds. In: Atala A, Lanza R, Thomson J, editors. Principles of regenerative medicine. 2nd ed. London, UK: Elsevier; 2010.
[164] Xie X, Wang Y, Zhao C, Guo S, Liu S, Jia W, et al. Comparative evaluation of MSCs from bone marrow and adipose tissue seeded in PRP-derived scaffold for cartilage regeneration. Biomaterials. 2012;33:7008-18.
[165] Bernabé PFE, Melo LGN, Cintra LTA, Gomes-Filho JE, Dezan Jr E, Nagata MJH. Bone healing in critical-size defects treated with either bone graft, membrane, or a combination of both materials: a histological and histometric study in rat tibiae. Clin Oral Implants Res. 2012;23:384-8.

APPENDIX

Appendix A

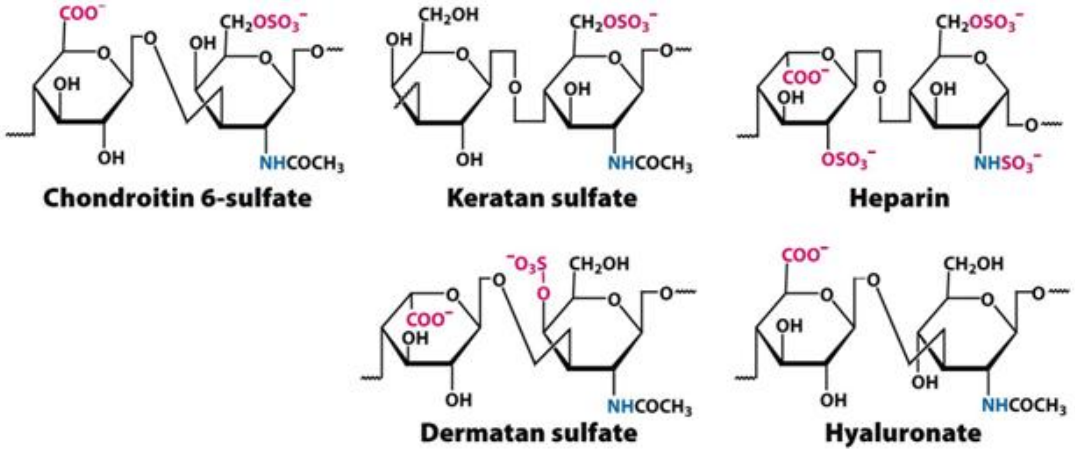

Figure A.1: Chemical structure of glycosaminoglycan chains including chondroitin 6-sulfate, keratan sulfate, heparin, dermatan sulfate and hyaluronate [157] .

VITA

Pelagie Marlene Favi was born in Natitingou, Benin, West Africa on September 23, 1980. She spent her early formative years living in Cotonou, Benin, West Africa. She moved to Bozeman, Montana, USA in her early teens with her family. She graduated from Bozeman High School, in Bozeman, Montana, in 1998.

She received her Bachelor's of Science degree in Chemical Engineering from Montana State University in May 2003. After graduating from Montana State University, Pelagie moved to Richmond, Virginia. There she worked for Altria Client Services (formerly Philip Morris USA) from 2003 to 2010 as an engineer in various organizations within the company including Product Assessment, Product Planning and Engineering, Product Manufacturing, and Product Design and Technology.

While working as an engineer, Pelagie attended Virginia Commonwealth University and continued her education in their masters' graduate program. She received her Masters' of Science degree in Biomedical Engineering from Virginia Commonwealth University in May 2008 under the supervision of Dr. Gary Bowlin. Her masters' thesis focused on using the electrospining technology to produce and evaluate biodegradable polymer blends for application as vascular prosthesis for small arteries (< 6 mm).

In August 2010, she enrolled in The University of Tennessee's graduate program to continue her education as a doctoral student. She is currently pursuing her Doctorate Degree in Polymer Engineering under the guidance of Dr. Roberto Benson in the Department of Materials Science and Engineering.